

Dissertation zur Erlangung des Doktorgrades der Fakultät für Chemie und Pharmazie
der Ludwig-Maximilians-Universität München

**Structural studies of 70S ribosomes in the presence
of antimicrobial agents**



Michael Graf

aus

Würselen, Deutschland

2018

Erklärung

Diese Dissertation wurde im Sinne von § 7 der Promotionsordnung vom 28. November 2011 von Herrn Prof. Dr. Daniel N. Wilson betreut.

Eidesstattliche Versicherung

Diese Dissertation wurde eigenständig und ohne unerlaubte Hilfe erarbeitet.

München, 08.05.2018

(Michael Graf)

Dissertation eingereicht am 08.05.2018

1. Gutachter: Herr Prof. Dr. Daniel N. Wilson
2. Gutachter: Herr Prof. Dr. Roland Beckmann

Mündliche Prüfung am 20.06.2018

Table of contents

Acknowledgements	V
List of original publications	VII
Contributions report	X
Abbreviations	XIII
Summary	XVI
1 Introduction	1
1.1 Bacterial translation machinery	1
1.2 Bacterial translation	4
1.2.1 Translation initiation	6
1.2.2 Translation elongation	9
1.2.3 Translation termination	21
1.2.4 Ribosome recycling	26
1.2.5 Interaction of L7/L12 with translational GTPases	27
1.3 Plastid-derived ribosomes	28
1.4 Antimicrobial peptides	34
1.4.1 Synthesis of PrAMPs	36
1.4.2 Uptake pathway of PrAMPs	37
1.4.3 Discovery of the intracellular target of PrAMPs	38
1.4.4 Determination of the ribosomal binding site of PrAMPs	39
2 Objectives of these studies	41
3 Cumulative thesis: Summary of publications	43
3.1 Publication 1 - Visualization of translation termination intermediates during RF3-mediated recycling of RF1	43
3.2 Publication 2 - Cryo-EM structure of the spinach chloroplast ribosome reveals the location of plastid-specific ribosomal proteins and extensions	44
3.3 Publication 3 - The proline-rich antimicrobial peptide Onc112 inhibits translation by blocking and destabilizing the initiation complex	45
3.4 Publication 4 - Structure of the mammalian antimicrobial peptide Bac7(1-16) bound within the exit tunnel of a bacterial ribosome	47
3.5 Publication 5 - Proline-rich antimicrobial peptides targeting protein synthesis	48
3.6 Publication 6 - An antimicrobial peptide that inhibits translation by trapping release factors on the ribosome	49
4 Discussion	51
4.1 Chloroplast ribosomes	51

4.2 Class I release factor recycling by RF3.....	53
4.3 Antimicrobial peptides.....	61
5 References	81
6 Publications	101

Acknowledgements

I would like to say thank you to Prof. Daniel N. Wilson for taking me as a PhD student and his restless efforts to train and supervise me. His lab constituted the best possible environment to conduct my work. Moreover, I am glad for every discussion, criticism and every little advice that helped me to improve my working habits. I had almost no restrictions and was able to improve my biochemical, computational and organizational skills. I could not imagine a better place to obtain my PhD degree.

I would like to thank Prof. Roland Beckmann for his expertise and the provided scientific environment which played a key role during my time in Munich and was indispensable for numerous publications.

Further I am grateful for the Munich EM facility with Dr. Otto Berninghausen, Charlotte Ungewickell and Susanne Rieder who played a major role in preparation of samples and the subsequent collection of high-resolution cryo-EM data.

I am glad for the help provided by Dr. Stefan Arenz. Stefan was crucial for introducing me to cryo-EM and he was always willing to discuss and solve problems. Furthermore, he helped me and others in hopeless situations, which interfered with our projects.

I want to thank Paul Huter for granting calmness and his efforts during manuscript preparations.

I would like to thank Dr. Thomas Becker, André Heuer and Dr. Christian Schmidt from the Beckmann lab for supportive discussions, for computational knowledge and provided resources.

Further I want to say thanks to Joanna Musial, Heidemarie Sieber for help with orders and Andrea Gilmozzi.

I want to say thank you to Romy Böttcher for making work and especially the morning a pleasure.

I would like to say thank you to Daniela Hess-Otto for being the framework of the laboratory in Hamburg. Daniela is indispensable for organizational issues, made our work easier and helped us to focus on our own scientific work.

I am glad for help from Caillan Crowe-McAuliffe who provided comments on manuscripts and was essential to create a nice working atmosphere in Hamburg.

Further I would like to say thank you to Dr. Bertrand Beckert for his helpful comments and advices.

In general, I want to say thanks to all our collaborators. Special thanks I want to address to Dr. Nora Vazquéz-Laslop and Prof. Alexander S. Mankin who accepted me as student for my master thesis in Chicago and were essential for my orientation in the ribosomal field. Moreover, as collaborators, they provided ideas and helped to discuss our obtained data.

Finally, I would like to say thank you to the greatest of all: Sarah. I am grateful for your help, support and advices. You helped me to stay calm and productive. You were essential for my whole work and indispensable for finishing my PhD.

List of original publications

Publication 1

Graf, M., Huter, P., Maracci, C., Peterek, M., Rodnina, M.V. and Wilson, D.N. (2018). Visualization of translation termination intermediates during RF3-mediated recycling of RF1. *Nature Communications*. (accepted)

Publication 2

Graf, M., Arenz, S., Huter, P., Donhofer, A., Novacek, J., and Wilson, D.N. (2017a). Cryo-EM structure of the spinach chloroplast ribosome reveals the location of plastid-specific ribosomal proteins and extensions. *Nucleic Acids Research*. 45, 2887-2896.

Publication 3

Seefeldt, A.C.*, Nguyen, F.*, Antunes, S.*, Perebaskine, N., **Graf, M.**, Arenz, S., Inampudi, K.K., Douat, C., Guichard, G., Wilson, D.N., et al. (2015). The proline-rich antimicrobial peptide Onc112 inhibits translation by blocking and destabilizing the initiation complex. *Nature Structural & Molecular Biology*. 22, 470-475.

Publication 4

Seefeldt, A.C.*, **Graf, M.***, Perebaskine, N., Nguyen, F., Arenz, S., Mardirossian, M., Scocchi, M., Wilson, D.N., and Innis, C.A. (2016). Structure of the mammalian antimicrobial peptide Bac7(1-16) bound within the exit tunnel of a bacterial ribosome. *Nucleic Acids Research*. 44, 2429-2438.

Publication 5

Graf, M.*, Mardirossian, M.* , Nguyen, F.* , Seefeldt, A.C., Guichard, G., Scocchi, M., Innis, C.A., and Wilson, D.N. (2017b). Proline-rich antimicrobial peptides targeting protein synthesis. *Natural Product Reports*. 34, 702-711.

Publication 6

Florin, T.*, Maracci, C.*, Graf, M.*, Karki, P., Klepacki, D., Berninghausen, O., Beckmann, R., Vazquez-Laslop, N., Wilson, D.N., Rodnina, M.V., Mankin, A.S. (2017). An antimicrobial peptide that inhibits translation by trapping release factors on the ribosome. ***Nature Structural & Molecular Biology***. 24, 752-757.

*These authors contributed equally to this work.

List of publications not included in this thesis:

Publication 7

Arenz, S., Bock, L.V., **Graf, M.**, Innis, C.A., Beckmann, R., Grubmuller, H., Vaiana, A.C., and Wilson, D.N. (2016). A combined cryo-EM and molecular dynamics approach reveals the mechanism of ErmBL-mediated translation arrest. ***Nature communications***. 7, 12026.

Publication 8

Arenz, S., Juette, M.F., **Graf, M.**, Nguyen, F., Huter, P., Polikanov, Y.S., Blanchard, S.C., and Wilson, D.N. (2016). Structures of the orthosomycin antibiotics avilamycin and evernimicin in complex with the bacterial 70S ribosome. ***Proceedings of the National Academy of Sciences USA***. 113, 7527-7532.

Publication 9

Prunetti, L., **Graf, M.**, Blaby, I.K., Peil, L., Makkay, A.M., Starosta, A.L., Papke, R.T., Oshima, T., Wilson, D.N., and de Crecy-Lagard, V. (2016). Deciphering the Translation Initiation Factor 5A Modification Pathway in Halophilic Archaea. ***Archaea***. 2016, 7316725.

Publication 10

Huter, P., Arenz, S., Bock, L.V., **Graf, M.**, Frister, J.O., Heuer, A., Peil, L., Starosta, A.L., Wohlgemuth, I., Peske, F., et al. (2017). Structural Basis for Polyproline-Mediated Ribosome Stalling and Rescue by the Translation Elongation Factor EF-P. ***Molecular Cell***. 68, 515-527 e516.

Contributions report

This PhD thesis describes work conducted under supervision of Prof. Daniel N. Wilson between November 2014 and April 2018 at the Gene Center Munich and the University of Hamburg. Many results of this work were obtained in collaboration with the laboratories of Prof. Roland Beckmann (Gene Center Munich), Prof. Axel C. Innis (University of Bordeaux), Prof. Alexander S. Mankin (University of Illinois at Chicago), Prof. Marina V. Rodnina (Max-Planck Institute Göttingen) and Prof. Marco Scocchi (University of Trieste). Cryo-EM data were collected by Dr. Otto Berninghausen (Beckmann lab), as well as Miroslav Peterek and Dr. Jiří Nováček from CEITEC Brno.

Publication 1 (Graf et al., 2018)

This study reports structural data on RF3-mediated recycling of the class I release factor RF1 from the *Escherichia coli* 70S ribosome and provides biochemical data on L7/L12 facilitated recruitment of RF1. I contributed to the publication in terms of cryo-EM sample preparation by *in vitro* reconstitution of the 70S complex. I processed the collected data and subsequently generated the molecular model, contributed to interpretation of the models and performed the rotation analysis of the obtained 70S ribosome states. I prepared all figures and assisted in manuscript writing.

Publication 2 (Graf et al., 2017a)

This publication presents the structure of the Spinach chloroplast ribosome at an average resolution of 3.6 Å for the large subunit and 5.4 Å for the small subunit. The structure describes the position of plastid-specific ribosomal proteins, as well as N- and C-terminal protein extensions of chloroplast ribosomal proteins. I performed the cryo-EM data analysis and generated the molecular model for the chloroplast ribosome. Furthermore, I contributed to the interpretation of the structural model and the preparation of the figures and assisted in writing of the manuscript.

Publication 3 (Seefeldt et al., 2015)

In this publication, the first structure of a PrAMP, namely Onc112, bound to the *Thermus thermophilus* 70S ribosome is reported. This publication further provides supporting biochemistry showing binding of Onc112 to the ribosome and inhibition of bacterial protein synthesis. I performed toe-print assays for this study (Figure 3b), which show inhibition of protein synthesis at translation initiation. Furthermore, I contributed to writing of this manuscript.

Publication 4 (Seefeldt et al., 2016)

This study reports the structure of Bac7, metalnikowin and pyrrhocoricin bound to the *Thermus thermophilus* 70S ribosome, as well as biochemical data on PrAMP binding, inhibition of protein synthesis and competition with the macrolide erythromycin in the polypeptide exit tunnel. I performed the erythromycin competition assays and the toe-print assays in this manuscript. The results of these assays show that all PrAMPs stall ribosomes at translation initiation and compete with binding of macrolide antibiotics. I prepared figures 3b, 4c and 5c. Moreover, I was involved in the manuscript preparation.

Publication 5 (Graf et al., 2017b)

This publication reviews the discovery, synthesis and cellular uptake of PrAMPs, as well as biochemical studies, which led to the identification of ribosomes as the primary target for PrAMPs. Furthermore, the publication reviews the structural data available on the *Thermus thermophilus* 70S ribosome-bound PrAMPs Onc112, Bac7, pyrrhocoricin and metalnikowin. I prepared all figures and contributed to the writing of the manuscript.

Publication 6 (Florin et al., 2017)

This publication reports biochemistry and the structure of the PrAMP Api137 in complex with post-hydrolysis 70S ribosomes from *Escherichia coli*. I performed biochemical disome assays, which led to the sample used for cryo-EM analysis. I

processed and analyzed the cryo-EM data and generated the molecular model of the complete 70S ribosome, which harbors RF1, deacyl-tRNA and Api137. In addition, I contributed to interpretation of the model and helped to write the manuscript. With regard to figures, I prepared figures 3 and 4, as well as supplementary figures 4, 5 and 6.

Abbreviations

2D	two-dimensional
A	adenine
A-site/-tRNA	acceptor site/tRNA
aa-tRNA	aminoacyl-tRNA
AMP	antimicrobial peptide
Api	apidaecin
ASD	anti-Shine-Dalgarno
ASL	anticodon stem loop
Bac	bactenecin
C	cytosine
cpL#	chloroplast protein # of the large subunit
cpS#	chloroplast protein # of the small subunit
Cryo-EM	cryo electron microscopy
CTD	C-terminal domain
CTE	C-terminal extension
D-arm	dihydrouridine harboring tRNA tertiary structure feature
DC	decoding center
DNA	deoxyribonucleic acid
Dro	drosocin
E-site/-tRNA	exit site/tRNA
EF-G	elongation factor GTPase
EF-Tu	elongation factor thermo-unstable
fMet	formyl-methionine
G-domain	GTPase domain
GAC	GTPase-associated center
GDP	guanosine-5'-diphosphate
GDPCP	5'-guanosyl-methylene-triphosphate
GDPNP	guanosine-5'-[β , γ -imido]-triphosphate
GTP	guanosine-5'-triphosphate
h#	helix # of the small ribosomal subunit
H#	helix# of the large ribosomal subunit
IC	initiation complex

IF	initiation factor
kDa	kilodalton
L#	large subunit protein #
LSU	(50S) large subunit
MDa	megadalton
Met	metalnikowin
MIC	minimal inhibitory concentration
N-state	non-rotated state 70S ribosome
NPET	nascent polypeptide exit tunnel
nt	nucleotide
NTD	N-terminal domain
NTE	N-terminal extension
Onc	oncocin
ORF	open reading frame
P-site/-tRNA	peptidyl site/tRNA
P _i	inorganic phosphate
PIC	pre-initiation complex
P _{int} -tRNA	intermediate state peptidyl tRNA
POST	post-translocation 70S ribosome
PoTC	post-termination complex
PrAMP	proline-rich antimicrobial peptide
PRE	pre-translocation 70S ribosome
PSRP	plastid-specific ribosomal protein
PTC	peptidyl transferase center
Pyr	pyrrhocoricin
R-state	rotated state 70S ribosome
RF	release factor
RNA	ribonucleic acid
mRNA	messenger RNA
rRNA	ribosomal RNA
tRNA	transfer RNA
RNC	ribosome nascent chain complex
r-Protein	ribosomal protein
RRF	ribosome recycling factor

S#	small subunit protein #
SD	Shine-Dalgarno
SRL	sarcin-ricin loop
SRP	signal recognition particle
SSER	systematic selection of functional sequences by enforced replacement
SSU	(30S) small subunit
T	thymine
T-arm	TΨC-arm; tertiary structure feature of a tRNA containing residues T, Ψ and C
U	uridine
Ψ	pseudouridine

Summary

During the process of protein synthesis, the ribosome translates mRNA-encoded nucleotide triplets (codons) into a polypeptide sequence using tRNA molecules as adapters. Starting with translation initiation, which comprises the placement of the 70S ribosome on the AUG start codon, protein synthesis further passes through the stages of translation elongation and translation termination. Each of these steps utilizes additional translation factors, which greatly increase translation fidelity and speed. The process of translation termination involves release factors RF1, RF2 and RF3. While RF1 and RF2 mediate the release of a nascent polypeptide from the 70S ribosome upon stop codon selection, RF3 facilitates the recycling of RF1 and RF2 after polypeptide release. We obtained cryo-EM structures of intermediate states of RF3-mediated recycling of RF1 and show that RF3 binding induces SSU rotation. RF3-induced SSU rotation ultimately leads to formation of rotated state ribosomes with P/E hybrid state tRNAs. RF3 moves as rigid-body with the SSU. RF3-induced SSU rotation fulfills a dual function. First, SSU rotation mediates accommodation of the G-domain of RF3 on the LSU and second, leads to destabilization of RF1 on the 70S ribosome. With regard to the recruitment of termination factors, our study shows that RF1 is recruited by L7/L12 to the ribosome. Consistently, we observe in one intermediate state density next to domain I of RF1, which can be assigned to one CTD of L7/L12. Knowing the exact mechanism of RF3 action may help in future to develop new antimicrobial agents that can be used in a clinical context.

Generally, various clinically relevant antibiotics target bacterial translation and thus allow infections to be fought without resulting in toxicity to the human body. However, the continuous rise in bacterial resistance highlights the need for new antibiotics that can be used to treat bacterial infections. Pro-rich antimicrobial peptides (PrAMPs) are a new promising source of antimicrobial agents, which show high potency against Gram-negative bacteria by interfering with protein synthesis, while exhibiting low toxicity in eukaryotes. PrAMPs are produced by the innate immune system of higher eukaryotes and are secreted in response to a bacterial infection. We report structural and biochemical data on PrAMP binding, as well as the exact mechanism of action. The binding site of all investigated PrAMPs is situated within nascent polypeptide exit tunnel. The mechanism of action allows class I PrAMPs to be distinguished from class II PrAMPs. Consistently, we show that class I PrAMPs, such

as Bac7, Onc112, pyrrhocoricin and metalnikowin block delivery of aa-tRNA by EF-Tu, whereas the class II PrAMP Api137 acts during translation termination and inhibits protein synthesis by trapping of RF1 on the 70S ribosome after the nascent chains have been released.

1 Introduction

Biochemistry embraces chemical reactions within living cells/organisms. As such, DNA replication, RNA transcription and protein synthesis (translation) constitute the three crucial chemical processes which are common in all living organisms and defined in the central dogma of molecular biology (Crick, 1958). Translation represents the last step of the central dogma in which the genetic information encoded in DNA is turned into a functional macromolecule, called protein. Although the genetic information is encoded in DNA, proteins are not decoded directly from DNA, but rather from messenger molecules which consist of RNA. These messenger ribonucleic acid (mRNA) molecules are generated during the process of transcription. DNA constitutes the template for the generation of mRNA. mRNA on the other hand functions as the template during translation in which nucleotide triplets (codons) are consecutively read from the 5' to 3' end, thereby dictating the exact sequence of the polymerized amino acids (primary sequence) (Crick et al., 1961). The nucleotide (nt) triplets are read from the mRNA by decoding factors, or transfer RNAs (tRNAs) that act as adaptors and carry the incorporated amino acid. In general, tRNAs exhibit a cloverleaf secondary structure with an acceptor stem, a T-arm, a D-arm and an anticodon stem (Holley et al., 1965; Kim et al., 1973). The amino acid is attached at the 3' acceptor end (CCA-end). Polymerization of a polypeptide is a unidirectional chemical process, which is characterized by the covalent linkage of an incoming amino-group to the carboxyl end (C-terminus) of a growing peptidyl moiety. The opposing end of a nascent polypeptide chain, which carries the first incorporated residue with a free amino-group, constitutes the N-terminus.

1.1 Bacterial translation machinery

The elongation of the liberated protein macromolecule is catalyzed by a large ribonucleoprotein complex, called a ribosome, which can be found in all kingdoms of life (McQuillen et al., 1959). The ribosome is the result of billions of years of evolution and consists of ribosomal RNA (rRNA) and ribosomal proteins. The ribosomal RNA (rRNA) builds up the catalytically active core of the machine, which is per definition a ribozyme (Ban et al., 2000; Cech, 2000; Hansen et al., 2002; Harms et al., 2001;

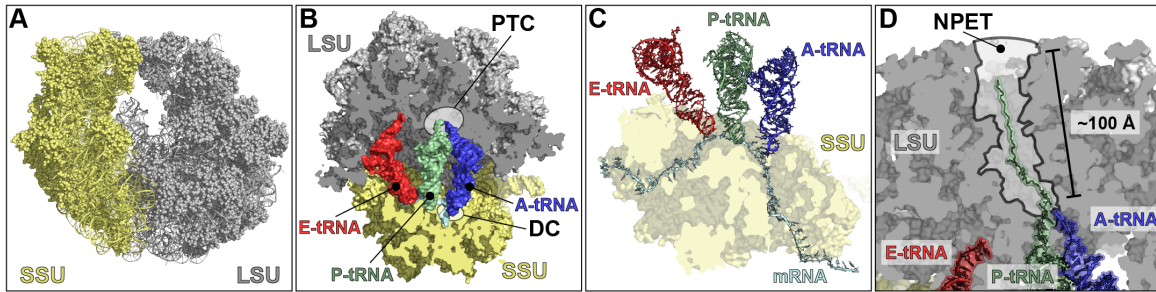


Figure 1 - Bacterial translation machinery. (A) Overview of the bacterial 70S ribosome consisting of a small 30S subunit (yellow) and a large 50S subunit (grey). (B) Transverse section of the 70S ribosome harboring an A-site tRNA (blue), a P-site tRNA (green) and an E-site tRNA (red). The catalytic centers on the LSU (grey) and the SSU (yellow) are highlighted by black contoured grey circles. The LSU harbors the peptidyl transferase center (PTC) and the SSU harbors the decoding center (DC). (C) Transverse section of the SSU (yellow) showing the path of the mRNA (cyan) and the mRNA-tRNA contact sites of A-site tRNA (blue), P-site tRNA (green), and E-site tRNA (red). (D) Overview of the LSU (grey) polypeptide exit tunnel (NPET) containing a nascent chain (MifM staller) attached to P-site tRNA (green). A-site (blue) and E-site tRNA (red) are shown for reference.

Nissen et al., 2000; Noller, 2012; Schlünzen et al., 2001). Ribosomal proteins are mostly bound to the surface with extensions reaching deeper into the translation machine. The catalytic core of the ribosome that possesses the activity for peptide bond formation, called the peptidyl transferase center (PTC), is especially highly conserved in all living organisms (Melnikov et al., 2012).

Overall, the eubacterial ribosome is a large (2.5 MDa) ribonucleoprotein particle consisting of a large ribosomal subunit (LSU, 50S) and a small ribosomal subunit (SSU, 30S) (Figure 1A) (Wilson and Nierhaus, 2005). The LSU and SSU come together to form a 70S ribosome (Figure 1A). The LSU consists of ~30 ribosomal proteins (33 proteins in *Escherichia coli*), one 23S and one 5S rRNA molecule (Nierhaus, 1991). The SSU contains ~20 ribosomal proteins (21 proteins in *E. coli*) and a single 16S rRNA molecule. LSU and SSU proteins are from here on designated with an 'L' or an 'S', respectively (e.g. SSU protein S5). Ribosomal proteins are synthetized by the classical translation pathway and ribosomal RNAs are transcribed directly from DNA (encoded in seven rRNA operons in *E. coli*) by RNA polymerases as one long immature RNA precursor. The immature precursors get post-transcriptionally processed by cleavage (Mathy et al., 2007; Nierhaus, 1991; Srivastava and Schlessinger, 1990) and modification (Chow et al., 2007), leading to the three different rRNAs. The mature rRNAs exhibit a complex three-dimensional structure which is characterized by distinct secondary structures, such as helices, and tertiary structures, such as domains. The LSU can be divided into six domains (I-VI) and the SSU can be divided into four domains, namely, the 5' domain (body), the central domain (platform), the 3' major domain (head) and the 3' minor domain (helix 44-45).

The LSU contains the catalytic activity for peptide bond formation in the PTC. The SSU facilitates decoding in the decoding center (DC) (Figure 1B) and plays a crucial role for the accuracy of the translation process. Just like the PTC, the key residues in the DC are formed by rRNA residues. The interactions between both subunits are maintained by eight major intersubunit bridges which involve RNA-RNA, protein-protein and RNA-protein interactions (Cate et al., 1999). Intersubunit bridges ensure the stability of the 70S ribosome and allow the coupling of the decoding capacities of the SSU on the one hand and the peptide transferase activity of the LSU on the other hand. Furthermore, the intersubunit bridges allow large conformational changes during the process of translation which are important for movement of tRNAs through the ribosome during translocation.

During protein synthesis adapter tRNAs bind to three distinct tRNA binding sites, called the aminoacyl (A) site, the peptidyl (P) site and the exit (E) site (Figure 1B), and establish codon-anticodon interactions with the protein encoding mRNA located on the SSU (Figure 1C). The tRNA binding-sites are located within the intersubunit space embraced by the LSU and the SSU. The protein encoding mRNA becomes inserted into the SSU through the mRNA channel (Figure 1C). The channel is located along the neck of the SSU at the interface of the head and body (Yusupova et al., 2001). The entry of the mRNA channel is formed by proteins S3, S4 and S5 (Yusupova et al., 2001). The mRNA channel exit site is surrounded by proteins S1, S7, S11, S18 and S21, as well as the 3' end of the 16S rRNA (Loveland and Korostelev, 2017; Yusupova et al., 2001). The anticodon, which distinguishes the incorporated amino acid, is located within the anticodon stem loop (ASL) of a tRNA (Figure 1C). An aminoacylated tRNA (aa-tRNA) generally enters the 70S ribosome via the ribosomal A-site and is subsequently handed over to the P-site after peptide bond formation as so called peptidyl-tRNA. After deacylation, which is the result of another round of peptide bond formation, tRNAs are passed to the E-site where they depart from the ribosome. Irrespective of the binding site, the tRNA 3'-end always interacts with the LSU. On the LSU the 3'-end of the A-site and P-site tRNA is stabilized by 23S rRNA loops termed A-loop (nts 2547-2561) and P-loop (nts 2246-2259) (*E. coli* numbering is used exclusively in this thesis). C75 within the 3'-end of the A-site tRNA basepairs with G2553 and C74 and C75 within the 3'-end of the P-site tRNA basepair with G2252 and G2251, respectively (Kim and Green, 1999; Moazed and Noller, 1989a; Nissen et al., 2000; Samaha et al., 1995). Besides the stabilization of the aminoacyl acceptor stem,

this also allows the proper placement of the attached amino acids inside the PTC that is indispensable for efficient peptide bond formation.

The growing polypeptide chain stays always attached to tRNAs bound in the ribosomal A- or P-site. The tRNAs bound in the ribosomal E-site are deacylated. Peptide bond formation takes place within the LSU of the 70S ribosome, the nascent chain has to exit the translation machinery through an exit tunnel located on the back of the LSU (Figure 1D) (Nissen et al., 2000). Starting at the PTC, the polypeptide exit tunnel has a total length of ~100 Å (Figure 1D), is 10-30 Å wide and covers ~30 amino acids of a growing protein (Nissen et al., 2000). While the tunnel is primarily build from rRNA, the narrowest section of the tunnel, that is 15 Å wide, is constricted by LSU proteins (L4 and L22) (Nissen et al., 2000). The very end of the polypeptide exit tunnel is build up from ribosomal RNA and proteins L23, L24 and L29 (Nissen et al., 2000).

1.2 Bacterial translation

The successful synthesis of a protein requires the exact definition of an open reading frame (ORF) in order to produce a functional product. The most crucial information for the establishment of an ORF is provided by an mRNA molecule itself. Accordingly, the minimal requirements for a normal bacterial mRNA are a start codon (mostly an AUG codon) and a stop codon (UAA, UAG or UGA). In addition, many prokaryotic mRNAs (~39% in *E. coli*) harbor a Shine-Dalgarno (SD) sequence seven to eight nucleotides upstream of the start codon (Chen et al., 1994). The start and the stop codon pre-define the ORF and the nucleotide triplets that are read consecutively from the 5' towards the 3' end of the mRNA. The SD sequence promotes the correct placement of the ribosome with the start codon placed within the P-site. The placement of the 70S ribosome on the start codon and the recruitment of the first fMet-tRNA^{fMet} to the P-site occurs during translation initiation (Figure 2A). Protein synthesis in general, passes through four major steps: Translation initiation, translation elongation, translation termination and subsequent ribosome recycling (Figure 2). The polymerization of the nascent chain takes place during translation elongation (Figure 2B). The starting point for translation elongation represents a fMet-tRNA_{fMet} placed in the P-site of the 70S ribosome during initiation (Figure 2A). In bacteria, this first incorporated methionine is formylated, thereby distinguishing it from canonical methionine used during later steps of translation elongation (Guillon et al., 1992; Lee et al., 1991; Seong and

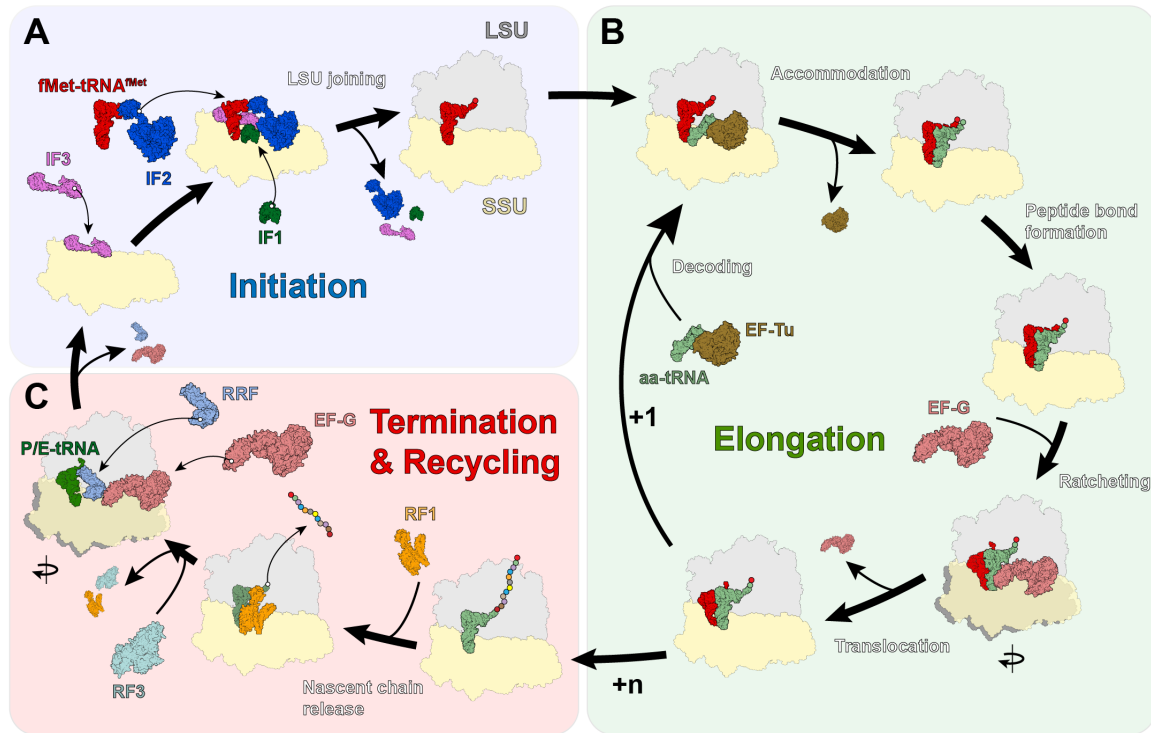


Figure 2 - Bacterial translation cycle. (A-C) Simplified scheme showing the steps of protein synthesis and important factors, which facilitate the polymerization process. Protein synthesis can be divided into steps of (A) translation initiation, (B) translation elongation and (C) translation termination/recycling. (A) Placement of fMet-tRNA^{Met} (red) in the ribosomal P-site is achieved during translation initiation. Translation initiation leads to the formation of a translation competent 70S initiation complex. Translation initiation is facilitated by initiation factors 1 to 3 (IF1-IF3) that bind to the SSU (yellow) and facilitate fMet-tRNA^{Met} recruitment, as well as LSU (grey) joining. IF1 is colored green, IF2 is colored blue and IF3 is colored magenta. (B) Translation elongation comprises the steps of aa-tRNA (pale green) delivery by EF-Tu (brown) to the ribosomal A-site, peptide bond formation and subsequent ribosome translocation facilitated by EF-G (salmon). Translocation of tRNAs to the consecutive tRNA binding site coincides with SSU (yellow) rotation relatively to the LSU (grey). Each round of translation elongation leads to the extension of the polymerized nascent chain by one amino acid (+1). (C) Termination takes place upon stop codon selection. Release of the nascent chain (harboring +n amino acids) is achieved by class I release factor RF1/2 (orange). RF1/2 becomes released from the 70S ribosome by class II release factor RF3 (cyan). After termination, splitting of the 70S ribosome into LSU (grey) and SSU (yellow) is carried out by RRF (light blue), as well as EF-G (salmon). Figure adapted from (Sohmen et al., 2009).

RajBhandary, 1987). Starting with formylated methionine attached to the tRNA in the P-site, the peptide chain becomes polymerized in a cyclic manner. Each translation elongation cycle results in the extension of the polypeptide chain by one amino acid (Figure 2B). The ribosome repetitively passes through steps of polypeptide polymerization and translocation of 3 nts of the mRNA per cycle and thereby manages to incorporate ~15-50 aa per second (Katunin et al., 2002). The repetitive cycling through the elongation steps stops as soon as the ribosome encounters a stop codon (Figure 2C). Once the stop codon is selected, the peptide chain is released from the tRNA and the 70S complex becomes recycled (Figure 2C).

All translation steps involve - besides the 70S ribosome as translational platform, tRNAs and mRNAs - other translation factors for each translation step. The additional translation factors greatly increase translational fidelity and speed. The different steps of protein synthesis and the involved factors will be treated in more detail in the following sections.

1.2.1 Translation initiation

Translation initiation is defined by the recruitment of fMet-tRNA^{fMet} to the P-site of the 70S ribosome (Allen et al., 2005; Hussain et al., 2016; Julian et al., 2011; Simonetti et al., 2008). Bound to the ribosome the fMet-tRNA^{fMet} is placed at the AUG start codon encoded within the mRNA (Allen et al., 2005; Hussain et al., 2016; Julian et al., 2011; Simonetti et al., 2008). Initiation involves three initiation factors (IFs), namely IF1, IF2 and IF3 (Figures 2A and 3A). Furthermore, the placement of the ribosome is often stabilized by interactions of the mRNA-encoded Shine-Dalgarno (SD) sequence with an anti-Shine-Dalgarno (ASD) sequence encoded within the 3' end of the 16S rRNA (Shine and Dalgarno, 1974; Steitz and Jakes, 1975). The formation of a translation-competent 70S initiation complex (70S-IC) proceeds via a 30S pre-initiation complex intermediate (30S-PIC) and a 30S initiation complex (30S-IC) intermediate (Grigoriadou et al., 2007a; Milon and Rodnina, 2012; Tomsic et al., 2000). The transition from a 30S-PIC to a 30S-IC occurs upon codon-anticodon recognition between mRNA and fMet-tRNA^{fMet} (Milon and Rodnina, 2012). Both 30S initiation complexes are characterized by the presence of all three initiation factors (Milon and Rodnina, 2012). To obtain the 30S-IC, the SSU undergoes a series of conformational changes which coincide with fMet-tRNA^{fMet} accommodation and distinct rotational movements of the SSU head (Gualerzi et al., 2001; Hussain et al., 2016; Julian et al., 2011; Lopez-Alonso et al., 2017). Rotational movements within the SSU, as well as the accommodation of the fMet-tRNA^{fMet} are mandatory to prevent steric clashes during subunit joining caused by H69 and L5 of the LSU (Hussain et al., 2016; Simonetti et al., 2008; Sprink et al., 2016). Initiation factors mediate these conformational changes and prevent premature joining of the LSU. The sequential order of initiation factor binding seems to be irrelevant, however, mRNA is likely to bind prior to fMet-tRNA^{fMet} (Hussain et al., 2016). Binding of the mRNA is possibly promoted through A-site latch opening and mRNA tunnel entry widening induced by the presence

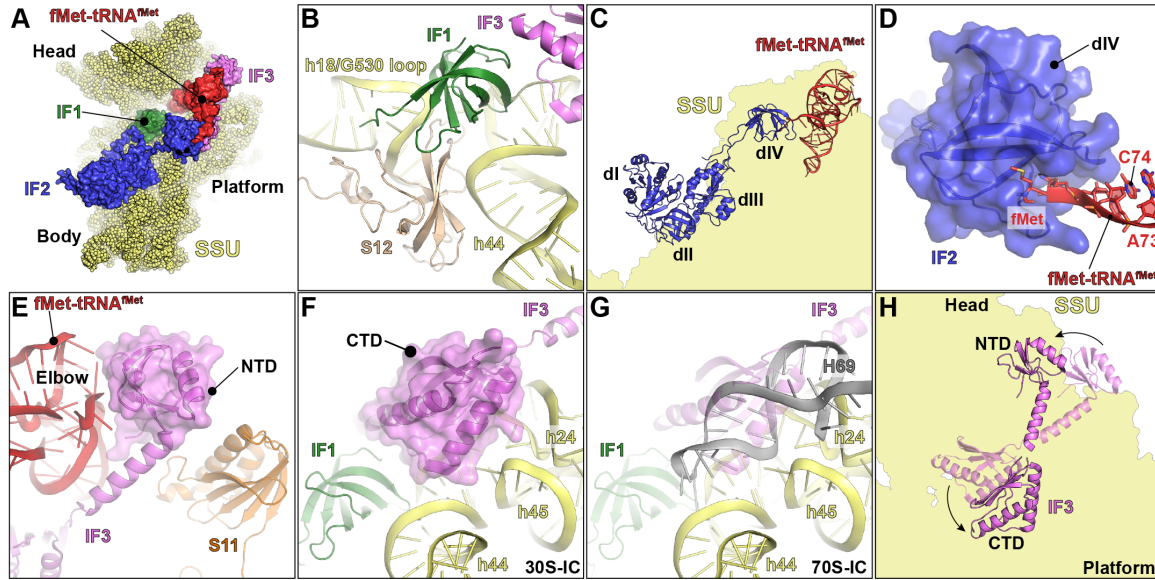


Figure 3 - Binding of initiation factors to the SSU. (A) Overview of the binding positions of IF1 (green), IF2 (blue), IF3 (magenta) and fMet-tRNA^{fMet} on the SSU (yellow spheres). (B) Interactions of IF1 with SSU h44 and h18, S12 and the C-terminal domain of IF3. (C) Model of IF2 with fMet-tRNA^{fMet} attached to domain IV. The SSU (yellow) is shown for reference. (D) Zoom of (C) showing interactions of IF2 domain IV with the fMet-moiety attached to the CCA-end of fMet-tRNA. (E) Contacts of the IF3 N-terminal domain (NTD) with the elbow of fMet-tRNA^{fMet} and protein S11. (F) Interactions of the CTD of IF3 with h24, h44, h45 and IF1. (G) Superimposition of 70S-IC and 30S-IC. The CTD of IF3 is incompatible with intersubunit bridge B2a/d. The intersubunit bridge is formed by LSU H69 and SSU helices h24, h44 and h45 during LSU joining. (H) Movement of the NTD and CTD of IF3 during translation initiation. The SSU (yellow) head and platform is indicated for reference. Figure based on (Hussain et al., 2016).

of initiation factors IF1 and IF3 (Hussain et al., 2016). fMet-tRNA^{fMet} has been proposed to bind to the SSU, which exhibits a swiveled head domain, and harbors at least IF1, IF3, as well as mRNA (Hussain et al., 2016).

IF1 is a compact single domain protein with an OB-fold (Sette et al., 1997). It binds to the SSU A-site next to S12, the G530 loop and 16S helix 44 (Figures 3A and 3B) (Carter et al., 2001; Dahlquist and Puglisi, 2000; Hussain et al., 2016; Simonetti et al., 2008). Bound to the SSU, IF1 enhances the binding activities of IF2 and IF3 (Hussain et al., 2016; Milon et al., 2012).

IF2, a translational GTPase with a five-domain structure (Figure 3C) (Simonetti et al., 2013; Simonetti et al., 2008), promotes recruitment of fMet-tRNA^{fMet} to the SSU and is involved in LSU joining (Allen et al., 2005; Marshall et al., 2009; Simonetti et al., 2008; Sprink et al., 2016). The GTPase activity resides within domain I (Figure 3C) (Simonetti et al., 2013). Recruitment of fMet-tRNA^{fMet} is mediated via interactions of IF2 domain IV (Figure 3C) (Hussain et al., 2016; Julian et al., 2011; Laursen et al., 2005; Simonetti et al., 2008; Sprink et al., 2016; Spurio et al., 2000). Domain IV directly interacts with the N-formylmethionine moiety of the fMet-tRNA. This allows IF2 to distinguish fMet-tRNA^{fMet} from an elongator Met-tRNA and protects fMet-tRNA^{fMet} from

premature deacylation (Figure 3D) (Guenneugues et al., 2000). Binding to the SSU is promoted by IF2 domains II and III (Hussain et al., 2016; Julian et al., 2011; Simonetti et al., 2013; Simonetti et al., 2008; Sprink et al., 2016). The ternary complex, consisting of IF2, GTP and fMet-tRNA^{fMet}, creates a scaffold which greatly increases the interaction surface for LSU joining (Simonetti et al., 2013; Simonetti et al., 2009; Simonetti et al., 2008).

IF2 and IF3 seem to have antagonistic activities (Milon and Rodnina, 2012). While IF2 promotes LSU joining, IF3 has anti-association activity that prevents premature subunit joining (Grigoriadou et al., 2007b; Grunberg-Manago et al., 1975). IF3 exhibits a two-domain dumbbell structure and binds to the platform at the SSU E-site (Figure 3A) (Biou et al., 1995; Garcia et al., 1995; Hussain et al., 2016; Julian et al., 2011; McCutcheon et al., 1999). The N-terminal domain (NTD) and the C-terminal domain (CTD) are connected via a flexible linker (Biou et al., 1995; Garcia et al., 1995; Hussain et al., 2016; Julian et al., 2011). The NTD is critical for initiation fidelity and recruitment of the correct fMet-tRNA^{fMet} (Hartz et al., 1990; Hartz et al., 1989). It binds near the SSU platform (Figure 3B) (Dallas and Noller, 2001; Fabbretti et al., 2007; Hussain et al., 2016; McCutcheon et al., 1999) and potentially establishes interactions with S11 (Figure 3E) (Hussain et al., 2016). Recruitment of the correct initiator tRNA is promoted through interactions of the NTD of IF3 with the elbow region of the fMet-tRNA^{fMet}, which are maintained throughout initiation (Figure 3E) (Hussain et al., 2016; Julian et al., 2011). Furthermore, IF3 monitors three G:C basepairs within the anticodon stem (G29-G31 and C39-C41) that are specific for tRNA^{fMet} (Hartz et al., 1990; Hartz et al., 1989; O'Connor et al., 2001; Risuleo et al., 1976; Sussman et al., 1996), as well as correct codon-anticodon interaction of fMet-tRNA^{fMet} and mRNA (Milon et al., 2008). The CTD binds next to the P-site on top of h44, establishing interactions with h24 and h45 (Figure 3F) (Hussain et al., 2016). Both IF3 domains undergo large conformational changes during initiation (Elvekrog and Gonzalez, 2013; Fabbretti et al., 2007; Hussain et al., 2016; Takahashi et al., 2013). The conformational changes allow fMet-tRNA^{fMet} accommodation and LSU joining (Hussain et al., 2016). Premature subunit joining is prevented by a steric clash of the CTD of IF3 with H69 of the LSU (Figure 3G) (Garcia et al., 1995; Hussain et al., 2016; McCutcheon et al., 1999). As the fMet-tRNA^{fMet} accommodates, the steric hindrance becomes resolved by CTD movement and the anti-association activity of IF3, preventing LSU subunit joining, is abolished (Hussain et al., 2016). The IF3 CTD moves from its binding position near

the P-site to a more distal position from the SSU neck (Figure 3H) (Hussain et al., 2016). H69 can then form an intersubunit bridge together with h44 of the SSU (Figure 3G).

Successful subunit joining leads to placement of the G-domain of IF2 next to the sarcin-ricin loop (SRL) of the LSU (La Teana et al., 2001; Qin et al., 2009; Sprink et al., 2016). The SRL rearranges a catalytic histidine (His448) within the G-domain (Sprink et al., 2016) which triggers GTP hydrolysis to GDP and Pi. Pi dissociates and IF2 releases fMet-tRNA^{fMet}, which accommodates in the ribosomal P-site (La Teana et al., 1996; Myasnikov et al., 2005). IF2-GDP constitutes the low affinity form that rapidly dissociates from the 70S ribosome together with IF1. Although it was shown that the release of IF3 is independent of GTP-hydrolysis (Goyal et al., 2015), IF3 dissociates after IF1 and IF2 as the 70S-IC matures (Milon et al., 2008). After dissociation of IF1 to IF3 the translation-competent 70S-IC enters the translation elongation cycle (Figures 2A and 2B).

1.2.2 Translation elongation

The term “translation elongation” refers to a repetitive sequence of events that lead to the successive extension of a nascent polypeptide chain (Figure 2B). The respective events include decoding, peptide bond formation and translocation (Figure 2B). Like translation initiation, elongation involves a set of factors binding to the ribosome that guarantee the translation fidelity and rapid protein synthesis progress. Generally, translation elongation requires a translation competent 70S ribosome with an empty A-site and an fMet-tRNA^{fMet} or a peptidyl-tRNA in the P-site. As described in section 1.2.1, the translation competent ribosome for the very first cycle of translation elongation is generated during initiation (Figure 2A). In contrast to initiation, elongation utilizes aa-tRNAs coding for all 20 amino acids instead of fMet-tRNA^{fMet}. The aa-tRNAs are delivered to the ribosome by a ternary complex consisting of the translational GTPase elongation factor thermounstable (EF-Tu), GTP and an aa-tRNA. Delivery of tRNAs by EF-Tu and subsequent accommodation in the ribosomal A-site requires accurate decoding within the DC of the SSU (Figure 2B). Delivery of aa-tRNA is followed by peptide bond formation, taking place on the LSU within the PTC. The peptide attached to the P-site tRNA is transferred to the aminoacyl moiety attached to the A-site tRNA (Figure 2B). During the very first elongation cycle just a single amino

acid (N-formylmethionine) is transferred from the P- to the A-site tRNA. Afterwards, the translocation of the ribosome along the mRNA is necessary. Ribosome translocation is achieved by movement of the ribosome bound tRNAs through the ribosome together with the base-paired mRNA. This leads to the freeing of the ribosomal A-site and the exposure of the next consecutive codon of the translated ORF. Translocation of the tRNAs together with the mRNA is facilitated by elongation factor GTPase (EF-G) (Figure 2B). Similar to initiation and translation elongation, especially translocation requires conformational changes within the 70S ribosome and bound factors. Conformational changes include rotations of the SSU body/platform and swiveling of the head as well as alternative conformations of tRNAs bound to the A- and P-sites. The latter changes facilitate the movement of the ribosome along the mRNA.

The process of translational decoding

As previously mentioned, amino acids are encoded within the mRNA as nucleotide triplets (codons). The mRNA runs through the neck of the SSU between the head and the platform (Yusupova et al., 2001). The mRNA codons exposed in the tRNA binding sites are decoded to an amino acid using tRNAs as adaptors (Figure 4A). On a structural level, this decoding is achieved by classical Watson-Crick base-pairing and involves the critical residues (DC nucleotides) A1492 and A1493 within h44 and G530 within h18 (530 loop) (Demeshkina et al., 2012; Jenner et al., 2010; Loveland et al., 2017; Ogle et al., 2001; Selmer et al., 2006). It has been suggested that these highly conserved nucleotides discriminate cognate codon-anticodon interactions from non-cognate interactions by monitoring the Watson-Crick basepair geometry between mRNA and tRNA (Ogle et al., 2001).

The decoding aa-tRNA is delivered to the SSU A-site by the EF-Tu ternary complex (Figure 4A) (Nissen et al., 1995). EF-Tu binds to non-rotated 70S ribosomes that adopt an open SSU conformation and bear an empty A-site (Loveland et al., 2017). The aa-tRNA stays attached to EF-Tu until decoding is accomplished (Figure 4B) (Loveland et al., 2017; Ogle and Ramakrishnan, 2005). EF-Tu interacts with h5 and h15 of the SSU shoulder and protein S12 (Figure 4A) (Loveland et al., 2017). Upon initial EF-Tu binding the aa-tRNA adopts a relaxed conformation and no interactions are established with the mRNA codon (Figure 4C) (Loveland et al., 2017; Nissen et al., 1995). The DC nucleotides A1492 and G530 adopt an “inactive” conformation (Figure

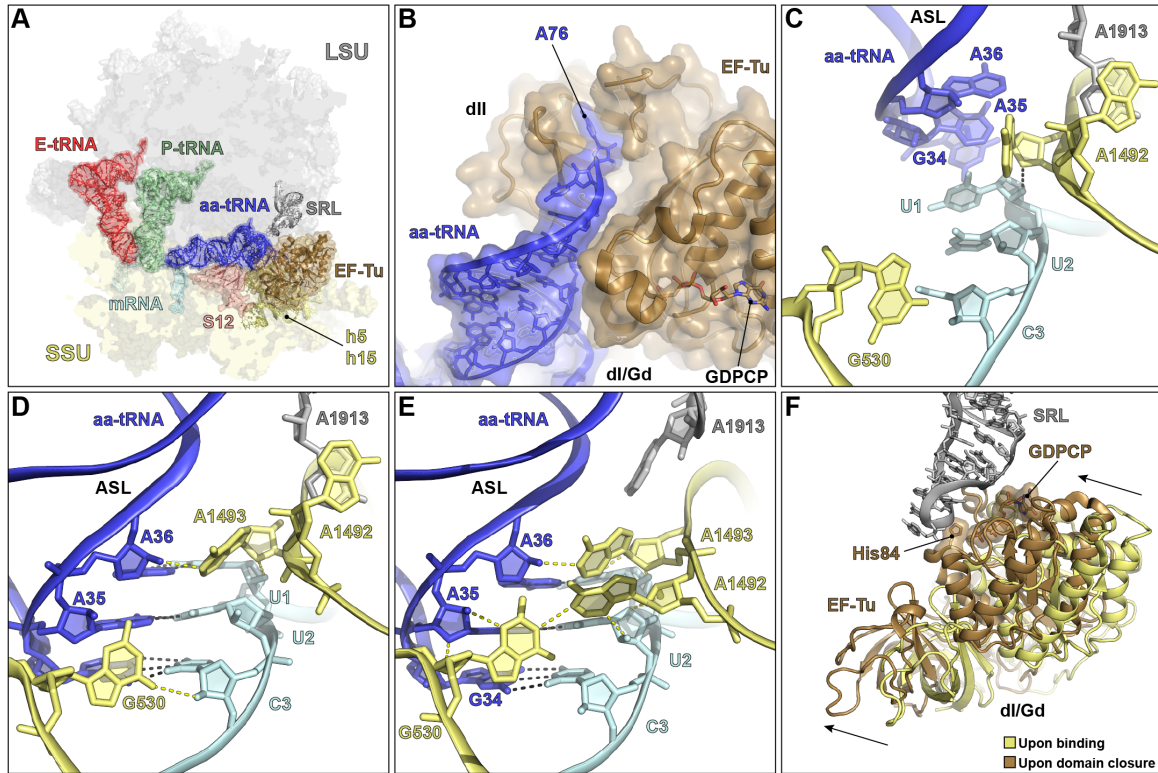


Figure 4 - Delivery of aa-tRNA by EF-Tu and subsequent decoding on the SSU. (A) Overview showing aa-tRNA (blue) delivery by EF-Tu (brown) to the A-site of the bacterial 70S ribosome harboring P-tRNA (green), E-tRNA (red) and mRNA (cyan) (Loveland et al., 2017). Binding of EF-Tu to the ribosome involves interactions with the SRL (grey), h5 (yellow), h15 (yellow) and SSU protein S12 (dark salmon). (B) Interactions of the CCA-end of unaccommodated tRNA (blue) with EF-Tu domain II (brown) (Loveland et al., 2017). (C-E) Conformational changes of 16S DC nucleotides (yellow) during decoding (Loveland et al., 2017). (C) Conformation of DC nucleotides before establishment of codon-anticodon interactions. A1492 and G530 adopt an inactive conformation. The tRNA ASL adopts a relaxed conformation. (D) Conformation of DC nucleotides upon establishment of codon-anticodon interactions between mRNA (cyan) and A-tRNA (blue). The ASL adopts a kinked conformation. G530 and A1493 start monitoring codon-interactions. (E) Active conformation of all DC nucleotides. A-minor interactions are monitored of the codon-anticodon helix. The kinked conformation of the A-tRNA ASL (blue) is maintained. (C-E) Hydrogen bonds between the nucleotide pairs are indicated by black dashed lines. Polar contacts between DC nucleotides and mRNA, as well as DC and tRNA are indicated by yellow dashed lines. (F) Accommodation of the G-domain of EF-Tu upon domain closure (Loveland et al., 2017). The G-domain approaches the SRL (grey), which arranges a catalytic histidine (His84) for GTP hydrolysis. The position of the G-domain upon initial binding is shown in yellow. The position of the G-domain after domain closure is shown in brown.

4C) (Loveland et al., 2017). Accordingly, while A1492 stays within h44 and stacks on A1913 from H69 of the 23S rRNA, G530 is located distal from the codon (Figure 4C). The DC nucleotide A1493 loosely interacts with the nucleotides exposed in the A-site (Figure 4C). As the ASL enters the A-site the anticodon of the aa-tRNA starts probing for Watson-Crick base-pairs with the exposed mRNA codon. The anticodon nucleotides flip out and the aa-tRNA ASL acquires a kinked conformation resulting in an A/T tRNA state (Figure 4D). G530 and A1493 start monitoring codon-anticodon base-pairing geometry (Figure 4D). G530 adopts an intermediate state and initially interacts with the codon-anticodon helix by hydrogen-bonding with the second

nucleotide of the anticodon and the third (3') nucleotide of the mRNA codon (Figure 4D). A1493 establishes interactions with the minor groove of the codon-anticodon helix (first base-pair) (Figure 4D) (Loveland et al., 2017; Nissen et al., 2001; Ogle et al., 2001). During the final stage G530 establishes an additional hydrogen-bond (Figure 4E). Decoding interactions now involve the first and second codon-anticodon base-pair as well (Figure 4E) (Loveland et al., 2017).

In general, the DC nucleotides act like a latch that closes upon successful establishment of cognate codon-anticodon interactions (Figure 4E) (Loveland et al., 2017). A1492 and A1493 form A-minor interactions and monitor the geometry of the first and second base-pair within the codon-anticodon interaction (Figure 4E) (Loveland et al., 2017; Nissen et al., 2001; Ogle et al., 2001). SSU-domain closure is induced by correct Watson-Crick base-pairing in the DC and leads to the accommodation of the EF-Tu G-domain (Figure 4F) (Loveland et al., 2017; Ogle et al., 2002; Schmeing et al., 2011; Voorhees et al., 2010). The G-domain approaches the sarcin-ricin loop (SRL) localized on the LSU (Figure 4F) (Loveland et al., 2017; Villa et al., 2009; Voorhees et al., 2010). The SRL is crucial for translational GTPases, since binding of the G-domain leads to the rearrangement of a catalytic histidine (His84 for EF-Tu) (Figure 4F) (Loveland et al., 2017; Villa et al., 2009; Voorhees et al., 2010). EF-Tu becomes activated and hydrolysis of GTP to GDP + P_i takes place (Loveland et al., 2017; Villa et al., 2009; Voorhees et al., 2010). As consequence, the aa-tRNA attached is released from EF-Tu and changes from an A/T state to a fully accommodated A/A state in the ribosomal A-site (Blanchard et al., 2004a; Douthwaite et al., 1983; Sanbonmatsu et al., 2005). EF-Tu departs from the ribosome and is free to form a ternary complex with another aa-tRNA for a subsequent round of the translation elongation cycle. The presence of a near-cognate ternary complex leads to perturbed latching of G530 and hence no SSU-domain closure occurs (Loveland et al., 2017). Accordingly, the lack of SSU-domain closure results in dissociation of the non-cognate tRNA from the ribosome. Noteworthy, A1492, A1493, as well as G530, generally neglect the third position of the codon-anticodon interaction, allowing unusual base-pairs, called wobble base-pairs (Figures 4C-E). Wobble base-pairs enable different codons to code for the same amino acid decoded by a single tRNA (Crick, 1966).

Peptide bond formation

After full accommodation of the aa-tRNA into the A-site, the extension of the nascent chain takes place in the PTC. As described before, the CCA-ends of the accommodated tRNAs in the A- and P-site are positioned and stabilized in the PTC by the A- and P-loop nucleotides (Moazed and Noller, 1989a). The alignment of the 3' ends and the respective attached moieties promotes peptide bond formation. During peptide bond formation the peptidyl chain attached to the CCA-end of the P-site tRNA is transferred to the aminoacyl moiety of the A-site tRNA. The whole reaction is driven by the energy stored in the ester linkage connecting the nascent chain to the P-site. The transfer of the peptide chain from the P- to the A-site requires a nucleophilic attack of the α -amine of the A-site aminoacyl moiety on the peptidyl ester of the P-tRNA. The LSU PTC provides the environment for successful transfer of the peptidyl moiety and ensures translation fidelity. Like decoding, peptide bond formation also involves conserved residues that facilitate the reaction. The most critical residues are G2583, U2584, U2585 and U2506 located within the central loop of the 23S rRNA domain V (Polacek and Mankin, 2005; Polikanov et al., 2014; Schmeing et al., 2005b; Voorhees et al., 2009), which upon full accommodation of the CCA-end of the aa-tRNA into the A-site of the PTC, adopt a specific conformation characterized by shifting of G2583, U2584 and U2585 and rotation of U2506 (Figure 5A) (Polikanov et al., 2014; Schmeing et al., 2005b; Voorhees et al., 2009). This conformation of the ribosome and its PTC residues is called the induced state (Figure 5A) (Polikanov et al., 2014; Schmeing et al., 2005b; Voorhees et al., 2009). U2585 is critical for peptide bond formation and protects the peptidyl-ester of the P-tRNA from premature hydrolysis in the uninduced state (Schmeing et al., 2005a; Schmeing et al., 2005b).

The need for deprotonation and the transfer of hydrogens has led to different concepts explaining the actual process of peptide bond formation. These primarily differ as to how the nucleophilic α -NH₂ group is generated and the path the described protons take. The older concept termed the 'proton shuttle' postulates that the 2'OH group of the peptidyl-tRNA functions like a shuttle by providing a hydrogen to the 3' oxygen of the released peptidyl moiety, while deprotonating the α -amine of the aminoacyl residue attached to the A-site tRNA (Schmeing et al., 2005a; Schmeing et al., 2005b; Schmeing et al., 2002; Trobro and Aqvist, 2005; Zaher et al., 2011). Problematic here is that many of the corresponding structural studies, which were used

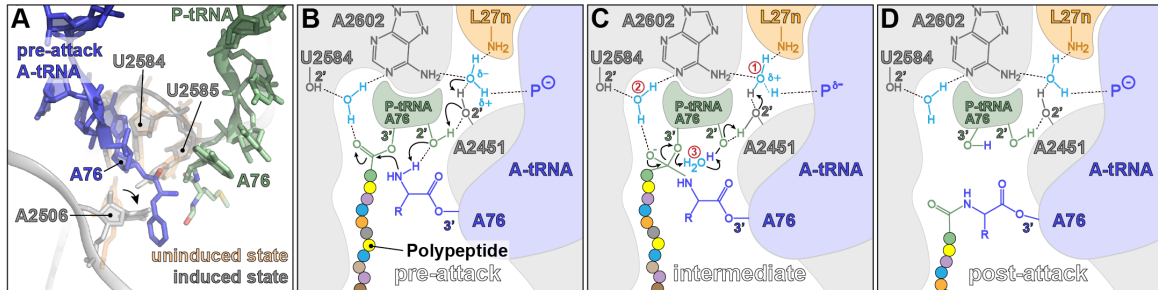


Figure 5 - The process of peptide bond formation. (A) Position of aminoacylated pre-attack A-tRNA (blue), peptidyl-P-tRNA (green) and 23S nucleotides A2506, U2584 and U2585 in the PTC (Polikanov et al., 2014). The conformation of PTC nucleotides in the uninduced state is shown in orange (Schmeing et al., 2005a; Schmeing et al., 2005b). The conformation of the 23S nucleotides after aa-A-tRNA accommodation (induced state) is shown in grey. (B-D) The chemical process of peptide bond formation (Polikanov et al., 2014). (B) Deprotonation of the α -amine of the A-site aminoacyl moiety and nucleophilic attack on the carbonyl carbon. (C) Formation of a tetrahedral intermediate. The critical water molecules (cyan) involved in this process are indicated with red numbers. (D) Breakdown of the tetrahedral intermediate leads to formation of the post-attack state. The polypeptide chain is finally attached to the A-tRNA and deacyl-tRNA is bound in the P-site of the ribosome.

to infer a 'proton-shuttle', involved solely the LSU in complex with reduced substrates, intermediate states or product analogs (Schmeing et al., 2005a; Schmeing et al., 2005b; Schmeing et al., 2002), thus preventing the observation of a fully native PTC in action. In contrast, a more recent concept based on structural studies with highly resolved (2.5 Å and 2.6 Å) *T. thermophilus* 70S ribosomes, called the 'proton wire', suggests the binding of three water molecules that facilitate successful peptide bond formation by serial transfer of protons (Figures 5B-D) (Polikanov et al., 2014). In addition to the mentioned rRNA residues, this model involves the N-terminus of L27. Generally, a proton-wire describes the translocation of protons utilizing a chain of coordinated water molecules (Nagle and Morowitz, 1978; Polikanov et al., 2014). The 'proton-wire' model for peptide bond formation was based on observations with 70S ribosomes containing complete tRNA molecules representing pre- and post-attack states (Figure 5A) (Polikanov et al., 2014). The pre-attack state contained non-hydrolysable fMet-NH-tRNA^{fMet} in the P-site and non-hydrolysable Phe-NH-tRNA^{Phe} in the A-site (Figure 5A). The post-attack state contained deacylated tRNA in the P-site and non-hydrolysable fMet-Phe-NH-tRNA^{Phe} in the A-site. In both pre- and post-attack structures the key residues that form the framework for peptide bond formation, namely U2506, G2583, U2584 and U2585, adopt almost exactly the same induced/rearranged conformation (Figure 5A) (Polikanov et al., 2014). The three water molecules, crucial for the proton-wire, become coordinated at three distinct spots inside the PTC (Figure 5B) (Polikanov et al., 2014). Water 1 is coordinated between the CCA-end of the A-tRNA, the N-terminal residue of L27, A2602 (H93) and A2451 (Figures 5B-D)

(Polikanov et al., 2014). The second water (water 2) is placed between the 2'-OH group of U2584 and A2602 (Figures 5B-D) (Polikanov et al., 2014). Additionally, in the pre-attack state water 2 establishes a contact with the carbonyl oxygen of the peptidyl moiety of the P-tRNA (Polikanov et al., 2014). Water molecule 3 shows the most dynamic interactions within pre- and post-attack states. While in the pre-attack state water 3 interacts with P-tRNA A76 by contacting N3, the 2'-OH group, as well as the 3'-O group (non-hydrolysable 3'-N group in this study), in the post-attack state water 3 interacts with the 2'-OH groups of C2063 and P-site A76, as well as the 3'-OH group of P-site A76 (Figures 5B-D) (Polikanov et al., 2014). During peptide bond formation it is hypothesized that the possibly deprotonated N-terminus of L27 together with a negatively charged oxygen of the A-site A76 5'-phosphate may lead to a partial negative charge of the oxygen of water 1 (Figure 5B) (Polikanov et al., 2014). As consequence, protonation of water 1 can occur which in turn leads to the deprotonation of the 2'-OH group of P-site A76 and subsequently to the deprotonation of the α -amine of aminoacyl moiety attached to the A-site tRNA (Figures 5B and 5C) (Polikanov et al., 2014). The created nucleophile α -NH₂ can attack the ester bond of the peptidyl moiety of the P-site tRNA, resulting in a tetrahedral intermediate (Figure 5C) (Polikanov et al., 2014). The hydrogen bond established by water 2 leads to an electrophilic carbonyl group that promotes the nucleophilic attack of the α -amine (Figures 5B and 5C) (Polikanov et al., 2014). Water 3 stabilizes the tetrahedral intermediate and facilitates the reversal of the deprotonation, which results in the release of the peptidyl moiety from the P-site tRNA and full attachment to the aminoacyl moiety attached to A76 of the A-site tRNA (Figures 5C and 5D) (Polikanov et al., 2014). The 70S ribosome with its deacylated tRNA in the P-site acquires a post-attack state (Figure 5D). The previously described data obtained from *T. thermophilus* ribosomes confirm for the first time the possible chemical importance of the L27 N-terminus (Polikanov et al., 2014), as suggested in earlier studies (Maguire et al., 2005; Wower et al., 1998). Structure-wise the close proximity of the NTD of L27 implicated a possible role in peptide bond formation (Voorhees et al., 2009). However, it is still unclear whether L27 is crucial for peptide bond formation in general (or just specific amino acids), since more recent studies indicated a rather less important role during peptide bond formation (Maracci et al., 2015). Nonetheless, the proton-wire model seems to fill gaps or correct uncertainties of the proton-shuttle model. Both described models of peptide bond formation are based on the results of at least partially artificial systems. Therefore,

peptide bond formation is likely to be a combination of both models involving the concept of wiring and shuttling.

Ribosome translocation

Peptide bond formation results in deacyl-tRNA in the P-site and peptidyl-tRNA in the A-site (Figure 2B). To allow another round of peptide bond formation translocation must take place to free the A-site for exposure of the next consecutive mRNA codon and aa-tRNA binding. Peptidyl-tRNA previously bound to the A-site is moved to the P-site and deacyl-tRNA previously bound to the P-site is moved to the E-site (Figure 2B). The mRNA is translocated indirectly due to established codon-anticodon interactions with the tRNAs. Ribosomes harboring deacyl-tRNA in the A-site and peptidyl-tRNA in the A-site are termed pre-translocation (PRE) state. Ribosomes after translocation of tRNAs from the A- to the P-site and from the P- to the E-site are in a post-translocation (POST) state. Translocation, as well as translation in general, can take place without additional factors (Pestka, 1968, 1969), since the ribosome itself provides all the necessary activities to carry out protein synthesis. Nonetheless, in absence of additional translation factors the translocation of tRNAs is rather slow. Therefore, the translation elongation cycle utilizes the translational GTPase EF-G to promote translocation (Figures 6A-D). The exact role of GTP hydrolysis for EF-G function is still not entirely clear. One possibility is that EF-G utilizes GTP for a power-stroke to facilitate movement of tRNAs through the translation machinery (Chen et al., 2016). Alternatively, translocation possibly involves a Brownian ratchet mechanism, which is temperature driven (Astumian, 1997; Cordova et al., 1992; Fischer et al., 2010; Frank and Gonzalez, 2010; Spirin, 2009; Wintermeyer et al., 2004). Regardless, the process of translocation requires large scale movements of both ribosomes and tRNAs. The movement of the tRNAs through the ribosomes is carried out in two steps (Agrawal et al., 1999; Bulkley et al., 2014; Munro et al., 2010; Noller, 1991; Salsi et al., 2014; Stark et al., 2000; Wang et al., 2007). First, the 3'-end of the tRNAs bound to the A- and P-site becomes dislocated on the LSU to the P- and E-sites, respectively (Figure 6B). Second, the ASL base-pairing with the mRNA sense codon is moved to subsequent tRNA binding site on the SSU (Figures 6C and 6D). Dislocation of the CCA-end of tRNAs can occur spontaneously and is indirectly driven by successful peptide bond formation and SSU rotation (Ermolenko et al., 2007; Noller, 1991). Accordingly, in the

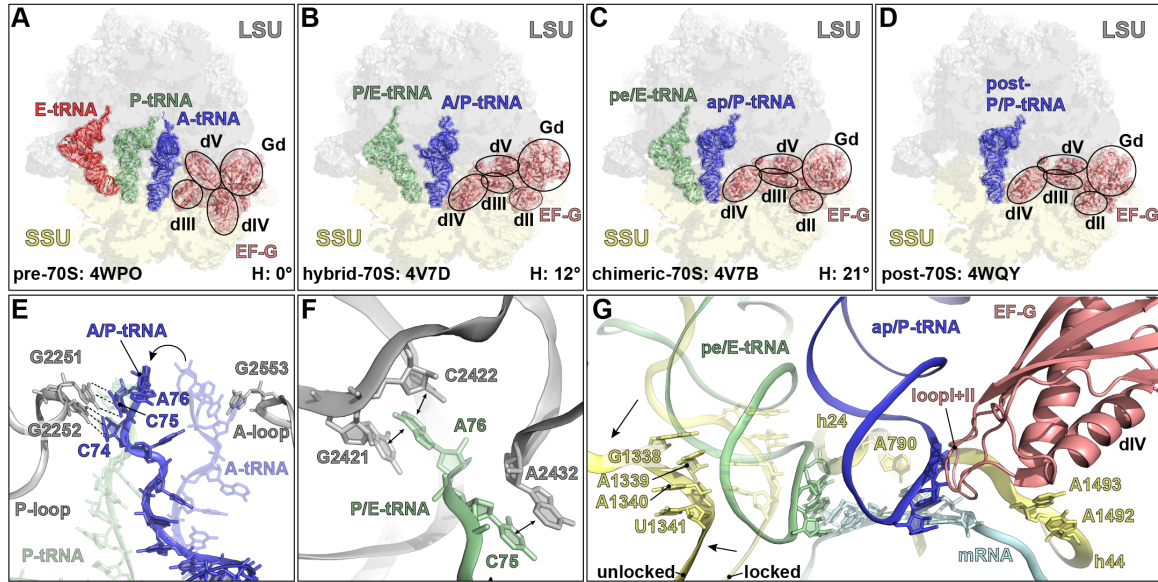


Figure 6 - EF-G promoted translocation. (A-D) Overview of obtained structures of EF-G (salmon) bound to 70S ribosomes. The LSU is shown in grey and the SSU is shown in yellow. The degree of head swivel observed for each complex is indicated at the bottom right of the panels. (A) PRE state ribosomes bound with EF-G (salmon) adopting a compact form and A-tRNA (blue), P-tRNA (green) and E-tRNA (red) in a classical state. (B-D) Ribosomal complexes with EF-G (salmon) bound in an elongated conformation (Lin et al., 2015). (B) Intermediate state 70S ribosome with hybrid state A/P-tRNA (blue) and P/E-tRNA (green) (Brilot et al., 2013). (C) Intermediate state 70S ribosome with chimeric state ap/ap-tRNA (blue) and pe/E-tRNA (green) (Ramrath et al., 2013). (D) POST state ribosome with translocated tRNA in the P-site (blue) (Lin et al., 2015). (E) Relocation of the CCA-ends of A-tRNA (faint blue) and P-tRNA (faint green), which leads to hybrid state formation (Lin et al., 2015). The relocated A-tRNA CCA-end (blue) basepairs with the P-loop nucleotides G2251 and G2252 upon hybrid state formation (Brilot et al., 2013). (F) Interactions of the relocated CCA-end of hybrid state P/E-tRNA (green) with LSU 23S nucleotides (grey). (G) Interactions of EF-G domain IV (salmon) with ap/P chimeric state tRNA (blue) (Ramrath et al., 2013). Movement of the tRNAs requires 'unlocking'. The lock is formed between the 16S rRNA (yellow) nucleotides G1338-U1341 and h24, which harbors nucleotides A790. The locked position of the nucleotides G1338-U1341 is shown in faint yellow. Chimeric state pe/E-tRNA is shown in green. The position of the maintained codon-anticodon interactions with mRNA (cyan) and the position of DC nucleotides A1493 and A1493 within h44 are shown for reference.

absence of a nascent chain attached to the P-site tRNA the 70S ribosome is no longer restricted to the classical state. Therefore, the ribosome starts to fluctuate between an intermediate rotated (R) and a non-rotated (N) state by a ~6° rotational movement of the complete SSU relative to the LSU (Blanchard et al., 2004b; Cornish et al., 2008; Munro et al., 2007). This rotation of the SSU was initially described as ratchet-like movement (Agrawal et al., 2000; Frank and Agrawal, 2000). In addition to SSU rotation, the SSU head was observed to undergo ~5° swiveling in rotated 70S ribosomes (Dunkle et al., 2011). Both, SSU rotation and head swiveling, coincide with movement of the 3'-end of A- and P-site tRNA on the LSU (Figure 6E). Consistently, the CCA-end of the P-tRNA moves from the PTC to the LSU E-site that is only available for deacylated tRNAs (Figure 6F) (Agirrezabala et al., 2008; Brilot et al., 2013; Dunkle et al., 2011). In this binding position C75 stacks upon A2432 and A76 is inserted between 23S rRNA nucleotides G2421 and C2422 (Figure 6F) (Agirrezabala et al.,

2008; Brilot et al., 2013; Dunkle et al., 2011). Because the previous interactions of the P-tRNA with P-loop are resolved (Figure 6E), now the 3'-end of the peptidyl-tRNA in the A-site can establish interactions with the P-loop (Figure 6E) (Agirrezabala et al., 2008; Julian et al., 2008). The resulting relocated states of the tRNAs were termed hybrid A/P and P/E states (Figure 6B) (Agirrezabala et al., 2008; Julian et al., 2008; Moazed and Noller, 1989b). Although EF-G preferentially binds to rotated ribosomes containing hybrid state tRNAs, it can in principle bind to non-rotated ribosomes (Dorner et al., 2006), but immediately drives them into a rotated state (Adio et al., 2015; Chen et al., 2011; Chen et al., 2013; Cornish et al., 2008; Holtkamp et al., 2014; Spiegel et al., 2007). It is not entirely clear in which conformational form EF-G binds to the non-rotated PRE state without creating a steric clash with an A/A or A/P state tRNA. Accordingly, most of the structural studies present data of rotated or non-rotated POST state 70S ribosomes (Figures 6B-D) (Agrawal et al., 1998; Connell et al., 2007; Frank and Agrawal, 2000; Gao et al., 2009; Ramrath et al., 2013; Ratje et al., 2010; Valle et al., 2003; Zhou et al., 2013, 2014). In these structures EF-G adopts an open/elongated conformation, binding 70S ribosomes primarily via its G-domain (domain I) in the intersubunit space between S12 and L14 (Gao et al., 2009; Lin et al., 2015; Pulk and Cate, 2013; Zhou et al., 2013). Domain IV mimics the ASL of a tRNA reaching to the DC on the SSU and is thought to perform the most crucial tasks (Figures 6B-D) (Agrawal et al., 1998; Nissen et al., 1995). As observed in viomycin bound PRE complexes, simultaneous placement of elongated EF-G and A/P-tRNA requires an additional swivel of the head by +7° (12° total) to avoid steric hindrance caused by the A-tRNA ASL (Figure 6B) (Brilot et al., 2013). However, the presence of viomycin leaves the physiological relevance of this complex questionable. Presumably, other conformational states exist that are in better agreement with binding to the PRE state. The existence of other EF-G forms is also supported by biochemical studies (Salsi et al., 2015). A recent higher resolution study suggests that EF-G can possibly adopt a compact form on PRE state ribosomes (Figure 6A) (Lin et al., 2015). While domain I and II were observed in a position similar to previous structural studies (Figures 6A-D), domain III and IV showed a previously unobserved conformation (Figure 6A) (Lin et al., 2015). Domain IV did not reach into the DC of the SSU, but instead is rotated backwards next to domain I and II (Figure 6A) (Lin et al., 2015). This movement is facilitated by domain V, which undergoes a simultaneous ~180° flipping and a ~90° rotational movement, while the overall position of this domain is not altered (Lin et al.,

2015). Problematic in the respective study is the approach used to form the complex, which makes the observations potentially artificial. First, EF-G binding to the ribosome was forced by fusion of the NTD of L9 to the N-terminus of EF-G (Lin et al., 2015). Second, the presence of dityromycin sterically clashes with EF-G domain III in the elongated form. Thus EF-G is forced into a compact form, which indirectly prevents movement of EF-G domain IV into close proximity to the ASL of an A-site tRNA. Nonetheless, the compact conformation of EF-G is a possible explanation for the previously observed binding of EF-G to N-state ribosomes in biochemical studies (Salsi et al., 2014; Salsi et al., 2015). The elongated EF-G most likely represents the active conformation.

Stabilization of R-state ribosomes through EF-G binding marks the first phase of translocation. Bound to R-state ribosomes, containing A/P- and P/E-tRNAs (Figure 6B), the task of elongated EF-G is to supervise and facilitate the complex movements of the ASLs on the SSU. Movement of the ASL of tRNAs requires the elimination of several energetic barriers (Noller et al., 2017). In the A-site, previously established decoding contacts with peptidyl-tRNA involving G530, A1492 and A1493 need to be disrupted (Figure 4E) (Noller et al., 2017). In the P-site, stabilization contacts of the SSU body involving C1400 and A790 have to be resolved (Noller et al., 2017). Furthermore, the movement of P-tRNA requires ‘unlocking’ (Savelsbergh et al., 2003; Spirin, 1968) of G1338-U1341 and A790 of the 16S rRNA. G1338-U1341 and A790 form a 13 Å constriction between P-site and E-site, which prevents the ASL from moving to the P-site (Figure 6G) (Noller et al., 2017). Elimination of all energetic barriers without actually impacting the stability of the codon-anticodon interactions is challenging, since the destabilization of codon-anticodon interactions possibly leads to the loss of the translational reading frame. EF-G is thought to overcome these problems and promote the maintenance of the reading frame by preventing mRNA slippage of the ribosome during translocation.

Stabilization of the A-site tRNA codon-anticodon helix during translocation is mediated by loops I and II at the tip of (elongated) EF-G domain IV (Figure 6G) (Ramrath et al., 2013; Zhou et al., 2014). These conserved loops establish interactions with the codon-anticodon helix of the A-site tRNA and replace the A-minor stabilization interactions of decoding nucleotides A1492 and A1493 (Figure 6G) (Gao et al., 2009; Khade and Joseph, 2011; Liu et al., 2014; Ramrath et al., 2013). Furthermore, loop I and loop II seem to act like a pawl that prevents the backward movement of the A-

tRNA to its previous binding position (Noller et al., 2017). Notably, movement of the P-site tRNA is not directly stabilized by EF-G (Figure 6G). Instead, the ASL of deacyl-P-tRNA is stabilized by the SSU head during translocation (Noller et al., 2017; Zhou et al., 2013). The respective contacts, which are maintained from N-state 70S ribosomes, involve the nucleotides G1338, A1339 and G966, as well as the CTD of proteins S9 and S13 (Noller et al., 2017; Zhou et al., 2013).

The steric block created by A790 and G1338-U1341, as well as contacts between the SSU body and P-site elements, are resolved during the second phase of translocation through head swiveling by 21° (Figures 6C and 6G) (+9° compared to initial binding) (Ramrath et al., 2013; Zhou et al., 2013, 2014). It is induced by interactions of EF-G domain IV with h34 of the 16S rRNA (Ratje et al., 2010) and coincides with backward rotation of the SSU (body/platform) (Ramrath et al., 2013; Zhou et al., 2013, 2014). Backward rotation mediates accommodation of the G-domain of EF-G on the LSU (Belardinelli et al., 2016; Ramrath et al., 2013; Zhou et al., 2013, 2014) and induces hydrolysis of GTP to GDP and P_i (Belardinelli et al., 2016).

However, after ‘unlocking’ of the constriction took place (Savelsbergh et al., 2003; Spirin, 1968) and contacts of the tip of EF-G domain IV with the codon-anticodon helix have been established, the ASL of the tRNAs move forward towards the next consecutive tRNA binding site on the SSU (Noller et al., 2017). The tRNAs adopt chimeric states termed ap/P-tRNA state and pe/E-tRNA state (Figures 6C and 6G) (Noller et al., 2017; Ramrath et al., 2013; Zhou et al., 2014). The lowercase letters indicate the position of the tRNA ASLs with elements of the head (a or p) and elements of the body (p or e) (Ramrath et al., 2012). Accordingly, ap/P-tRNA establishes simultaneous contacts with A-site elements of the head, as well as P-site elements of the body and the pe/E-tRNA establishes simultaneous contacts with P-site elements of the head, as well as E-site elements of the body. Chimeric states become resolved by a final clockwise movement of the SSU head that occurs together with release of P_i (Belardinelli et al., 2016; Noller et al., 2017; Savelsbergh et al., 2003; Savelsbergh et al., 2005). Clockwise (backward) swiveling of the SSU head results in N-state 70S and the full translocation of deacyl-tRNA to the E-site and peptidyl-tRNA to the P-site, adopting an E/E and a P/P state, respectively (Figure 6D) (Noller et al., 2017). GDP-bound EF-G departs from the POST state 70S ribosome and leaves a vacant A-site. The deacyl-tRNA bound to the E-site is released and the ribosome can enter the next translation elongation cycle.

1.2.3 Translation termination

When the translating ribosome encounters one of the three stop codons, namely UAA, UAG or UGA, the translation elongation cycle comes to an end and the polypeptide chain is released from the 70S ribosome during the termination process (Figure 2C) (Brenner et al., 1965; Capecchi, 1967; Weigert and Garen, 1965). Termination involves binding of class I peptide chain release factors RF1 or RF2 to the A-site of POST state 70S ribosomes (Figure 2C) (Capecchi, 1967). RF1 and RF2 have a four-domain structure and couple the termination signal exposed in the A-site of the DC to release of the polypeptide chain at the PTC (Figure 7A) (Zhou et al., 2012a). Domains II and IV form a super-domain responsible for decoding of the mRNA stop codon exposed in the DC (Figure 7A). Domain III reaches into the PTC and thereby facilitates the liberation of the polypeptide chain (Figure 7A). Importantly, the domains crucial for successful termination, namely super-domain II/IV and domain III, harbor specialized motifs that allow accurate stop codon recognition and efficient release of the peptide in the PTC, respectively. Similar to canonical decoding, termination involves the DC nucleotides G530, A1492 and A1493 (Korostelev et al., 2008; Laurberg et al., 2008; Weixlbaumer et al., 2008), which together with a β -sheet provided by domain II recognize the exposed stop signal in the DC. Upon stop codon selection and RF binding, A1492 moves outward from h44 (Korostelev et al., 2008; Laurberg et al., 2008; Ogle et al., 2001; Selmer et al., 2006; Weixlbaumer et al., 2008). A1493 stays in a 'flipped-in' conformation and stacks upon 23S nucleotide A1913, which occupies the space of non-flipped A1492 (Korostelev et al., 2008; Laurberg et al., 2008; Weixlbaumer et al., 2008). G530 establishes a stacking interaction with nucleotide in the third position of the stop codon (Korostelev et al., 2008; Laurberg et al., 2008; Weixlbaumer et al., 2008). The motif within the β -sheet of domain II involved in stop codon recognition differs between RF1 and RF2. RF1 harbors the tripeptide Pro-Val-Thr (PVT) sequence (Figure 7B) whereas RF2 has instead the Ser-Pro-Phe (SPF) motif (Figure 7C) (Ito et al., 2000). The sequence motifs allow both factors to recognize UAA yet distinguish between UAG and UGA codons. Consistently, decoding of the very first position of a stop codon is carried out by both factors similarly (Figures 7B and 7C): The N-terminal part of α -helix 5, present in both class I release factors,

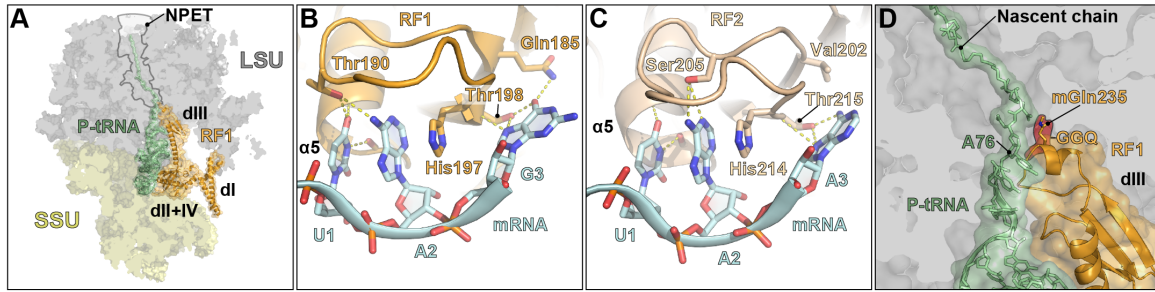


Figure 7 – Class I peptide chain release factor binding. (A) Overview of a 70S ribosome with RF1 (orange) and P-tRNA (green). The P-tRNA carries the MifM staller nascent chain at the CCA-end (Sohmen et al., 2015). The nascent chain reaches down the polypeptide exit tunnel (NPET), which is located on the LSU (grey). The position of the domains of RF1 is indicated in black. (B–C) Interactions of domain II/IV of RF1 and RF2 with the stop codon nucleotides encoded by an mRNA (cyan). (B) Interactions of RF1 (orange) with a UAG stop codon (cyan) (Laurberg et al., 2008; Pierson et al., 2016). (C) Interactions of RF2 (wheat) with a UAA stop codon (cyan) (Pierson et al., 2016; Weixlbaumer et al., 2008). (D) Zoom of (A) showing the relative position of the methylated GGQ motif (red) to the nascent chain that is attached to P-tRNA (green) (Pierson et al., 2016). The GGQ motif is situated within domain III of RF1 (orange).

contributes two hydrogen bonds and allows RFs to validate the presence of a uridine in the first position (Figures 7B and 7C) (Korostelev et al., 2008; Laurberg et al., 2008; Petry et al., 2005; Weixlbaumer et al., 2008). The second codon position, crucial for RFs to distinguish between UAG and UGA codons, is the only position that involves direct interactions with the PVT or SPF motifs of RF1/2 (Figures 7B and 7C) (Zhou et al., 2012a). The Thr of the PVT motif (RF1) (Figure 7B) (Korostelev et al., 2010; Laurberg et al., 2008) and the Ser (Korostelev et al., 2008; Weixlbaumer et al., 2008) of the SPF motif (RF2) (Figure 7C) directly contact the second position by establishing hydrogen bonds (Zhou et al., 2012a). In this way, RF1 forms one hydrogen bond in the presence of adenine in the second position (Figure 7B) (Korostelev et al., 2010; Laurberg et al., 2008) and RF2 makes two hydrogen bonds with a purine nucleotide, guanine and adenine, in the second position (Figure 7C) (Korostelev et al., 2008; Weixlbaumer et al., 2008). The determination of the third position of the stop codon involves a Thr and a Gln residue in RF1 (Figure 7B) (Korostelev et al., 2010; Laurberg et al., 2008) and a Thr, as well as a Val residue in RF2 (Figure 7C) (Korostelev et al., 2008; Weixlbaumer et al., 2008). These residues monitor the Hoogsteen edges of the base in the third position (Figures 7B and 7C) (Zhou et al., 2012a). In addition to the described discrimination activities of domain II of the RFs, stop codon recognition is further stabilized by other amino acids to ensure termination fidelity. For example, His197 in RF1 (Figure 7B) (Laurberg et al., 2008) and His214 in RF2 (Figure 7C) (Weixlbaumer et al., 2008) stack upon the purine base of the nucleotide in the second position of the stop codon.

The successful decoding of the stop codon leads to conformational changes within the switch loop of RF1/2 (Youngman et al., 2008; Zhou et al., 2012a). As a consequence of switch loop rearrangements, RF1/2 domain III accommodates into the PTC of the LSU (Figure 7D) (Youngman et al., 2008; Zhou et al., 2012a). Domain III harbors a tripeptide Gly-Gly-Gln (GGQ) motif that facilitates the release of the nascent chain (Figure 7D) that is conserved between RF1 and RF2 (as well as the evolutionarily unrelated eukaryotic termination release factor eRF1) (Frolova et al., 1999; Mora et al., 2003; Seit-Nebi et al., 2001; Shaw and Green, 2007; Zavialov et al., 2002). Therefore, RF1 and RF2 utilize the same mechanism for polypeptide chain release. As part of this mechanism, a water molecule is utilized as an acceptor for the nascent peptide to release it from the ribosome (Tate and Brown, 1992). The water molecule fulfills the same function during termination as the deprotonated α -amine during transpeptidation (Kuhlenkoetter et al., 2011; Trobro and Aqvist, 2009) by attacking the carbonyl linking the peptidyl moiety to the P-site tRNA (Kuhlenkoetter et al., 2011; Trobro and Aqvist, 2009). Molecular dynamic simulations suggest that the conserved GGQ motif positions the crucial water molecule in the PTC next to nucleotide A76 of the P-tRNA that carries the peptidyl moiety (Trobro and Aqvist, 2009). It presumably involves the 23S rRNA residue A2451, the 2'-hydroxyl of A76 and the backbone NH-group of the glutamine residue (Trobro and Aqvist, 2009). Strikingly, glycine residues in the first two positions of the GGQ motif are more critical for placement of the water molecule than glutamine in the third (Mora et al., 2003; Shaw and Green, 2007; Zavialov et al., 2002). Mutagenesis of either glycine leads to strong effects on translation termination (Mora et al., 2003; Shaw and Green, 2007; Zavialov et al., 2002). This is caused by the unique conformation of the GGQ motif, which is constrained by the achiral nature of glycine residues and their dedicated torsion angles (Zhou et al., 2012a). In absence of the glycine residues, the placement of the GGQ, as well as the water molecule inside the PTC is perturbed (Mora et al., 2003; Shaw and Green, 2007; Zavialov et al., 2002). This contrasts with alterations of the Gln which were observed to have only rather mild effects (Shaw and Green, 2007; Zavialov et al., 2002). Instead, the glutamine (*E. coli* Gln235) has been suggested to be crucial for the nucleophile specificity (Shaw and Green, 2007). In any case, the backbone NH-group is involved in the coordination of the water molecule and seems to be important for stabilization of a tetrahedral intermediate and the final product (Laurberg et al., 2008). The tetrahedral intermediate results from the nucleophilic attack of the

coordinated water, possibly carrying an oxyanion stabilized by the NH-group (Laurberg et al., 2008). After successful cleavage, the peptidyl moiety is released from the ribosome and the deacyl-tRNA stays bound to the ribosome. The deacyl-tRNA is stabilized by the backbone NH-group through hydrogen bonding with 3'-hydroxyl of A76 (Laurberg et al., 2008). Due to the minor relevance of the side chain, replacement of Gln by other amino acids, like alanine, is acceptable and primarily affects the rate of release (Mora et al., 2003; Seit-Nebi et al., 2001; Shaw and Green, 2007; Zavialov et al., 2002), since the presence of the amino-group is not altered (Laurberg et al., 2008). However, under natural conditions RF1 and RF2 carry a post-translational modified GGQ motif. N5 of the Gln side chain becomes methylated by the methyltransferase HemK (Dincbas-Renqvist et al., 2000; Heurgue-Hamard et al., 2002; Pierson et al., 2016; Zeng and Jin, 2018). Methylation of the Gln side chain possibly plays a more crucial role in coordination of water together with the backbone NH-group of the glutamine residue (Shaw and Green, 2007). This concept is supported by a recent X-ray crystallography study, which resolved the exact conformation of the methylated Gln side chain (Zeng and Jin, 2018). The authors describe that in presence of the Gln methylation the side chain adopts a conformation which allows the exact positioning of the carbonyl carbon for coordination of the nucleophilic water molecule (Zeng and Jin, 2018).

After nascent peptide release, RF1/2 and deacyl-tRNA stay bound to the ribosome (Figure 2C). The termination release factor 3 (RF3), a class II RF, dissociates ribosome-bound RF1/2 and returns them to the pool of translation factors available for protein synthesis (Figure 2C) (Freistroffer et al., 1997; Goldstein and Caskey, 1970). RF3 is a three-domain protein and shows high structural similarity to other translational GTPases like EF-G, EF-Tu and IF2 (Gao et al., 2007; Jin et al., 2011; Kihira et al., 2012; Zhou et al., 2012b). Domain I (G-domain) harbors the GTPase activity and is activated by contacting the SRL (Lin et al., 2015; Loveland et al., 2017; Zhou et al., 2012b). Domain II and III are linked via a flexible linker and establish contacts with the SSU that allow RF3 binding (Gao et al., 2007; Zhou et al., 2012b), in particular with S12 and 16S rRNA helices h5 and h15 (Jin et al., 2011; Zhou et al., 2012a; Zhou et al., 2012b). However, in contrast to the previous termination step, binding of RF3 does not require an mRNA signal exposed in the A-site. Possibly facilitated by L7/L12 (Carlson et al., 2017; Pallesen et al., 2013), RF3 binds most likely in its GTP-bound form to 70S ribosomes irrespective of the presence of termination factors and deacyl-

or peptidyl-tRNA (Adio et al., 2018; Koutmou et al., 2014; Peske et al., 2014). Furthermore, RF3 binding can occur even before release of the nascent chain from the ribosomes (Pre-hydrolysis 70S ribosome) (Adio et al., 2018). RF3 binding in complex with GDP has been discussed as well (Zavialov et al., 2001; Zavialov et al., 2002) but seems to be unlikely due to the presence of large excess of GTP over GDP inside the eubacterial cell under native conditions (Adio et al., 2018; Bennett et al., 2009). Nonetheless, the actual substrate for RF3-GTP action is a post-hydrolysis 70S ribosome harboring deacyl-tRNA in the P-site and RF1/2 in the A-site. The mechanism of factor dissociation was investigated in the last 15 years utilizing biochemistry, as well as cryo-EM and X-ray crystallography. Biochemical studies implied a mechanism driven by RF3 that leads to the formation of R-state ribosomes by SSU rotation (Adio et al., 2018; Ermolenko et al., 2007; Koutmou et al., 2014). Factor induced SSU rotation most likely leads to disengagement of RF1/2 domain III and superdomain II/IV from the ribosome. This view is supported by structural studies investigating RF3-GDP((C/N)P) bound to different ribosomal complexes (Gao et al., 2007; Jin et al., 2011; Kihira et al., 2012; Pallesen et al., 2013; Zhou et al., 2012b). In the presence of deacyl-tRNA, as well as in absence of other ligands/factors, all 70S-RF3 complexes showed rotational movement of the SSU by up to 9° and SSU head swiveling of 4-14° (Jin et al., 2011; Zhou et al., 2012b). Independent of the rotational state of the ribosome, superimpositions of RF1/2 in its binding site and corresponding RF3 structures show no steric hindrance for simultaneous binding of class I and class II release factors. Thus, rotation-driven dissociation of RF1/2 seems to be the most likely concept of RF3 mediated RF1/2 dissociation (Gao et al., 2007; Jin et al., 2011; Kihira et al., 2012; Pallesen et al., 2013; Zhou et al., 2012b). What remained unclear from previous studies is the underlying mechanism inducing subunit rotation and whether RF3 undergoes large conformational changes prior to GTPase activation. Furthermore, it has been discussed that GTP hydrolysis is not necessary for the actual process of RF1/2 recycling, but rather for dissociation of RF3 from the ribosome (Adio et al., 2018; Peske et al., 2014). This contrasts with EF-Tu and EF-G, which hydrolyze GTP before/during their action on the ribosome.

1.2.4 Ribosome recycling

Ribosomes and factors involved in protein synthesis are not single-use instruments. Therefore, mRNA has to be released and post-termination ribosomes have to be recovered after successful translation in a process called 'ribosome recycling' (Janosi et al., 1994; Karimi et al., 1999). While ribosome recycling itself is not crucial for protein synthesis *per se*, it is crucial to prevent depletion of the pool of ribosomal subunits ready for recruitment to mRNA. The process of ribosome recycling involves previously described translation elongation factor EF-G and an additional factor called ribosome recycling factor (RRF) (Figure 2C). Both factors are compulsory for recycling, since they act in concert in a GTP-dependent fashion (Hirokawa et al., 2006; Hirokawa et al., 2005; Peske et al., 2005; Zavialov et al., 2005). Successful recycling requires binding of RRF to post-termination complex (PoTC) in the intersubunit space prior to EF-G association (Borg et al., 2016; Dunkle et al., 2011; Prabhakar et al., 2017). There are numerous structures showing RRF bound to 70S ribosomes (Fu et al., 2016; Kim et al., 2000; Nakano et al., 2003; Saikrishnan et al., 2005; Selmer et al., 1999; Toyoda et al., 2000; Yokoyama et al., 2012; Yoshida et al., 2001). Two of these available structures are complexes showing RRF and EF-G simultaneously bound to 70S-PoTC (Fu et al., 2016; Yokoyama et al., 2012). RRF consists of two domains that are linked via a flexible linker that allows domain movement (Fu et al., 2016; Weixlbaumer et al., 2007). Characteristic for the structure of RRF is a three-helix bundle (domain I) that reaches up to the PTC (Dunkle et al., 2011). The loop at the tip of the bundle contacts the LSU P-loop (Dunkle et al., 2011). α -Helix 3 of the bundle is involved in ribosome binding by contacting H71 of the 23S rRNA (Dunkle et al., 2011). Domain II of RRF contacts the SSU via protein S12 (Dunkle et al., 2011; Fu et al., 2016; Gao et al., 2005). Binding of RRF to PoTC stabilizes R-states containing P/E hybrid state deacyl-tRNAs (Dunkle et al., 2011). Accordingly, $\sim 9^\circ$ SSU body/platform counterclockwise rotation and $\sim 4^\circ$ head swivel was observed upon RRF binding (Dunkle et al., 2011). Simultaneous positioning of RRF and either tRNA in a P/P-state (Dunkle et al., 2011), or RF1/2 (Pavlov et al., 1997), is not possible due to a steric block created by the three-helix bundle of RRF, which reaches up to the PTC and blocks the A- and P-site cleft on the LSU (Dunkle et al., 2011). Hence, binding is dedicated to complexes after peptide chain release and RF1/2 dissociation. However, ribosome splitting is presumably facilitated through domain II (Dunkle et al., 2011; Yokoyama et al., 2012),

which can adopt at least two different conformations in presence or absence of EF-G. Upon binding of EF-G and subsequent GTP hydrolysis RRF domain II rearranges towards domain I in close proximity to intersubunit bridge B2a (H69 and h44)(Fu et al., 2016; Wilson et al., 2005). Interactions between RRF and EF-G are generally different compared to EF-G/tRNA interactions (Yokoyama et al., 2012). While the tip of EF-G domain IV interacts with the tRNA ASL during translocation, no tRNA contact was observed in the RRF-EF-G structure (Yokoyama et al., 2012). Instead interactions between the junction of EF-G domain II-III and RRF domain II are present (Yokoyama et al., 2012). Problematic is the use of RRF and EF-G from different organisms in the respective study which in combination were shown to be inactive (Ito et al., 2002). Mechanistically it was suggested that EF-G induced conformational changes in domain II distort subunit bridges, such as B2a (Fu et al., 2016; Wilson et al., 2005; Yokoyama et al., 2012) and thereby dissociating the 70S ribosome into LSU and SSU. IF3 binding to the SSU then occludes interactions with the LSU and acts as starting point for another round of translation initiation (Hirokawa et al., 2005; Peske et al., 2005; Prabhakar et al., 2017). Furthermore, it was suggested that IF3 binding is also involved in dissociation of tRNA and mRNA from the SSU (Karimi et al., 1999; Prabhakar et al., 2017). Ribosome recycling connects translation termination with translation initiation and allows a handover between both steps of the cycle.

1.2.5 Interaction of L7/L12 with translational GTPases

Translational GTPases, such as EF-Tu, EF-G, IF2 and RF3, are indispensable for translation speed and fidelity. Binding of translational GTPases to the ribosome and subsequent GTPase activation involves the L7/L12 stalk, which is located on the LSU. The L7/L12 stalk comprises the 23S helices 42 to 44 (stalk base) and a pentameric (in *E. coli*) protein complex (Diaconu et al., 2005). The 23S rRNA stalk base forms the backbone of the L7/L12 stalk (Diaconu et al., 2005). The attached pentameric protein complex consists of two L7/L12 dimers, which are linked via their NTD to L10 (Diaconu et al., 2005). The L7/L12 NTD and CTD are connected through a flexible linker (Diaconu et al., 2005; Liljas and Gudkov, 1987). The CTD was observed to interact with the G-domain of translational GTPases, such as EF-Tu (Kothe et al., 2004; Stark et al., 1997), EF-G (Gao et al., 2009; Nechifor et al., 2007; Tourigny et al., 2013; Zhou et al., 2013, 2014), IF2 (Simonetti et al., 2013) and RF3 (Pallesen et al., 2013). This is

consistent with biochemical studies showing that EF-Tu, EF-G, RF3 and IF2 binding depends on the presence of L7/L12 (Wahl and Moller, 2002). The L7/L12 CTD can presumably ‘fish’ for translation factors in the cytoplasm and hence increase the efficiency of translation. Due to the presence of four CTDs in the *E. coli* L7/L12 stalk and six CTDs in the *T. thermophilus* L7/L12 stalk, several translation factors can establish interactions with L7/L12 stalk simultaneously. The importance for translation efficiency has been shown in various biochemical experiments. Accordingly, while one dimer of L7/L12 leads to basic levels of translation *in vitro*, the presence of two dimers leads to significantly increased translation efficiency (Mandava et al., 2012). The complete absence of the L7/L12 protein results in a strongly reduced rate of protein synthesis catalyzed by EF-G and EF-Tu (Koteliantsky et al., 1977). Nonetheless, L7/L12 does not affect the translation efficiency solely by binding to the G-domain of translational GTPases. It was observed that interactions with L7/L12 stimulate the GTPase activity of translation factors, like EF-G, EF-Tu, IF2 and LepA (Carlson et al., 2017; Mohr et al., 2002; Savelbergh et al., 2000). The absence of L7/L12 results in reduced GTPase activity and perturbed P_i release (Mohr et al., 2002).

Noteworthy, until recently there were no indications whether L7/L12 is involved in recruitment of non-GTPase translation factors, such as class I release factors. However, our studies on 70S ribosomes in complex with Api137, RF1 and RF3 revealed an unassigned density adjacent to domain I of RF1, which likely constitutes one of the four L7/L12 CTDs. Thus, the L7/L12 stalk seems to be involved in class I release factor recruitment as well (see discussion).

1.3 Plastid-derived ribosomes

Considering that living organisms constitute isolated systems with membranes shielding them from the environment, it is not surprising that evolution resulted in alterations of cellular machineries. Chloroplasts are a good example of isolated evolution. Chloroplasts are the result of an endosymbiotic event approximately 1 billion years ago that led to engulfment of a photosynthetic cyanobacterium by a eukaryotic cell (Price et al., 2012). Chloroplasts as such, are crucial for plants due to their function in carbon fixation, which is the result of photosynthesis. Photosynthesis takes place in the thylakoid membrane of chloroplasts and requires synthesis of protein components of the photosystem I and II complex as well as adenosine triphosphate synthase (Schmitz-Linneweber et al., 2001). The majority of the required chloroplast proteins

are synthesized outside the plastid and encoded within the eukaryotic host cell genome. A minor subset of proteins is encoded by the remaining chloroplast genome and synthesized inside the organelle by a specialized ribosome (Yamaguchi and Subramanian, 2000, 2003; Yamaguchi et al., 2000).

Protein synthesis inside chloroplasts is carried out by ribosomes that are similar to bacterial 70S ribosomes. Consistently, 70S chlororibosomes harbor a SSU and a LSU (Figures 8A-C). Just like ribosomes from other organisms and all kingdoms of life, the rRNA core shows high sequence conservation. Thus, it seems plausible that the same principles underlay protein synthesis. Nonetheless, despite similarities that derive from a common progenitor (Margulis, 1971; Price et al., 2012; Sagan, 1967), clear differences in the set of ribosomal proteins (Yamaguchi and Subramanian, 2000, 2003; Yamaguchi et al., 2000) and rRNA are evident (Schmitz-Linneweber et al., 2001). The overall tendency is an increase in protein mass (Reyes-Prieto et al., 2007). The rRNA nucleotide number stayed approximately the same (+13 nts), although chloroplast rRNA harbors numerous insertions and deletions compared to *E. coli* rRNA. Interestingly, the LSU of the chlororibosome harbors 23S, 5S and a 4.8S rRNA (Figures 8A-C). The 4.8S rRNA molecule, consisting of 103 nucleotides, is the result of a 3'-end fragmentation of the 23S rRNA. As a consequence, the 23S rRNA is truncated and consists of a total of 2,810 nucleotides compared to the *E. coli* 23S rRNA with 2,904 nucleotides. The most obvious differences between bacterial and chloroplast 70S ribosomes are six additional plastid-specific ribosomal proteins (PSRP1-6) (Figures 8A-C) and the lack of LSU proteins L25 and L30 (Yamaguchi and Subramanian, 2000, 2003; Yamaguchi et al., 2000). PSRP1-4 associate with the SSU (Figures 8A and 8C); PSRP5 and PSRP6 bind to the LSU (Figures 8A and 8B). PSRP3-5 were shown to be essential in *Arabidopsis thaliana* chloroplasts (Tiller et al., 2012). In addition to PSRP1-6, most of the plastid proteins harbor N- or C-terminal extensions (NTE and CTE), which together with PSRPs account for the increased rRNA/protein ratio (Yamaguchi and Subramanian, 2000, 2003; Yamaguchi et al., 2000). NTEs and CTEs compensate for rRNA deletions and allow reshaping of the ribosomal features (Ahmed et al., 2017; Ahmed et al., 2016; Bieri et al., 2017; Graf et al., 2017a). Reshaping of ribosomal features is especially important considering that the translational process in chloroplasts exhibits significant differences. In contrast to bacteria, more than 70% of all mRNAs in chloroplasts do not harbor a SD-sequence

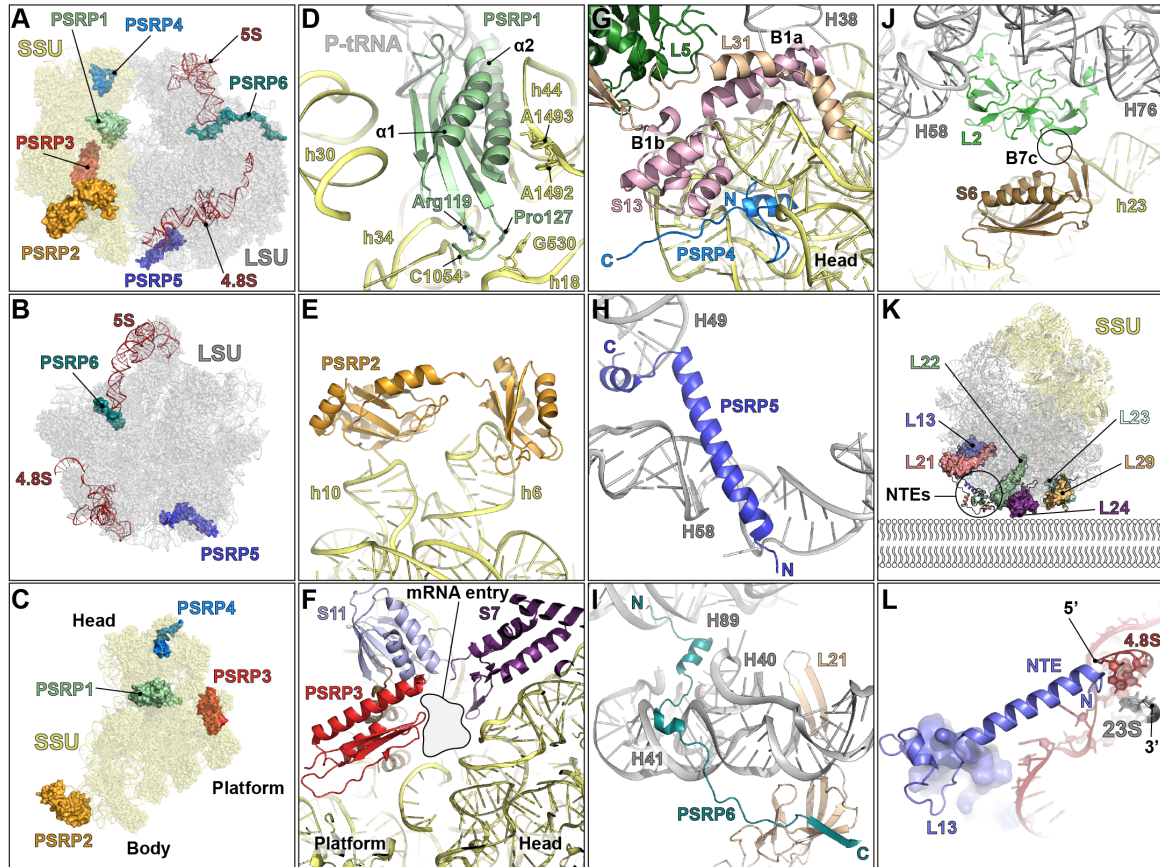


Figure 8 Chloroplast ribosome. (A-C) Overview of the structure of the chloroplast ribosome harboring PSRP1 (pale green), PSRP2 (orange), PSRP3 (red), PSRP4 (light blue), PSRP5 (dark blue) and PSRP6 (teal). The LSU is shown in grey and the SSU is shown in yellow. 5S and 4.8S rRNA are shown in dark red. (A) Interface view of the 70S ribosome consisting of a LSU (grey) and a SSU (yellow) (Ahmed et al., 2017). (B) Crown view of the LSU (Ahmed et al., 2017; Ahmed et al., 2016; Bieri et al., 2017; Graf et al., 2017a). (C) Interface view of the SSU (Ahmed et al., 2017). (D) Interactions of PSRP1 (pale green) with SSU (yellow) helices h18, h30, h34 and h44. Arg119 and Pro127 of PSRP1 protect C1054 and G530, respectively (Bieri et al., 2017). A1492 and A1493 of h44 are stabilized in a partially flipped conformation. The model was superimposed with P-tRNA (faint grey) to show the evidence of a steric block by PSRP1 that prevents tRNAs from binding. (E) PSRP2 (orange) bound to h6 and h10 (both yellow) at the foot of the SSU (Ahmed et al., 2017). (F) PSRP3 (red) binding site at the mRNA tunnel entry (grey filling with black contour) at the interface between the SSU (yellow) head and platform in close proximity to S7 (purple) and S11 (light blue) (Ahmed et al., 2017). (G) Interactions of PSRP4 (light blue) with the SSU head (yellow) and intersubunit bridges B1b and B1a (Ahmed et al., 2017; Bieri et al., 2017). Intersubunit B1a comprises LSU H38 (grey) and SSU protein S13 (pink). Intersubunit bridge B1b comprises S13 (pink), L5 (dark green) and L31 (wheat). (H) Interactions of PSRP5 (dark blue) with 23S rRNA helices (grey) H40, H41 and H49 (Bieri et al., 2017; Graf et al., 2017a). (I) Interactions of PSRP6 (teal) with the LSU (grey) (Ahmed et al., 2017; Bieri et al., 2017; Graf et al., 2017a). The N-terminal part of PSRP6 interacts with H40, H41 and H89. The C-terminal part of the proteins provides a β -strand to L21 (wheat). (J) Previously unobserved intersubunit bridge between SSU protein S6 (brown) and LSU protein L2 (green) (Bieri et al., 2017). The LSU helices (grey) H58 and H76, as well as the SSU helix h23 (yellow) are shown for reference. (K) Hypothetical interaction surface of the LSU (grey) with bacterial membrane that is created by the N-terminal extension (NTEs) of LSU proteins L13 (slate), L21 (salmon) and S22 (pale green) (Graf et al., 2017a). The NTEs interact with each other extensively (encircled area). The proteins L23 (cyan), L24 (purple) and L29 (brown) are shown for reference. (L) Stabilization of the 23S rRNA (grey) 3'-end and the 4.8S rRNA (dark red) 5'-end by the helical NTE of L13 (slate) (Bieri et al., 2017; Graf et al., 2017a).

(Drechsel and Bock, 2011; Hirose et al., 1998; Ruf and Koessel, 1988) and the protein targeting signal-recognition particle (SRP) lacks an RNA molecule directly involved in

localization (Richter et al., 2010).

However, the structure of chlororibosomes at higher resolution was recently presented in five different publications (Ahmed et al., 2017; Ahmed et al., 2016; Bieri et al., 2017; Forsberg et al., 2017; Graf et al., 2017a). All publications are in good agreement with each other and show just minor differences. The presented structures allowed the assignment of many of the protein extensions, the unambiguous placement of PSRPs and clarification of aberrations within rRNA and chloroplast ribosomal proteins compared to bacteria. All results, taken together with old studies, bring us a step closer to understand how translation in chloroplasts works.

The role of PSRP1, also known as translation factor pY, was clarified previously (Sharma et al., 2010). PSRP1 is a homologue of the bacterial stress response factor YifA (pY) (Agafonov et al., 2001; Vila-Sanjurjo et al., 2004) and therefore not a chlororibosome specific protein *per se* (Sharma et al., 2010). PSRP1 modulates protein synthesis in response to stress, such as lack of light (Sharma et al., 2010). Upon stress, PSRP1-mediated modulation of protein synthesis is achieved by binding to the mRNA channel on the SSU and contacting DC nucleotides (Figure 8D) (Bieri et al., 2017; Sharma et al., 2010). Contacts with the DC are thought to prevent degradation of the ribosome. Furthermore, PSRP1 occupies the SSU A- and P-site, which sterically occludes binding of tRNAs (Ahmed et al., 2017; Bieri et al., 2017; Graf et al., 2017a; Vila-Sanjurjo et al., 2004). As a consequence, translation is inhibited under stress conditions (Ahmed et al., 2017; Bieri et al., 2017; Sharma et al., 2010). The blockage of the A/P-site, and hence protein synthesis, involves contacts with numerous elements of the SSU. PSRP1 α -helix 1 contacts the backbone of 16S helix 44 (Figure 8D) (Bieri et al., 2017). Binding to the mRNA channel occurs through α -helix 2 that is positioned on top and prevents binding of a transcript (Figure 8D) (Bieri et al., 2017). In the DC PSRP1 induces partial flipping of DC nucleotides A1492 and A1493 (*E. coli* numbering) (Ahmed et al., 2017; Bieri et al., 2017). G530 and C1054 (*E. coli* numbering) are protected by interactions with Pro127 and Arg119 of PSRP1 (Figure 8D) (Bieri et al., 2017). PSRP1 binding is further stabilized by interactions of the CTE that harbors two histidine residues (His178 and His181) and mimics the mRNA nucleotide base in the ribosomal E-site (Bieri et al., 2017). An extended loop between β -strand 2 and 3 establishes interactions with 16S helices 18 and 34 (Figure 8D) (Bieri et al., 2017).

The exact function of PSRP2 and PSRP3 remains mostly elusive. Biochemical assays indicated a chaperone function for PSRP2 under stress conditions (Xu et al., 2013). Other studies suggest that binding of both factors primarily compensates for the deletion of 16S rRNA nucleotides in h6 and h10 at the SSU foot (Sharma et al., 2007). However, two recent chlororibosome reconstructions contradict the simultaneous binding of PSRP2 and PSRP3 to the foot (Ahmed et al., 2017; Forsberg et al., 2017). Although an additional density at the tip of h6 and h10 has been observed (Ahmed et al., 2017; Bieri et al., 2017; Forsberg et al., 2017), another spare density is present at the mRNA tunnel exit (Ahmed et al., 2017; Forsberg et al., 2017). Using 8 Å filtered maps, the density was assigned by Ahmed and colleagues to PSRP3 (Figure 8F) (Ahmed et al., 2017). This allowed the placement of the entire PSRP2 at the tip of h6 and h10 (Figure 8E) (Ahmed et al., 2017). Thus, PSRP2 alone compensates for rRNA truncations. Structurally, PSRP2 is comprised of two domains connected by a linker (Figure 8E) (Ahmed et al., 2017). Nonetheless, the overall density at the respective positions is rather poor (Ahmed et al., 2017; Bieri et al., 2017; Forsberg et al., 2017). Therefore, none of the recent reconstructions allowed unambiguous placement of protein homology models with side chain accuracy. Notably, Bieri and colleagues do not see the respective additional density at the mRNA tunnel exit at all (Bieri et al., 2017). In their model, PSRP2 and PSRP3 were placed at the foot, in accordance to the original suggested model (Sharma et al., 2007). This is surprising, since evaluation of the deposited map showed no density for PSRP3 at the tip of h6. Furthermore, simultaneous placement of PSRP2 and PSRP3 requires significant N-terminal truncation of PSRP2 due to the lack of additional unassigned density. Considering these differences, it seems unlikely that PSRP2 and PSRP3 bind side by side to the spur.

PRSP4 is a short (46 aa) protein, which has homology to the *T. thermophilus* protein bTHX that binds to the head of the SSU (Wimberly et al., 2000). Consistently, PSRP4 is also seen to bind in the analogous position in chlororibosomes (Figure 8G) (Ahmed et al., 2017; Bieri et al., 2017). A counterpart in *E. coli* does not exist. Binding to the SSU is thought to stabilize the SSU head, as well as contacts between the LSU and the SSU (Ahmed et al., 2017; Bieri et al., 2017). Stabilization is achieved through interactions with 16S rRNA and intersubunit bridge B1a (Ahmed et al., 2017) as well as B1b (Figure 8G) (Ahmed et al., 2017; Bieri et al., 2017). The respective interactions

involve the core of the protein, conserved between *T. thermophilus* and chloroplasts, contacting h41 and h42 of the 16S rRNA (Ahmed et al., 2017; Bieri et al., 2017).

In recent studies, PSRP5, which is largely enriched in positively charged residues, was found to interact with H58 through its N-terminal α -helix (Figure 8H) (Bieri et al., 2017; Graf et al., 2017a). This contradicts older low-resolution structures where PSRP5 was positioned incorrectly near the L1 stalk (Sharma et al., 2007). A shorter α -helical portion at the C-terminus of PSRP5 contacts the minor groove of H49 (Figure 8H) (Bieri et al., 2017; Graf et al., 2017a). Positioning of the protein most likely serves as compensation for H63 that is lacking in chlororibosomes and contacts H58, H59 and H60 in *E. coli* ribosomes (Bieri et al., 2017). Hence, PSRP5 seems to be required for stabilization by taking over functions from rRNA residues.

PSRP6 was identified as a protein with an extended conformation (Figure 8I) (Ahmed et al., 2016; Bieri et al., 2017; Graf et al., 2017a). The positively charged N-terminal portion containing two small α -helices interacts with the negatively charged backbone of the 23S rRNA (Figure 8I) (Bieri et al., 2017; Graf et al., 2017a). The interactions involve the minor grooves of H40, H42 and H89 (Figure 8I) (Bieri et al., 2017; Graf et al., 2017a). The C-terminal portion of PSRP6 does not contact rRNA (Figure 8I) (Graf et al., 2017a), but instead contributes a β -strand to the β -sheet of L21 (Figure 8I) (Graf et al., 2017a). Nonetheless, despite identification of the binding position of PSRP6, the exact role and function of the protein remains unclear.

Many of the chloroplast protein extensions replace rRNA residues, stabilize the altered rRNA network and introduce new features to the ribosome architecture. Such features include intersubunit bridges, reshaping of the mRNA tunnel, restructuring of the polypeptide exit tunnel and the formation of an expanded membrane interaction surface.

CTEs of SSU protein cpS6 and LSU protein cpL2 form a previously unobserved intersubunit bridge, termed B7c (Figure 8J) (Bieri et al., 2017).

The SSU proteins cpS1, cpS4 and cpS5 rebuild the chloroplast mRNA tunnel entry/exit. Rebuilding of the tunnel entry occurs through cpS3, cpS4 with an internal insertion and the NTE of cpS5 (Bieri et al., 2017). All proteins together form a confined mRNA tunnel entry (Bieri et al., 2017). In addition, the NTE of cpS5 mediates between proteins by interacting with cpS1, cpS3 and cpS4 (Bieri et al., 2017). The SSU protein cpS1 reaches from the tunnel entry to the tunnel exit on the solvent side of the SSU. The extension of cpS1 is primarily involved in reshaping of the mRNA tunnel exit (Bieri

et al., 2017). Reshaping of both tunnel entry and tunnel exit was suggested to be required for translation initiation in chloroplasts utilizing cis- and trans-acting elements that compensate for altered translation initiation (Ahmed et al., 2017; Bieri et al., 2017; Sugiura, 2014; Zerges, 2000).

The polypeptide tunnel exit becomes restructured by NTEs of cpL23 and cpL24, as well as a CTE of cpL29 (Ahmed et al., 2016; Bieri et al., 2017; Graf et al., 2017a). The CTE of cpL29 and the NTE of cpL23 contact each other and replace truncated 23S rRNA helix 9 present in *E. coli* (Ahmed et al., 2016; Bieri et al., 2017; Graf et al., 2017a). Reshaping of the polypeptide tunnel exit is thought to be the result of a coevolution, which took place together with reduction of cpSRP54 lacking an RNA molecule (Bieri et al., 2017; Richter et al., 2010). Consistently, the additional protein residues might be required for additional contacts that allow cpSRP54 mediated protein localization in chloroplasts (Ahmed et al., 2016; Bieri et al., 2017; Graf et al., 2017a).

Targeting to thylakoid membranes is possibly facilitated through protein extensions of cpL13, cpL21 and cpL22 (Figure 8K) (Graf et al., 2017a). The NTE of cpL13, the NTE of cpL21 and the CTE of cpL22 extensively interact with each other and increase the surface of the LSU (Figure 8K) (Graf et al., 2017a). The expanded surface constitutes a suitable candidate for membrane interactions (Figure 8K). Assuming such interactions, the polypeptide tunnel exit would face the thylakoid membrane.

An example for the stabilization by protein extensions is the fragmented 23S rRNA (Figure 8L). Fragmentation of the rRNA into two separate molecules, namely 4.8S and 23S rRNA, led to the loss of nucleotides in-between (-16 nts) as well as the creation of exposed 5'- and 3'-ends. The helical NTE provided by cpL13 contacts the 5'-end of the 4.8S rRNA and the 3'-end of the 23S rRNA via positively charged residues and thereby stabilizes each terminus (Figure 8L) (Bieri et al., 2017; Graf et al., 2017a).

1.4 Antimicrobial peptides

Continuous competition of organisms in a quickly changing environment results in the development of a wide range of survival strategies which grant some organisms advantages over others - a principal that has been described by Charles Darwin almost 150 years ago (Darwin, 1869). One strategy of microorganisms is the invasion of

multicellular organisms, such as mammals, that provide a nutritive environment for successful bacterial progression and proliferation. Bacterial invasion of an organism occurs through lesions and mucosae for example. To prevent the establishment of an infection, higher eukaryotes developed an immune system that ideally prevents but at least restricts and eliminates further bacterial proliferation. The first line of defense represents the innate system. The innate immune system recognizes pathogens by specialized receptors and establishes a non-specific immune response by recruitment of phagocytic cells, such as macrophages and neutrophils. At the site of infection these cells either release a deadly compound cocktail or engulf the foreign organism and subsequently kill it inside the cell. The released cocktail contains antimicrobial peptides (AMPs) as well as other agents, such as reactive oxygen species. Due to the nearly unlimited number of amino acid combinations, AMPs are capable of attacking almost every extra-/intra-cellular site and process of a bacterial pathogen (Brogden, 2005). Among those extracellular targets is the bacterial cell wall and the bacterial membrane (Brogden, 2005). Intracellular targets include fundamental processes like bacterial replication, transcription and translation (Brogden, 2005; Graf et al., 2017b). The intrinsic diversity of peptides combined with the need for compounds fighting bacterial infections, make AMPs a valuable and promising source for future antibiotics that can be possibly used in a clinical setting.

AMPs can be classified based on their amino acid composition, as well as their specific target (Jenssen et al., 2006). One specific group, called Proline-rich AMPs (PrAMPs), belongs to the subclass of cationic peptides, which are characterized by a high content of proline and arginine residues (Graf et al., 2017b). Starting with the identification of the first PrAMP in the late 1980s by HPLC, namely apidaecin from the honey bee *Apis mellifera* (Casteels et al., 1989), more PrAMPs have been identified in higher eukaryotes, like mammals and arthropods (Agerberth et al., 1991; Bulet et al., 1993; Casteels et al., 1990; Chernysh et al., 1996; Cociancich et al., 1994; Gennaro et al., 1989; Huttner et al., 1998; Knappe et al., 2010; Mardirossian et al., 2018; Schnapp et al., 1996; Schneider and Dorn, 2001; Shamova et al., 1999; Stensvag et al., 2008). Among mammals, PrAMPs have been identified in cows (Gennaro et al., 1989), dolphins (Mardirossian et al., 2018), goats (Shamova et al., 1999), pigs (Agerberth et al., 1991), as well as sheep (Huttner et al., 1998; Shamova et al., 1999). Arthropod PrAMPs were found in crabs (Stensvag et al., 2008) and numerous insects (Bulet et al., 1993; Casteels et al., 1989; Casteels et al., 1990; Chernysh et al., 1996;

Cociancich et al., 1994; Knappe et al., 2010; Schneider and Dorn, 2001). Equivalent to apidaecin (Casteels et al., 1989), the nomenclature of PrAMPs predominantly corresponds to the origin of identification. Accordingly, PrAMPs from *Tursiops truncates* (bottlenose dolphin) are termed Tur1A and Tur1B (Mardirossian et al., 2018), peptides from *Bos taurus* (cattle) are called bactenecins (Gennaro et al., 1989) and *Oncopeltus fasciatus* (milkweed bug) derived PrAMPs are termed oncocins (Knappe et al., 2010; Schneider and Dorn, 2001). Noteworthy, peptides with high sequence similarity are commonly named after the source in which the PrAMP was first discovered. Thus, PrAMPs from *Capra hircus* (goat) and *Ovis aries* (sheep) (Huttner et al., 1998; Shamova et al., 1999), which show similarity to *Bos taurus* peptides, are called bactenecins as well.

1.4.1 Synthesis of PrAMPs

As mentioned before, PrAMPs are primarily produced upon bacterial infection by cells of the innate immune system, called phagocytes (Zasloff, 2002). Phagocyte progenitors, immature myeloid cells in mammals, synthesize PrAMPs as inactive precursors and store these in granules (Graf et al., 2017b; Zanetti et al., 1990; Zanetti et al., 1991). Storage of PrAMPs as inactive precursors in granules serves different functions. First, it protects the producing cell from harm by the peptide, and second, it allows a fast pathogen response by avoiding time-consuming protein synthesis. Activation of the inactive precursors occurs at the target site by proteolytic cleavage (Zanetti et al., 1990; Zanetti et al., 1991). The respective proteases are stored separately from the inactive precursors in a different set of granules (Zanetti et al., 1990; Zanetti et al., 1991). In mammals PrAMP-containing granules are called large granules, and protease-harboring granules are termed azurophil granules (Zanetti et al., 1990; Zanetti et al., 1991). Activation of precursors is induced by simultaneous exocytosis into extra-cellular space or bacteria-containing phagosomes (Zanetti et al., 1990; Zanetti et al., 1991). However, the overall structure of PrAMP precursors, as well as the resulting path of activation differs between organisms and PrAMPs (Graf et al., 2017b). Although not all mechanisms of peptide activation have so far been clarified, a single-peptide activation mechanism can be distinguished from a multi-peptide activation mechanism (Graf et al., 2017b). All mammalian PrAMPs seem to be activated by the single-peptide mechanism. Insect PrAMPs activated through a multi-

peptide activation mechanism are apidaecin (from *Apis mellifera*) (Casteels-Josson et al., 1993) as well as riptocin (from *Riptortus pedestris*) (Graf et al., 2017b). The single-peptide mechanism involves an mRNA coding for a polypeptide sequence harboring a preceding pre-sequence (~20-30 aa), a pro-sequence (~20-100 aa) and a Pro-Arg-rich sequence (Bulet et al., 1993; Graf et al., 2017b; Storici and Zanetti, 1993; Zanetti et al., 1993). The pro-sequence is placed either before (e.g. bactenecin and PR-39) (Storici and Zanetti, 1993; Zanetti et al., 1993) or after the PrAMP (e.g. drosocin) (Bulet et al., 1993). The multi-peptide mechanism comprises an mRNA coding for multiple PrAMPs that are intercepted by an inactivating oligopeptide linker, such as "RR-EAEPEAEP" from *Apis mellifera* (Casteels et al., 1989; Casteels-Josson et al., 1993). Proteolytic cleavage sites at the N- and C-terminus of the linker liberate the peptide (Casteels et al., 1989; Casteels-Josson et al., 1993). Similar to single PrAMP coding mRNAs, the multi-coding messages harbor a pre- (~15-20 aa) and pro-sequence (~13-16 aa) at the very beginning of the polypeptide (Casteels et al., 1989; Casteels-Josson et al., 1993). Noteworthy, the amino acid sequences of the PrAMPs encoded by the multi-peptide messages can vary significantly. In accordance, the multi-peptide activation mechanism leads to the liberation of different isoforms.

1.4.2 Uptake pathway of PrAMPs

The vast majority of antimicrobial peptides utilized by the innate immune system target the bacterial membrane and thereby facilitate lysis of the pathogenic cell (Brogden, 2005). This contrasts with PrAMPs, which were shown to inhibit bacterial growth at low concentrations through a non-lytic mechanism (Casteels and Tempst, 1994; Castle et al., 1999; Otvos, 2002; Scocchi et al., 2011). At high concentrations, PrAMPs, such as Bac7, were reported to have lytic activity as well (Scocchi et al., 2011). Regardless, the utilization of a non-lytic mechanism of action initially raised the question of putative uptake pathways. Mutagenesis experiments led to the identification of two key players responsible for PrAMP uptake, namely SbmA (Mattiuzzo et al., 2007) and more recently MdtM (Krizsan et al., 2015b). While SbmA seems to be the major transporter for PrAMP uptake, the inner membrane protein MdtM seems to play just a minor role in antimicrobial peptide internalization (Krizsan et al., 2015b). The major transporter SbmA is a 46.5 kDa protein localized in the inner membrane of Gram-negative bacteria (Mattiuzzo et al., 2007). SbmA internalizes PrAMPs, as well as other antimicrobial

agents using an electrochemical proton gradient (Runti et al., 2013). Besides peptide uptake, the general function of SbmA remains elusive. Among Gram-negative bacteria homologs of SbmA can be found in *Enterobacteriaceae*, like *Escherichia* species and *Salmonella* species and *Pseudomonadales*, like *Acinetobacter baumannii*, as well as in α - and ϵ -proteobacteria, such as *Neisseria meningitis* and *Campylobacter* species, respectively (Graf et al., 2017b).

1.4.3 Discovery of the intracellular target of PrAMPs

Biochemical studies within the last 50 years led to a controversy about the primary intracellular target of PrAMPs. Although at first, translation was suggested as the putative target for PrAMP inhibition (Castle et al., 1999), co-immunoprecipitation experiments contradicted this theory and resulted in the identification of chaperone assisted folding as primary target for PrAMPs (Otvos et al., 2000). In the course of these investigations, biotinylated derivatives of pyrrhocoricin (Pyr), drosocin (Dro) and apidaecin (Api) analogs were purified with anti-biotin antibodies and observed to co-purify with the chaperone DnaK (Otvos et al., 2000). In a similar fashion to pyrrhocoricin, drosocin and apidaecin, coupling of the N-terminal 35 amino acids of bactnecin-7 (Bac7) to 2-chlorotriyl resins also resulted in co-purification of DnaK (Scocchi et al., 2009). The direct visualization of PrAMP binding to DnaK was achieved using X-ray crystallography (Knappe et al., 2011b; Zahn et al., 2013; Zahn et al., 2014). PrAMPs were observed to bind to the cleft of DnaK, which represents the canonical binding site of DnaK substrates (Knappe et al., 2011b; Zahn et al., 2013; Zahn et al., 2014). However, soon after structures of PrAMPs in complex with DnaK had been obtained reasonable doubts about the working concept were raised. Experiments with *E. coli* *dnaK* deletion strains resulted in susceptibilities comparable to wildtype *E. coli* strains (Krizsan et al., 2014; Scocchi et al., 2009). Therefore, co-immunoprecipitation experiments with labeled PrAMPs and *E. coli* lysate were used again to identify an alternative target. As result, ribosomes were determined as alternative binding sites for PrAMPs (Krizsan et al., 2014; Mardirossian et al., 2014). Subsequent binding assays, as well as *in-vitro* translation experiments, indicated that ribosomal protein synthesis is the primary process inhibited by PrAMPs (Krizsan et al., 2014; Mardirossian et al., 2014).

1.4.4 Determination of the ribosomal binding site of PrAMPs

As consequence of the newly discovered ribosome binding and inhibition capacity of PrAMPs, it became interesting to resolve structures of 70S ribosomes in complex with different peptides and to determine the mode of action for each peptide. Thus, it remained elusive whether all PrAMPs bind in the same position and whether they exhibit the same mechanism of inhibition. The first PrAMP to be resolved on the bacterial ribosome was an oncocin (Onc) from milkweed bugs (*Oncopeltus fasciatus*) (Roy et al., 2015; Seefeldt et al., 2015), followed by bactenecin-7 (Bac7) from cows (*Bos taurus*), metalnikowin (Met) from the green shield bug (*Palomena prasina*) and pyrrhocoricin (Pyr) from the firebug (*Pyrrhocoris apterus*) (Gagnon et al., 2016; Seefeldt et al., 2016). The latest resolved structures of PrAMPs are Api137 from the honey bee (*Apis mellifera*) (Florin et al., 2017) and Tur1A from bottlenose dolphins (*Tursiops truncates*) (Mardirossian et al., 2018). The only structure resolved by cryo-EM is a Api137 containing 70S ribosomal complex (Florin et al., 2017).

All PrAMPs were found to bind to the polypeptide tunnel in an extended conformation, which overlaps with the path of a nascent chain (Florin et al., 2017; Gagnon et al., 2016; Mardirossian et al., 2018; Roy et al., 2015; Seefeldt et al., 2016; Seefeldt et al., 2015). The extended conformation probably results from the high-content of arginine residues in combination with *trans*-proline (Graf et al., 2017b). As shown by the structural studies, binding of PrAMPs involves a series of polar contacts, as well as stacking interactions between the peptide and the ribosome (Graf et al., 2017b). Interactions of Bac7 and Tur1A with the ribosome predominantly involve arginine side chains (Gagnon et al., 2016; Mardirossian et al., 2018; Seefeldt et al., 2016). Nonetheless, the primary difference between all PrAMPs resides within the mode of action, as well as the binding orientation. Accordingly, the N-terminus of class I PrAMPs is situated within the A-site binding pocket, whereas the C-terminus reaches down the polypeptide exit tunnel. Compared to a nascent chain, class I PrAMPs bind with an opposite orientation. This contrasts with the class II PrAMP Api137, which binds to the polypeptide exit tunnel with a similar orientation to a nascent chain. The N-terminus of Api137 is situated deeper in the tunnel and the C-terminus reaches into the PTC but not further into the A-site binding pocket. In general, PrAMP residues buried in the polypeptide tunnel are less crucial for antimicrobial activity than the residues in the PTC or A-site binding pocket. The termini located in the A-site

distinguish the mode of action. Consistently, the N-terminal residues of class I PrAMPs, located in the A-site binding pocket, inhibit the transition from translation initiation to translation elongation by sterically overlapping with an accommodated A-tRNA. Class II PrAMPs specifically inhibit translation termination by establishing interactions with deacyl-P-tRNA and RF1 (see discussion).

2 Objectives of these studies

Class II release factor RF3 (Publication 1)

The class I release factors RF1 and RF2 mediate the release of a nascent polypeptide from the 70S ribosome upon stop codon selection. Recycling of RF1 and RF2 from the 70S ribosome is mediated by the class II release factor RF3. Dissociation of RF1 or RF2 is presumably the result of SSU rotation, which is induced through RF3 binding. Although structural data on RF3-bound 70S ribosomes are available, the exact series of events and interactions, which ultimately lead to dissociation of RF1 and RF2 from the ribosomes, remain partially obscure. Especially intermediate states that harbor RF1, RF3 and deacyl-tRNA simultaneously are highly interesting to understand the exact mechanism of RF3 action. The aim of this work is to obtain high resolution structures of intermediate states of RF3-mediated recycling, which contain (besides RF3) RF1 and tRNA. Intermediate states will give insights into the changing interactions between the ribosome, tRNA, RF1 and RF3. Further it may become clear whether RF3 undergoes conformational changes and how RF3 exactly drives rotation of the SSU.

Chloroplast ribosomes (Publication 2)

Chloroplast 70S ribosomes are characterized by an increased ratio of protein to rRNA residues. Consistently, chlororibosomes harbor compared to *Escherichia coli* 70S ribosomes numerous additional protein extension and six plastid specific ribosomal proteins (PSRPs). With regard to rRNA residues, although the total number of nucleotides stayed approximately the same, chlororibosomes exhibit numerous rRNA deletions and insertions. However, older biochemical analysis allowed the rough assignment of PSRPs to the LSU (PSRP5 and PSRP6) and the SSU (PSRP1 to PSRP4). The precise localization of protein extensions and PSRPs requires structural data. While the binding position of PSRP1 has been determined before in a 9.4 Å low resolution structure, the exact binding position of PSRP2 to PSRP5 remained partially elusive. The aim of this work is the determination of a higher resolution structure of the chlororibosome, which allows the unambiguous localization of protein and rRNA alterations. Knowing the resulting structural features will help to understand how the chlororibosome satisfies special functional requirements within chloroplasts.

Proline-rich antimicrobial peptides (Publication 3, 4, 5 and 6)

The continuously rising numbers of bacterial strains showing resistances towards numerous clinically relevant antibiotics, increases the demand for the discovery of new potent compounds. Antimicrobial peptides (AMPs) constitute one promising source. Antimicrobial peptides are produced by the innate immune system of higher eukaryotes in response to a wide range of bacteria to prevent the establishment of an infection. Proline-rich antimicrobial peptides represent a subclass of antimicrobial peptides, which are enriched in Pro and Arg residues. Despite original description of DnaK as major target for PrAMPs, more recently ribosomes were identified as primary target for inhibition. The aim of this works is the reconstruction of high-resolution complexes of 70S ribosomes together with different PrAMPs. The obtained complexes will allow the identification of the ribosomal binding site of PrAMPs and the determination of the mechanism of action, which leads to protein synthesis inhibition.

3 Cumulative thesis: Summary of publications

3.1 Publication 1 - Visualization of translation termination intermediates during RF3-mediated recycling of RF1

Graf, M., Huter, P., Maracci, C., Peterek, M., Rodnina, M.V. and Wilson, D.N.

Nature Communications. (2018) (accepted)

When the translation machinery encounters an UAA, UAG or UGA stop codon, the polymerized polypeptide chain is released from the 70S ribosome. Decoding of stop codons occurs through class I release factors RF1 and RF2. After peptide chain release, RF1 and RF2 are dissociated from the ribosome by the action of class II release factor RF3. The mechanism by which the decoding factors are recycled from the ribosome by RF3 has remained partially elusive. Previous higher resolution structural studies reported 70S ribosomes in complex with RF3, but in absence of RF1 or RF2 (Gao et al., 2007; Jin et al., 2011; Klaholz et al., 2004; Zhou et al., 2012b). The authors suggested a rotation-based recycling of RF1 by RF3. Accordingly, RF3 was observed to induce SSU body/platform rotation of up to 10° and up to 4° swiveling of the SSU head. This ultimately leads to formation of R-state ribosomes with P/E hybrid-state deacyl-tRNA.

We obtained five reconstructions of 70S-bound RF3 using the antimicrobial peptide Api137 with resolutions ranging from 3.8 to 4.4 Å. On the basis of four of these reconstructions, which presumably represent intermediate states of RF3-mediated RF1 recycling, we describe an improved model for the mechanism of RF3 action. The four intermediates, which harbor RF1 and RF3, show different degrees of SSU rotation and SSU head swivel. Strikingly, this is the first time an R-state 70S ribosome was observed in complex with RF1. As suggested by previous studies, ejection of RF1/2 correlates with the progress of SSU rotational movement. In our obtained structures, we observe destabilization of RF1 binding with ribosomes that adopt fully rotated states. Moreover, we suggest that RF3 GTPase activation is the result of a previously unobserved rotational accommodation of the RF3 G-domain on the sarcin-ricin loop. In general, RF3-induced SSU rotation fulfills a dual function. First, SSU rotation leads to disengagement of RF1/2 domain II and III from the ribosomal DC and PTC, respectively and second, it contributes to GTPase activation of RF3, which is thought

to be required for RF3 dissociation. Besides RF3-induced SSU rotation we observe a new P-tRNA state. This new tRNA state seems to be a secondary effect of the RF3-induced movement. The tRNA, termed P_{int} -tRNA, exhibits an unusual Watson-Crick base-pairing with the P-loop of the 23S rRNA. The P_{int} -tRNA CCA-end is shifted by 10 Å outward the PTC. C75, as well as A76 are observed to base-pair with G2253 and G2252. P-loop interactions normally involve contacts of nucleotides G2252 and G2251 with tRNA nucleotides C75 and A76, respectively. The relevance of this state is not clear, but presumably represents an intermediate tRNA conformation previous to the formation of P/E tRNAs.

In accordance to a previous low-resolution cryo-EM study (Pallesen et al., 2013) we observe interactions of one copy of L7/L12 with RF3. Maps filtered to 7 Å allowed us the assignment of an 'arc'-like density to the CTD of L7/L12 next to the G'-domain of RF3. Strikingly, we observed another density in our 7 Å filtered maps, which we could assign to a second CTD of an L7/L12 dimer. The second CTD seems to facilitate recruitment of RF1 via domain I. To our knowledge, this is the first example of the recruitment of a translation factor without GTPase activity by L7/L12 to the *Escherichia coli* 70S ribosome.

3.2 Publication 2 - Cryo-EM structure of the spinach chloroplast ribosome reveals the location of plastid-specific ribosomal proteins and extensions

Graf, M., Arenz, S., Huter, P., Donhofer, A., Novacek, J., and Wilson, D.N.

Nucleic Acids Research. 45, 2887-2896. (2017)

Chloroplasts are the result of an endosymbiotic event billion years ago and are crucial for carbon fixation in plants. The proteins involved in photosynthesis as well as other required proteins inside the organelle are produced by specialized chlororibosomes, which are similar to eubacterial 70S ribosomes. As shown by initial biochemical studies the major differences between *Escherichia coli* 70S ribosomes and chlororibosomes is an increased ratio of protein to rRNA (Yamaguchi and Subramanian, 2000, 2003; Yamaguchi et al., 2000). While the number of rRNA residues stayed approximately the same, chloroplast ribosomes acquired plastid-specific ribosomal proteins (PSRPs), as well as N- and C-terminal extensions within ribosomal proteins. The only significant loss in protein mass represents the absence of ribosomal proteins L25 and L30. With

respect to the rRNA, chloroplast ribosomes harbor, compared to *E. coli*, numerous additions and deletions of rRNA residues. The most obvious difference is the existence of a 4.8S rRNA that is the result of a 3' fragmentation of the chloroplast 23S rRNA.

Although lower resolution structures of these chlororibosomes at 9.4 Å exist (Sharma et al., 2007), no higher resolution structures were available that allow placement of all plastid-specific ribosomal proteins and the identification of N- and C-terminal extensions of chloroplast ribosomal proteins. We provide a 3.6 Å reconstruction of the large subunit and a 5.4 Å reconstruction of the small subunit. The resolution of the LSU allowed us to generate a molecular model that contains 2961 rRNA residues out of 3035 (98%) and 3422 amino acids of r-proteins out of 5036 (68%). The LSU model helps to visualize alterations in rRNA and proteins residues. We observe the absence of L25 and L30 and the presence of additional densities, which account for chlororibosome-specific protein residues. Consistently, we were able to unambiguously localize the binding sites for PSRP5 and PSRP6 on the LSU. Despite low resolution of the SSU, we were further able to assign densities to PSRP1 and PSRP4. With respect to other ribosomal proteins, we managed to identify and model protein extensions of LSU ribosomal proteins. The extensions are involved in reshaping the chlororibosome structure. We suggest that reshaping allows the ribosome to cope with the altered functional requirements inside the chloroplast. The extensions stabilize the differing rRNA network and provide additional contacts with the surrounding. This possibly allows improved interactions with the reduced signal recognition particle (SRP), which only harbors the protein component SRP54. Furthermore, we suggest that a large conglomerate of NTEs/CTEs of cpL13, cpL21 and cpL22 provides an extended surface for interactions with the thylakoid membrane.

3.3 Publication 3 - The proline-rich antimicrobial peptide Onc12 inhibits translation by blocking and destabilizing the initiation complex

Seefeldt, A.C.* , Nguyen, F.* , Antunes, S.* , Perebaskine, N., Graf, M., Arenz, S., Inampudi, K.K., Douat, C., Guichard, G., Wilson, D.N.

Nature Structural & Molecular Biology. 22, 470-475. (2015)

Although PrAMPs, such as oncocins, were initially suggested to inhibit DnaK (Otvos et al., 2000), it was shown more recently that *Escherichia coli* dnaK deletion strains

remain susceptible to PrAMPs (Krizsan et al., 2014; Mardirossian et al., 2014). This led to the identification of ribosomes as an alternative target for PrAMP action. The lack of newly discovered antimicrobials combined with the increasing number of bacteria which are resistant to antibiotics, make PrAMPs attractive lead compounds for future medicine. To elucidate the actual binding site of PrAMPs, the X-ray structure of Onc112, a 19 aa long derivative of oncocin, was resolved in complex with *Thermus thermophilus* 70S ribosomes and an fMet-tRNA^{fMet} at a resolution of 3.1 Å. The structure shows that Onc112 binds within the nascent polypeptide exit tunnel (NPET), overlapping with the path of a nascent chain. Unlike a nascent chain, PrAMP Onc112 binds with a reverse orientation to the upper NPET. The N-terminus is located at the PTC in the ribosomal A-site and the C-terminal residues reach deeper into the NPET. Binding in general is facilitated by an extensive hydrogen bonding network and several stacking interactions, which are established with the surrounding rRNA residues of the NPET. With respect to the mechanism of inhibition, we observe that the C-terminal residues are predominantly important for stable binding and uptake of Onc112. Consistently, our biochemical data show that Onc112 derivatives with C-terminal deletions exhibit reduced antimicrobial activity *in vitro* but no activity *in vivo*. The N-terminal residues that reach into the ribosomal A-site are crucial for translation inhibition. Superimposition of the N-terminal residues with an accommodated pre-attack A-site tRNA show a severe steric hindrance, which presumably prevents coexistence of Onc112 and A-tRNA on the 70S ribosome. Thus, delivery of an aa-tRNA by EF-Tu is presumably possible, but the subsequent accommodation into the ribosomal A-site is excluded. In contrast, a tRNA bound to the ribosomal P-site, carrying a single or no amino acid, does not clash with 70S-bound Onc112. As shown by *in vitro* toe-print assays, the steric clash, generated between the 3'-end of an accommodated A-tRNA and the N-terminal residues of Onc112, results in stalling and destabilization of the 70S ribosome at the AUG initiation site of an open-reading frame (ORF). Because inhibition of protein synthesis requires *in vivo* import of PrAMPs into the cytoplasm of a bacterial cell, we further validated the pathway of Onc112 uptake via the transporter SbmA. In accordance, *in vivo* cell-culture experiments with *E. coli* *sbmA* deletion strains show that efficient uptake and inhibition of Onc112 is perturbed in absence of the transporter SbmA.

3.4 Publication 4 - Structure of the mammalian antimicrobial peptide Bac7(1-16) bound within the exit tunnel of a bacterial ribosome

Seefeldt, A.C.* Graf, M.*, Perebaskine, N., Nguyen, F., Arenz, S., Mardirossian, M., Scocchi, M., Wilson, D.N., and Innis, C.A.

Nucleic Acids Research. 44, 2429-2438. (2016)

The proline-rich antimicrobial peptide Onc112 was shown to bind to the nascent polypeptide exit tunnel (NPET) (Roy et al., 2015; Seefeldt et al., 2015). For other antimicrobial peptides, such as mammalian bactenecins, the ribosomal binding site remained obscure. Sequence alignments of Onc112 with mammalian bactenecin-7 (Bac7) as well as insect metalnikowin and pyrrhocoricin indicate similarities, which imply binding at the same location as reported before. To investigate the binding location of other PrAMPs, we obtained three X-ray structures of Bac7, metalnikowin and pyrrhocoricin in complex with *Thermus thermophilus* 70S ribosomes and fMet-tRNA^{fMet}. In general, binding and inhibition of the peptides presented in this study is very similar to Onc112. The PrAMPs Bac7, metalnikowin and pyrrhocoricin bind to the NPET and overlap with the path of a nascent chain. Binding of PrAMPs involves both polar contacts and stacking interactions. Due to the higher content in arginine residues, contacts of Bac7 with the surrounding rRNA residues primarily involve the side chains of the arginine residues. The N-terminal residues of all peptides are situated within the ribosomal A-site and the C-terminal residues reach down the NPET. The N-terminal residues are relevant for antimicrobial activity and the C-terminal residues are presumably more crucial for uptake. Binding of Bac7 derivatives to the NPET was validated in competition assays with the macrolide erythromycin (Ery), which binds to the NPET and hence clashes with the path of PrAMPs. Our data show that Bac7 derivatives compete with Ery present in the NPET for ribosome binding. When comparing the structure of all our resolved PrAMPs, the most significant difference is observed for the N-terminus. In comparison to Onc112, metalnikowin and pyrrhocoricin, Bac7 harbors four additional amino acids at the N-terminus, which form a short loop that reaches deeper into the A-site binding pocket. Independent of the number of N-terminal residues, all resolved PrAMPs are incompatible with the CCA-end of an accommodated A-site tRNA but allow binding of tRNA in the P-site. Accordingly, toe-print assays show that PrAMPs inhibit 70S initiation complexes at the

AUG start site of an open reading frame and do not allow further transition to translation elongation. This is consistent with the previously described model of inhibition by Onc112. Interestingly, *in vitro* translation assays with rabbit reticulocyte extract show that PrAMPs do not exclusively inhibit bacterial translation. Accordingly, our data indicate that Bac7 can inhibit eukaryotic translation as well. Nonetheless, based on the model of Bac7 synthesis, targeting and inhibition, we hypothesize that inhibition of translation within PrAMP producing cells is not possible because PrAMPs are produced by cells of the innate immune system as inactive precursors that are targeted to large granules and thus cannot harm ribosomes of the producing cell. Upon bacterial infection the inactive precursors are released from the large granules into the extracellular space and activated by protease cleavage. The proteases are stored separately in azurophil granules and released together with precursor PrAMPs during the establishment of an infection.

3.5 Publication 5 - Proline-rich antimicrobial peptides targeting protein synthesis

Graf, M.*, Mardirossian, M.* , Nguyen, F., Seefeldt*, A.C., Guichard, G., Scocchi, M., Innis, C.A., and Wilson, D.N.

Natural Product Reports. 34, 702-711. (2017)

The innate immune system of higher eukaryotes utilizes a broad spectrum of antimicrobial agents to prevent infection by pathogens. One group of agents, identified in some mammals and insects, are the proline-rich antimicrobial peptides (PrAMPs). As shown by recent biochemical and structural studies, PrAMPs inhibit protein synthesis by binding to the nascent polypeptide exit tunnel and obstructing of the A-site binding pocket. In this review, we compare the recently obtained structures of Onc112, Bac7, metalnikowin and pyrrhocoricin in complex with *Thermus thermophilus* 70S ribosomes (Gagnon et al., 2016; Roy et al., 2015; Seefeldt et al., 2016; Seefeldt et al., 2015) and summarize the current concepts of PrAMP synthesis, targeting and inhibition. In general, PrAMPs are synthesized as inactive precursors by cells of the innate immune system. In the presence of a pathogen the inactive precursors are secreted into extracellular space or pathogen-containing phagosomes and activated by protease cleavage. In general, a single-peptide activation mechanism can be distinguished from multi-peptide activation mechanism. Import of PrAMPs is

predominantly facilitated by the SbmA transporter (Mattiuzzo et al., 2007) and to a lesser extent by the MdtM transporter (Krizsan et al., 2015a). Once bound to the nascent polypeptide exit tunnel, the path of PrAMPs overlaps with the path of a nascent chain. However, in contrast to a nascent chain, PrAMPs bind in an inverted orientation to the tunnel. Consistently, the N-terminal residues are located in the A-site binding pocket and the C-terminal residues are located in the upper polypeptide exit tunnel. Biochemical studies have shown that the N-terminal residues are crucial for protein synthesis inhibition and the C-terminal residues are thought to be important for the import of PrAMPs. Inhibition of protein synthesis by the N-terminal residues results in inhibition of 70S initiation complexes at the AUG start site with fMet-tRNA^{fMet} bound in the P-site.

3.6 Publication 6 - An antimicrobial peptide that inhibits translation by trapping release factors on the ribosome

Florin, T.* , Maracci, C.* , Graf, M.*, Karki, P., Klepacki, D., Berninghausen, O., Beckmann, R., Vazquez-Laslop, N., Wilson, D.N., Rodnina, M.V., Mankin, A.S.

Nature Structural & Molecular Biology. 24, 752-757. (2017)

Proline-rich antimicrobial peptides (PrAMPs) constitute tools of the innate immune system to fight invading bacteria. Previous structural and biochemical studies showed that PrAMPs, such as Onc112, pyrrhocoricin, metalnikowin and Bac7, inhibit protein synthesis by binding to the nascent polypeptide exit tunnel (NPET) of eubacterial 70S ribosomes and blocking of the transition from translation initiation to translation elongation (Gagnon et al., 2016; Roy et al., 2015; Seefeldt et al., 2016; Seefeldt et al., 2015). Contrasting these initial studies, we describe that Api137, a derivate of the naturally occurring PrAMP apidaecin, inhibits protein synthesis by an alternative mechanism i.e. by trapping RF1 on a terminating 70S ribosome. To our knowledge, this is the first description of a compound that specifically inhibits translation termination. To determine the exact binding site, we resolved the structure of Api137 in complex with *Escherichia coli* 70S ribosomes by cryo-EM and performed biochemical protection assays. The reconstruction of the 70S ribosome exhibited an average resolution of ~3.4 Å. Like other previously reported PrAMPs, we observe binding of Api137 to the NPET. The path of Api137 overlaps with the path of a nascent chain. Contrasting Onc112, Bac7, metalnikowin and pyrrhocoricin, Api137 binds in a

similar orientation to a nascent polypeptide. The N-terminal residues are situated in the upper NPET and the C-terminal residues reach into the PTC, but not further into the A-site binding pocket. Binding and inhibition involves hydrogen bonding, as well as stacking interactions within the NPET. Trapping of RF1 is the result of specific interactions of the C-terminal Arg17 of Api137 with 23S rRNA residues and the conserved GGQ-motif of RF1. Furthermore, we observe interactions of Leu18 with the deacyl-tRNA present in the P-site of the *E. coli* 70S ribosome. However, trapping of RF1 on the 70S ribosome is only the primary effect of Api137 inhibition. The secondary effect, which contributes to the inhibition of bacterial growth *in vivo*, is the depletion of the pool of class I release factors that are available for translation termination. As a consequence, we observe in biochemical assays accumulation of 70S ribosomes harboring peptidyl-tRNAs and stop codon read-through.

4 Discussion

4.1 Chloroplast ribosomes

Our structural studies provide deeper insights into the structure of the chloroplast ribosome. In general, the most pronounced differences between bacterial ribosomes and chlororibosomes are the absence of L25 and L30, as well as the presence of plastid specific ribosomal proteins (PSRPs) 1-6, protein extensions (internal insertions and N-/C-terminal extensions) (Yamaguchi and Subramanian, 2000, 2003; Yamaguchi et al., 2000) and a 4.8S rRNA, which is the result of a 3' fragmentation of the chloroplast 23S rRNA. In our cryo-EM studies the LSU was resolved with resolutions reaching up to 3.6 Å and the SSU was resolved with resolutions up to 5.4 Å. The well-resolved LSU allowed us to determine the binding site of PSRP5 and PSRP6 with side chain accuracy. We identified PSRP5 as an elongated protein with a long N-terminal α -helix that contacts H58 and a shorter C-terminal α -helix, which establishes contacts with H49. PSRP6 exhibits a long-extended conformation as well and is situated near the central protuberance. The N-terminal fraction of PSRP6 exhibits two short α -helices, which interact with H40, H41 and H89. The C-terminal fraction provides a β -strand to protein L21. In general, the placement of PSRP5 and PSRP6 is in good agreement with other reconstructions published around the same time (Ahmed et al., 2017; Ahmed et al., 2016; Bieri et al., 2017). One exception was that Ahmed and colleagues placed PSRP5 with an inverted orientation (Ahmed et al., 2016) compared to us. Nonetheless, sidechain information in our map as well as secondary structure predictions and the released chlororibosome model by Bieri and colleagues gave us confidence that PSRP5 was modeled correctly in our model and with the correct orientation. Secondary structure predictions anticipated the presence of a short helix at the C-terminus and a long helix at the N-terminus. PSRP6 was modelled in all published models in a similar orientation and with no register shifts (Ahmed et al., 2017; Ahmed et al., 2016; Bieri et al., 2017).

However, in contrast to the other chlororibosome structures (Ahmed et al., 2017; Bieri et al., 2017), which provided higher resolutions for the SSU, we were only able to roughly assign the locations of PSRP1-4 on the SSU. Consistently, on the SSU unassigned densities were identified by us at the head, at the neck of the SSU between head and platform and at the spur. At the SSU neck two unassigned densities were

identified. The smaller density in this region was not observed in any of the other chlororibosome cryo-EM structures (Ahmed et al., 2017; Bieri et al., 2017). Thus, it is possible that this density is a map artifact, resulting from the low resolution of the SSU. The second bigger density observed in the neck region was assigned to PSRP1. The assignment of the density to PSRP1 was based on secondary structure features and is in agreement with initial low-resolution cryo-EM reconstructions by Sharma and colleagues (Sharma et al., 2007) as well as more recent models by Bieri et al. and Ahmed et al. (Ahmed et al., 2017; Bieri et al., 2017). The other two densities observed at the SSU head and spur did not show clear secondary structure features. The density at the spur reaches from 16S rRNA helix h6 to h10 and exhibits a long dumbbell shape. In accordance to Ahmed and colleagues, this density presumably belongs to full-length PSRP2 (Ahmed et al., 2017). The density at the SSU head was assigned by us to PSRP4 (bTHXc) and is consistent with the position of the *T. thermophilus* protein bTHX (Wimberly et al., 2000), which has high sequence similarity to PSRP4. As described by others (Ahmed et al., 2017; Bieri et al., 2017), PSRP4 is presumably responsible for stabilization of the head region and the establishment of contacts with intersubunit bridges B1a and B1b. However, we did not observe additional densities, which can be assigned to PSRP3, neither at the mRNA tunnel entry, nor somewhere else on the SSU.

In addition to PSRP1-6, we managed to model numerous differences in the chlororibosome ribosomal proteins compared to *E. coli* ribosomal proteins (Graf et al., 2017a). More than five residues of N- and/or C-terminal extensions have been modelled for L13, L15, L21, L22, L24, L27, L29 and L34. An insertion was modelled for protein L33. Protein deletions were observed and modelled for L2, L19 and L23. The alterations of the ribosomal proteins reshape the chlororibosome and presumably result in differences in translation activity. The most striking examples for the stabilization of the rRNA by protein extensions were observed by us for the NTE of LSU protein L13 and the CTE of L27. Consistent with the other reported structures of chlororibosomes, the NTE of L13 stabilizes the 5'-end of the 4.8S rRNA and the 3' of the truncated 23S rRNA (Ahmed et al., 2017; Ahmed et al., 2016; Bieri et al., 2017; Graf et al., 2017a). Moreover, we report that the CTE of L27 allows stabilization of a three-way junction of H38 (Graf et al., 2017a). In general, functional reshaping of the chloroplast ribosome was observed especially at the surface of the LSU (Ahmed et al., 2017; Ahmed et al., 2016; Bieri et al., 2017; Graf et al., 2017a). Accordingly, N-terminal

and C-terminal extensions L23, L24 and L29 reshape the ribosomal exit tunnel. Reshaping of the polypeptide exit tunnel presumably represents an adaption to the structural reduction of chloroplast SRP, which is crucial for targeting of the 70S ribosome to the thylakoid membrane. In contrast to *E. coli* SRP, which consists of a 4.5S RNA and protein SRP54, chloroplast SRP just exhibits the protein component. The protein extension of L23, L24 and L29 presumably provide additional contacts for SRP54 that allow targeting of the ribosome to the membrane. Additional contacts with the membrane are potentially provided by the NTEs of L13 and L21 as well as the CTE of protein L22, which build an extensive conglomerate (Graf et al., 2017a).

Overall it was possible for us to model more than 75% of the extensions of LSU proteins visible in our structure. Modelling of more residues was not possible due to the lack of resolution and intrinsic flexibilities within the extension. The residues, which were not modelled, are possibly involved in targeting processes and are just stabilized in presence of additional factors.

4.2 Class I release factor recycling by RF3

RF1/2 recycling by RF3

The translational GTPase RF3 recycles class I release factors from post-hydrolysis ribosomes. To date, there have been five structural studies published that have investigated the mechanism of RF3 action on the bacterial 70S ribosome (Gao et al., 2007; Jin et al., 2011; Klaholz et al., 2004; Pallesen et al., 2013; Zhou et al., 2012b). All of the higher resolution structural studies elucidating the mechanism of class I release factor recycling by RF3 do not provide information on simultaneous binding of RF1 and RF3 (Jin et al., 2011; Zhou et al., 2012b). The only existing structural study on RF1 and (apo-) RF3 is a low-resolution reconstruction and thus does not provide much structural as well as mechanistic insight into RF3 action (Pallesen et al., 2013). Furthermore, it is not clear how physiologically relevant the binding of apo-RF3 is for the process of RF1/2 recycling (Adio et al., 2018; Koutmou et al., 2014). However, common to the higher resolution RF3-70S structures is that the SSU is rotated by up to 9° and the head is swiveled by up to 14° (Jin et al., 2011; Zhou et al., 2012b). No rotation was observed for the low-resolution reconstruction harboring RF1 and RF3

(Pallesen et al., 2013). None of the previously reported structures show intermediate states of RF3 action and dissociation of class I release factors from the ribosome.

Utilizing Api137, a termination specific translation inhibitor (see section 4.3) (Florin et al., 2017), it was possible for us to *in vitro* reconstitute a termination complex consisting of *E. coli* 70S ribosome, P-tRNA and RF1-GAQ decoding a UAA stop codon. By further addition of RF3-GDPCP to this complex and subsequent cryo-EM analysis it was possible for us to obtain five different reconstructions containing RF3. The overall resolution reached from 3.8 Å to 4.4 Å. The reconstructions provide new insights into the recycling process of RF1 by RF3. Reconstruction I to IV presumably represent intermediate states, which harbor RF1, P-tRNA and RF3 simultaneously (Figure 9A). These states show different degrees of SSU rotation and head swivel. The fifth reconstruction constitutes a rotated 70S complex that solely harbors RF3 and no other factor (RF3-only). The latter complex presumably represents empty 70S ribosomes, which are suitable for RF3 binding but do not constitute the actual substrate for recycling. Release of deacyl-tRNA from the ribosome occurs after RRF and EF-G facilitated 70S recycling by IF3 (Prabhakar et al., 2017). Although RF3 shows high affinity to 70S ribosomes, independent of the presence of other ligands, it exhibits no splitting activity and does not remove tRNAs from the ribosomal complex. Hence, the other four complexes are likely to represent more physiological states of RF3-mediated recycling.

Due to the proposed model of RF3 induced SSU rotation, which leads to RF1/2 disengagement from the terminating ribosome, we suggest that the degree of head swivel and SSU rotation corresponds to the stage of RF3-mediated recycling. Accordingly, each state most likely represents snapshots of SSU movement during RF3 action. The SSU rotation ranges from 0.8° in the first state and 9.6° in the fourth state. The observed head swivel is rather mild and ranges from 1.1° in state I to 3.6° in state IV. In the RF3-only state, SSU rotation of 8.2° was observed and head swivel of 5.7°. The observed head swivel in state I to IV is limited compared to RF3-only ribosomes, because of the presence of tRNA. This is also consistent with the previously described X-ray structure of a 70S-RF3 complex containing P/E-tRNA, which showed a milder head swivel of 4° (Jin et al., 2011). In contrast, the RF3-only structure shows similar to the previously reported 70S-RF3 complex, which is lacking tRNA, stronger swiveling (Zhou et al., 2012b). Noteworthy, the head swivel observed for our RF3-only state represents an average value of several head conformations.

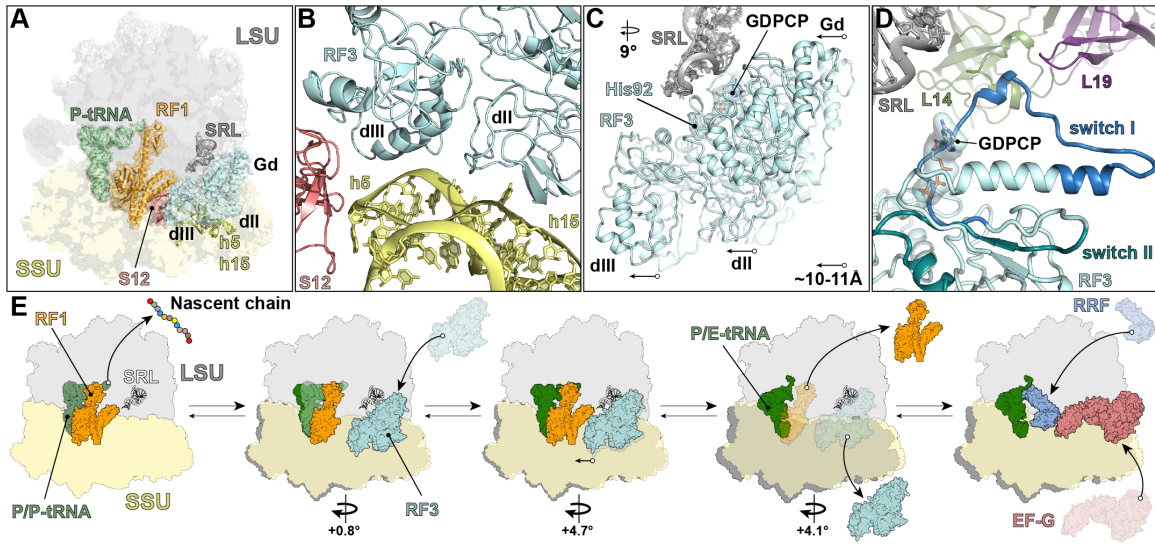


Figure 9 – Class I release factor recycling by RF3. (A) Overview of the 70S ribosome bound with RF3 (cyan), RF1 (orange) and deacyl-P-tRNA (pale green). Binding of RF3 to the ribosome involves interactions with SSU protein S12 (dark salmon), h5 and h15 (both in yellow). The SRL (grey with black outline), which is crucial for GTP hydrolysis of translational GTPases, is shown on the LSU (grey). (B) Zoom of (A) showing the interactions of RF3 (cyan) domain II and III with the SSU (yellow) via h5 and h15, as well as protein S12 (dark salmon). (C) Movement of RF3, which results from SSU rotation relatively to the LSU. RF3 moves as rigid body and approaches the SRL (grey). The position of RF3 upon initial binding is shown faint. The position of RF3 at later stages is shown in cyan. The position of the domains are indicated next to RF3 in black letters. (D) Model of a previously unobserved conformation of switch I (dark blue) within the G-domain of RF3 (cyan). Switch I contacts LSU proteins L14 (dark green) and L19 (purple). Switch II (teal) within the G-domain of RF3 and the SRL (grey) are shown for reference. (E) Model of RF3 action. The LSU is shown in grey and the SSU is shown in yellow. RF1 (orange) releases the polymerized peptide chain from the P-tRNA (green). RF3 (cyan) binds to post-hydrolysis complexes and induces SSU rotation. SSU rotation leads to release of RF1 and accommodation of RF3 on the LSU. At a maximum rotation of 9.6° the G-domain of RF3 comes in close proximity to the SRL (black contoured helix). This presumably triggers GTP hydrolysis and RF3 release. RRF binds after RF1 and RF3 release to rotated 70S ribosomes harboring P/E hybrid state tRNA. Together with EF-G RRF splits the ribosome into subunits.

Thus, the maximum degree of head swivel is most likely higher than 5.7° and therefore in good agreement with the strong head swivel of up to 14° observed by others in absence of tRNA (Zhou et al., 2012b). Regardless, state IV, which shows 9.6° of SSU rotation and 3.6° of head swivel, we consider as fully rotated ribosomes.

As described by previous structural studies, RF3 interacts with h5, h15 and S12 (Figure 9B) (Jin et al., 2011; Zhou et al., 2012b). The contacts are maintained by RF3 through-out the recycling process and independent of the degree of SSU rotation. Contrasting previously proposed models (Klaholz et al., 2004), RF3 does not undergo large conformational changes and rather moves as rigid body with the SSU. Consistent with the degree of SSU rotation, RF3 rotates by 9° relatively to the LSU (Figure 9C). This equals a movement of 10 to 11 Å (Figure 9C). Interestingly, there seem to be no major interactions of RF3 with the LSU. The only direct interaction of RF3 with the LSU was observed by us in state I and involves switch I of RF3, which is crucial for GTP

hydrolysis (Figure 9D). In this state switch I adopts a previously unobserved extended conformation with a short helical section that comes into close proximity of L14 and L19 (Figure 9D). This interaction with the LSU is possibly involved in creating a force that drives SSU rotation. Furthermore, the extended conformation possibly prevents backward rotation of the ribosome to an N-state and premature GTP-hydrolysis, since breakdown of GTP to GDP and P_i requires a closed conformation of switch I. The closed conformation was previously observed in the 70S-RF3 X-ray structure by Zhou and colleagues (Zhou et al., 2012b) but not in any of our states. This possibly indicates that further SSU rotation has to be applied to the 70S ribosome in order to adopt a closed switch I conformation. Nonetheless, much further movement beyond 10° SSU rotation is not possible due to steric constraints created by domain I of RF3 and the LSU. This steric block created by the LSU results in ‘wedging’ of RF3 and the SRL. Consistently, state IV comes into close proximity of the SRL. Further movement towards the SRL presumably leads to switch I closure and rearrangement of the catalytic His92 (Zhou et al., 2012b). It is still not entirely clear whether GTP hydrolysis precedes RF1 release and whether RF3 can possibly dissociate (prematurely) before RF1 recycling took place. Accordingly, biophysical studies by Adio and colleagues suggest that dissociation of RF1 and RF3 is rather random (Adio et al., 2018). In our studies, the presence of a non-hydrolysable GTP-analog prevents the observation of subsequent processes that occur because of GTP hydrolysis. Therefore, we cannot exclude the existence of a checkpoint that prevents premature GTP hydrolysis and release of RF3 before successful RF1/2 liberation. Regardless, the general mechanism leading to GTP hydrolysis, distinguishes the GTPase activation of RF3 from other translational GTPases. While GTP hydrolysis of EF-Tu and EF-G is triggered upon SSU domain closure, hydrolysis of RF3 bound GTP is independent of domain closure and results from SSU rotation. A comparable movement of the G-domain, which leads to accommodation on the SRL, has been described before only for IF2 (Sprink et al., 2016). Nonetheless, in contrast to RF3, accommodation of IF2 involves a counterclockwise movement of the SSU instead of a clockwise movement. Therefore, our reported mechanism of accommodation is considerably different from all other translational GTPases described so far, showing domain closure or a counterclockwise movement that leads to accommodation. Moreover, the movement between state I and state II of the G-domain of IF2, which was described by Sprink and colleagues, is far smaller when compared to the movement of the G-domain of

RF3. While the G-domain of RF3 shows an average movement of \sim 10 Å, the G-domain of IF2 shows only a movement of \sim 2 Å. Although, the distances between the catalytic His448 and the SRL of state I and state II differ only by less than 1 Å, Sprink and colleagues suggest that the G-domain shift of \sim 2 Å ultimately results in GTP hydrolysis (Sprink et al., 2016). Regardless, it is unclear whether GTP hydrolysis by IF2 could in principle occur before movement into state II. For RF3, biochemical assays show that GTP hydrolysis is triggered when the 70S ribosome reaches a fully rotated state (Adio et al., 2018; Koutmou et al., 2014). With regard to the two reported 70S-ICs in complex with IF2 (Sprink et al., 2016), biochemical assays are lacking that show GTP hydrolysis takes place in 70S-IC state II or earlier. Based on the reported states, it is not possible to address this issue and to assume that hydrolysis occurs after such small counterclockwise movement of the G-domain. The presence of non-hydrolysable GTP-analog occludes the moment of GTP hydrolysis within the reported complexes and it requires the observation of at least one additional intermediate state to anticipate the series of events that lead to hydrolysis (including rearrangement of catalytic His448). However, with respect to RF3, the distance between the G-domain and the SRL as well as the absence of a closed conformation of switch I do not promote earlier GTP hydrolysis before the 70S ribosome reaches a fully rotated state. Consequently, RF3-induced clockwise SSU rotation fulfills a dual function. First, it results in the release of RF1 from the ribosome and second, it triggers GTP hydrolysis in a fully rotated ribosome. In general, the different activation mechanism of translational GTPases is also reflected by the position of the G-domains of EF-Tu, EF-G and IF2 compared to RF3. Relative to the SRL, the G-domain of EF-Tu (Loveland et al., 2017), EF-G (Li et al., 2015) and IF2 (Sprink et al., 2016) is rotated by 24 to 31° compared to the G-domain of RF3.

The general presence of RF1 and RF3 in the fully rotated state, as well as the milder rotated states, distinguishes our complex from the previously described higher- and low-resolution studies and gives first insights into the departure process of RF1. Moreover, binding of RF1 to R-state ribosomes was never described in any other publication. Consistent with the existing model for RF3 mediated RF1 recycling (Adio et al., 2018; Koutmou et al., 2014; Peske et al., 2014), we see departure of RF1 from fully rotated ribosomes where the G-domain of RF3 is in close proximity to the SRL. Compared to the intermediate states I-III the density of RF1 in the ribosomal A-site of state IV shows higher flexibility. This implies that in fully rotated ribosomes domain II/IV

on the SSU and domain III on the LSU become disengaged from the ribosome and hence destabilize 70S-bound RF1. Based on the observation of a direct contact between RF1 and RF3 in the structural study by Pallesen and colleagues it has been suggested that the dissociation of RF1 is the result of SSU rotation and an increasing steric clash between domain I of RF1 and domain III of RF3 (Pallesen et al., 2013). In none of our complexes we do observe such direct contacts between RF1 and RF3. Instead the destabilization of RF1 appears to be solely driven by SSU rotation that leads to a shift of ~4 Å of domain II/IV of RF1, when comparing state III and state IV of our reconstructions.

Intermediate tRNA conformation induced by SSU rotation

In the absence of RF3, the 70S ribosome adopts an N-state with the deacyl-tRNA in a classical P/P state. As RF3 binds, the SSU rotates and the tRNA in the P-site moves from a classical P/P state via an intermediate P-tRNA state (P_{int}) to a P/E hybrid state. P_{int} -tRNA we observe for state I-III of our reconstructions. In state IV, which represents a fully rotated ribosome, the tRNA adopts a P/E-hybrid state. The P_{int} state observed for state I to III is different from any other tRNA conformation observed before. The 3'-end of the P-tRNA is shifted by ~9 Å out of the PTC and exhibits altered P-loop interactions. Normally, the CCA-end nucleotides C74 and C75 of a P/P-tRNA Watson-Crick base-pair with the P-loop nucleotides G2251 and G2252, respectively. By contrast, the P_{int} -tRNA nucleotide C74 and C75 base-pair with G2253 and G2252, respectively, of the P-loop. Furthermore, the tRNA elbow region shifts by ~15 Å. The altered base-pairing is presumably caused by the rotation of the SSU. Movement of the CCA-end out of the PTC is probably necessary to allow further movement of the P-tRNA to a P/E hybrid state. It cannot be excluded that the P_{int} -tRNA is shifted by two nucleotides but the observed density does not support interactions between purine-purine (A76 and G2252) and pyrimidine-pyrimidine (C74 and C2254) nucleotides within the first and third position, respectively, of the CCA-end. Placement of A76 opposing G2252 would result in a steric clash of the nucleobases and does not allow (wobble) base-pairing. Moreover, the distance between C74 and C2254 is too far to enable base-pairing. Regardless of a one or two nucleotide shift, our observation of P_{int} -tRNAs probably represents a snap-shot of the transition to hybrid tRNA states, which has not been described so far.

It is not entirely clear whether this intermediate tRNA state represents a physiological conformation and why it was not observed so far. One explanation is the presence of additional factors, such as EF-G or RRF, in high-resolution cryo-EM and X-ray structure studies, which lead to fast accumulation of a single or just a few major intermediate states, and hence prevent the observations of P_{int} -states (Brilot et al., 2013; Dunkle et al., 2011; Li et al., 2015; Lin et al., 2015). In case of X-ray structures, crystal packing prevents the observation of several different conformational/intermediate states. Accordingly, the observation of specific states primarily depends i.a. on the conditions and the presence of inhibitors. With respect to cryo-EM reconstructions, the lack of higher resolution information may play a role as well. Consistently, cryo-EM studies investigating different tRNA intermediate states exhibited rather low resolution and did not allow the observation of smaller shifts at the 3' end of a tRNA (Agirrezabala et al., 2008; Agirrezabala et al., 2012; Fischer et al., 2010). In other high-resolution cryo-EM studies the presence of additional factors, such as EF-G or RRF, leads to fast accumulation of a single or major intermediate states and thus prevents the observations of P_{int} -states (Brilot et al., 2013; Dunkle et al., 2011; Li et al., 2015; Lin et al., 2015). With respect to our obtained complexes we cannot exclude that Api137 induces the outward movement of the tRNA. Nonetheless, an argument that favors a physiological role of the P_{int} -tRNA derives from the conservation of the P-loop. The P-loop nucleotide G2253, which Watson-Crick base-pairs with P_{int} -tRNA nucleotide C74, is conserved in all kingdoms and thus generally allows alternative base-pairing upon SSU rotation (RNACentral, 2017). In future studies it will be necessary to clarify the role of G2253 and whether it is crucial for the transition of a P-tRNA from a P/P state to a P/E hybrid state.

RF1 recruitment by L7/L12

Ribosomal protein L7/L12 was shown to interact with translational GTPases bound to the ribosome (Gao et al., 2009; Kothe et al., 2004; Pallesen et al., 2013; Simonetti et al., 2013; Stark et al., 1997; Tourigny et al., 2013; Zhou et al., 2013, 2014). It is not entirely clear whether L7/L12 is generally involved in the recruitment of translation factors. Nonetheless, biochemical studies show that L7/L12 promotes GTP hydrolysis and P_i release of translational GTPases (Figures 10A) (Carlson et al., 2017; Mohr et al., 2002; Savelbergh et al., 2000). The first structural evidence for interactions of the

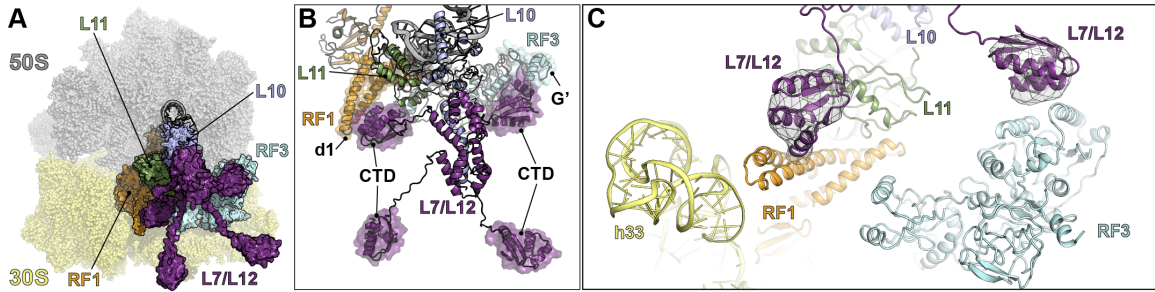


Figure 10 - Interactions of translation factors with L7/L12. (A) Overview of the 70S ribosome with two dimers of L7/L12 (purple) (Diaconu et al., 2005), RF1 (orange), RF3 (cyan), L10 (light blue) and L11 (green). (B) Zoom of (A) showing interactions of two L7/L12 (purple) CTDs (Diaconu et al., 2005) with the G'-domain (G') of RF3 and domain I (d1) of RF1. The CTDs of L7/L12 are connected to the CTD of L10 (light blue) via the NTD of L7/L12. LSU protein L11 (green) is shown for reference. (C) Cryo-EM density and rigid-body fitted model for the CTD of L7/L12 (purple) (Diaconu et al., 2005), which contacts RF3 (cyan) and RF1 (orange). SSU h33 (yellow), L10 (light blue) and L11 (green) are shown for reference.

translational GTPase RF3 with L7/L12 was provided by Pallesen and colleagues, which described an extra 'arc'-like density next to the G-domain of RF3 (Pallesen et al., 2013). Similarly, we observe in all of our reconstructions unassigned density adjacent to the G-domain of RF3 (Figure 10B and 10C). Using 7 Å filtered maps and the structural model of the L7/L12 CTD from *Thermotoga maritima* it was possible for us to assign this density to one CTD of a L7/L12 (Figure 10C) (Diaconu et al., 2005). Strikingly, in state III we observed another additional density with a comparable size next to RF1 domain I (Figure 10C). Although the features of both observed densities are rather weak, we are confident that both locations represent binding sites for L7/L12 CTDs. The involvement of L7/L12 in RF1 recruitment was confirmed by biophysical assays. In a L7/L12 depleted system the release of a nascent chain from pre-hydrolysis 70S ribosomes is clearly perturbed. To our knowledge this is the first example of a translation factor without GTPase activity that is recruited to the ribosome by L7/L12.

In each case, the L7/L12 CTD binds to an α -helix bundle that is provided by either the G-domain of RF3 or domain I of RF1 (Figures 10B and 10C). Nonetheless, the placement of two independent CTDs of L7/L12 into a rather feature-less density represents a vulnerable structural model. To further improve our concept, which shows simultaneous interactions of RF1 and RF3 with L7/L12, we tried to generate the complete structural model of the 70S ribosome that harbors the pentameric protein complex consisting of two L7/L12 dimers and the protein L10 (Figure 10A). In general, dimerization of L7/L12 is achieved by the NTD (Figure 10B). The CTD that fishes for translation factors is tethered to the NTD via a long flexible linker (Figures 10B and 10C). Attachment of each L7/L12 dimer to the stalk base occurs through the dimerized NTDs, which are located on the α -helical CTD of protein L10 (Figure 10B). Our

complete model shows that the position of the CTD next to domain I of RF1 and the G'-domain of RF3 allows proper attachment to the NTD (Figures 10A and 10B). The linker between the NTD and CTD of L7/L12 is long enough to allow simultaneous interaction with RF1 as well as RF3 on the ribosome (Figures 10B and 10C). Overall, this model shows that the L7/L12 protein is not dedicated to interactions with translational GTPases and stimulation of GTP hydrolysis but also allows recruitment of RF1.

4.3 Antimicrobial peptides

Our biochemical and structural studies identified the binding site of class I and class II PrAMPs as well as the corresponding mode of action. Although class I and class II PrAMPs share some basic features, such as Pro- and Arg-richness, the overall binding mode is generally different. Common for both classes is the binding site within the polypeptide tunnel of the ribosome.

Binding of class I PrAMPs in general

Class I PrAMPs bind to the ribosome with an inverted orientation compared to a nascent polypeptide i.e. with the N-terminus located in the A-site and the C-terminus extending down the polypeptide exit tunnel (Figure 11A). The PrAMP binding site on the ribosome can be divided into sections located within the A-site binding pocket, the A-site crevice and the upper region of the polypeptide exit tunnel. The N-terminal residues reaching into the ribosomal A-site determine the mechanism of inhibition. The C-terminal residues reaching into the polypeptide exit tunnel seem to be less crucial for binding and the inhibitory activity of PrAMPs. Accordingly, in none of the present structures the residues at the very C-terminus were resolved (Gagnon et al., 2016; Mardirossian et al., 2018; Roy et al., 2015; Seefeldt et al., 2016; Seefeldt et al., 2015). Furthermore, in biochemical studies investigating Bac7 fragments, deletion of up to 19 amino acids at the C-terminus did not abolish PrAMP activity (Benincasa et al., 2004). In contrast, deletion of the amino acids valine and aspartate from the N-terminus of oncocins, which are positioned in the A-site binding pocket, leads to strongly reduced activity and underlines the crucial function of the N-terminus for antimicrobial activity (Gagnon et al., 2016). The most striking similarity between all class I PrAMPs is a

conserved core, which harbors a PRP motif. In all our resolved class I PrAMP 70S complexes so far, the PRP motif of each PrAMP was located in exactly the same position with exactly the same conformation (Gagnon et al., 2016; Mardirossian et al., 2018; Roy et al., 2015; Seefeldt et al., 2016; Seefeldt et al., 2015). However, the amino acid composition, the number of residues and the number of established contacts within the A-site binding pocket are the most obvious differences among class I PrAMPs (Gagnon et al., 2016; Mardirossian et al., 2018; Roy et al., 2015; Seefeldt et al., 2016; Seefeldt et al., 2015). Consistently, while just four N-terminal amino acids of insect Onc112, metalnikowin and pyrrhocoricin reach into the A-site binding pocket (Figure 11B) (Gagnon et al., 2016; Roy et al., 2015; Seefeldt et al., 2016; Seefeldt et al., 2015), seven additional amino acids are present in mammalian Bac7 and Tur1A (Figure 11C) (Gagnon et al., 2016; Mardirossian et al., 2018; Seefeldt et al., 2016). The additional residues present in Bac7 and Tur1A form a short loop, which acts like an A-site anchor, and seems to be specific for mammalian PrAMPs (Gagnon et al., 2016; Mardirossian et al., 2018; Seefeldt et al., 2016).

Binding of insect PrAMPs Onc112, metalnikowin and pyrrhocoricin

The amino acid sequence of the shorter N-terminus of insect PrAMPs is conserved between Onc112, pyrrhocoricin and metalnikowin (Graf et al., 2017b). Interaction within the A-site binding pocket and A-site crevice involves polar contacts as well as stacking interactions (Figure 11B) (Gagnon et al., 2016; Roy et al., 2015; Seefeldt et al., 2016; Seefeldt et al., 2015). Polar contacts are established by the peptide backbone and side chains of the amino acid residues in the second and third position (Figure 11B) (Seefeldt et al., 2016; Seefeldt et al., 2015). Consistently, Asp2 of insect PrAMPs contacts the 2'-OH group of C2507 and the base of G2553 (Seefeldt et al., 2016; Seefeldt et al., 2015). The sidechain of Lys3 establishes a hydrogen bond with the phosphate-oxygen of the 23S rRNA nucleotide A2453 (Seefeldt et al., 2016; Seefeldt et al., 2015). Examples for backbone interactions are provided by Val1 (Figure 11B). While the α -carbonyl oxygen of Val1 interacts with the nucleobase of C2573, the α -amine of Val1 contacts the ribose of C2507 (Seefeldt et al., 2016; Seefeldt et al., 2015).

Residues five to seven of insect PrAMPs are located within the A-site crevice (Seefeldt et al., 2016; Seefeldt et al., 2015). Among those residues, Tyr6 is the most

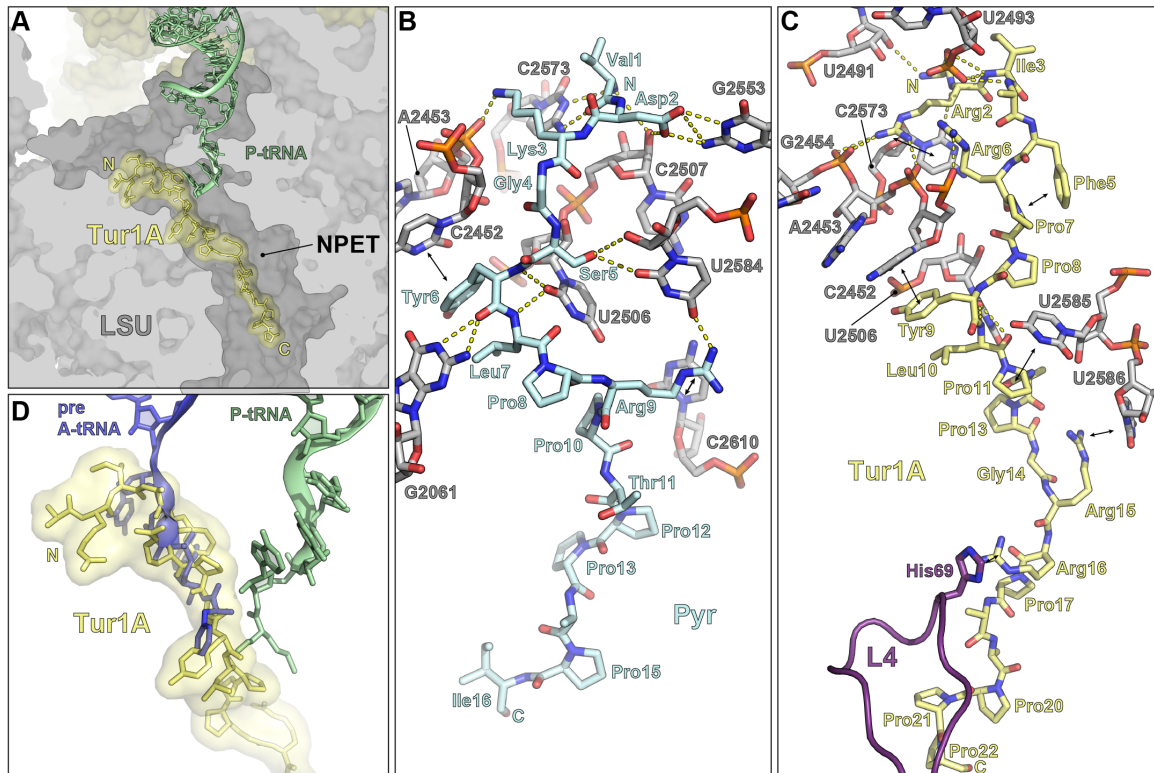


Figure 11 - Binding site of class I PrAMPs. (A) Overview showing the binding site of Tur1A within the LSU (grey) polypeptide exit tunnel (NPET) with P-tRNA (green) shown for reference (Mardirossian et al., 2018). The N- and C-terminus of Tur1A is indicated by the letters N and C, respectively. (B-C) Established interactions of (B) Pyr (Gagnon et al., 2016; Seefeldt et al., 2016) and (C) Tur1A (Mardirossian et al., 2018) within the NPET. Hydrogen bonds are indicated by yellow dashed lines. Stacking interactions are indicated by black two-headed arrows. (B) Pyr (cyan) establishes interactions solely with 23S rRNA residues (grey) (Gagnon et al., 2016; Seefeldt et al., 2016). (C) Tur1A (yellow) establishes interactions with 23S rRNA residues (grey), as well as protein L4 (purple) (Mardirossian et al., 2018). (D) Superimposition of Tur1A (yellow) (Mardirossian et al., 2018) and accommodated pre-attack aa-tRNA (blue) (Polikanov et al., 2014).

conserved and therefore present in all insect PrAMPs (Graf et al., 2017b; Seefeldt et al., 2016; Seefeldt et al., 2015). Tyr6 contributes to A-site crevice binding, as well as antimicrobial activity by establishing a stacking interaction with C2452 (Figure 11B) (Seefeldt et al., 2016; Seefeldt et al., 2015). Replacement of Tyr6 by Ala results in a 32-fold decreased activity (Knappe et al., 2011b). This contrasts with positions 5 and 7, which seem to be less critical for binding. While Onc112 harbors a proline residue in position 5, metalnikowin and pyrrhocoricin have in the same position an aspartate and a serine residue, respectively (Seefeldt et al., 2016; Seefeldt et al., 2015). Furthermore, the leucine residue in position 7 of Onc112 and pyrrhocoricin is an arginine residue in metalnikowin. The alteration of residues 5 and 7 results in different hydrogen bonding patterns within the A-site crevice. Asp5 in metalnikowin establishes hydrogen bonds with U2584 and U2585. Arg7 of metalnikowin contacts A2503 and the backbone phosphate of G2505. Ser5, which is present in pyrrhocoricin, interacts with

U2584 (Figure 11B). Leu7 does not establish interactions, either in Onc112, nor in pyrrhocoricin. Hydrogen bonds in the A-site crevice, which are common for all insect PrAMPs involve the peptide backbone. Accordingly, the backbone α -carbonyl oxygen, the α -amine of Tyr6 and the α -amine of Leu7/Arg7 contact the U2506 nucleobase (Figure 11B).

As mentioned before, the number of resolved residues at the C-terminus differs between PrAMPs. With respect to insect PrAMPs, 6 aa of Onc112, 5 aa of metalnikowin and 4 aa of pyrrhocoricin were not resolved in our studies (Seefeldt et al., 2016; Seefeldt et al., 2015). However, the visualized residues at the C-terminus of insect PrAMPs were observed to establish just a single hydrogen bond and a single stacking pair within the upper polypeptide exit tunnel (Figure 11B). Both interactions involve Arg9 of the conserved PRP motif (Figure 11B). The hydrogen bond is established with 23S nucleotide U2584. The stacking interaction is observed with C2610 (Figure 11B). The presence of only two interactions underlines the minor importance of the C-terminus of insect PrAMPs in binding.

Binding of mammalian PrAMPs Bac7 and Tur1A

Binding of mammalian Bac7 and Tur1A to the A-site binding pocket and the A-site crevice of eubacterial 70S ribosomes also involves polar contacts of the peptide backbone and the amino acid side chains (Figure 11C) (Mardirossian et al., 2018; Seefeldt et al., 2016). Four of eight positions in Bac7 and Tur1A harbor arginine residues in the LSU A-site binding pocket, which establish an extensive hydrogen bonding network as well as a single stacking interaction. The stacking interaction is observed between Arg2 and C2573 (Figure 11C). Compared to insect PrAMPs, this stacking interaction replaces the backbone contact of Val1 with the nucleobase of C2573 (Figure 11C) (Mardirossian et al., 2018; Seefeldt et al., 2016; Seefeldt et al., 2015). Hydrogen bonds are evident for all arginine residues in the A-site binding pocket (Figure 11C) (Mardirossian et al., 2018; Seefeldt et al., 2016). The sidechain of Arg1 interacts with the nucleobase of U2555. Hydrogen bonds with the 23S rRNA backbone are established by the sidechains of Arg2 (G2454 and A2453), Arg4 (C2452 and G2494) and Arg6 (A2453 and U2493). Interactions of the peptide backbone are present for the α -amines of Arg1, Arg2, Ile3 and Arg4, which contact U2491, C2573, U2492 and U2493, respectively.

The overall contacts of Bac7 and Tur1A with the A-site crevice are comparable to insect PrAMPs (Figures 11B and 11C) (Mardirossian et al., 2018; Seefeldt et al., 2016; Seefeldt et al., 2015). Insect PrAMP residues five to seven correspond to mammalian PrAMP residues eight to ten. Backbone interactions involve the α -carbonyl oxygen and α -amine of residue 9, as well as the α -amine of residue 10 that contacts the U2506 nucleobase (Figure 11C) (Mardirossian et al., 2018; Seefeldt et al., 2016). Similar to Onc112, position eight and ten harbor proline and leucine residues (Mardirossian et al., 2018; Seefeldt et al., 2016; Seefeldt et al., 2015). Except for the described backbone interactions, the side chains of both residues do not establish hydrogen bonds with the surrounding tunnel (Figure 11C) (Mardirossian et al., 2018; Seefeldt et al., 2016). Nonetheless, similar to Tyr6, which is present in all insect PrAMPs, residue nine of Bac7 and Tur1A establishes a stacking interaction with C2452 (Figure 11C) (Mardirossian et al., 2018; Seefeldt et al., 2016; Seefeldt et al., 2015). As observed for insect PrAMPs, Tur1A base stacking involves a Tyr residue as well (Figure 11C). Bac7 instead harbors an arginine residue in this position that stacks upon C2452 (Seefeldt et al., 2016; Seefeldt et al., 2015).

Due to the enrichment in arginine residues compared to insect PrAMPs, Bac7 and Tur1A establish more interactions within the upper polypeptide exit tunnel (Mardirossian et al., 2018; Seefeldt et al., 2016). The majority of these contacts involve stacking interactions. In the case of Tur1A, two stacking interactions are observed (Figure 11C), such that Arg15 and Arg16 stack upon U2586 and His69 of L4, respectively (Figure 11C) (Mardirossian et al., 2018). The C-terminus of Bac7 establishes three stacking interactions with the surrounding tunnel (Seefeldt et al., 2016). Namely, Arg12, Arg14 and Arg16 form stacking interactions with C2610, U2586 and A2062, respectively. The stacking interactions of Arg12 with C2610 is analogous to the tunnel interaction of Arg9 in insect PrAMPs (Seefeldt et al., 2016; Seefeldt et al., 2015).

Binding of class II PrAMP Api137

Api137, which is derived from wildtype apidaecin from *Apis mellifera*, is a class II PrAMP. In contrast to other (class I) PrAMPs, Api137 binds to the polypeptide tunnel with a similar orientation to a nascent chain (Figures 12A and 12B) (Florin et al., 2017). The C-terminal residues Arg17 and Leu18 are located in the A-site crevice but do not

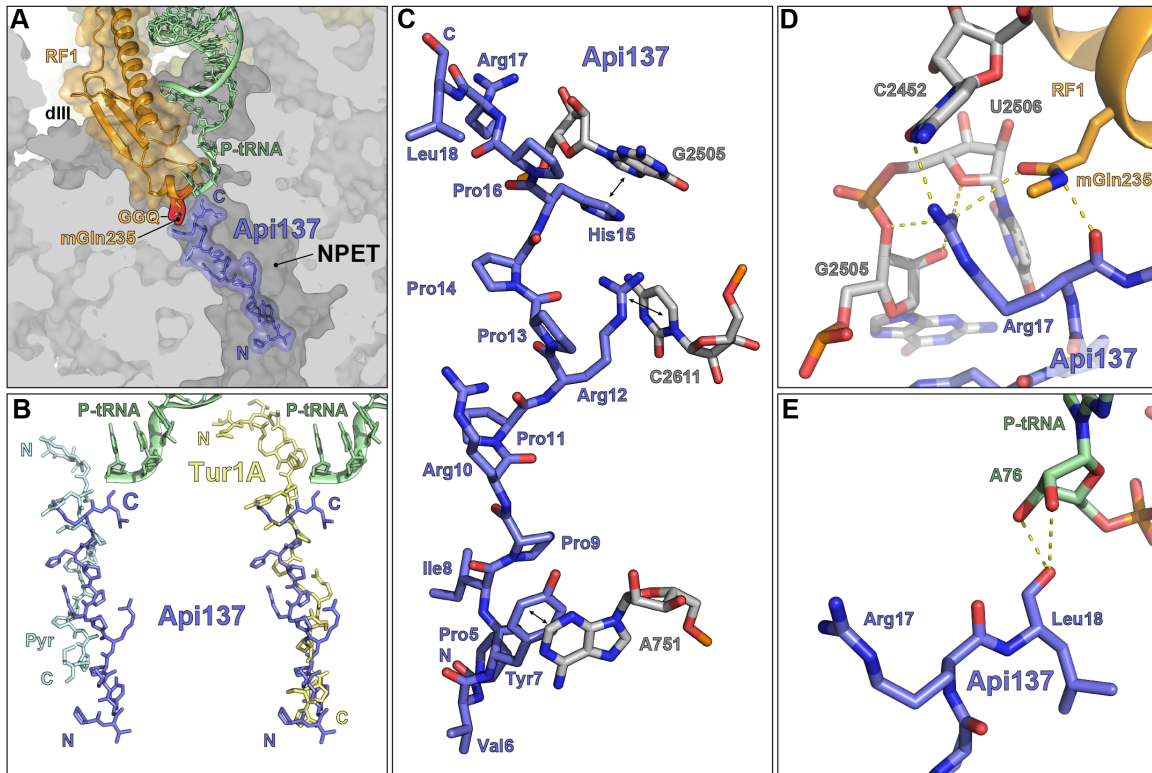


Figure 12 - Binding site of class II PrAMP Api137. **(A)** Overview showing the binding site of Api137 (slate) within the LSU (grey) polypeptide exit tunnel (NPET) in presence of P-tRNA (green) and RF1 (orange) (Florin et al., 2017). The GGQ motif is highlighted in red. The N- and C-terminus of Api137 is indicated by the letters N and C, respectively. **(B)** Superimposition of Api137 (slate) and Pyr (left; cyan) (Gagnon et al., 2016; Seefeldt et al., 2016) or Tur1A (right; yellow) (Mardirossian et al., 2018). P-tRNA (green is shown for reference). **(C)** Interactions of Api137 (slate) with 23S rRNA nucleotides (grey) located in the NPET (Florin et al., 2017). Stacking interactions are indicated by black two-headed arrows. **(D-E)** Interactions of Api137 in presence of **(D)** RF1 (orange) and **(E)** P-tRNA (green) (Florin et al., 2017). **(D)** Arg17 contacts 23S rRNA nucleotides and Gln235 of RF1. **(E)** Leu18 of Api137 contacts A76 of the deacylated tRNA located in the P-site.

reach into the LSU A-site binding pocket. Placement of Arg17 and Leu18 in the A-site crevice is crucial for the mechanism of action of Api137. For instance, exchange of Arg17 by Ala leads to decreased activity against *E. coli* ribosomes (Castle et al., 1999). The N-terminal residues pass down the polypeptide tunnel (Figures 12A and 12C) (Florin et al., 2017). In our structure, the last four residues at the N-terminus are not resolved. Nonetheless, compared to class I PrAMPs binding of Api137 to the polypeptide tunnel is solely facilitated by stacking interactions (Figure 12C) (Florin et al., 2017; Seefeldt et al., 2016; Seefeldt et al., 2015). Stacking interactions are observed between Tyr7 and A751, Arg12 and C2611 as well as His15 and the nucleobase of G2505 (Figure 12C) (Florin et al., 2017). In addition to stacking interactions, polar contacts are established in the PTC with RF1 and the deacylated P-site tRNA (Figures 12D and 12E). The side chain of the penultimate residue Arg17 is coordinated between 23S rRNA residues and Gln235 of the RF1 GGQ-motif (Figure

12D). The 23S rRNA contacts comprise hydrogen bonds with the nucleobase of C2452, the 2' and the 3'-oxygen of G2505 and the ribose of U2506 (Figure 12D). Gln235 interacts with Arg17 through the carbonyl oxygen of the side chain (Figure 12D). Leu18 appears to establish two interactions via the N-terminal OH-group (Figure 12E). These interactions include the 2'-OH and the 3'-OH of A76 of deacyl-P-tRNA (Figure 12E). The overall altered interaction network compared to class I PrAMPs forms the basis for the unique mechanism of action of Api137.

Mechanism of action of class I and class II PrAMPs

Under normal conditions ribosomal protein synthesis passes through the phases of translation initiation, translation elongation and translation termination (Figure 2). Translation initiation involves the placement of an fMet-tRNA^{fMet} over an AUG start codon in the P-site of the 70S ribosome (Figure 2A). The CCA-end that carries the fMet-moiety is placed in the PTC and the 3'-end establishes contacts with the P-loop of the LSU. Translation elongation comprises the EF-Tu mediated delivery and subsequent accommodation of an aa-tRNA to the ribosomal A-site, transpeptidation in the PTC and translocation catalyzed by EF-G (Figure 2B). Accommodation coincides with the establishment of interactions between the CCA-end of the A-site tRNA and the A-loop within the 23S rRNA. During translation termination the nascent chain is released from the ribosome with aid of the peptide chain release factor RF1 or RF2 (Figure 2C). Both classes of PrAMPs inhibit protein synthesis by binding to the polypeptide tunnel of bacterial 70S ribosomes, yet binding of each class of PrAMPs results in inhibition of different steps of the translation cycle (Florin et al., 2017; Gagnon et al., 2016; Roy et al., 2015; Seefeldt et al., 2016; Seefeldt et al., 2015). In the case of class I PrAMPs, the residues crucial for translation interference are located in the A-site binding pocket (Seefeldt et al., 2016; Seefeldt et al., 2015). In the case of the class II PrAMP Api137, the important residues are located in the PTC (Florin et al., 2017).

In presence of class I PrAMPs the A-site crevice and the A-site binding pocket are blocked by the N-terminal residues of the PrAMP (Figure 11D) (Gagnon et al., 2016; Mardirossian et al., 2018; Roy et al., 2015; Seefeldt et al., 2016; Seefeldt et al., 2015). This allows placement of an fMet-tRNA^{fMet} during translation initiation but perturbs delivery of the first aa-tRNA by EF-Tu (Mardirossian et al., 2018; Seefeldt et al., 2016; Seefeldt et al., 2015). Although decoding on the SSU is in principle possible,

subsequent accommodation following release from EF-Tu is blocked due to the steric hindrance generated by the N-terminal residues of class I PrAMPs. Accordingly, superimposition with pre-attack 70S ribosomes carrying an accommodated aa-tRNA in the A-site shows incompatibility of the A-tRNA CCA-end and the N-terminal residues of PrAMPs (Figure 11D) (Graf et al., 2017b). The same steric clash also prevents binding of PrAMPs during translation elongation. To avoid steric clashes with a peptidyl-tRNA, binding presumably occurs between translation termination and translation initiation. In general, class I PrAMPs inhibit the transition from translation initiation to translation elongation as confirmed by biochemical experiments (Mardirossian et al., 2018; Seefeldt et al., 2016; Seefeldt et al., 2015). In accordance, toe-print assays showed that translation in presence of class I PrAMPs indeed leads to ribosomal stalling at the AUG start codon. Further translation elongation is not possible.

Initial biochemical investigations of class II PrAMP Api137 assumed that translation inhibition occurs in a similar fashion to the first class of PrAMPs by binding to the polypeptide tunnel and inhibition of the transition from translation initiation to elongation. The major argument for this theory was the high content in proline and arginine residues that is common for all PrAMPs (Florin et al., 2017; Graf et al., 2017b). Surprisingly, our biochemical toe-prints assays showed that translation termination instead of translation initiation is affected (Florin et al., 2017). An explanation for this observation was provided by the previously described structural data and biophysical experiments. In contrast to the class I PrAMPs, Api137 binds to polypeptide tunnel without blocking the A-site binding pocket (Florin et al., 2017; Graf et al., 2017b). Thus, binding of a deacylated tRNA to the ribosomal A- and P-site is in principle possible (Florin et al., 2017). However, the C-terminal residues Arg17 and Leu18 establish very specific interactions with class I release factor RF1 (Figures 12D and 12E) (Florin et al., 2017). The resulting hydrogen bonding network further stabilizes Api137 in the tunnel and keeps RF1 bound to the ribosome (Figure 12C). Interestingly, RF1 trapping is not the major reason for inhibition of bacterial cell growth *in vivo*. Biochemical assays show that the presence of Api137 leads to stop codon read-through and depletion of the endogenous pool of RF1 available for translation termination. Hence, RF1 trapping on the ribosome just indirectly inhibits bacterial growth by preventing nascent chain release from other ribosomal complexes.

Validation of the 70S ribosome as a major PrAMP target

Although our studies show binding and inhibition of PrAMPs to 70S ribosomes, it is necessary to confirm that the translation machinery is the only target of PrAMPs. The tool of choice for this validation are mutagenesis experiments. In the course of these mutagenesis studies, bacterial cells are exposed to sub-inhibitory concentrations of a compound in culture, which leads to acquirement of rRNA or protein sequence alterations that allow bacteria to escape the inhibitory action. Protein or rRNA alterations in general, can affect inhibition either more directly, e.g. by decreasing the affinity to the binding site, or more indirectly, e.g. by preventing compound uptake into the cell.

Problematic for the identification of rRNA mutations is the presence of several rRNA operons in *E. coli*. Thus, acquirement of a single mutation within one rRNA operon does not affect the complete pool of rRNAs incorporated into ribosomes. To avoid this issue, the identification of rRNA mutations, which confer resistance to PrAMPs, requires the use of special *E. coli* strains, called squires (SQ) strains (Asai et al., 1999). The SQ strains exhibit a single rRNA allele that is encoded by an extra-genomic plasmid. The genetically encoded operons, coding for 5S, 16S and 23S rRNA, are absent. By exposing a SQ strain in culture to PrAMPs, it was possible to identify 23S rRNA mutations conferring resistance against the insect PrAMPs Onc112 (Gagnon et al., 2016) and Api137 (Florin et al., 2017).

The identified 23S rRNA residues are A2503 and A2059. Single or double mutation of A2503 and/or A2059 was shown to result in a 4- to 16-fold decreased susceptibility of *E. coli* cells against Onc112 and Api137 (Florin et al., 2017; Gagnon et al., 2016). Normally, A2503 and A2059 stack upon each other and stabilize adjacent nucleotides, such as A2062. The decreased susceptibility against both PrAMPs is presumably caused by conformational changes of nucleotides 2503 and 2059 as well as neighboring residues, which are crucial for stable binding of PrAMPs. Consistently, our structural data show that A2503 and A2059 are situated in close proximity to Api137 (Florin et al., 2017). Although no hydrogen bonds are observed for both nucleotides, the close proximity to Api137 possibly allows van-der-Waals interactions. Upon mutation, these interactions are presumably perturbed and result in a decreased binding affinity of Api137 towards the 70S ribosome. This contrasts the effect of A2503 and A2059 mutation on Onc112 binding (Gagnon et al., 2016). In presence of Onc112,

A2503 hydrogen bonds with A2062 and stabilizes the nucleotide in a 90° rotated conformation, which is crucial for accommodation of Onc112 in its binding site (Roy et al., 2015; Seefeldt et al., 2015). The non-rotated conformation of A2062 represents a steric block that prevents binding of Onc112 in the NPET. However, independent of the effect of the A2503 and A2059 mutation on neighboring rRNA residues, the decreased susceptibility against Onc112 and Api137 is a clear evidence for ribosomes as major target for the inhibition by PrAMPs.

With respect to protein alterations, most of the initially identified mutations, conferring resistance to PrAMPs, were dedicated to the coding gene of the *SbmA* transporter. The primary reason for this is possibly the lower cost in fitness for bacteria grown under lab conditions. Accordingly, *sbmA* deficient *E. coli* cells stay viable and exhibit lower susceptibility against PrAMPs, such as Bac7 (Mattiuzzo et al., 2007). In contrast, sequence alterations within functionally important regions are not well tolerated (Sato et al., 2006). Nonetheless, for Api137 it was possible to identify mutations within proteins by culturing *E. coli* cells that express multiple copies of an *sbmA* coding plasmid (Florin et al., 2017). The presence of multiple copies of the *sbmA* gene makes the acquirement of the same resistance mutation in all plasmids highly unlikely and ensures continuous uptake of PrAMPs into the bacterial cell. Consequently, the bacterial cell is forced to acquire alternative resistance mechanisms, which help to validate the ribosome as primary target for PrAMP action. Overall, it was possible to identify Api137 resistance mutations within ribosomal proteins as well as RF1 and RF2. Mutations within ribosomal proteins, which confer resistance against Api137, result from mutation of L4 residue Lys63 to Glu and from deletion of L22 residues 82 to 84 (Florin et al., 2017). Furthermore, decreased susceptibility against Api137 is observed for mutation of L16 Arg81 to Cys.

Ribosomal proteins L4 and L22 harbor each an extended loop that form together the central constriction within the polypeptide exit tunnel. The observed mutations within L4 and L22 presumably lead to reordering of these loops, which were shown in our structure to directly or indirectly stabilize binding of Api137 in the polypeptide tunnel (Florin et al., 2017). Thus, Arg61 of L4 provides a putative hydrogen bond to binding of Api137. Mutation of Lys63 could reorder the extension, which contains the interacting Arg61 and hence possibly destabilize binding of Api137. In contrast, deletion of L22 residues 82 to 84 presumably destabilizes Api137 binding more indirectly by contraction of the extended loop of L22. The extended loop of L22

contacts the 23S rRNA backbone and stabilizes H34. H34 harbors nucleotide A751 that stacks upon Api137 residue Tyr6 and is crucial for stable binding. The contraction of the extended loop of L22 most likely causes reordering of H34 and hence, destabilization of Api137 by the lacking stacking interaction between Tyr6 and 23S rRNA residue A751.

Arg81 of L16, which can confer resistance to Api137 upon mutation to Cys, stabilizes P-loop nucleotide G2251 via two hydrogen bonds (Florin et al., 2017). One hydrogen bond is established with the phosphate-oxygen backbone and one hydrogen bond is established with the nucleobase of G2251. As described in section 1.1, P-loop nucleotide G2251 Watson-Crick base-pairs with C75 of a P-site tRNA and stabilizes the CCA-end in the PTC for peptide bond formation. In presence of Api137, the C-terminal residue Leu18 contacts A76 of the P-tRNA. The interaction between Leu18 and the 3'-end of the P-tRNA stabilizes Api137 binding to the ribosome. Upon mutation of Arg81 of L16 to Cys, both polar interactions with nucleotide G2251 are resolved and possibly lead to higher flexibility within the P-loop and the CCA-end of a P-tRNA. As consequence, the binding affinity of Api137 towards the ribosome is reduced.

In addition to ribosomal protein mutations, more resistance mutations against Api137 were identified within RF1 and RF2. In this context, mutation of Arg262 to Cys and Gln280 to Leu in RF2 as well as Asp241 to Gly in RF1 leads to significantly reduced susceptibility of *E. coli* cells against Api137 (Florin et al., 2017). The cause of the decreased susceptibility is most likely a destabilization of the binding of RF1 and RF2, which overcomes the stabilizing interactions of Api137 with the GGQ-motif of RF1 and RF2. Accordingly, RF1 binding to the 70S ribosome is stabilized by a single polar contact of 23S nucleotide C2573 with Asp241. Mutation of Asp241 to Gly prevents an interaction with C2573 and hence could promote dissociation of RF1. Similar to RF1, mutation of RF2 residues Arg262 to Cys and Gln280 to Leu resolves interactions with 23S rRNA nucleotides C2556 and U2492, respectively. This could promote dissociation of RF2 since the interactions of Arg17 of Api137 are presumably insufficient to trap RF2 on the ribosome.

It is noteworthy that none of the rRNA or protein mutations conferred complete resistance against Onc112 and Api137. Nonetheless, all mutations taken together are rather strong arguments favoring the ribosome as the major target of these PrAMPs. A major problem for identifying more resistance mutations against PrAMPs is the high conservation of rRNA residues involved in PrAMP binding (RNACentral, 2017). As a

consequence, mutation of interacting residues would result in dramatically decreased PTC activity and therefore in reduced viability of bacterial cells (Sato et al., 2006; Thompson et al., 2001). An example is C2452, which is located within the A2451 region (23S nts 2448 to 2554). C2452 establishes a stacking interaction with Tur1A (Mardirossian et al., 2018) and pyrrhocoricin (Gagnon et al., 2016; Seefeldt et al., 2016) via a Tyr residue and a polar contact with Arg17 of Api137 (Florin et al., 2017). Using an SSER approach, Sato and colleagues showed in 2006 that except for A2448 and A2453 all nucleotides within the A2451 region are essential for ribosomal function (Sato et al., 2006). Consistently, it is not possible to select for viable C2452 mutants.

With regard to mammalian PrAMPs, such as Bac7 and Tur1A, no rRNA or ribosomal protein resistance mutations have been identified so far. In general, the identification of mutations conferring resistance to mammalian PrAMPs is more difficult. In contrast to insect PrAMPs, mammalian PrAMP Bac7 and Tur1A are considerably longer (Graf et al., 2017b). Mammalian PrAMPs show a full-length of 39 to 60 aa, while insect PrAMPs show a full-length between 15 and 34 amino acids. Although both, insect and mammalian PrAMPs, target ribosomes and inhibit translation, it was shown for full-length Bac7, which is very similar to Tur1A (Mardirossian et al., 2018), that a lytic mode of action is also evident (Podda et al., 2006). Only truncated derivatives of Bac7, like Bac7(1-16), solely inhibit protein synthesis without permeabilizing the bacterial membrane (Podda et al., 2006; Seefeldt et al., 2016). Selection for resistance mutations is in principle possible but it is difficult for bacteria to acquire mutations that affect both modes of action (lytic and non-lytic) of mammalian full-length PrAMPs (Lai and Gallo, 2009; Peschel and Sahl, 2006). As a consequence, bacteria remain susceptible against full-length antimicrobial peptides in culture. With respect to the previously described rRNA mutations conferring resistance to Onc112 and Api137 (A2503C and A2059G), no elevated MIC was observed in presence of Tur1A and Bac7 upon mutation of these residues (Gagnon et al., 2016; Mardirossian et al., 2018). Regardless, as described before, the selection for more rRNA resistance mutations is rather difficult since nucleotide alterations within the NPET that are involved in binding of mammalian PrAMPs would lead to strongly perturbed PTC activity (Sato et al., 2006).

Access of the NPET by Api137

Binding of class I PrAMPs presumably takes place after recycling of the 70S ribosome and previous to translation initiation (Graf et al., 2017b). With respect Api137, it remains obscure at which stage of translation termination binding occurs and how the binding site in the NPET is accessed. Although the 70S ribosome constitutes a porous complex, the binding site within the polypeptide tunnel must be accessed either from the PTC or from the tunnel exit (Voss et al., 2006). Due to the size of Api137, it is not possible to access the NPET by lateral diffusion through the LSU. Regardless, considering the length of ~100 Å and the width of the polypeptide tunnel with a diameter of less than 15 Å at the narrowest section (Nissen et al., 2000), it seems more difficult for a longer peptide to access the binding site from the back of the LSU through the tunnel exit. Regardless, a further limitation for the access of the binding site constitutes the presence of additional factors in the ribosomal tRNA binding sites. Accordingly, the space taken by RF1/2 in the A-site and deacyl-tRNA in the P-site during termination limits the access of Api137 to its binding site from the PTC (Florin et al., 2017). The only alternative is the access of the binding site via the tunnel exit on the back of the LSU. Consequently, Api137 presumably enters the 70S ribosome via the exit and diffuses to the binding site, which is located in the upper NPET.

With respect to the timing of binding, Api137 cannot access the binding site at all stages during termination. First, the presence of a nascent chain in the polypeptide exit tunnel during translation elongation represents a steric block that is incompatible with simultaneous binding of Api137. Second, Api137 action requires 70S-bound RF1 and P-tRNA, which interact via Gln235 of the GGQ-motif and A76 with Arg17 and Leu18, respectively (Florin et al., 2017). As consequence, binding of Api137 has to occur after peptide chain release and before RF1/2 departure from the post-hydrolysis 70S ribosome.

However, binding of Api137 can in principle also occur at a later stage of termination. Consistently, our recent RF3 cryo-EM study shows that RF1/2 departures from R-state 70S ribosomes with the deacyl-tRNA in a P/E hybrid state. The disruption of the CCA-end P-loop interactions and subsequent movement of the 3'-end to the E-site on the LSU, which is necessary for P/E hybrid state formation, leads to liberation of space in the PTC. This space most likely allows Api137 to enter the polypeptide exit tunnel. It is not clear whether binding at this late stage of termination is sufficient to

trap RF1/2 before dissociation or recycling by RF3 can take place. However, despite the possibility of binding of Api137 to the ribosome during RF1/2 recycling, this scenario seems to play just a minor role for RF1/2 trapping. In any case, it requires further biochemical studies to distinguish the time point of Api137 binding as well as the access to the NPET.

PrAMPs as novel tools to investigate protein synthesis

Knowing the exact mechanisms of action, PrAMPs represent a useful tool to further investigate the process of protein synthesis. One great possibility arises from the fact that PrAMPs either inhibit translation initiation or translation termination. Accordingly, class I PrAMPs stall 70S ribosomes at the AUG start codon (Gagnon et al., 2016; Mardirossian et al., 2018; Roy et al., 2015; Seefeldt et al., 2016; Seefeldt et al., 2015). Class II PrAMPs trap 70S ribosomes at stop codons (Florin et al., 2017). By utilizing the mechanism of action of each class it is possible to perform ribosomal profiling. Ribosomal profiling is based on deep sequencing and allows monitoring of *in vivo* translated mRNAs with codon accuracy (Brar and Weissman, 2015; Ingolia et al., 2009). In order to gain sequence information of the translated ORFs, ribosome protected mRNA fragments are purified. The purification of these protected fragments is a multi-step process. First, 70S ribosomes are stalled *in vivo* by translation inhibitors and purified together with the associated mRNA. Second, the fraction of the mRNA, which is not protected from the 70S ribosomes, becomes cleaved during RNase treatment. Afterwards, the ribosome protected fragments are released from the 70S ribosome and become modified with an anchor sequence. The resulting fragments that carry an anchor sequence are subjected to deep sequencing. Generally, ribosomal profiling allowed numerous labs to screen for actively translated ORFs in bacterial as well as eukaryotic cells under various conditions (Brar and Weissman, 2015). One of the most challenging problems in the field of profiling is the identification of start and stop sites. Accordingly, many of the translation inhibitors that are effective against eubacteria block more than one stage of protein synthesis (e.g. initiation and elongation) (Wilson, 2009). Examples for antibiotics, which inhibit multiple stages of protein synthesis, are thiopeptides and ribotoxins. Regardless, no inhibitor is known so far that specifically inhibits termination (Svidritskiy et al., 2013; Wilson, 2009). Therefore, Api137 represents an opportunity, because it specifically inhibits translation

termination by trapping RF1/2 on the ribosome (Florin et al., 2017). Both PrAMP classes together allow inhibition of the very first step and the very last step of translation without interfering with translation elongation (Florin et al., 2017; Mardirossian et al., 2018; Seefeldt et al., 2016; Seefeldt et al., 2015). As consequence, inhibition of ribosomal translation *in vivo* by class I or class II PrAMPs can in principle lead to the accumulation of 70S ribosomes at the start and stop codon, respectively, and thus possibly allow the identification of new ORFs. Noteworthy, the only limitation for the identification of new ORFs in bacteria is the presence of the SbmA transporter that ensures uptake of PrAMPs in culture at μ M concentrations (Scocchi et al., 2011). Accordingly, the determination of ORFs in Gram-positive bacteria, such as *Bacillus subtilis*, would require the introduction of the *sbmA* gene and successful expression and incorporation of the SbmA transporter in the membrane of Gram-positive bacteria.

Another possibility is the use of class II PrAMP Api137 as tool to allow incorporation of non-canonical amino acids as well as the generation of specific read-through products. As mentioned above, trapping of RF1 on the ribosomes by Api137 ultimately leads to depletion of RF1 from the pool of available termination factors (Florin et al., 2017). As a consequence, termination in general is perturbed since no class I release factor is available for peptide chain release. As shown by our biochemical assays, the absence of peptide release events leads to stop codon read-through and thus to the creation of unintended protein products. The stop codon read-through can be utilized to generate specific proteins in presence of Api137. Furthermore, a vacant A-site potentially allows easier delivery of non-canonical amino-acids by amber suppressor tRNAs.

Development of PrAMPs (Api137) with improved activities to yield future therapeutics

The continuously rising number of bacterial strains with resistances increases the demand for the discovery and the development of new therapeutics to treat infections. Consistently, antimicrobial peptides, such as Api137, represent interesting targets for future medicine. At this stage there are numerous AMPs under clinical trials. One example is pexiganan (Locilex®), which is currently in phase III clinical trials and used as topical cream to treat infected diabetic foot ulcers (Greber and Dawgul, 2017). In general, AMPs have one major advantage over small molecule drugs that are commonly used in medicine to treat infections (Mahlapuu et al., 2016). AMPs constitute

natural products composed of amino acids, which upon degradation do not result in toxic metabolites. Nonetheless, besides this one advantage AMPs face several problems, which are necessary to rule out before a clinical application is possible. In this context, the composition of AMPs out of amino acids also constitutes the biggest disadvantage since the peptides are prone to degradation by proteases. Therefore, the high abundance of proteases in the digestive tract results in a low oral bioavailability of AMPs (Vlieghe et al., 2010). The term bioavailability refers to the efficiency of uptake (e.g. into blood circulation or by a cell), which is crucial for the effectiveness of a drug against a specific target, such as pathogenic bacteria. To improve the poor bioavailability of AMPs it is possible to employ different approaches (Mahlapuu et al., 2016). This includes modification of the N- or C-termini and substitution of natural amino acids by unnatural amino acids, such as D-amino acid.

With respect to PrAMPs Api137 and Onc112, many attempts were made to obtain sequences with improved properties such as increased antimicrobial activity, solubility and serum stability, which is equivalent to decreased vulnerability against proteolytic cleavage (Berthold et al., 2013; Czihal et al., 2012; Knappe et al., 2011a; Knappe et al., 2010; Knappe et al., 2011b). In accordance, Api137 (Berthold et al., 2013) and Onc112 (Knappe et al., 2011a) represent derivatives of apidaecin-1b and oncocin with increased serum stability, which are the result of N-terminal and C-terminal modifications, respectively. Instead of an asparagine residue, Api137 harbors an ornithine residue with a tetramethylguanidinyl moiety at the N-terminus (Berthold et al., 2013). Onc112 harbors at the C-terminus an amino-group instead of an carboxyl-group and two D-Arg residues in position 15 and 19 (Knappe et al., 2011a). More modifications can be introduced based on our structural data.

The obtained structures of PrAMPs give direct insight into the interactions of Api137 and Onc112 with the 70S ribosome and the mechanism of action (Florin et al., 2017; Seefeldt et al., 2015). As described before, bacterial resistance against Api137 and Onc112 arises from rRNA and protein (only Api137) mutations (Florin et al., 2017; Gagnon et al., 2016). All of these mutations destabilize binding of Api137 and Onc112. Knowing the exact interactions of PrAMPs with the 70S ribosome possibly helps to generate second generation PrAMPs that are immune to the acquired bacterial resistances. Consistently, destabilization of PrAMPs in the presence of any of these mutations can be compensated by additional contacts with the polypeptide exit tunnel. In order to establish additional contacts within the NPET it is necessary introduce

amino acid substitutions. Important during this process is the maintenance of contacts, which are crucial for inhibition and the maintenance of the elongated structure of PrAMPs, which is essential for binding to the polypeptide exit tunnel. With regard to Api137, contacts important for protein synthesis inhibition are established by Tyr7, Arg12, His15, Arg17 and Leu18 (Florin et al., 2017). The other residues mostly constitute Pro residues and are presumably important for the elongated conformation of Api137. Nonetheless, future studies have to investigate the importance of each Pro residue and whether substitution results in an altered activity of the Api137. One approach is an alanine-scanning mutagenesis (Cunningham and Wells, 1989). Alanine-scanning mutagenesis allows the identification of important residues for inhibition by step-wise replacement of each Api137 residue with Ala.

Regardless, Pro residues 5, 9 and 13 seem to be less suitable for substitutions. Pro5 constitutes the last resolved residues of Api137 with no residues in close proximity, which allow additional contacts (Florin et al., 2017). Pro9 stacks upon Tyr7, and thus stabilizes the stacking interaction between Tyr7 and 23S nucleotide A751. Similar to Pro5, Pro13 is situated in a position with no tunnel residues in the vicinity. Even substitution by large amino acids, such as Arg and Lys, are not sufficient to reach the surrounding rRNA residues. This contrasts with Pro residues 11, 14 and 16, which are more suitable for substitutions. Noteworthy, none of these Pro residues is in optimal distance to 23S nucleotides, which would allow stacking interactions with aromatic amino acid substitutions, even when considering all possible side chain conformations. Therefore, possible substitutions primarily rely on the introduction of additional polar contacts.

Pro11 is located close to the tip of the extended loop of L4 and 23S nucleotide A2059. Mutagenesis to Asn or Asp would allow an additional hydrogen bond with A2059. Larger amino acids, like Arg, in the same position result in a steric clash that would presumably destabilize Api137. Nonetheless, substitution of Pro11 with Asn or Asp can possibly overcome the A2059C mutation that is thought to abolish stabilizing van-der-Waals interactions with Api137.

The only potential stacking interaction that can be introduced through mutation of Pro14 to Arg. Arg instead of Pro14 could lead to stacking upon the nucleobase of A2062. Alternatively, mutation of Pro14 to a smaller amino acid, such as Thr, possibly allows the establishment of two additional hydrogen bonds of the side chain OH-group

with the nucleobases of A2062 and A2503. Similar to mutation of Pro11 to Asn or Asp, mutation of Pro14 can potentially overcome the A2503G resistance mutation.

Pro16 is situated in the vicinity of the PTC nucleotides U2506 and U2585. Substitution of Pro16 with the small amino acid Thr presumably leads to an additional hydrogen bond between the side chain OH-group and the nucleobase of U2506. Replacement with larger amino acids most likely does not lead to additional contacts because of the confined space at the position of Pro16.

Besides substitution of Pro residues, other substitutions most likely lead to reduced or loss of Api137 activity. In accordance, substitution of Arg17, which is crucial for RF1 trapping, results in dramatically reduced activity of Api137 (Castle et al., 1999). The only substitution at the C-terminus that seems to be possible is the replacement of Leu18. Leu18 appears to play a less critical role for Api137 action, since deletion of Leu18 shows milder effects than replacement of Arg17 by Ala (Krizsan et al., 2014). Nonetheless, Leu18 establishes two hydrogen bonds via the C-terminal OH-group with A76 of the deacyl-P-tRNA that contribute to stable binding of Api137. Substitution of Leu18 by other amino acid does not resolve the polar contacts of the OH-group but can potentially lead to additional contacts through the amino acid side chain. The most promising substitution represents an exchange of Leu18 by Arg. An Arg residue in position 18 can provide two additional contacts with the ribose of U2585 and U2586.

Another possibility to improve the properties of AMPs is the fusion of two different AMP molecules resulting in a chimeric molecule. An example for such chimera AMPs are artilysins, which are the result of coupling of bacteriophage endolysins with another AMP (Briers and Lavigne, 2015; Briers et al., 2014a; Briers et al., 2014b; Defraine et al., 2016). Endolysins decompose the peptidoglycan of the bacterial cell wall. By fusion to other AMPs uptake of endolysins into the cytoplasm of Gram-negative bacteria is promoted. In the context of PrAMPs, fusion of class I and class II PrAMPs can possibly improve the overall binding activities. Although the orientation of class I and class II PrAMPs is different (Florin et al., 2017; Graf et al., 2017b), an interesting combination would be a chimera consisting of Api137 and pyrrhocoricin. Compared to class I PrAMPs (Graf et al., 2017b), Api137 establishes more contacts within upper nascent polypeptide exit tunnel (Florin et al., 2017). This contrasts pyrrhocoricin, which establishes primarily contacts with the A-site binding pocket and the A-site crevice (Gagnon et al., 2016; Seefeldt et al., 2016). Superimposition of pyrrhocoricin and Api137 shows that Pro16 of Api137 and Pro8 of pyrrhocoricin are

located in the same position within the tunnel (Figure 12B). Using the N-terminal residues of pyrrhocoricin with a reversed amino acid sequence, it would be possible to fuse the sequence 'PLYSGKDV' to a truncated derivate of Api137, which is lacking Arg17 and Leu18. The result is a chimeric PrAMP, which reaches into the A-site binding pocket while establishing additional interactions within polypeptide tunnel. However, it is not clear whether the reversed sequence of pyrrhocoricin still exhibits the same contacts within the A-site crevice and A-site binding pocket. Nonetheless, this approach is one possible example for the improvement of PrAMPs.

Implications for toxicity of Api137 in eukaryotes

As described before, usage of PrAMPs as therapeutics requires low toxicity in humans. Since PrAMPs target the 70S ribosome and inhibit protein synthesis of eubacteria, it needs clarification whether PrAMPs inhibit human translation as well. To have an inhibitory effect on human cells it requires first, the uptake of PrAMPs into the cytoplasm and second, binding to the eukaryotic ribosome. With regard to Bac7, our biochemical data show that Bac7 is capable of inhibiting *in vitro* protein synthesis in a rabbit reticulocyte extract (Seefeldt et al., 2016). Similarly, it is necessary to validate whether Api137 can bind and inhibit human 80S ribosomes. Our cryo-EM structure of 70S ribosomes in complex with RF1 and Api137 shows that Api137 binding primarily involves interactions with universally conserved rRNA residues (RNACentral, 2017) and the GGQ motif at the tip of RF1 domain III (Florin et al., 2017). The latter GGQ-motif is conserved within bacteria as well as evolutionary unrelated eukaryotic eRF1 (Frolova et al., 1999; Mora et al., 2003; Seit-Nebi et al., 2001; Shaw and Green, 2007; Zavialov et al., 2002). Assuming that Api137 is taken up by human cells, the conservation of both rRNA residues and the GGQ-motif of the class I release factors implies that Api137 is active against human 80S ribosomes and hence would be unsuitable for use as a therapeutic. Superimposition of a mammalian 80S ribosome in complex with eRF1 (Shao et al., 2016) and the 70S *E. coli* ribosome in complex with RF1 and Api137 (Florin et al., 2017) shows that binding of Api137 is in principle compatible with binding to both eubacterial and eukaryotic ribosomes. All observed contacts between Api137 and the 70S-RF1 complex could be established with an 80S-eRF1 complex as well. Therefore, inhibition of human translation termination by Api137 seems to be likely. Nonetheless, inhibition of human 80S ribosomes would still require

uptake of Api137 from the extra-cellular space. Gram-negative bacteria, like *E. coli*, actively uptake Api137, even at low concentrations, with the SbmA transporter. This transporter is absent from eukaryotic cells. Consistently, uptake of PrAMPs into the cytoplasm of human cells would require diffusion through the plasma membrane but this is unlikely due to the properties of Api137. Similar to most of the AMPs, Api137 exhibits a positive net charge that has been suggested to interfere with the lytic action or uptake of AMPs into eukaryotic cells (Yeaman and Yount, 2003). Bacterial cells exhibit a negatively charged cytoplasmic membrane surface, which promotes adsorption of positively charged AMPs and subsequent insertion into the membrane or uptake into the cell. Eukaryotic membranes, by contrast, exhibit a more neutral surface that do not promote adsorption of AMPs. Future experiments will be required to determine *in vivo* and *in vitro* whether Api137 is taken up by human cells and whether it is toxic or even teratogenic. A possibility to test for toxicity or teratogenicity *in vivo* are studies with mice or zebrafish embryos (Nagel, 2002). Inhibition of protein synthesis can be tested *in vitro* by the previously mentioned rabbit reticulocyte extract or, alternatively, using wheat germ extract.

5 References

- Adio, S., Senyushkina, T., Peske, F., Fischer, N., Wintermeyer, W., and Rodnina, M.V. (2015). Fluctuations between multiple EF-G-induced chimeric tRNA states during translocation on the ribosome. *Nat Commun* 6, 7442.
- Adio, S., Sharma, H., Senyushkina, T., Karki, P., Maracci, C., Wohlgemuth, I., Holtkamp, W., Peske, F., and Rodnina, M.V. (2018). Dynamics of ribosomes and release factors during translation termination in *E. coli*. *bioRxiv*.
- Agafonov, D.E., Kolb, V.A., and Spirin, A.S. (2001). Ribosome-associated protein that inhibits translation at the aminoacyl-tRNA binding stage. *EMBO Rep* 2, 399-402.
- Agerberth, B., Lee, J.Y., Bergman, T., Carlquist, M., Boman, H.G., Mutt, V., and Jornvall, H. (1991). Amino acid sequence of PR-39. Isolation from pig intestine of a new member of the family of proline-arginine-rich antibacterial peptides. *Eur J Biochem* 202, 849-854.
- Agirrezabala, X., Lei, J., Brunelle, J.L., Ortiz-Meoz, R.F., Green, R., and Frank, J. (2008). Visualization of the hybrid state of tRNA binding promoted by spontaneous ratcheting of the ribosome. *Mol Cell* 32, 190-197.
- Agirrezabala, X., Liao, H.Y., Schreiner, E., Fu, J., Ortiz-Meoz, R.F., Schulten, K., Green, R., and Frank, J. (2012). Structural characterization of mRNA-tRNA translocation intermediates. *Proc Natl Acad Sci U S A* 109, 6094-6099.
- Agrawal, R., Penczek, P., Grassucci, R., and Frank, J. (1998). Visualization of elongation factor G on the *Escherichia coli* 70S ribosome: The mechanism of translocation. *Proc Natl Acad Sci USA* 95, 6134 - 6138.
- Agrawal, R.K., Heagle, A.B., Penczek, P., Grassucci, R.A., and Frank, J. (1999). EF-G-dependent GTP hydrolysis induces translocation accompanied by large conformational changes in the 70S ribosome. *Nature Struct Biol* 6, 643-647.
- Agrawal, R.K., Spahn, C.M.T., Penczek, P., Grassucci, R.A., Nierhaus, K.H., and Frank, J. (2000). Visualization of tRNA movements on the *Escherichia coli* 70S ribosome during the elongation cycle. *J Cell Biol* 150, 447-459.
- Ahmed, T., Shi, J., and Bhushan, S. (2017). Unique localization of the plastid-specific ribosomal proteins in the chloroplast ribosome small subunit provides mechanistic insights into the chloroplastic translation. *Nucleic Acids Res* 45, 8581-8595.
- Ahmed, T., Yin, Z., and Bhushan, S. (2016). Cryo-EM structure of the large subunit of the spinach chloroplast ribosome. *Sci Rep* 6, 35793.
- Allen, G., Zavialov, A., Gursky, R., Ehrenberg, M., and Frank, J. (2005). The cryo-EM structure of a translation initiation complex from *Escherichia coli*. *Cell* 121, 703-712.
- Asai, T., Zaporjets, D., Squires, C., and Squires, C.L. (1999). An *Escherichia coli* strain with all chromosomal rRNA operons inactivated: complete exchange of rRNA genes between bacteria. *Proc Natl Acad Sci U S A* 96, 1971-1976.
- Astumian, R.D. (1997). Thermodynamics and kinetics of a Brownian motor. *Science* 276, 917-922.
- Ban, N., Nissen, P., Hansen, J., Moore, P.B., and Steitz, T.A. (2000). The complete atomic structure of the large ribosomal subunit at 2.4 Å resolution. *Science* 289, 905-920.

- Belardinelli, R., Sharma, H., Caliskan, N., Cunha, C.E., Peske, F., Wintermeyer, W., and Rodnina, M.V. (2016). Choreography of molecular movements during ribosome progression along mRNA. *Nat Struct Mol Biol* 23, 342-348.
- Benincasa, M., Scocchi, M., Podda, E., Skerlavaj, B., Dolzani, L., and Gennaro, R. (2004). Antimicrobial activity of Bac7 fragments against drug-resistant clinical isolates. *Peptides* 25, 2055-2061.
- Bennett, B.D., Kimball, E.H., Gao, M., Osterhout, R., Van Dien, S.J., and Rabinowitz, J.D. (2009). Absolute metabolite concentrations and implied enzyme active site occupancy in *Escherichia coli*. *Nat Chem Biol* 5, 593-599.
- Berthold, N., Czihal, P., Fritzsche, S., Sauer, U., Schiffer, G., Knappe, D., Alber, G., and Hoffmann, R. (2013). Novel apidaecin 1b analogs with superior serum stabilities for treatment of infections by gram-negative pathogens. *Antimicrob Agents Chemother* 57, 402-409.
- Bieri, P., Leibundgut, M., Saurer, M., Boehringer, D., and Ban, N. (2017). The complete structure of the chloroplast 70S ribosome in complex with translation factor pY. *EMBO J* 36, 475-486.
- Biou, V., Shu, F., and Ramakrishnan, V. (1995). X-ray crystallography shows that translational initiation factor IF3 consists of two compact alpha/beta domains linked by an alpha-helix. *EMBO J* 14, 4056-4064.
- Blanchard, S.C., Gonzalez, R.L., Kim, H.D., Chu, S., and Puglisi, J.D. (2004a). tRNA selection and kinetic proofreading in translation. *Nat Struct Mol Biol* 11, 1008-1014.
- Blanchard, S.C., Kim, H.D., Gonzalez, R.L., Jr., Puglisi, J.D., and Chu, S. (2004b). tRNA dynamics on the ribosome during translation. *Proc Natl Acad Sci USA* 101, 12893-12898.
- Borg, A., Pavlov, M., and Ehrenberg, M. (2016). Complete kinetic mechanism for recycling of the bacterial ribosome. *RNA* 22, 10-21.
- Brar, G.A., and Weissman, J.S. (2015). Ribosome profiling reveals the what, when, where and how of protein synthesis. *Nat Rev Mol Cell Biol* 16, 651-664.
- Brenner, S., Stretton, A.O.W., and Kaplan, S. (1965). Genetic code: the 'nonsense' triplets for chain termination and their suppression. *Nat* 206, 994-998.
- Briers, Y., and Lavigne, R. (2015). Breaking barriers: expansion of the use of endolysins as novel antibacterials against Gram-negative bacteria. *Future Microbiol* 10, 377-390.
- Briers, Y., Walmagh, M., Grymonprez, B., Biebl, M., Pirnay, J.P., Defraine, V., Michiels, J., Cenens, W., Aertsen, A., Miller, S., et al. (2014a). Art-175 is a highly efficient antibacterial against multidrug-resistant strains and persisters of *Pseudomonas aeruginosa*. *Antimicrob Agents Chemother* 58, 3774-3784.
- Briers, Y., Walmagh, M., Van Puyenbroeck, V., Cornelissen, A., Cenens, W., Aertsen, A., Oliveira, H., Azeredo, J., Verween, G., Pirnay, J.P., et al. (2014b). Engineered endolysin-based "Artilyns" to combat multidrug-resistant gram-negative pathogens. *MBio* 5, e01379-01314.
- Brilot, A.F., Korostelev, A.A., Ermolenko, D.N., and Grigorieff, N. (2013). Structure of the ribosome with elongation factor G trapped in the pretranslocation state. *Proc Natl Acad Sci U S A* 110, 20994-20999.
- Brogden, K.A. (2005). Antimicrobial peptides: pore formers or metabolic inhibitors in bacteria? *Nat Rev Microbiol* 3, 238-250.
- Bulet, P., Dimarcq, J.L., Hetru, C., Lagueux, M., Charlet, M., Hegy, G., Van Dorsselaer, A., and Hoffmann, J.A. (1993). A novel inducible antibacterial peptide of *Drosophila* carries an O-glycosylated substitution. *J Biol Chem* 268, 14893-14897.

- Bulkley, D., Brandi, L., Polikanov, Y.S., Fabbretti, A., O'Connor, M., Gualerzi, C.O., and Steitz, T.A. (2014). The antibiotics dityromycin and GE82832 bind protein S12 and block EF-G-catalyzed translocation. *Cell Rep* 6, 357-365.
- Capecci, M.R. (1967). Polypeptide chain termination in vitro: isolation of a release factor. *Proc Natl Acad Sci, USA* 58, 1144-1151.
- Carlson, M.A., Haddad, B.G., Weis, A.J., Blackwood, C.S., Shelton, C.D., Wuerth, M.E., Walter, J.D., and Spiegel, P.C., Jr. (2017). Ribosomal protein L7/L12 is required for GTPase translation factors EF-G, RF3, and IF2 to bind in their GTP state to 70S ribosomes. *FEBS J* 284, 1631-1643.
- Carter, A.P., Clemons, W.M., Jr., Brodersen, D.E., Morgan-Warren, R.J., Hartsch, T., Wimberly, B.T., and Ramakrishnan, V. (2001). Crystal structure of an initiation factor bound to the 30S ribosomal subunit. *Science* 291, 498-501.
- Casteels, P., Ampe, C., Jacobs, F., Vaeck, M., and Tempst, P. (1989). Apidaecins: antibacterial peptides from honeybees. *EMBO J* 8, 2387-2391.
- Casteels, P., Ampe, C., Riviere, L., Van Damme, J., Elicone, C., Fleming, M., Jacobs, F., and Tempst, P. (1990). Isolation and characterization of abaecin, a major antibacterial response peptide in the honeybee (*Apis mellifera*). *Eur J Biochem* 187, 381-386.
- Casteels, P., and Tempst, P. (1994). Apidaecin-type peptide antibiotics function through a non-poreforming mechanism involving stereospecificity. *Biochem Biophys Res Commun* 199, 339-345.
- Casteels-Josson, K., Capaci, T., Casteels, P., and Tempst, P. (1993). Apidaecin multipeptide precursor structure: a putative mechanism for amplification of the insect antibacterial response. *EMBO J* 12, 1569-1578.
- Castle, M., Nazarian, A., Yi, S.S., and Tempst, P. (1999). Lethal effects of apidaecin on *Escherichia coli* involve sequential molecular interactions with diverse targets. *J Biol Chem* 274, 32555-32564.
- Cate, J.H., Yusupov, M.M., Yusupova, G.Z., Earnest, T.N., and Noller, H.F. (1999). X-ray crystal structures of 70S ribosome functional complexes. *Science* 285, 2095-2104.
- Cech, T. (2000). Structural biology. The ribosome is a ribozyme. *Science* 289, 878-879.
- Chen, C., Cui, X., Beausang, J.F., Zhang, H., Farrell, I., Cooperman, B.S., and Goldman, Y.E. (2016). Elongation factor G initiates translocation through a power stroke. *Proc Natl Acad Sci U S A* 113, 7515-7520.
- Chen, C., Stevens, B., Kaur, J., Cabral, D., Liu, H., Wang, Y., Zhang, H., Rosenblum, G., Smilansky, Z., Goldman, Y.E., et al. (2011). Single-molecule fluorescence measurements of ribosomal translocation dynamics. *Mol Cell* 42, 367-377.
- Chen, H.Y., Bjerknes, M., Kumar, R., and Jay, E. (1994). Determination of the optimal aligned spacing between the Shine-Dalgarno sequence and the translation initiation codon of *Escherichia coli* mRNAs. *Nucleic Acids Res* 22, 4953-4957.
- Chen, J., Petrov, A., Tsai, A., O'Leary, S.E., and Puglisi, J.D. (2013). Coordinated conformational and compositional dynamics drive ribosome translocation. *Nat Struct Mol Biol* 20, 718-727.
- Chernysh, S., Cociancich, S., Briand, J.P., Hetru, C., and Bulet, P. (1996). The inducible antibacterial peptides of the Hemipteran insect *Palomena prasina*: Identification of a unique family of proline-rich peptides and of a novel insect defensin. *Journal of Insect Physiology* 42, 81-89.

- Chow, C.S., Lamichhane, T.N., and Mahto, S.K. (2007). Expanding the nucleotide repertoire of the ribosome with post-transcriptional modifications. *ACS Chem Biol* 2, 610-619.
- Cociancich, S., Dupont, A., Hegy, G., Lanot, R., Holder, F., Hetru, C., Hoffmann, J.A., and Bulet, P. (1994). Novel inducible antibacterial peptides from a hemipteran insect, the sap-sucking bug *Pyrrhocoris apterus*. *Biochem J 300 (Pt 2)*, 567-575.
- Connell, S.R., Takemoto, C., Wilson, D.N., Wang, H., Murayama, K., Terada, T., Shirouzu, M., Rost, M., Schuler, M., Giesebrecht, J., et al. (2007). Structural basis for interaction of the ribosome with the switch regions of GTP-bound elongation factors. *Mol Cell* 25, 751-764.
- Cordova, N.J., Ermentrout, B., and Oster, G.F. (1992). Dynamics of single-motor molecules: the thermal ratchet model. *Proc Natl Acad Sci U S A* 89, 339-343.
- Cornish, P.V., Ermolenko, D.N., Noller, H.F., and Ha, T. (2008). Spontaneous intersubunit rotation in single ribosomes. *Mol Cell* 30, 578-588.
- Crick, F.H. (1958). On protein synthesis. *Symp Soc Exp Biol* 12, 138-163.
- Crick, F.H., Barnett, L., Brenner, S., and Watts-Tobin, R.J. (1961). General nature of the genetic code for proteins. *Nature* 192, 1227-1232.
- Crick, F.H.C. (1966). Codon-anticodon pairing: The wobble hypothesis. *J Mol Biol* 19, 548-555.
- Cunningham, B.C., and Wells, J.A. (1989). High-resolution epitope mapping of hGH-receptor interactions by alanine-scanning mutagenesis. *Science* 244, 1081-1085.
- Czihal, P., Knappe, D., Fritsche, S., Zahn, M., Berthold, N., Piantavigna, S., Muller, U., Van Dorpe, S., Herth, N., Binas, A., et al. (2012). Api88 is a novel antibacterial designer peptide to treat systemic infections with multidrug-resistant Gram-negative pathogens. *ACS Chem Biol* 7, 1281-1291.
- Dahlquist, K.D., and Puglisi, J.D. (2000). Interaction of translation initiation factor IF1 with the *E. coli* ribosomal A site. *J Mol Biol* 299, 1-15.
- Dallas, A., and Noller, H.F. (2001). Interaction of translation initiation factor 3 with the 30S ribosomal subunit. *Mol Cell* 8, 855-864.
- Darwin, C. (1869). *On the Origin of species by means of natural selection or the preservation of favoured races in the struggle for life*, 5th edn (London: Murray).
- Defraine, V., Schuermans, J., Grymonprez, B., Govers, S.K., Aertsen, A., Fauvert, M., Michiels, J., Lavigne, R., and Briers, Y. (2016). Efficacy of Artilysin Art-175 against Resistant and Persistent *Acinetobacter baumannii*. *Antimicrob Agents Chemother* 60, 3480-3488.
- Demeshkina, N., Jenner, L., Westhof, E., Yusupov, M., and Yusupova, G. (2012). A new understanding of the decoding principle on the ribosome. *Nature* 484, 256-259.
- Diaconu, M., Kothe, U., Schlunzen, F., Fischer, N., Harms, J.M., Tonevitsky, A.G., Stark, H., Rodnina, M.V., and Wahl, M.C. (2005). Structural basis for the function of the ribosomal L7/12 stalk in factor binding and GTPase activation. *Cell* 121, 991-1004.
- Dincbas-Renqvist, V., Engstrom, A., Mora, L., Heurgue-Hamard, V., Buckingham, R., and Ehrenberg, M. (2000). A post-translational modification in the GGQ motif of RF2 from *Escherichia coli* stimulates termination of translation. *EMBO J* 19, 6900-6907.

- Dorner, S., Brunelle, J.L., Sharma, D., and Green, R. (2006). The hybrid state of tRNA binding is an authentic translation elongation intermediate. *Nat Struct Mol Biol* 13, 234-241.
- Douthwaite, S., Garrett, R.A., and Wagner, R. (1983). Comparison of *E. coli* tRNAPhe in the free state, in the ternary complex and in the ribosomal A and P sites by chemical probing. *Eur J Biochem* 131, 261-269.
- Drechsel, O., and Bock, R. (2011). Selection of Shine-Dalgarno sequences in plastids. *Nucleic Acids Res* 39, 1427-1438.
- Dunkle, J.A., Wang, L., Feldman, M.B., Pulk, A., Chen, V.B., Kapral, G.J., Noeske, J., Richardson, J.S., Blanchard, S.C., and Cate, J.H. (2011). Structures of the bacterial ribosome in classical and hybrid states of tRNA binding. *Science* 332, 981-984.
- Elvekrog, M.M., and Gonzalez, R.L., Jr. (2013). Conformational selection of translation initiation factor 3 signals proper substrate selection. *Nat Struct Mol Biol* 20, 628-633.
- Ermolenko, D.N., Majumdar, Z.K., Hickerson, R.P., Spiegel, P.C., Clegg, R.M., and Noller, H.F. (2007). Observation of intersubunit movement of the ribosome in solution using FRET. *J Mol Biol* 370, 530-540.
- Fabbretti, A., Pon, C.L., Hennelly, S.P., Hill, W.E., Lodmell, J.S., and Gualerzi, C.O. (2007). The real-time path of translation factor IF3 onto and off the ribosome. *Mol Cell* 25, 285-296.
- Fischer, N., Konevega, A.L., Wintermeyer, W., Rodnina, M.V., and Stark, H. (2010). Ribosome dynamics and tRNA movement by time-resolved electron cryomicroscopy. *Nature* 466, 329-333.
- Florin, T., Maracci, C., Graf, M., Karki, P., Klepacki, D., Berninghausen, O., Beckmann, R., Vazquez-Laslop, N., Wilson, D.N., Rodnina, M.V., et al. (2017). An antimicrobial peptide that inhibits translation by trapping release factors on the ribosome. *Nat Struct Mol Biol* 24, 752-757.
- Forsberg, B.O., Aibara, S., Kimanis, D., Paul, B., Lindahl, E., and Amunts, A. (2017). Cryo-EM reconstruction of the chlororibosome to 3.2 Å resolution within 24 h. *IUCrJ* 4, 723-727.
- Frank, J., and Agrawal, R.K. (2000). A ratchet-like inter-subunit reorganization of the ribosome during translocation. *Nature* 406, 318-322.
- Frank, J., Jr., and Gonzalez, R.L. (2010). Structure and dynamics of a processive Brownian motor: the translating ribosome. *Annu Rev Biochem* 79, 381-412.
- Freistroffer, D.V., Pavlov, M.Y., MacDougall, J., Buckingham, R.H., and Ehrenberg, M. (1997). Release factor RF3 in *E. coli* accelerates the dissociation of release factors RF1 and RF2 from the ribosome in a GTP-dependent manner. *EMBO J* 16, 4126-4133.
- Frolova, L., Tsivkovskii, R., Sivolobova, G., Oparina, N., Serpinski, O., Blinov, V., Tatkov, S., and Kisilev, L. (1999). Mutations in the highly conserved GGQ motif of class 1 polypeptide release factors abolish the ability of human eRF1 to trigger peptidyl-tRNA hydrolysis. *RNA* 5, 1014-1020.
- Fu, Z., Kaledhonkar, S., Borg, A., Sun, M., Chen, B., Grassucci, R.A., Ehrenberg, M., and Frank, J. (2016). Key Intermediates in Ribosome Recycling Visualized by Time-Resolved Cryoelectron Microscopy. *Structure* 24, 2092-2101.
- Gagnon, M.G., Roy, R.N., Lomakin, I.B., Florin, T., Mankin, A.S., and Steitz, T.A. (2016). Structures of proline-rich peptides bound to the ribosome reveal a common mechanism of protein synthesis inhibition. *Nucleic Acids Res* 44, 2439-2450.

- Gao, H., Zhou, Z., Rawat, U., Huang, C., Bouakaz, L., Wang, C., Cheng, Z., Liu, Y., Zavialov, A., Gursky, R., et al. (2007). RF3 induces ribosomal conformational changes responsible for dissociation of class I release factors. *Cell* 129, 929-941.
- Gao, N., Zavialov, A.V., Li, W., Sengupta, J., Valle, M., Gursky, R.P., Ehrenberg, M., and Frank, J. (2005). Mechanism for the disassembly of the posttermination complex inferred from cryo-EM studies. *Mol Cell* 18, 663-674.
- Gao, Y.G., Selmer, M., Dunham, C.M., Weixlbaumer, A., Kelley, A.C., and Ramakrishnan, V. (2009). The structure of the ribosome with elongation factor G trapped in the posttranslocational state. *Science* 326, 694-699.
- Garcia, C., Fortier, P.L., Blanquet, S., Lallemand, J.Y., and Dardel, F. (1995). Solution structure of the ribosome-binding domain of *E. coli* translation initiation factor IF3. Homology with the U1A protein of the eukaryotic spliceosome. *J Mol Biol* 254, 247-259.
- Gennaro, R., Skerlavaj, B., and Romeo, D. (1989). Purification, composition, and activity of two bactenecins, antibacterial peptides of bovine neutrophils. *Infect Immun* 57, 3142-3146.
- Goldstein, J.L., and Caskey, C.T. (1970). Peptide chain termination: Effect of protein S on ribosomal binding of release factors. *Proc Natl Acad Sci, USA* 67, 537-543.
- Goyal, A., Belardinelli, R., Maracci, C., Milon, P., and Rodnina, M.V. (2015). Directional transition from initiation to elongation in bacterial translation. *Nucleic Acids Res* 43, 10700-10712.
- Graf, M., Arenz, S., Huter, P., Donhofer, A., Novacek, J., and Wilson, D.N. (2017a). Cryo-EM structure of the spinach chloroplast ribosome reveals the location of plastid-specific ribosomal proteins and extensions. *Nucleic Acids Res* 45, 2887-2896.
- Graf, M., Mardirossian, M., Nguyen, F., Seefeldt, A.C., Guichard, G., Scocchi, M., Innis, C.A., and Wilson, D.N. (2017b). Proline-rich antimicrobial peptides targeting protein synthesis. *Nat Prod Rep* 34, 702-711.
- Greber, K.E., and Dawgul, M. (2017). Antimicrobial Peptides Under Clinical Trials. *Curr Top Med Chem* 17, 620-628.
- Grigoriadou, C., Marzi, S., Kirillov, S., Gualerzi, C.O., and Cooperman, B.S. (2007a). A quantitative kinetic scheme for 70 S translation initiation complex formation. *J Mol Biol* 373, 562-572.
- Grigoriadou, C., Marzi, S., Pan, D., Gualerzi, C.O., and Cooperman, B.S. (2007b). The translational fidelity function of IF3 during transition from the 30 S initiation complex to the 70 S initiation complex. *J Mol Biol* 373, 551-561.
- Grunberg-Manago, M., Dessen, P., Pantaloni, D., Godefroy-Colburn, T., Wolfe, A.D., and Dondon, J. (1975). Light-scattering studies showing the effect of initiation factors on the reversible dissociation of *Escherichia coli* ribosomes. *J Mol Biol* 94, 461-478.
- Gualerzi, C.O., Brandi, L., Caserta, E., Garofalo, C., Lammi, M., La Teana, A., Petrelli, D., Spurio, R., Tomsic, J., and Pon, C.L. (2001). Initiation factors in the early events of mRNA translation in bacteria. *Cold Spring Harb Symp Quant Biol* 66, 363-376.
- Guenneugues, M., Caserta, E., Brandi, L., Spurio, R., Meunier, S., Pon, C.L., Boelens, R., and Gualerzi, C.O. (2000). Mapping the fMet-tRNA^{fMet} binding site of initiation factor IF2. *EMBO J* 19, 5233-5240.

- Guillon, J.M., Meinnel, T., Mechulam, Y., Lazennec, C., Blanquet, S., and Fayat, G. (1992). Nucleotides of transfer RNA Governing the Specificity of Escherichia-Coli Methionyl-transfer RNA(Met)f Formyltransferase. *J Mol Biol* 224, 359-367.
- Hansen, J.L., Schmeing, T.M., Moore, P.B., and Steitz, T.A. (2002). Structural insights into peptide bond formation. *Proc Natl Acad Sci USA* 99, 11670-11675.
- Harms, J., Schluenzen, F., Zarivach, R., Bashan, A., Gat, S., Agmon, I., Bartels, H., Franceschi, F., and Yonath, A. (2001). High resolution structure of the large ribosomal subunit from a mesophilic eubacterium. *Cell* 107, 679-688.
- Hartz, D., Binkley, J., Hollingsworth, T., and Gold, L. (1990). Domains of initiator transfer RNA and initiation codon crucial for initiator transfer RNA selection by *Escherichia coli* IF3. *Gene Dev* 4, 1790-1800.
- Hartz, D., McPheeters, D.S., and Gold, L. (1989). Selection of the initiator tRNA by *Escherichia coli* initiation factors. *Genes Dev* 3, 1899-1912.
- Heurgue-Hamard, V., Champ, S., Engstrom, A., Ehrenberg, M., and Buckingham, R. (2002). The hemK gene in *Escherichia coli* encodes the N(5)-glutamine methyltransferase that modifies peptide release factors. *EMBO J* 21, 769-778.
- Hirokawa, G., Demeshkina, N., Iwakura, N., Kaji, H., and Kaji, A. (2006). The ribosome-recycling step: consensus or controversy? *Trends Biochem Sci* 31, 143-149.
- Hirokawa, G., Nijman, R., Raj, V., Kaji, H., Igarashi, K., and Kaji, A. (2005). The role of ribosome recycling factor in dissociation of 70S ribosomes into subunits. *RNA* 11, 1317-1128.
- Hirose, T., Kusumegi, T., and Sugiura, M. (1998). Translation of tobacco chloroplast rps14 mRNA depends on a Shine-Dalgarno-like sequence in the 5'-untranslated region but not on internal RNA editing in the coding region. *FEBS Lett* 430, 257-260.
- Holley, R., Apgar, J., Everett, G., Marquisee, M., Merrill, S., Renswick, J., and Zamir, A. (1965). Structure of a ribonucleic acid. *Science* 147, 1462-1465.
- Holtkamp, W., Cunha, C.E., Peske, F., Konevega, A.L., Wintermeyer, W., and Rodnina, M.V. (2014). GTP hydrolysis by EF-G synchronizes tRNA movement on small and large ribosomal subunits. *EMBO J* 33, 1073-1085.
- Hussain, T., Llacer, J.L., Wimberly, B.T., Kieft, J.S., and Ramakrishnan, V. (2016). Large-Scale Movements of IF3 and tRNA during Bacterial Translation Initiation. *Cell* 167, 133-144 e113.
- Huttner, K.M., Lambeth, M.R., Burkin, H.R., Burkin, D.J., and Broad, T.E. (1998). Localization and genomic organization of sheep antimicrobial peptide genes. *Gene* 206, 85-91.
- Ingolia, N.T., Ghaemmaghami, S., Newman, J.R., and Weissman, J.S. (2009). Genome-wide analysis *in vivo* of translation with nucleotide resolution using ribosome profiling. *Science* 324, 218-223.
- Ito, K., Fujiwara, T., Toyoda, T., and Nakamura, Y. (2002). Elongation factor G participates in ribosome disassembly by interacting with ribosome recycling factor at their tRNA-mimicry domains. *Mol Cell* 9, 1263-1272.
- Ito, K., Uno, M., and Nakamura, Y. (2000). A tripeptide 'anticodon' deciphers stop codons in messenger RNA. *Nature* 403, 680-684.
- Janosi, L., Shimizu, I., and Kaji, A. (1994). Ribosome recycling factor (ribosome releasing factor) is essential for bacterial growth. *Proc Natl Acad Sci USA* 91, 4249-4253.

- Jenner, L., Demeshkina, N., Yusupova, G., and Yusupov, M. (2010). Structural rearrangements of the ribosome at the tRNA proofreading step. *Nat Struct Mol Biol* 17, 1072-1078.
- Jenssen, H., Hamill, P., and Hancock, R.E. (2006). Peptide antimicrobial agents. *Clin Microbiol Rev* 19, 491-511.
- Jin, H., Kelley, A.C., and Ramakrishnan, V. (2011). Crystal structure of the hybrid state of ribosome in complex with the guanosine triphosphatase release factor 3. *Proc Natl Acad Sci U S A* Epub.
- Julian, P., Konevega, A.L., Scheres, S.H., Lazaro, M., Gil, D., Wintermeyer, W., Rodnina, M.V., and Valle, M. (2008). Structure of ratcheted ribosomes with tRNAs in hybrid states. *Proc Natl Acad Sci U S A* 105, 16924-16927.
- Julian, P., Milon, P., Agirrezabala, X., Lasso, G., Gil, D., Rodnina, M.V., and Valle, M. (2011). The Cryo-EM structure of a complete 30S translation initiation complex from *Escherichia coli*. *PLoS Biol* 9, e1001095.
- Karimi, R., Pavlov, M., Buckingham, R., and Ehrenberg, M. (1999). Novel roles for classical factors at the interface between translation termination and initiation. *Mol Cell* 3, 601-609.
- Katunin, V.I., Muth, G.W., Strobel, S.A., Wintermeyer, W., and Rodnina, M.V. (2002). Important contribution to catalysis of peptide bond formation by a single ionizing group within the ribosome. *Mol Cell* 10, 339-346.
- Khade, P.K., and Joseph, S. (2011). Messenger RNA interactions in the decoding center control the rate of translocation. *Nat Struct Mol Biol* 18, 1300-1302.
- Kihira, K., Shimizu, Y., Shomura, Y., Shibata, N., Kitamura, M., Nakagawa, A., Ueda, T., Ochi, K., and Higuchi, Y. (2012). Crystal structure analysis of the translation factor RF3 (release factor 3). *FEBS Lett* 586, 3705-3709.
- Kim, D., and Green, R. (1999). Base-pairing between 23S rRNA and tRNA in the ribosomal A site. *Mol Cell* 4, 859-864.
- Kim, K.K., Min, K., and Suh, S.W. (2000). Crystal structure of the ribosome recycling factor from *Escherichia coli*. *EMBO J* 19, 2362-2370.
- Kim, S.H., Quigley, G.J., Suddath, F.L., McPherson, A., Sneden, D., Kim, J.J., Weinzierl, J., and Rich, A. (1973). Three-dimensional structure of yeast phenylalanine transfer RNA: folding of the polynucleotide chain. *Science* 179, 285-288.
- Klaholz, B., Myasnikov, A., and Van Heel, M. (2004). Visualization of release factor 3 on the ribosome during termination of protein synthesis. *Nature* 427, 862-865.
- Knappe, D., Kabankov, N., and Hoffmann, R. (2011a). Bactericidal oncocin derivatives with superior serum stabilities. *Int J Antimicrob Agents* 37, 166-170.
- Knappe, D., Piantavigna, S., Hansen, A., Mechler, A., Binas, A., Nolte, O., Martin, L.L., and Hoffmann, R. (2010). Oncocin (VDKPPYLPRLPRPRPRRIYNR-NH₂): a novel antibacterial peptide optimized against gram-negative human pathogens. *J Med Chem* 53, 5240-5247.
- Knappe, D., Zahn, M., Sauer, U., Schiffer, G., Strater, N., and Hoffmann, R. (2011b). Rational design of oncocin derivatives with superior protease stabilities and antibacterial activities based on the high-resolution structure of the oncocin-DnaK complex. *ChemBioChem* 12, 874-876.
- Korostelev, A., Asahara, H., Lancaster, L., Laurberg, M., Hirschi, A., Zhu, J., Trakhanov, S., Scott, W.G., and Noller, H.F. (2008). Crystal structure of a translation termination complex formed with release factor RF2. *Proc Natl Acad Sci U S A* 105, 19684-19689.

- Korostelev, A., Zhu, J., Asahara, H., and Noller, H.F. (2010). Recognition of the amber UAG stop codon by release factor RF1. *The EMBO journal* 29, 2577-2585.
- Koteliansky, V.E., Domogatsky, S.P., Gudkov, A.T., and Spirin, A.S. (1977). EF-dependent reactions on ribosomes deprived of proteins L7 and L12. *FEBS Lett* 73, 6-11.
- Kothe, U., Wieden, H.J., Mohr, D., and Rodnina, M.V. (2004). Interaction of helix D of elongation factor Tu with helices 4 and 5 of protein L7/12 on the ribosome. *J Mol Biol* 336, 1011-1021.
- Koutmou, K.S., McDonald, M.E., Brunelle, J.L., and Green, R. (2014). RF3:GTP promotes rapid dissociation of the class 1 termination factor. *RNA* 20, 609-620.
- Krizsan, A., Knappe, D., and Hoffmann, R. (2015a). Influence of the yjl-mdtM Gene Cluster on the Antibacterial Activity of Proline-Rich Antimicrobial Peptides Overcoming *Escherichia coli* Resistance Induced by the Missing SbmA Transporter System. *Antimicrob Agents Chemother* 59, 5992-5998.
- Krizsan, A., Prahl, C., Goldbach, T., Knappe, D., and Hoffmann, R. (2015b). Short Proline-Rich Antimicrobial Peptides Inhibit Either the Bacterial 70S Ribosome or the Assembly of its Large 50S Subunit. *Chembiochem* 16, 2304-2308.
- Krizsan, A., Volke, D., Weinert, S., Strater, N., Knappe, D., and Hoffmann, R. (2014). Insect-derived proline-rich antimicrobial peptides kill bacteria by inhibiting bacterial protein translation at the 70S ribosome. *Angew Chem Int Ed Engl* 53, 12236-12239.
- Kuhlenkoetter, S., Wintermeyer, W., and Rodnina, M.V. (2011). Different substrate-dependent transition states in the active site of the ribosome. *Nature* 476, 351-354.
- La Teana, A., Gualerzi, C.O., and Dahlberg, A.E. (2001). Initiation factor IF 2 binds to the alpha-sarcin loop and helix 89 of *Escherichia coli* 23S ribosomal RNA. *RNA* 7, 1173-1179.
- La Teana, A., Pon, C.L., and Gualerzi, C.O. (1996). Late events in translation initiation. Adjustment of fMet-tRNA in the ribosomal P-site. *J Mol Biol* 256, 667-675.
- Lai, Y., and Gallo, R.L. (2009). AMPed up immunity: how antimicrobial peptides have multiple roles in immune defense. *Trends Immunol* 30, 131-141.
- Laurberg, M., Asahara, H., Korostelev, A., Zhu, J., Trakhanov, S., and Noller, H.F. (2008). Structural basis for translation termination on the 70S ribosome. *Nature* 454, 852-857.
- Laursen, B.S., Sorensen, H.P., Mortensen, K.K., and Sperling-Petersen, H.U. (2005). Initiation of protein synthesis in bacteria. *Microbiol Mol Biol Rev* 69, 101-123.
- Lee, C.P., Seong, B.L., and Rajbhandary, U.L. (1991). Structural and Sequence Elements Important for Recognition of *Escherichia-Coli* Formylmethionine Transfer RNA by Methionyl-Transfer RNA Transformylase Are Clustered in the Acceptor Stem. *J Biol Chem* 266, 18012-18017.
- Li, W., Liu, Z., Korpella, R.K., Langlois, R., Sanyal, S., and Frank, J. (2015). Activation of GTP hydrolysis in mRNA-tRNA translocation by elongation factor G. *Sci Adv* 1.
- Liljas, A., and Gudkov, A.T. (1987). The structure and dynamics of ribosomal protein L12. *Biochimie* 69, 1043-1047.
- Lin, J., Gagnon, M.G., Bulkley, D., and Steitz, T.A. (2015). Conformational changes of elongation factor G on the ribosome during tRNA translocation. *Cell* 160, 219-227.

- Liu, G., Song, G., Zhang, D., Zhang, D., Li, Z., Lyu, Z., Dong, J., Achenbach, J., Gong, W., Zhao, X.S., et al. (2014). EF-G catalyzes tRNA translocation by disrupting interactions between decoding center and codon-anticodon duplex. *Nat Struct Mol Biol* 21, 817-824.
- Lopez-Alonso, J.P., Fabbretti, A., Kaminishi, T., Iturrioz, I., Brandi, L., Gil-Carton, D., Gualerzi, C.O., Fucini, P., and Connell, S.R. (2017). Structure of a 30S pre-initiation complex stalled by GE81112 reveals structural parallels in bacterial and eukaryotic protein synthesis initiation pathways. *Nucleic Acids Res* 45, 2179-2187.
- Loveland, A.B., Demo, G., Grigorieff, N., and Korostelev, A.A. (2017). Ensemble cryo-EM elucidates the mechanism of translation fidelity. *Nature* 546, 113-117.
- Maguire, B.A., Beniaminov, A.D., Ramu, H., Mankin, A.S., and Zimmermann, R.A. (2005). A protein component at the heart of an RNA machine: the importance of protein L27 for the function of the bacterial ribosome. *Mol Cell* 20, 427-435.
- Mahlapuu, M., Hakansson, J., Ringstad, L., and Bjorn, C. (2016). Antimicrobial Peptides: An Emerging Category of Therapeutic Agents. *Front Cell Infect Microbiol* 6, 194.
- Mandava, C.S., Peisker, K., Ederth, J., Kumar, R., Ge, X., Szaflarski, W., and Sanyal, S. (2012). Bacterial ribosome requires multiple L12 dimers for efficient initiation and elongation of protein synthesis involving IF2 and EF-G. *Nucleic Acids Res* 40, 2054-2064.
- Maracci, C., Wohlgemuth, I., and Rodnina, M.V. (2015). Activities of the peptidyl transferase center of ribosomes lacking protein L27. *RNA* 21, 2047-2052.
- Mardirossian, M., Grzela, R., Giglione, C., Meinnel, T., Gennaro, R., Mergaert, P., and Scocchi, M. (2014). The host antimicrobial peptide Bac71-35 binds to bacterial ribosomal proteins and inhibits protein synthesis. *Chem Biol* 21, 1639-1647.
- Mardirossian, M., Perebaskine, N., Benincasa, M., Gambato, S., Hofmann, S., Huter, P., Müller, C., Hilpert, K., Innis, C.A., Tossi, A., et al. (2018). The dolphin proline-rich antimicrobial peptide Tur1A inhibits protein synthesis by targeting the bacterial ribosome. *Cell Chemical Biology*.
- Margulis, L. (1971). The origin of plant and animal cells. *Am Sci* 59, 230-235.
- Marshall, R.A., Aitken, C.E., and Puglisi, J.D. (2009). GTP hydrolysis by IF2 guides progression of the ribosome into elongation. *Mol Cell* 35, 37-47.
- Mathy, N., Benard, L., Pellegrini, O., Daou, R., Wen, T., and Condon, C. (2007). 5'-to-3' exoribonuclease activity in bacteria: role of RNase J1 in rRNA maturation and 5' stability of mRNA. *Cell* 129, 681-692.
- Mattiuzzo, M., Bandiera, A., Gennaro, R., Benincasa, M., Pacor, S., Antcheva, N., and Scocchi, M. (2007). Role of the *Escherichia coli* SbmA in the antimicrobial activity of proline-rich peptides. *Mol Microbiol* 66, 151-163.
- McCutcheon, J.P., Agrawal, R.K., Philips, S.M., Grassucci, R.A., Gerchman, S.E., Clemons, W.M., Ramakrishnan, V., and Frank, J. (1999). Location of translational initiation factor IF3 on the small ribosomal subunit. *Proc Natl Acad Sci USA* 96, 4301-4306.
- McQuillen, K., Roberts, R.B., and Britten, R.J. (1959). Synthesis of Nascent Protein by Ribosomes in *Escherichia Coli*. *Proc Natl Acad Sci U S A* 45, 1437-1447.
- Melnikov, S., Ben-Shem, A., Garreau de Loubresse, N., Jenner, L., Yusupova, G., and Yusupov, M. (2012). One core, two shells: bacterial and eukaryotic ribosomes. *Nat Struct Mol Biol* 19, 560-567.
- Milon, P., Konevega, A.L., Gualerzi, C.O., and Rodnina, M.V. (2008). Kinetic checkpoint at a late step in translation initiation. *Mol Cell* 30, 712-720.

- Milon, P., Maracci, C., Filonava, L., Gualerzi, C.O., and Rodnina, M.V. (2012). Real-time assembly landscape of bacterial 30S translation initiation complex. *Nat Struct Mol Biol* 19, 609-615.
- Milon, P., and Rodnina, M.V. (2012). Kinetic control of translation initiation in bacteria. *Crit Rev Biochem Mol Biol* 47, 334-348.
- Moazed, D., and Noller, H.F. (1989a). Interaction of tRNA with 23S rRNA in the ribosomal A, P, and E sites. *Cell* 57, 585-597.
- Moazed, D., and Noller, H.F. (1989b). Intermediate states in the movement of transfer RNA in the ribosome. *Nature* 342, 142-148.
- Mohr, D., Wintermeyer, W., and Rodnina, M.V. (2002). GTPase activation of elongation factors Tu and G on the ribosome. *Biochemistry* 41, 12520-12528.
- Mora, L., Heurgue-Hamard, V., Champ, S., Ehrenberg, M., Kisseelev, L.L., and Buckingham, R.H. (2003). The essential role of the invariant GGQ motif in the function and stability in vivo of bacterial release factors RF1 and RF2. *Mol Microbiol* 47, 267-275.
- Munro, J.B., Altman, R.B., O'Connor, N., and Blanchard, S.C. (2007). Identification of two distinct hybrid state intermediates on the ribosome. *Mol Cell* 25, 505-517.
- Munro, J.B., Wasserman, M.R., Altman, R.B., Wang, L., and Blanchard, S.C. (2010). Correlated conformational events in EF-G and the ribosome regulate translocation. *Nat Struct Mol Biol*.
- Myasnikov, A., Marzi, S., Simonetti, A., Giuliodori, A., Gualerzi, C., Yusupova, G., Yusupov, M., and Klaholz, B. (2005). Conformational transition of initiation factor 2 from the GTP- to GDP-bound state visualized on the ribosome. *Nat Struct Mol Biol* 12, 1145-1149.
- Nagel, R. (2002). DarT: The embryo test with the Zebrafish *Danio rerio*--a general model in ecotoxicology and toxicology. *ALTEX 19 Suppl 1*, 38-48.
- Nagle, J.F., and Morowitz, H.J. (1978). Molecular mechanisms for proton transport in membranes. *Proc Natl Acad Sci U S A* 75, 298-302.
- Nakano, H., Yoshida, T., Uchiyama, S., Kawachi, M., Matsuo, H., Kato, T., Ohshima, A., Yamaichi, Y., Honda, T., Kato, H., et al. (2003). Structure and binding mode of a ribosome recycling factor (RRF) from mesophilic bacterium. *J Biol Chem* 278, 3427-3436.
- Nechifor, R., Murataliev, M., and Wilson, K.S. (2007). Functional interactions between the G' subdomain of bacterial translation factor EF-G and ribosomal protein L7/L12. *J Biol Chem* 282, 36998-37005.
- Nierhaus, K.H. (1991). The assembly of prokaryotic ribosomes. *Biochimie* 73, 739-755.
- Nissen, P., Hansen, J., Ban, N., Moore, P.B., and Steitz, T.A. (2000). The structural basis of ribosome activity in peptide bond synthesis. *Science* 289, 920-930.
- Nissen, P., Ippolito, J.A., Ban, N., Moore, P.B., and Steitz, T.A. (2001). RNA tertiary interactions in the large ribosomal subunit: the A-minor motif. *Proc Natl Acad Sci USA* 98, 4899-4903.
- Nissen, P., Kjeldgaard, M., Thirup, S., Polekhina, G., Reshetnikova, L., Clark, B.F., and Nyborg, J. (1995). Crystal structure of the ternary complex of Phe-tRNAPhe, EF-Tu, and a GTP analog. *Science* 270, 1464-1472.
- Noller, H.F. (1991). Ribosomal RNA and Translation. *Annu Rev Biochem* 60, 191-227.
- Noller, H.F. (2012). Evolution of protein synthesis from an RNA world. *Cold Spring Harb Perspect Biol* 4, a003681.
- Noller, H.F., Lancaster, L., Zhou, J., and Mohan, S. (2017). The ribosome moves: RNA mechanics and translocation. *Nat Struct Mol Biol* 24, 1021-1027.

- O'Connor, M., Gregory, S.T., Rajbhandary, U.L., and Dahlberg, A.E. (2001). Altered discrimination of start codons and initiator tRNAs by mutant initiation factor 3. *Rna A Publication of the Rna Society* 7, 969-978.
- Ogle, J.M., Brodersen, D.E., Clemons Jr, W.M., Tarry, M.J., Carter, A.P., and Ramakrishnan, V. (2001). Recognition of cognate transfer RNA by the 30S ribosomal subunit. *Science* 292, 897-902.
- Ogle, J.M., Murphy, F.V., Tarry, M.J., and Ramakrishnan, V. (2002). Selection of tRNA by the ribosome requires a transition from an open to a closed form. *Cell* 111, 721-732.
- Ogle, J.M., and Ramakrishnan, V. (2005). Structural insights into translational fidelity. *Annu Rev Biochem* 74, 129-177.
- Otvos, L., Jr. (2002). The short proline-rich antibacterial peptide family. *Cell Mol Life Sci* 59, 1138-1150.
- Otvos, L., Jr., O, I., Rogers, M.E., Consolvo, P.J., Condie, B.A., Lovas, S., Bulet, P., and Blaszczyk-Thurin, M. (2000). Interaction between heat shock proteins and antimicrobial peptides. *Biochemistry* 39, 14150-14159.
- Pallesen, J., Hashem, Y., Korkmaz, G., Korpella, R.K., Huang, C., Ehrenberg, M., Sanyal, S., and Frank, J. (2013). Cryo-EM visualization of the ribosome in termination complex with apo-RF3 and RF1. *Elife* 2, e00411.
- Pavlov, M.Y., Freistroffer, D.V., Heurgue-Hamard, V., Buckingham, R.H., and Ehrenberg, M. (1997). Release factor RF3 abolishes competition between release factor RF1 and ribosome recycling factor (RRF) for a ribosome binding site. *J Mol Biol* 273, 389-401.
- Peschel, A., and Sahl, H.G. (2006). The co-evolution of host cationic antimicrobial peptides and microbial resistance. *Nat Rev Microbiol* 4, 529-536.
- Peske, F., Kuhlenkoetter, S., Rodnina, M.V., and Wintermeyer, W. (2014). Timing of GTP binding and hydrolysis by translation termination factor RF3. *Nucleic Acids Res* 42, 1812-1820.
- Peske, F., Rodnina, M., and Wintermeyer, W. (2005). Sequence of steps in ribosome recycling as defined by kinetic analysis. *Mol Cell* 18, 403-412.
- Pestka, S. (1968). Studies on the formation of tRNA-ribosome complexes. III. The formation of peptide bonds by ribosomes in the absence of supernatant enzymes. *J Biol Chem* 243, 2810-2820.
- Pestka, S. (1969). Studies on the formation of transfer ribonucleic acid-ribosome complexes. X. Phenylalanyl-oligonucleotide binding to ribosomes and the mechanism of chloramphenicol action. *Biochem Biophys Res Commun* 36, 589-595.
- Petry, S., Brodersen, D., Murphy, F.t., Dunham, C., Selmer, M., Tarry, M., Kelley, A., and Ramakrishnan, V. (2005). Crystal structures of the ribosome in complex with release factors RF1 and RF2 bound to a cognate stop codon. *Cell* 123, 1255-1266.
- Pierson, W.E., Hoffer, E.D., Keedy, H.E., Simms, C.L., Dunham, C.M., and Zaher, H.S. (2016). Uniformity of Peptide Release Is Maintained by Methylation of Release Factors. *Cell reports* 17, 11-18.
- Podda, E., Benincasa, M., Pacor, S., Micali, F., Mattiuzzo, M., Gennaro, R., and Scocchi, M. (2006). Dual mode of action of Bac7, a proline-rich antibacterial peptide. *Biochim Biophys Acta* 1760, 1732-1740.
- Polacek, N., and Mankin, A.S. (2005). The ribosomal peptidyl transferase center: structure, function, evolution, inhibition. *Crit Rev Biochem Mol Biol* 40, 285-311.

- Polikanov, Y.S., Steitz, T.A., and Innis, C.A. (2014). A proton wire to couple aminoacyl-tRNA accommodation and peptide-bond formation on the ribosome. *Nat Struct Mol Biol* 21, 787-793.
- Prabhakar, A., Capece, M.C., Petrov, A., Choi, J., and Puglisi, J.D. (2017). Post-termination Ribosome Intermediate Acts as the Gateway to Ribosome Recycling. *Cell Rep* 20, 161-172.
- Price, D.C., Chan, C.X., Yoon, H.S., Yang, E.C., Qiu, H., Weber, A.P., Schwacke, R., Gross, J., Blouin, N.A., Lane, C., et al. (2012). Cyanophora paradoxa genome elucidates origin of photosynthesis in algae and plants. *Science* 335, 843-847.
- Pulk, A., and Cate, J.H. (2013). Control of ribosomal subunit rotation by elongation factor G. *Science* 340, 1235970.
- Qin, H., Grigoriadou, C., and Cooperman, B.S. (2009). Interaction of IF2 with the ribosomal GTPase-associated center during 70S initiation complex formation. *Biochemistry* 48, 4699-4706.
- Ramrath, D.J., Lancaster, L., Sprink, T., Mielke, T., Loerke, J., Noller, H.F., and Spahn, C.M. (2013). Visualization of two transfer RNAs trapped in transit during elongation factor G-mediated translocation. *Proc Natl Acad Sci U S A* 110, 20964-20969.
- Ramrath, D.J., Yamamoto, H., Rother, K., Wittek, D., Pech, M., Mielke, T., Loerke, J., Scheerer, P., Ivanov, P., Teraoka, Y., et al. (2012). The complex of tmRNA-SmpB and EF-G on translocating ribosomes. *Nature* 485, 526-529.
- Ratje, A.H., Loerke, J., Mikolajka, A., Brunner, M., Hildebrand, P.W., Starosta, A.L., Donhofer, A., Connell, S.R., Fucini, P., Mielke, T., et al. (2010). Head swivel on the ribosome facilitates translocation by means of intra-subunit tRNA hybrid sites. *Nature* 468, 713-716.
- Reyes-Prieto, A., Weber, A.P., and Bhattacharya, D. (2007). The origin and establishment of the plastid in algae and plants. *Annu Rev Genet* 41, 147-168.
- Richter, C.V., Bals, T., and Schunemann, D. (2010). Component interactions, regulation and mechanisms of chloroplast signal recognition particle-dependent protein transport. *Eur J Cell Biol* 89, 965-973.
- Risuleo, G., Gualerzi, C., and Pon, C. (1976). Specificity and properties of the destabilization, induced by initiation factor IF-3, of ternary complexes of the 30S ribosomal subunit. *Eur J Biochem* 67, 603-613.
- RNAcentral (2017). RNAcentral: a comprehensive database of non-coding RNA sequences. *Nucleic Acids Res* 45, D128-D134.
- Roy, R.N., Lomakin, I.B., Gagnon, M.G., and Steitz, T.A. (2015). The mechanism of inhibition of protein synthesis by the proline-rich peptide oncocin. *Nat Struct Mol Biol* 22, 466-469.
- Ruf, M., and Koessel, H. (1988). Occurrence and spacing of ribosome recognition sites in mRNAs of chloroplasts from higher plants. *Febs Lett* 240, 41-44.
- Runti, G., Lopez Ruiz Mdel, C., Stoilova, T., Hussain, R., Jennions, M., Choudhury, H.G., Benincasa, M., Gennaro, R., Beis, K., and Scocchi, M. (2013). Functional characterization of SbmA, a bacterial inner membrane transporter required for importing the antimicrobial peptide Bac7(1-35). *J Bacteriol* 195, 5343-5351.
- Sagan, L. (1967). On the origin of mitosing cells. *J Theor Biol* 14, 255-274.
- Saikrishnan, K., Kalapala, S., Varshney, U., and Vijayan, M. (2005). X-ray structural studies of *Mycobacterium tuberculosis* RRF and a comparative study of RRFs of known structure. Molecular plasticity and biological implications. *J Mol Biol* 345, 29-38.

- Salsi, E., Farah, E., Dann, J., and Ermolenko, D.N. (2014). Following movement of domain IV of elongation factor G during ribosomal translocation. *Proc Natl Acad Sci U S A* **111**, 15060-15065.
- Salsi, E., Farah, E., Netter, Z., Dann, J., and Ermolenko, D.N. (2015). Movement of elongation factor G between compact and extended conformations. *J Mol Biol* **427**, 454-467.
- Samaha, R.R., Green, R., and Noller, H.F. (1995). A base pair between tRNA and 23S rRNA in the peptidyl transferase center of the ribosome. *Nature* **377**, 309-314.
- Sanbonmatsu, K.Y., Joseph, S., and Tung, C.S. (2005). Simulating movement of tRNA into the ribosome during decoding. *Proc Natl Acad Sci U S A* **102**, 15854-15859.
- Sato, N.S., Hirabayashi, N., Agmon, I., Yonath, A., and Suzuki, T. (2006). Comprehensive genetic selection revealed essential bases in the peptidyl-transferase center. *Proc Natl Acad Sci U S A* **103**, 15386-15391.
- Savelsbergh, A., Katunin, V.I., Mohr, D., Peske, F., Rodnina, M.V., and Wintermeyer, W. (2003). An elongation factor G-induced ribosome rearrangement precedes tRNA-mRNA translocation. *Mol Cell* **11**, 1517-1523.
- Savelsbergh, A., Mohr, D., Kothe, U., Wintermeyer, W., and Rodnina, M.V. (2005). Control of phosphate release from elongation factor G by ribosomal protein L7/12. *EMBO J* **24**, 4316-4323.
- Savelsbergh, A., Mohr, D., Wilden, B., Wintermeyer, W., and Rodnina, M.V. (2000). Stimulation of the GTPase activity of translation elongation factor G by ribosomal protein L7/12. *J Biol Chem* **275**, 890-894.
- Schlünzen, F., Zarivach, R., Harms, J., Bashan, A., Tocilj, A., Albrecht, R., Yonath, A., and Franceschi, F. (2001). Structural basis for the interaction of antibiotics with the peptidyl transferase centre in eubacteria. *Nature* **413**, 814-821.
- Schmeing, T.M., Huang, K.S., Kitchen, D.E., Strobel, S.A., and Steitz, T.A. (2005a). Structural insights into the roles of water and the 2' hydroxyl of the P site tRNA in the peptidyl transferase reaction. *Mol Cell* **20**, 437-448.
- Schmeing, T.M., Huang, K.S., Strobel, S.A., and Steitz, T.A. (2005b). An induced-fit mechanism to promote peptide bond formation and exclude hydrolysis of peptidyl-tRNA. *Nature* **438**, 520-524.
- Schmeing, T.M., Seila, A.C., Hansen, J.L., Freeborn, B., Soukup, J.K., Scaringe, S.A., Strobel, S.A., Moore, P.B., and Steitz, T.A. (2002). A pre-translocational intermediate in protein synthesis observed in crystals of enzymatically active 50S subunits. *Nat Struct Biol* **9**, 225-230.
- Schmeing, T.M., Voorhees, R.M., Kelley, A.C., and Ramakrishnan, V. (2011). How mutations in tRNA distant from the anticodon affect the fidelity of decoding. *Nat Struct Mol Biol* **18**, 432-436.
- Schmitz-Linneweber, C., Maier, R.M., Alcaraz, J.P., Cottet, A., Herrmann, R.G., and Mache, R. (2001). The plastid chromosome of spinach (*Spinacia oleracea*): complete nucleotide sequence and gene organization. *Plant Mol Biol* **45**, 307-315.
- Schnapp, D., Kemp, G.D., and Smith, V.J. (1996). Purification and characterization of a proline-rich antibacterial peptide, with sequence similarity to bactenecin-7, from the haemocytes of the shore crab, *Carcinus maenas*. *Eur J Biochem* **240**, 532-539.
- Schneider, M., and Dorn, A. (2001). Differential infectivity of two *Pseudomonas* species and the immune response in the milkweed bug, *Oncopeltus fasciatus* (Insecta: Hemiptera). *J Invertebr Pathol* **78**, 135-140.

- Scocchi, M., Lüthy, C., Decarli, P., Mignogna, G., Christen, P., and Gennaro, R. (2009). The Proline-rich Antibacterial Peptide Bac7 Binds to and Inhibits in vitro the Molecular Chaperone DnaK. *Int J Pept Res Ther* 15, 147-155.
- Scocchi, M., Tossi, A., and Gennaro, R. (2011). Proline-rich antimicrobial peptides: converging to a non-lytic mechanism of action. *Cell Mol Life Sci* 68, 2317-2330.
- Seefeldt, A.C., Graf, M., Perebaskine, N., Nguyen, F., Arenz, S., Mardirossian, M., Scocchi, M., Wilson, D.N., and Innis, C.A. (2016). Structure of the mammalian antimicrobial peptide Bac7(1-16) bound within the exit tunnel of a bacterial ribosome. *Nucleic Acids Res* 44, 2429-2438.
- Seefeldt, A.C., Nguyen, F., Antunes, S., Perebaskine, N., Graf, M., Arenz, S., Inampudi, K.K., Douat, C., Guichard, G., Wilson, D.N., et al. (2015). The proline-rich antimicrobial peptide Onc112 inhibits translation by blocking and destabilizing the initiation complex. *Nat Struct Mol Biol* 22, 470-475.
- Seit-Nebi, A., Frolova, L., Justesen, J., and Kisseelev, L. (2001). Class-1 translation termination factors: invariant GGQ minidomain is essential for release activity and ribosome binding but not for stop codon recognition. *Nucleic Acids Res* 29, 3982-3987.
- Selmer, M., Al-Karadaghi, S., Hirakawa, G., Kaji, A., and Liljas, A. (1999). Crystal structure of *Thermotoga maritima* ribosome recycling factor: A tRNA mimic. *Science* 286, 2349-2352.
- Selmer, M., Dunham, C., Murphy, F.t., Weixlbaumer, A., Petry, S., Kelley, A., Weir, J., and Ramakrishnan, V. (2006). Structure of the 70S ribosome complexed with mRNA and tRNA. *Science* 313, 1935-1942.
- Seong, B., and RajBhandary, U.L. (1987). *Escherichia coli* formylmethionine tRNA: mutations of GGG:CCC sequence conserved in anticodon stem of initiator tRNAs affect initiation of protein synthesis and conformation of anticodon loop. *Proc Natl Acad Sci USA* 84(2), 334-338.
- Sette, M., vanTilborg, P., Spurio, R., Kaptein, R., Paci, M., Gualerzi, C.O., and Boelens, R. (1997). The structure of the translational initiation factor IF1 from E-coli contains an oligomer-binding motif. *EMBO J* 16, 1436-1443.
- Shamova, O., Brogden, K.A., Zhao, C., Nguyen, T., Kokryakov, V.N., and Lehrer, R.I. (1999). Purification and properties of proline-rich antimicrobial peptides from sheep and goat leukocytes. *Infect Immun* 67, 4106-4111.
- Shao, S., Murray, J., Brown, A., Taunton, J., Ramakrishnan, V., and Hegde, R.S. (2016). Decoding Mammalian Ribosome-mRNA States by Translational GTPase Complexes. *Cell* 167, 1229-1240 e1215.
- Sharma, M.R., Donhofer, A., Barat, C., Marquez, V., Datta, P.P., Fucini, P., Wilson, D.N., and Agrawal, R.K. (2010). PSRP1 is not a ribosomal protein, but a ribosome-binding factor that is recycled by the ribosome-recycling factor (RRF) and elongation factor G (EF-G). *J Biol Chem* 285, 4006-4014.
- Sharma, M.R., Wilson, D.N., Datta, P.P., Barat, C., Schluenzen, F., Fucini, P., and Agrawal, R.K. (2007). Cryo-EM study of the spinach chloroplast ribosome reveals the structural and functional roles of plastid-specific ribosomal proteins. *Proc Natl Acad Sci U S A* 104, 19315-19320.
- Shaw, J.J., and Green, R. (2007). Two distinct components of release factor function uncovered by nucleophile partitioning analysis. *Mol Cell* 28, 458-467.
- Shine, J., and Dalgarno, L. (1974). The 3'-terminal sequence of *E. coli* 16S rRNA: Complementarity to nonsense triplets and ribosome binding sites. *Proc Natl Acad Sci USA* 71, 1342-1346.

- Simonetti, A., Marzi, S., Billas, I.M., Tsai, A., Fabbretti, A., Myasnikov, A.G., Roblin, P., Vaiana, A.C., Hazemann, I., Eiler, D., *et al.* (2013). Involvement of protein IF2 N domain in ribosomal subunit joining revealed from architecture and function of the full-length initiation factor. *Proc Natl Acad Sci U S A* **110**, 15656-15661.
- Simonetti, A., Marzi, S., Jenner, L., Myasnikov, A., Romby, P., Yusupova, G., Klaholz, B.P., and Yusupov, M. (2009). A structural view of translation initiation in bacteria. *Cell Mol Life Sci* **66**, 423-436.
- Simonetti, A., Marzi, S., Myasnikov, A.G., Fabbretti, A., Yusupov, M., Gualerzi, C.O., and Klaholz, B.P. (2008). Structure of the 30S translation initiation complex. *Nature* **455**, 416-420.
- Sohmen, D., Chiba, S., Shimokawa-Chiba, N., Innis, C.A., Berninghausen, O., Beckmann, R., Ito, K., and Wilson, D.N. (2015). Structure of the *Bacillus subtilis* 70S ribosome reveals the basis for species-specific stalling. *Nat Commun* **6**, 6941.
- Sohmen, D., Harms, J.M., Schlunzen, F., and Wilson, D.N. (2009). Enhanced SnapShot: Antibiotic inhibition of protein synthesis II. *Cell* **139**, 212-212 e211.
- Spiegel, P.C., Ermolenko, D.N., and Noller, H.F. (2007). Elongation factor G stabilizes the hybrid-state conformation of the 70S ribosome. *RNA* **13**, 1473-1482.
- Spirin, A.S. (1968). [On the mechanism of ribosome function. The hypothesis of locking-unlocking of subparticles]. *Dokl Akad Nauk SSSR* **179**, 1467-1470.
- Spirin, A.S. (2009). How does a scanning ribosomal particle move along the 5'-untranslated region of eukaryotic mRNA? Brownian Ratchet model. *Biochemistry* **48**, 10688-10692.
- Sprink, T., Ramrath, D.J., Yamamoto, H., Yamamoto, K., Loerke, J., Ismer, J., Hildebrand, P.W., Scheerer, P., Burger, J., Mielke, T., *et al.* (2016). Structures of ribosome-bound initiation factor 2 reveal the mechanism of subunit association. *Sci Adv* **2**, e1501502.
- Spurio, R., Brandi, L., Caserta, E., Pon, C.L., Gualerzi, C.O., Misselwitz, R., Krafft, C., Welfle, K., and Welfle, H. (2000). The C-terminal subdomain (IF2 C-2) contains the entire fMet-tRNA binding site of initiation factor IF2. *J Biol Chem* **275**, 2447-2454.
- Srivastava, A.K., and Schlessinger, D. (1990). Mechanism and regulation of bacterial ribosomal RNA processing. *Annu Rev Microbiol* **44**, 105-129.
- Stark, H., Rodnina, M.V., Rinkeappel, J., Brimacombe, R., Wintermeyer, W., and Vanheel, M. (1997). Visualization of Elongation Factor Tu On the *Escherichia Coli* Ribosome. *Nature* **389**, 403-406.
- Stark, H., Rodnina, M.V., Wieden, H.J., van Heel, M., and Wintermeyer, W. (2000). Large-scale movement of elongation factor G and extensive conformational change of the ribosome during translocation. *Cell* **100**, 301-309.
- Steitz, J.A., and Jakes, K. (1975). How ribosomes select initiator regions in mRNA: Base pair formation between the 3' terminus of 16S rRNA and the mRNA during initiation of protein synthesis in *E. coli*. *Proc Natl Acad Sci USA* **72**, 4734-4738.
- Stensvag, K., Haug, T., Sperstad, S.V., Rekdal, O., Indrevoll, B., and Styrvold, O.B. (2008). Arasin 1, a proline-arginine-rich antimicrobial peptide isolated from the spider crab, *Hyas araneus*. *Dev Comp Immunol* **32**, 275-285.
- Storici, P., and Zanetti, M. (1993). A cDNA derived from pig bone marrow cells predicts a sequence identical to the intestinal antibacterial peptide PR-39. *Biochem Biophys Res Commun* **196**, 1058-1065.

- Sugiura, M. (2014). Plastid mRNA translation. *Methods Mol Biol* 1132, 73-91.
- Sussman, J.K., Simons, E.L., and Simons, R.W. (1996). *Escherichia coli* translation initiation factor 3 discriminates the initiation codon *in vivo*. *Mol Microbiol* 21, 347-360.
- Svidritskiy, E., Ling, C., Ermolenko, D.N., and Korostelev, A.A. (2013). Blasticidin S inhibits translation by trapping deformed tRNA on the ribosome. *Proc Natl Acad Sci USA* 110, 12283-12288.
- Takahashi, S., Isobe, H., Ueda, T., and Okahata, Y. (2013). Direct monitoring of initiation factor dynamics through formation of 30S and 70S translation-initiation complexes on a quartz crystal microbalance. *Chemistry* 19, 6807-6816.
- Tate, W.P., and Brown, C.M. (1992). Translational termination: "stop" for protein synthesis or "pause" for regulation of gene expression. *Biochemistry* 31, 2443-2450.
- Thompson, J., Kim, D.F., O'Connor, M., Lieberman, K.R., Bayfield, M.A., Gregory, S.T., Green, R., Noller, H.F., and Dahlberg, A.E. (2001). Analysis of mutations at residues A2451 and G2447 of 23S rRNA in the peptidyltransferase active site of the 50S ribosomal subunit. *Proc Natl Acad Sci USA* 98, 9002-9007.
- Tiller, N., Weingartner, M., Thiele, W., Maximova, E., Schottler, M.A., and Bock, R. (2012). The plastid-specific ribosomal proteins of *Arabidopsis thaliana* can be divided into non-essential proteins and genuine ribosomal proteins. *Plant J* 69, 302-316.
- Tomsic, J., Vitali, L.A., Daviter, T., Savelbergh, A., Spurio, R., Striebeck, P., Wintermeyer, W., Rodnina, M.V., and Gualerzi, C.O. (2000). Late events of translation initiation in bacteria: a kinetic analysis. *EMBO J* 19, 2127-2136.
- Tourigny, D.S., Fernandez, I.S., Kelley, A.C., and Ramakrishnan, V. (2013). Elongation factor G bound to the ribosome in an intermediate state of translocation. *Science* 340, 1235490.
- Toyoda, T., Tin, O.F., Ito, K., Fujiwara, T., Kumasaka, T., Yamamoto, M., Garber, M.B., and Nakamura, Y. (2000). Crystal structure combined with genetic analysis of the *Thermus thermophilus* ribosome recycling factor shows that a flexible hinge may act as a functional switch. *RNA* 6, 1432-1444.
- Trobro, S., and Aqvist, J. (2005). Mechanism of peptide bond synthesis on the ribosome. *Proc Natl Acad Sci U S A* 102, 12395-12400.
- Trobro, S., and Aqvist, J. (2009). Mechanism of the translation termination reaction on the ribosome. *Biochemistry* 48, 11296-11303.
- Valle, M., Zavialov, A., Sengupta, J., Rawat, U., Ehrenberg, M., and Frank, J. (2003). Locking and unlocking of ribosomal motions. *Cell* 114, 123-134.
- Vila-Sanjurjo, A., Schuwirth, B.S., Hau, C.W., and Cate, J.H.D. (2004). Structural basis for the control of translational initiation during stress. *Nature Struct Mol Biol* 11, 1054-1059.
- Villa, E., Sengupta, J., Trabuco, L.G., LeBarron, J., Baxter, W.T., Shaikh, T.R., Grassucci, R.A., Nissen, P., Ehrenberg, M., Schulten, K., *et al.* (2009). Ribosome-induced changes in elongation factor Tu conformation control GTP hydrolysis. *Proc Natl Acad Sci U S A* 106, 1063-1068.
- Vlieghe, P., Lisowski, V., Martinez, J., and Khrestchatsky, M. (2010). Synthetic therapeutic peptides: science and market. *Drug Discov Today* 15, 40-56.
- Voorhees, R.M., Schmeing, T.M., Kelley, A.C., and Ramakrishnan, V. (2010). The mechanism for activation of GTP hydrolysis on the ribosome. *Science* 330, 835-838.

- Voorhees, R.M., Weixlbaumer, A., Loakes, D., Kelley, A.C., and Ramakrishnan, V. (2009). Insights into substrate stabilization from snapshots of the peptidyl transferase center of the intact 70S ribosome. *Nat Struct Mol Biol* 16, 528-533.
- Voss, N.R., Gerstein, M., Steitz, T.A., and Moore, P.B. (2006). The geometry of the ribosomal polypeptide exit tunnel. *J Mol Biol* 360, 893-906.
- Wahl, M., and Moller, W. (2002). Structure and function of the acidic ribosomal stalk proteins. *Curr Protein Pept Sci* 3, 93-106.
- Wang, Y., Qin, H., Kudaravalli, R.D., Kirillov, S.V., Dempsey, G.T., Pan, D., Cooperman, B.S., and Goldman, Y.E. (2007). Single-molecule structural dynamics of EF-G-ribosome interaction during translocation. *Biochemistry* 46, 10767-10775.
- Weigert, M.G., and Garen, A. (1965). Base composition of non-sense codons in *E.coli*. *Nature* 206, 992.
- Weixlbaumer, A., Jin, H., Neubauer, C., Voorhees, R., Petry, S., Kelley, A., and Ramakrishnan, V. (2008). Insights into translational termination from the structure of RF2 bound to the ribosome. *Science* 322, 953-956.
- Weixlbaumer, A., Petry, S., Dunham, C.M., Selmer, M., Kelley, A.C., and Ramakrishnan, V. (2007). Crystal structure of the ribosome recycling factor bound to the ribosome. *Nat Struct Mol Biol* 14, 733-737.
- Wilson, D.N. (2009). The A-Z of bacterial translation inhibitors. *Crit Rev Biochem Mol Biol* 44, 393-433.
- Wilson, D.N., and Nierhaus, K.H. (2005). Ribosomal Proteins in the Spotlight. *Crit Rev Biochem Mol Biol* 40, 243-267.
- Wilson, D.N., Schluenzen, F., Harms, J.M., Yoshida, T., Ohkubo, T., Albrecht, R., Buerger, J., Kobayashi, Y., and Fucini, P. (2005). X-ray crystallography study on ribosome recycling: the mechanism of binding and action of RRF on the 50S ribosomal subunit. *EMBO J* 24, 251-260.
- Wimberly, B.T., Brodersen, D.E., Clemons, W.M., Morgan-Warren, R.J., Carter, A.P., Vonrhein, C., Hartsch, T., and Ramakrishnan, V. (2000). Structure of the 30S ribosomal subunit. *Nature* 407, 327-339.
- Wintermeyer, W., Peske, F., Beringer, M., Gromadski, K.B., Savelsbergh, A., and Rodnina, M.V. (2004). Mechanisms of elongation on the ribosome: dynamics of a macromolecular machine. *Biochem Soc Trans* 32, 733-737.
- Wower, I., Wower, J., and Zimmermann, R. (1998). Ribosomal protein L27 participates in both 50 S subunit assembly and the peptidyl transferase reaction. *J Biol Chem* 273, 19847-19852.
- Xu, T., Lee, K., Gu, L., Kim, J.I., and Kang, H. (2013). Functional characterization of a plastid-specific ribosomal protein PSRP2 in *Arabidopsis thaliana* under abiotic stress conditions. *Plant Physiol Biochem* 73, 405-411.
- Yamaguchi, K., and Subramanian, A.R. (2000). The plastid ribosomal proteins. Identification of all the proteins in the 50 S subunit of an organelle ribosome (chloroplast). *J Biol Chem* 275, 28466-28482.
- Yamaguchi, K., and Subramanian, A.R. (2003). Proteomic identification of all plastid-specific ribosomal proteins in higher plant chloroplast 30S ribosomal subunit. *Eur J Biochem* 270, 190-205.
- Yamaguchi, K., von Knoblauch, K., and Subramanian, A.R. (2000). The plastid ribosomal proteins. Identification of all the proteins in the 30 S subunit of an organelle ribosome (chloroplast). *J Biol Chem* 275, 28455-28465.
- Yeaman, M.R., and Yount, N.Y. (2003). Mechanisms of antimicrobial peptide action and resistance. *Pharmacol Rev* 55, 27-55.

- Yokoyama, T., Shaikh, T.R., Iwakura, N., Kaji, H., Kaji, A., and Agrawal, R.K. (2012). Structural insights into initial and intermediate steps of the ribosome-recycling process. *EMBO J* 31, 1836-1846.
- Yoshida, T., Uchiyama, S., Nakano, H., Kashimori, H., Kijima, H., Ohshima, T., Saihara, Y., Ishino, T., Shimahara, H., Yokose, K., *et al.* (2001). Solution structure of the ribosome recycling factor from *Aquifex aeolicus*. *Biochemistry* 40, 2387-2396.
- Youngman, E.M., McDonald, M.E., and Green, R. (2008). Peptide release on the ribosome: mechanism and implications for translational control. *Annu Rev Microbiol* 62, 353-373.
- Yusupova, G.Z., Yusupov, M.M., Cate, J.H., and Noller, H.F. (2001). The path of messenger RNA through the ribosome. *Cell* 106, 233-241.
- Zaher, H.S., Shaw, J.J., Strobel, S.A., and Green, R. (2011). The 2'-OH group of the peptidyl-tRNA stabilizes an active conformation of the ribosomal PTC. *EMBO J* 30, 2445-2453.
- Zahn, M., Berthold, N., Kieslich, B., Knappe, D., Hoffmann, R., and Strater, N. (2013). Structural studies on the forward and reverse binding modes of peptides to the chaperone DnaK. *J Mol Biol* 425, 2463-2479.
- Zahn, M., Kieslich, B., Berthold, N., Knappe, D., Hoffmann, R., and Strater, N. (2014). Structural identification of DnaK binding sites within bovine and sheep bactenecin Bac7. *Protein Pept Lett* 21, 407-412.
- Zanetti, M., Del Sal, G., Storici, P., Schneider, C., and Romeo, D. (1993). The cDNA of the neutrophil antibiotic Bac5 predicts a pro-sequence homologous to a cysteine proteininase inhibitor that is common to other neutrophil antibiotics. *J Biol Chem* 268, 522-526.
- Zanetti, M., Litteri, L., Gennaro, R., Horstmann, H., and Romeo, D. (1990). Bactenecins, defense polypeptides of bovine neutrophils, are generated from precursor molecules stored in the large granules. *J Cell Biol* 111, 1363-1371.
- Zanetti, M., Litteri, L., Griffiths, G., Gennaro, R., and Romeo, D. (1991). Stimulus-induced maturation of probactenecins, precursors of neutrophil antimicrobial polypeptides. *J Immunol* 146, 4295-4300.
- Zasloff, M. (2002). Antimicrobial peptides in health and disease. *N Engl J Med* 347, 1199-1200.
- Zavialov, A.V., Buckingham, R.H., and Ehrenberg, M. (2001). A posttermination ribosomal complex is the guanine nucleotide exchange factor for peptide release factor RF3. *Cell* 107, 115-124.
- Zavialov, A.V., Hauryliuk, V.V., and Ehrenberg, M. (2005). Splitting of the posttermination ribosome into subunits by the concerted action of RRF and EF-G. *Mol Cell* 18, 675-686.
- Zavialov, A.V., Mora, L., Buckingham, R.H., and Ehrenberg, M. (2002). Release of peptide promoted by the GGQ motif of class 1 release factors regulates the GTPase activity of RF3. *Mol Cell* 10, 789-798.
- Zeng, F., and Jin, H. (2018). Conformation of methylated GGQ in the Peptidyl Transferase Center during Translation Termination. *Sci Rep* 8, 2349.
- Zerges, W. (2000). Translation in chloroplasts. *Biochimie* 82, 583-601.
- Zhou, J., Korostelev, A., Lancaster, L., and Noller, H.F. (2012a). Crystal structures of 70S ribosomes bound to release factors RF1, RF2 and RF3. *Curr Opin Struct Biol* 22, 733-742.
- Zhou, J., Lancaster, L., Donohue, J.P., and Noller, H.F. (2013). Crystal structures of EF-G-ribosome complexes trapped in intermediate states of translocation. *Science* 340, 1236086.

- Zhou, J., Lancaster, L., Donohue, J.P., and Noller, H.F. (2014). How the ribosome hands the A-site tRNA to the P site during EF-G-catalyzed translocation. *Science* 345, 1188-1191.
- Zhou, J., Lancaster, L., Trakhanov, S., and Noller, H.F. (2012b). Crystal structure of release factor RF3 trapped in the GTP state on a rotated conformation of the ribosome. *RNA* 18, 230-240.

6 Publications

2018

1. **Graf, M.**, Huter, P., Maracci, C., Peterek, M., Rodnina, M.V. and Wilson, D.N. (2018). Visualization of translation termination intermediates during RF3-mediated recycling of RF1. *Nature Communications*. (accepted)

2017

2. Florin, T.*, Maracci, C.*., **Graf, M.***, Karki, P., Klepacki, D., Berninghausen, O., Beckmann, R., Vazquez-Laslop, N., Wilson, D.N., Rodnina, M.V., Mankin, A.S. (2017). An antimicrobial peptide that inhibits translation by trapping release factors on the ribosome. *Nature Structural & Molecular Biology*. 24, 752-757.
3. **Graf, M.***, Mardirossian, M.*., Nguyen, F., Seefeldt*, A.C., Guichard, G., Scocchi, M., Innis, C.A., and Wilson, D.N. (2017b). Proline-rich antimicrobial peptides targeting protein synthesis. *Natural Product Reports*. 34, 702-711.
4. **Graf, M.**, Arenz, S., Huter, P., Donhofer, A., Novacek, J., and Wilson, D.N. (2017a). Cryo-EM structure of the spinach chloroplast ribosome reveals the location of plastid-specific ribosomal proteins and extensions. *Nucleic Acids Research*. 45, 2887-2896.

2016

5. Seefeldt, A.C.*., **Graf, M.***, Perebaskine, N., Nguyen, F., Arenz, S., Mardirossian, M., Scocchi, M., Wilson, D.N., and Innis, C.A. (2016). Structure of the mammalian antimicrobial peptide Bac7(1-16) bound within the exit tunnel of a bacterial ribosome. *Nucleic Acids Research*. 44, 2429-2438.

2015

6. Seefeldt, A.C.*, Nguyen, F.*, Antunes, S.*, Perebaskine, N., Graf, M., Arenz, S., Inampudi, K.K., Douat, C., Guichard, G., Wilson, D.N., et al. (2015). The proline-rich antimicrobial peptide Onc112 inhibits translation by blocking and destabilizing the initiation complex. *Nature Structural & Molecular Biology*. 22, 470-475.

*These authors contributed equally to this work.

Visualization of translation termination intermediates during RF3-mediated recycling of RF1

Michael Graf¹, Paul Huter¹, Cristina Maracci², Miroslav Peterek³, Marina V. Rodnina², Daniel N. Wilson^{1,4*}

¹ Institute for Biochemistry and Molecular Biology, University of Hamburg, Martin-Luther-King-Platz 6, 20146 Hamburg, Germany

² Department of Physical Biochemistry, Max Planck Institute for Biophysical Chemistry, Göttingen, Germany.

³ Central European Institute of Technology (CEITEC), Masaryk University, Kamenice 5, 62500 Brno, Czech Republic.

⁴ Lead Contact

*Correspondence to: daniel.wilson@chemie.uni-hamburg.de

ABSTRACT

During translation termination in prokaryotes, the decoding release factors RF1 and RF2 are recycled from the ribosome by the translational GTPase RF3. While high-resolution structures of the individual termination factors on the ribosome exist, direct structural insight into how RF3 mediates dissociation of the decoding release factors has been lacking. Here we present an ensemble of cryo-electron microscopy structures of translation termination complexes simultaneously bound with both RF1 and RF3. Binding of RF3 to the ribosome induces small subunit (SSU) rotation and swivelling of the head, yielding intermediate states with shifted P-site tRNAs and RF1 conformations. RF3 does not directly eject RF1 from the ribosome, but rather induces full rotation of the SSU that indirectly dislodges RF1 from its binding site. SSU rotation is also coupled to the accommodation of the GTPase domain of RF3 on the large subunit (LSU), thereby promoting GTP hydrolysis and dissociation of RF3 from the ribosome.

The termination phase of translation is signalled by the appearance of a stop codon of the mRNA within the A-site of the ribosome. In bacteria, stop codons are recognized by the decoding release factors RF1 and RF2, which facilitate release of the nascent polypeptide chain attached to the P-site tRNA¹⁻⁴. RF1 and RF2 display distinct but overlapping stop codon specificities, such that RF1 decodes UAG and UAA and RF2 decodes UGA and UAA. Both RF1 and RF2 contain a universally conserved GGQ motif that is critical for peptide release⁵⁻⁹. Structures of RF1 and RF2 in complex with termination state ribosomes have revealed how conserved residues within the superdomain 2/4 specifically recognize the stop codon on the small subunit (SSU)¹⁰⁻¹⁴. On the large subunit (LSU), the conserved GGQ motif within domain 3 is located at the peptidyltransferase center (PTC) and facilitates peptidyl-tRNA hydrolysis¹⁰⁻¹⁴. Following peptidyl-tRNA hydrolysis, the decoding RFs dissociate from the ribosome in a process that is stimulated by the action of a third release factor, the translational GTPase RF3^{15,16}.

Crystal structures of RF3 confirm structural similarity to other translational GTPases such as EF-Tu^{17,18}. Like EF-Tu, RF3 binds to the ribosome with high affinity in the GTP form¹⁹⁻²³. GTP hydrolysis is not required for the decoding factors to dissociate from the ribosome^{21,22}, but rather facilitates dissociation of RF3 from the ribosome^{22,23}. RF3-GTP binds to ribosomes irrespective of the presence or absence of the decoding release factors, and also interacts with both pre- and post-hydrolysis complexes²¹⁻²³. Biophysical studies indicate that binding of RF3 in the GTP form promotes the conversion of non-rotated RF1- or RF2-bound ribosomes into a rotated state^{22,24,25}. Recently, an antimicrobial peptide that binds to the post-hydrolysis ribosome and prevents RF1 dissociation has been reported (**Fig. 1a**)^{22,26}. This peptide, named apidaecin137 (API), prevents RF1 dissociation even in the presence of RF3²².

Cryo-EM and X-ray structures exist of RF3-GDP(C/N)P (non-hydrolysable GTP analogues) bound to rotated ribosomes with P/E-hybrid state tRNAs but without the decoding release factors (**Fig. 1b**)^{17,27-29}. Although the RF3 binding site overlaps with that of other translational GTPases, such as EF-Tu and EF-G, the G-domain of RF3 adopts a distinct orientation on the ribosome^{28,29}. Superimposition of the RF3 and RF1/RF2 ribosome structures revealed no overlap in the factor binding sites, suggesting that RF3 indirectly promotes RF1/RF2 dissociation via inducing ribosomal subunit rotation^{14,17,28-30}. A low-resolution (9.7 Å) cryo-EM structure of RF1 and apo-RF3 (no nucleotide form) bound to a non-rotated ribosome has been determined³⁰, however, the physiological relevance of this complex remains unclear^{21,23}. By contrast, structures of decoding factors on termination state ribosomes in the presence of the active GTP-like form of RF3 have so been lacking.

Here we present an ensemble of structures of ribosomes with tRNA, RF1 and RF3 bound simultaneously. The structures reveal that binding of RF3-GDPCP to the complex induces rotation

of the SSU relative to the LSU. RF3 does not interact with RF1 in any of the structures, but rather mediates dissociation of RF1 indirectly by inducing SSU rotation. SSU rotation also facilitates accommodation of RF3 on the LSU, where the G domain interacts with the sarcin-ricin loop (SRL), which is necessary to stimulate GTP hydrolysis. Thus, RF3-mediated subunit rotation plays a dual role during termination, namely, to dislodge the decoding release factors from the ribosome, but also to facilitate dissociation of RF3 itself.

RESULTS

Cryo-EM structures of termination complexes bearing RF1 and RF3

In order to visualize both RF1 and RF3 simultaneously on the ribosome, we initially assembled a termination complex *in vitro* with RF1-GAQ mutant decoding a UAA stop codon in the A-site. This ribosome-tRNA-RF1 complex was then briefly incubated with RF3-GDPCP before being applied to cryo-grids and plunge-frozen. A low-resolution cryo-EM analysis revealed that the termination complex could be sorted into 8 classes, the majority of which contained either non-rotated ribosomes with RF1 but no RF3 or rotated ribosomes bearing RF3 but no RF1 (**Supplementary Fig. 1a**). The single class that appeared to contain both RF1 and RF3 had strong density for RF3 but poor density for RF1. Binding of RF1 and RF3 to the ribosome thus appeared to be nearly mutually exclusive, suggesting that RF3-GDPCP could recycle RF1-GAQ from the termination complex ribosomes, which is consistent with previous biochemical reports^{22,24,25}. To increase the proportion of termination complexes containing both RF1 and RF3 bound simultaneously, we repeated the experiment in the presence of API, which was previously shown to prevent RF1 dissociation even in the presence of RF3-GTP²⁶. Because API binds to the exit tunnel and replaces the nascent peptide, by addition of API we selectively stabilized those complexes where the nascent peptide was released despite the use of the RF1 mutant that is slow in catalysing hydrolysis of peptidyl-tRNA^{7,9}. Using this complex, cryo-EM data was collected on a Titan Krios transmission electron microscope (TEM) with a Falcon II direct electron detector (DED) and processed with RELION 2.1³¹. A total of 525,595 ribosomal particles were sorted into eight distinct ribosomal subpopulations (**Supplementary Fig. 1b**). The four major subpopulations, states I-IV (15.2-22.4%; 79,975-117,725 particles), all contained P-site tRNA, RF1 and RF3 but were conformational distinct from one another (**Fig. 1c-f**). States I-IV were refined to average resolutions of 3.8 Å (State I, II) and 3.9 Å (State III and IV) (**Supplementary Fig. 1c-g** and **Table 1**). Additionally, four minor subpopulations were present in the dataset, resulting in two additional low-resolution 70S-RF1-RF3 populations (see **Methods**), vacant 50S subunits (10.3%, 53,850 particles) and RF3 bound to rotated vacant 70S ribosomes (5.8%, 30,535 particles) (**Supplementary Fig. 1b**). Since the latter subpopulation did not contain a P/E-tRNA, we believe it represents a state where RF3-GDPCP bound directly to vacant 70S ribosomes, rather than to the ribosome-RF1-GAQ complexes. Local resolution calculations of the RF3-70S complex revealed that while the core of the ribosomal subunits reaches 4.0 Å (**Supplementary Fig. 2a,b**), there is high conformational flexibility in this state. This is particularly evident in the rotation of SSU relative to the LSU and swivelling of the SSU head, but also in the positioning of the L1 stalk and RF3 itself (**Supplementary Fig. 2a,b**). By contrast, states I-IV are more conformationally homogeneous, with local resolutions reaching 3.5 Å within the core of both ribosomal subunits. Flexibility is

predominantly observed at the periphery of the ribosome, namely, for the L1, L11 and L7/L12 stalks where local resolutions exceeded 7.5 Å (**Supplementary Fig. 2a,b**). Local resolution calculations also indicated some conformational flexibility within the ribosome-bound ligands (**Supplementary Fig. 2c**). The resolution of the P-site tRNA and RF1 was highest (3.5-4.0 Å) for the regions that interact with the SSU and LSU, whereas the linking regions were significantly worse (>7.5 Å), such as the elbow of the tRNA, RF1 domain I and the linker between domains II and III of RF1 (**Supplementary Fig. 2c**). In states I-IV, the local resolution of the ligands was significantly better than that observed in the RF3-70S complex (**Supplementary Fig. 2c**). Molecular models of states I-IV and the RF3-70S complex were initially generated using rigid-body and domain-wise fitting of the ribosomal subunits, tRNA, RF1 and RF3 crystal structures to the cryo-EM map density, before manual adjustment, refinement and validation (**Supplementary Fig. 2d**; see **Methods**; **Table 1**). All states contained API bound within the ribosomal exit tunnel, where the interaction between Arg17 of API and the Gln235 (Q235 of the GGQ motif) of RF1 (**Supplementary Fig. 3a-e**) traps RF1 on the ribosome as reported previously²⁶.

Binding of RF3 induces ribosomal subunit rotation and head swivel

The major global movements distinguishing states I-IV and the RF3-70S complex are the rotation of the SSU relative to the LSU as well as swivelling of the SSU head relative to the body (**Fig. 2a-e** and **Supplementary Video 1**). The previously reported X-ray crystallography structures of RF3-70S complexes^{28,29} revealed SSU rotation of ~10° (clockwise when viewed from the intersubunit interface) compared to a classical (non-rotated) ribosome, such as the RF1-API-70S complex²⁶ (**Supplementary Table 1**). We also observed a similar degree of subunit rotation in the RF3-70S complex (**Fig. 2a**), whereas states I, II, III and IV displayed a range of intermediate levels of rotation, namely, 0.8°, 1.8°, 5.5° and 9.6°, respectively (**Fig. 2b-e** and **Supplementary Video 1**). In the X-ray crystallography structures of the RF3-70S complexes, the degree of head swivel differed dramatically from one another and was suggested to be dependent on the presence or absence of the hybrid P/E-site tRNA^{28,29}. In the absence of the P/E-site tRNA, the head was swivelled ~14° compared to the body²⁹, whereas only ~3-4° head swivelling was observed when the P/E-site tRNA was present²⁸ (**Supplementary Table 1** and **Supplementary Video 2**). In our RF3-70S complex lacking a tRNA (**Supplementary Fig. 2**), we observed an intermediate level (~6°) of head swivel (**Fig. 2a**, **Supplementary Table 1** and **Supplementary Video 2**). However, as noted above, the head is highly dynamic in our RF3-70S complex (**Supplementary Fig. 2a,b**) and thus the value reflects an average of multiple different swivel conformations of the head. This supports the suggestion that the large degree of head swivel observed in one of the X-ray crystallography structure of the RF3-70S complex

is indeed due to the absence of the P/E-site tRNA²⁹. Consistently, in states I-IV that contain P- or P/E-site tRNAs, the maximum head swivel observed was $\sim 3.6^\circ$ (**Fig. 2b-e** and **Supplementary Table 1**). Moreover, the degree of head swivel appeared to be loosely correlated to that of subunit rotation, as the degree of swivelling also increased from state I to IV, namely, 1.1° to 3.6° , respectively (**Fig. 2b-e**). The degree of rotation ($\sim 10^\circ$) and head swivel ($\sim 4-6^\circ$) observed here in state IV and RF3-70S complex is similar to that observed previously for translation elongation states with hybrid A/P- and P/E-site tRNAs (Table S1)³²⁻³⁷.

Subunit rotation leads to P-site tRNAs with remodelled P-loop interactions

The SSU rotation and head swivel observed in states I-IV is also accompanied by a corresponding shift of the P-site tRNA (**Fig. 3a** and **Supplementary Video 1**). Compared to the classical P-site tRNA in the RF1-API-70S complex in the absence of RF3, the tRNA is rotated towards the E-site by $\sim 13^\circ$ in state I-III and by $\sim 38^\circ$ in state IV (**Fig. 3a**). For state IV, this generates a hybrid P/E-tRNA where the CCA-end of the tRNA interacts with the E-site on the LSU, as observed for hybrid P/E-site tRNA during translation elongation³²⁻³⁷. By contrast, the intermediate P-site tRNA positions observed in states I-III still have the CCA-end located at the peptidyl-transferase center (PTC) of the LSU. A classical P-site tRNA is positioned at the PTC via base-pairing of the C74 and C75 of the CCA-end of the P-site tRNA with nucleotides G2252 and G2251, respectively, of the P-loop (helix H80) of the 23S rRNA (**Fig. 3b**). By contrast, the rotation of the P-site tRNA observed in states I-III results in a shift of the CCA-end of the P-site tRNA out of the PTC by $\sim 9 \text{ \AA}$ (**Fig. 3c,d**). Surprisingly, we observed re-base-pairing of the CCA-end of the P-site tRNA intermediate with the P-loop nucleotides, such that C74 and C75 were base-paired with G2253 and G2252, respectively. In addition, A73 of the P-site tRNA appeared to flip to establish a non-canonical wobble base-pair with C2254 (**Fig. 3c,d**). In contrast to the canonical P-site tRNA where the electron density was clearly resolved for the complete CCA-end, no density was visible for the terminal A76 of the P-site tRNA intermediate in states I-III, therefore assignment of the acylation state of the P_{int}-tRNA was not possible (**Supplementary Fig. 3f-h**). We do not believe that the CCA-end of the P_{int}-tRNA is shifted by two nucleotides, such that A76, C74 and C75 base-pair with G2252, G2253 and C2254, respectively, because the density does not support a purine-purine (A76-G2252) interaction in the first position, nor a pyrimidine-pyrimidine (C74-C2254) interaction at the third position (**Supplementary Fig. 3i**). Moreover, the density for A73 observed in the P/P-tRNA is not observed in the P_{int}-tRNA (**Supplementary Fig. 3j-l**), which would be expected if C74 interacts with C2254 and prevents A73 from establishing this interaction. Regardless of one or two nucleotide shift, to our

knowledge, such re-base-pairing of the CCA-end of a P-site tRNA with the P-loop has not been observed previously.

Subunit rotation is concomitant with RF3 accommodation on the large subunit

In the RF3-70S complex and states I-IV, RF3 is observed to rotate as a rigid body together with the SSU (**Fig. 4a** and **Supplementary Video 1**). The overall conformation of RF3 is the same as observed in the previous RF3-70S complexes^{28,29}, differing from the free RF3 form by the shift of domains 2 and 3 relative to domains 1^{17,18,28,29}. Because of the coordinated movement of RF3 with the SSU, the interactions between domain 2 and 3 of RF3 with ribosomal protein S12 and helices h5 and h15 of the 16S rRNA, as described previously^{28,29}, are maintained in all states. Relative to the LSU, however, RF3 moves by up to 10-11 Å when comparing states I to IV, bringing the G-domain of RF3 in state IV into closer proximity of the sarcin-ricin loop (SRL, H95 of the 23S rRNA) (**Fig. 4b** and **Supplementary Fig. 4a**). Because the SRL is critical for stimulating the GTPase activity of translation factors³⁸, this suggests that the SSU rotation is necessary for efficient activation of the GTPase activity of RF3. Evidence for progressive accommodation of translational GTPases on the LSU, as well as GTPase activation by the SRL, has been observed for other translational GTPases, such as eEF1A³⁹, SelB³² and EF-Tu⁴⁰ (**Supplementary Fig. 4b**). However, in these latter cases, the translational GTPases bind to non-rotated ribosomes and accommodation of the GTPase appears to be mediated by SSU domain closure^{32,39-41}, rather than by rotation as observed here for RF3. Despite the sequence and structural conservation of the G-domain of RF3 with other translation GTPases, the G-domain of RF3 adopts a distinct orientation on the ribosome^{28,29}. With respect to the SRL, the G-domain of RF3 is rotated by 24-31° when compared with other translational GTPases, such as IF2, EF-Tu and EF-G (**Supplementary Fig. 4c-f**). Within the limits of the resolution, the switch II loop conformation of the G-domain of RF3 in states I-IV is consistent with that observed in previous structures of RF3^{17,18,28,29}, where it interacts with the γ -phosphate of the GDPCP (**Fig. 4c**). While the switch I loop is poorly ordered in states II-IV, we observed a well-defined conformation in state I, where it interacts with ribosomal proteins L14 and L19, but not with the SRL (**Fig. 4c**). The switch I loop is disordered in many previous structures of RF3^{17,18,28}, although ordered conformations were previously reported in the *E. coli* RF3-70S structure²⁹ as well as the *Desulfovibrio vulgaris* RF3 in complex with the alarmone ppGpp¹⁸. However, they are significantly different from that observed here in state I (**Supplementary Fig. 5a-f**). The interaction of the switch I loop conformation of RF3 with L14 and L19 is the only direct contact that RF3 establishes with the LSU in state I, and thus may be important for facilitating accommodation of RF3 on the ribosome.

A dual role for L7/L12 during translation termination

The GTPase activity of translational GTPases, such as EF-Tu and EF-G^{42,43} as well as RF3⁴⁴, is stimulated by the ribosomal L7/L12 stalk, a pentameric complex consisting of four copies of L7/L12 tethered to the ribosomal protein L10. In states I-IV, we observe an additional density that we attribute to the C-terminal domain (CTD) of one copy of L7/L12 interacting with the G' domain of RF3 (Fig. 5a,b), as observed in previous RF3-70S cryo-EM structures^{17,30}, and consistent with NMR⁴⁵ and mutagenesis studies⁴⁴. L7/L12 was shown to stimulate Pi release from EF-G following hydrolysis of GTP to GDP and Pi, enabling the low affinity GDP conformation of EF-G to be adopted and thereby facilitating the dissociation of EF-G from the ribosome⁴⁶. However, L7/L12 has also been implicated in promoting binding of translational GTPases, such as EF-G and EF-Tu, to the ribosome^{43,47}. Surprisingly, in state III, an extra density is observed that we attributed to a second CTD of L7/L12, which bridges domain I of RF1 with the ribosomal protein L11 (Fig. 5b). This extra density can also be seen in the cryo-EM map of the previously reported RF1-API-70S complex (Supplementary Fig. 5g,h)²⁶, but cannot be seen in states I-II and IV due to the delocalized RF1 domain I. In state III, domain I of RF1 is better resolved, compared to states I and II, due to head swivelling on the SSU and closure of the L11 stalk base of the LSU (Fig. 5b). By contrast, transition from state III to IV involves additional head swivelling and opening of the L11 stalk base, which leads to loss of interaction and destabilization of domain I of RF1 (Fig. 5c). Thus, our observations suggest that in addition to stimulating the GTPase activity of RF3, L7/L12 may also be involved in facilitating the binding of the termination decoding factors to the ribosome. To test this hypothesis we prepared ribosome termination complexes using L7/L12-depleted (Δ L7/L12) ribosomes⁴² and determined the apparent affinity of RF1 by peptide hydrolysis (Fig. 5d, see Methods). The Δ L7/L12 ribosomes showed a markedly decreased affinity for RF1, compared to wildtype (wt) ribosomes bearing L7/L12 (Fig. 5d). We further confirmed this result by measuring the kinetics of RF1 binding via fluorescence resonance energy transfer from a dye-labeled fMet-tRNA^{fMet} and a quencher-labeled RF1-GAQ (RF1-GAQ_{Qsy9}) (Fig. 5e)²⁶. Binding of RF1-GAQ to the Δ L7/L12 ribosomes was 150-fold slower than to wt ribosomes, indicating that the contribution of L7/L12 to RF1 recruitment is large.

Subunit rotation leads to destabilization of RF1 on the ribosome

Unlike the previous low-resolution (9.7 Å) cryo-EM structure of apo-RF3-RF1-70S complex where contact was reported between RF1 and RF3³⁰, we do not observe interaction between RF1 and RF3 in any of the structures determined here. The closest distance between the two factors is seen in state III where domain I of RF1 becomes ordered such that α -helix 2 of domain 1 of RF1 comes within 9 Å of RF3 domain 3 (Fig. 5b). Thus, we conclude that RF3 does not use a direct steric overlap in

binding site to dissociate RF1 from the ribosome. Instead, our results suggest that RF3 dislodges RF1 from its binding site, indirectly, by inducing SSU rotation, as postulated previously^{17,28,29}. The density for RF1 remains well-resolved through-out states I-III, indicating that RF1 is stably bound to the ribosome despite the increase in rotation (0.8-5.5°) of the SSU (**Fig. 6a**). By contrast, the density for RF1 is poorly resolved in state IV, indicating that RF1 becomes destabilized from its binding site on the ribosome (**Fig. 6a,b**). Increased flexibility of RF1 in state IV is also supported by local resolution calculations (**Supplementary Fig. 2c**). Transition from state III to IV involves further clockwise rotation of the SSU (from 5.5° to 9.6°), which results in a shift of domain 2/4 of RF1 by 4 Å compared to state III (**Fig. 6a,c**). Because domain 3 of RF1 remains static at the PTC of the LSU, the movement can be described by a rotation of 6° that is accommodated by the long flexible linkers connecting domain 2/4 with domain 3 of RF1 (**Fig. 6c**). We believe that it was possible to capture the RF1 conformation in state IV only because the complex was formed in the presence of API, which prevented the complete dissociation of RF1 from the rotated ribosome. We note that transition from state III to IV also encompasses additional head swivel (from 1.6° to 3.6°) as well as opening of the stalk base (**Fig. 5c**), both of which destabilize domain 1 of RF1 and may facilitate dissociation of RF1 from the ribosome. Additionally, the formation of a hybrid P/E-tRNA due to the fully rotated SSU in state IV also leads to loss of interaction of RF1 with the P/P-tRNA, which may also contribute to destabilization of RF1 binding. Specifically, the interactions between Glu155 and His156 in domain 2/4 and Arg256 in domain 3 of RF1 with the ASL and CCA-end of a P/P-tRNA, respectively, are lost upon P/E-tRNA in state IV (**Fig. 6d,e**).

CONCLUSION

Based on our ensemble of termination intermediates (states I-IV), as well as the available literature, we present a model for RF3-mediated dissociation of RF1 during translation termination (**Fig. 7a-e**). A stop codon in the A site is recognized by the decoding factors RF1 (or RF2), which catalyse hydrolysis of the peptidyl-tRNA (**Fig. 7a**). The observed interaction between the CTD of one copy of L7/L12 and domain 1 of RF1 in the RF1-API-70S complex (**Fig. 7a**), as well as the RF1-API-RF3-70S complex (state I), is supported by our experimental findings (**Fig. 5d,e**) showing that L7/L12 plays an important role in delivery of RF1 to the ribosome, as reported previously for EF-Tu and EF-G^{42,43}. To date, all reported structures of decoding factors RF1 (and RF2) were bound to ribosomes with non-rotated conformations¹⁴, including the apo-RF3-RF1-70S complex³⁰. By contrast, we observe that binding of RF3 to the ribosome in states I-IV that contain RF1 induces rotation of the SSU relative to the LSU (**Fig. 7b-e**). While we have ordered states I-IV based on the degree of subunit rotation, we acknowledge that the exact biological sequence of states cannot be ascertained from our

study. Nevertheless, we believe that this order produces a logical sequence of events that provide a working model for decoding factor recycling by RF3. In state I, we observe that even a small degree (0.8°) of subunit rotation induced by RF3 results in a shifted position of the P-site tRNA, such that it partially rotates out of the PTC in the direction of the E-site (**Fig. 7b**). The resulting intermediate P-site tRNA (P_{int} -tRNA) displays unusual base-pairing between the CCA-end of the tRNA and the P-loop of the PTC (**Fig. 3**). Moreover, we observe ordering of the switch I loop in the G domain of RF3 (**Fig. 4c**), which establishes the sole interaction with the LSU and maybe therefore be important for accommodation of RF3 on the ribosome. Further subunit rotation ($+4.7^\circ$) as well as the head swivel observed in state III leads to a stabilization of domain I of RF1 and further accommodation of RF3 on the LSU (**Fig. 7c**). In state III, domain I of RF1 comes within 9 \AA of RF3 (**Fig. 5b**), which is the closest distance between the two factors in any of the structures reported here. The absence of interaction between RF1 and RF3 in states I-IV indicates that RF3 must indirectly induce RF1 dissociation from the ribosome. Indeed, in state IV, we observe that further rotation ($+4.1^\circ$) of the SSU leads to a destabilization in the binding of RF1 (**Fig. 7d**). We note that transition from states III to IV also encompasses additional head swivelling and movement of the L11 away from RF1, as well as loss of interaction with the P/E-tRNA, which may also contribute to the destabilization of RF1 binding (**Fig. 5c**). The large degree (9.6°) of SSU rotation observed in state IV brings the G domain of RF3 into close proximity of the SRL on the LSU (**Fig. 7d**). Thus, we predict that subunit rotation is necessary to stimulate the GTPase activity of RF3 and thereby facilitate dissociation of the low affinity RF3-GDP from the ribosome (**Fig. 7d**). As reported previously, we also observe interaction of the CTD of L7/L12 with the G' domain of RF3 in states I-IV, suggesting that L7/L12 may also play a role in GTPase activation and dissociation of RF3 (**Fig. 7d**). Because RF1 and RF3 are trapped on the ribosome with API and GDPCP in our structures, we cannot distinguish the order of dissociation of RF1 and RF3. Nevertheless, our structures suggest that RF1 and RF3 dissociation are both coupled to full rotation of the SSU, and are therefore likely to occur within a very similar timeframe, as reported recently using biophysical assays^{22,48}. We note the product remaining after the action of RF1 and RF3 is a rotated ribosome complex with a hybrid P/E-site tRNA, which is the exact substrate for the next phase of translation, namely, ribosome recycling via the binding of RRF and EF-G⁴⁹⁻⁵³ (**Fig. 7e**).

METHODS

Preparation of the ribosomal complex

Ribosomes from the *E. coli* strain MRE600, initiation factors, fMet-tRNA^{fMet} and its fluorescein-labeled derivative were prepared as described^{54,55}. L7/L12 depleted ribosomes were prepared by NH₄Cl and ethanol treatment as described⁴². The ribosome complexes were assembled on the synthetic ‘start-stop’ mRNA as follows: 70S (1 μ M), initiation factors 1, 2 (2 μ M) and 3 (1.5 μ M), start-stop mRNA (3 μ M) and f[³H]Met-tRNA^{fMet} (1.5 μ M) were incubated in buffer A (30 mM HEPES pH 7.4, 70 mM NH₄Cl, 5 mM MgCl₂, 30 mM KCl) in the presence of GTP (1 mM) for 30 minutes at 37°C and purified through sucrose cushion as described²³. The ribosome pellets were resuspended in buffer A, flash frozen in liquid nitrogen, and stored at -80°C.

E. coli strain and growth conditions

E. coli BL21 strain was used for the expression of RF1-GAQ and RF3. Cells were grown in LB medium supplemented with the required antibiotic, and expression was induced by addition of 0.5 mM IPTG.

Purification of peptide chain release factors

RF1, RF1-GAQ (RF1-G234A), RF3 and the single-cysteine RF1-GAQ were expressed and purified by affinity chromatography as described^{22,26}. RF1-GAQ was labeled with Qsy9²².

Cryo-grid preparation for the 70S-tRNA-RF1-RF3 complex

All following steps were performed in buffer B (30 mM HEPES pH 7.4, 70 mM NH₄Cl, 5 mM MgCl₂, 30 mM KCl). For grid preparation, 5 OD A₂₆₀/ml of ribosomes were used. RF3 was initially incubated with 1 mM of GDPCP at 37°C for 15 minutes. Subsequently, the ribosome-tRNA complexes were incubated with a 2.5x excess of the RF1-GAQ mutant and with or without 50 μ M API (NovoPro Biosciences Inc.) for 1 minute at room temperature. Afterwards a 7.5x excess of RF3-GDPCP over 70S ribosomes was added to the RF1-GAQ containing ribosome complexes and kept on ice for less than 5 minutes before cryo-grid preparation. All samples were applied to 2 nm precoated Quantifoil R3/3 holey carbon supported grids and vitrified using a Vitrobot Mark IV (FEI company).

Cryo-electron microscopy and single-particle reconstruction.

The low resolution data collection of the 70S-tRNA-RF1-RF3 complex, which was prepared in the absence of API, was conducted using a Tecnai G2 Spirit TEM equipped with a TemCam-F816 camera (TVIPS) at 120 kV using a pixel size of 2.85 Å. The high resolution data collection of the 70S-tRNA-

RF1-RF3 complex, which was prepared in the presence of API, was performed using an FEI Titan Krios transmission electron microscope equipped with a Falcon II direct electron detector at 300 kV using a pixel size of 1.061 Å and an under-defocus range of -0.8 to -1.6 µm resulting in a total number of 5,670 micrographs. Each micrograph was recorded as a series of 16 frames (2.7 e⁻/Å² pre-exposure; 2.7 e⁻/Å² dose per frame). All frames (accumulated dose of 45.9 e⁻/Å²) were aligned using the Unblur software⁵⁶, and power spectra, defocus values, astigmatism and estimation of micrograph resolution were determined by GCTF⁵⁷. Micrographs showing Thon rings beyond 4.0 Å resolution were further used. Automatic particle picking was performed using Gautomatch (<http://www.mrc-lmb.cam.ac.uk/kzhang/>), and single particles were processed using the Relion2.1 software package³¹. Initial 2D classification/alignment was performed with 703,379 particles. Subsequently, promising 2D classes with a total number of 525,595 ribosomal particles were selected and subjected to 3D refinement using an *E. coli*-70S ribosome as a reference structure. Initial alignment and subsequent 3D classification was performed using 3-times decimated data. The initially refined particles were 3D classified into 8 classes. Class 1 to 4 were refined again and subjected to another 3D classification. Sorting of class 1-4 resulted in 4, 4, 3 or 3 additional subclasses, respectively. The most stable subclass of each 3D classification was then 3D-refined. To further increase the resolution of RF3, we applied a focussed mask on RF3. For 3D classification, the same reference was used as for the 3D refinement. The maximum resolution was observed for state I and state II, extending to <3.9 Å (FSC_{0.143}) (**Supplementary Fig. 1**). The local resolution of the final maps was computed using ResMap⁵⁸ (**Supplementary Fig. 2**). The final maps were sharpened by dividing the maps by the modulation transfer function of the detector and by applying an automatically determined negative B factor to the maps using Relion2.1³¹. For model building the final maps were locally filtered using the SPHIRE cryo-EM software suite⁵⁹. Resolution was estimated using the “gold standard” criterion (FSC = 0.143)^{60,61}.

Molecular modelling and map-docking procedures

The molecular models for the ribosome were based on the *E. coli*-70S-EF-Tu structure (PDB: 5AFI)⁶². The models of RF3 and GDPCP are based on the structure of *E. coli* RF3-GDPNP bound to *Thermus thermophilus* 70S (PDB: 4V85)²⁹. The structure of RF1-GAQ and API is based on the recently published *E. coli*-70S-API-RF1 structure (PDB: 5O2R)²⁶. The tRNA_f^{Met} in the classical state is derived from an *E. coli* 70S initiation complex containing the ribosomal rescue factor ArfA (PDB: 5U9F)⁶³. The tRNA_f^{Met} in the P/E hybrid state is based on the hybrid state tRNA_f^{Met} from the *T. thermophilus* RF3-GDPCP-70S structure (PDB: 4V8O)²⁸. The rRNA domains and proteins were rigid-body fitted into the respective EM-map using Chimera⁶⁴. The models were manually adjusted

and refined using Coot⁶⁵. Due to the lack of density, domain I of RF1-GAQ was not modelled for states I-II and IV, whereas it was possible to generate a poly-Ala model of domain I of RF1-GAQ for state III. The complete atomic model of the respective complexes were refined into the locally filtered maps using *phenix.real_space_refine* with secondary structure restraints calculated by PHENIX 1.13⁶⁶. Cross-validation against over-fitting was performed as described elsewhere⁶⁷. The statistics of the refined model were obtained using MolProbity⁶⁸ (**Table 1**).

Calculation of rotation angles

Rotation angles were calculated using PyMol Molecular Graphics Systems (Version 1.8 Schrödinger) (**Supplementary Table 1**). The body/platform (including h44) rotation was calculated relatively to the 50S ribosomal subunit. Accordingly, for body/platform rotations the molecular models were aligned based on the 23S rRNA using state I (this study) as reference. The head swivel was calculated relatively to the 30S body/platform. In order to get comparable values for head swivelling, the compared molecular models were aligned based on the 16S rRNA of the body/platform using state I (this study) as reference.

RMSD and vector calculations

Root mean square deviation (RMSD) values were calculated between related alpha-carbon (protein) or phosphate atoms (rRNA) using PyMol Molecular Graphics Systems (Version 1.8 Schrödinger). The reported RF1-API-70S structure²⁶ was used as reference. All compared models were aligned to the 50S subunit of state I (this study). The 30S protein or rRNA residues of the reference structure were colored according to the determined RMSD of each atom. Vectors were calculated between shifted alpha-carbon and phosphate atoms using the same reference²⁶. The vectors were colored based on their length (distance between atoms).

Peptide hydrolysis

Ribosome termination complexes (10 nM) prepared with wildtype or ΔL7/L12 ribosomes were mixed with increasing concentrations of RF1 for 10 s at 37°C in buffer A. Reactions were quenched with a solution containing TCA (10%) and ethanol (50%). After centrifugation (30 min, 16,000 x g) the amount of released [³H]Met in the supernatant was quantified by radioactive counting.

Rapid kinetics

Rapid kinetic experiments were performed on an SX-20MV stopped-flow apparatus (Applied Photophysics, Leatherhead, UK), by rapidly mixing equal volumes (60 µl) of reactants at 37°C in

buffer A. Binding of RF1-GAQ was monitored by mixing termination complex labelled with fluorescein (50 nM) with RF1-GAQ_{QSY9} (300 nM). Fluorescein was excited at 470 nm and monitored after passing a KV500 filter (Schott, Mainz, Germany).

Figure preparation

All figures showing electron densities and atomic models were generated using UCSF Chimera⁶⁴ and PyMol Molecular Graphics Systems (Version 1.8 Schrödinger).

REFERENCES

1. Copech, M.R. Polypeptide chain termination in vitro: isolation of a release factor. *Proc. Natl. Acad. Sci., USA* **58**, 1144-1151 (1967).
2. Scolnick, E., Tompkins, R., Caskey, T. & Nirenberg, M. Release factors differing in specificity for terminator codons. *Proc. Natl Acad. Sci. USA* **61**, 768-774 (1968).
3. Nakamura, Y., Ito, K. & Isaksson, L.A. Emerging understanding of translation termination. *Cell* **87**, 147-150 (1996).
4. Dunkle, J.A. & Cate, J.H. Ribosome structure and dynamics during translocation and termination. *Annu Rev Biophys* **39**, 227-44 (2010).
5. Frolova, L. et al. Mutations in the highly conserved GGQ motif of class 1 polypeptide release factors abolish the ability of human eRF1 to trigger peptidyl-tRNA hydrolysis. *RNA* **5**, 1014-1020 (1999).
6. Seit-Nebi, A., Frolova, L., Justesen, J. & Kisseelev, L. Class-1 translation termination factors: invariant GGQ minidomain is essential for release activity and ribosome binding but not for stop codon recognition. *Nucleic Acids Res.* **29**, 3982-3987 (2001).
7. Zavialov, A.V., Mora, L., Buckingham, R.H. & Ehrenberg, M. Release of peptide promoted by the GGQ motif of class 1 release factors regulates the GTPase activity of RF3. *Mol. Cell* **10**, 789-798 (2002).
8. Mora, L. et al. The essential role of the invariant GGQ motif in the function and stability in vivo of bacterial release factors RF1 and RF2. *Mol. Microbiol.* **47**, 267-275 (2003).
9. Shaw, J.J. & Green, R. Two distinct components of release factor function uncovered by nucleophile partitioning analysis. *Mol Cell* **28**, 458-67 (2007).
10. Laurberg, M. et al. Structural basis for translation termination on the 70S ribosome. *Nature* **454**, 852-857 (2008).
11. Korostelev, A. et al. Crystal structure of a translation termination complex formed with release factor RF2. *Proc Natl Acad Sci U S A* **105**, 19684-9 (2008).
12. Weixlbaumer, A. et al. Insights into translational termination from the structure of RF2 bound to the ribosome. *Science* **322**, 953-6 (2008).
13. Jin, H., Kelley, A.C., Loakes, D. & Ramakrishnan, V. Structure of the 70S ribosome bound to release factor 2 and a substrate analog provides insights into catalysis of peptide release. *Proc Natl Acad Sci U S A* **107**, 8593-8598 (2010).
14. Zhou, J., Korostelev, A., Lancaster, L. & Noller, H.F. Crystal structures of 70S ribosomes bound to release factors RF1, RF2 and RF3. *Curr Opin Struct Biol* **22**, 733-42 (2012).
15. Goldstein, J.L. & Caskey, C.T. Peptide chain termination: Effect of protein S on ribosomal binding of release factors. *Proc. Natl. Acad. Sci., USA* **67**, 537-543 (1970).
16. Freistroffer, D.V., Pavlov, M.Y., MacDougall, J., Buckingham, R.H. & Ehrenberg, M. Release factor RF3 in *E. coli* accelerates the dissociation of release factors RF1 and RF2 from the ribosome in a GTP-dependent manner. *EMBO J.* **16**, 4126-4133 (1997).
17. Gao, H. et al. RF3 induces ribosomal conformational changes responsible for dissociation of class I release factors. *Cell* **129**, 929-941 (2007).
18. Kihira, K. et al. Crystal structure analysis of the translation factor RF3 (release factor 3). *FEBS Lett* **586**, 3705-9 (2012).
19. Pel, H., Moffat, J., Ito, K., Nakamura, Y. & Tate, W. *Escherichia coli* release factor 3: Resolving the paradox of a typical G protein structure and atypical function with guanine nucleotides. *RNA* **4**, 47-54 (1998).
20. Zavialov, A.V., Buckingham, R.H. & Ehrenberg, M. A posttermination ribosomal complex is the guanine nucleotide exchange factor for peptide release factor RF3. *Cell* **107**, 115-124 (2001).
21. Koutmou, K.S., McDonald, M.E., Brunelle, J.L. & Green, R. RF3:GTP promotes rapid dissociation of the class 1 termination factor. *RNA* **20**, 609-20 (2014).

22. Adio, S. et al. Dynamics of ribosomes and release factors during translation termination in *E. coli*. *bioRxiv* (2018).
23. Peske, F., Kuhlenkoetter, S., Rodnina, M.V. & Wintermeyer, W. Timing of GTP binding and hydrolysis by translation termination factor RF3. *Nucleic Acids Res* **42**, 1812-20 (2014).
24. Ermolenko, D.N. et al. Observation of intersubunit movement of the ribosome in solution using FRET. *J Mol Biol* **370**, 530-40 (2007).
25. Sternberg, S.H., Fei, J., Prywes, N., McGrath, K.A. & Gonzalez, R.L., Jr. Translation factors direct intrinsic ribosome dynamics during translation termination and ribosome recycling. *Nat Struct Mol Biol* **16**, 861-8 (2009).
26. Florin, T. et al. An antimicrobial peptide that inhibits translation by trapping release factors on the ribosome. *Nat Struct Mol Biol* **24**, 752-757 (2017).
27. Klaholz, B., Myasnikov, A. & Van Heel, M. Visualization of release factor 3 on the ribosome during termination of protein synthesis. *Nature* **427**, 862-865 (2004).
28. Jin, H., Kelley, A.C. & Ramakrishnan, V. Crystal structure of the hybrid state of ribosome in complex with the guanosine triphosphatase release factor 3. *Proc. Natl Acad. Sci. U S A*, Epub (2011).
29. Zhou, J., Lancaster, L., Trakhanov, S. & Noller, H.F. Crystal structure of release factor RF3 trapped in the GTP state on a rotated conformation of the ribosome. *RNA* **18**, 230-40 (2012).
30. Pallesen, J. et al. Cryo-EM visualization of the ribosome in termination complex with apo-RF3 and RF1. *Elife* **2**, e00411 (2013).
31. Kimanis, D., Forsberg, B.O., Scheres, S.H. & Lindahl, E. Accelerated cryo-EM structure determination with parallelisation using GPUs in RELION-2. *Elife* **5**(2016).
32. Fischer, N. et al. The pathway to GTPase activation of elongation factor SelB on the ribosome. *Nature* (2016).
33. Fischer, N., Konevega, A.L., Wintermeyer, W., Rodnina, M.V. & Stark, H. Ribosome dynamics and tRNA movement by time-resolved electron cryomicroscopy. *Nature* **466**, 329-333 (2010).
34. Zhang, W., Dunkle, J.A. & Cate, J.H. Structures of the ribosome in intermediate states of ratcheting. *Science* **325**, 1014-7 (2009).
35. Julian, P. et al. Structure of ratcheted ribosomes with tRNAs in hybrid states. *Proc Natl Acad Sci U S A* **105**, 16924-7 (2008).
36. Agirrezabala, X. et al. Structural characterization of mRNA-tRNA translocation intermediates. *Proc Natl Acad Sci U S A* **109**, 6094-9 (2012).
37. Brilot, A.F., Korostelev, A.A., Ermolenko, D.N. & Grigorieff, N. Structure of the ribosome with elongation factor G trapped in the pretranslocation state. *Proc Natl Acad Sci U S A* **110**, 20994-9 (2013).
38. Maracci, C. & Rodnina, M.V. Review: Translational GTPases. *Biopolymers* **105**, 463-75 (2016).
39. Behrmann, E. et al. Structural snapshots of actively translating human ribosomes. *Cell* **161**, 845-57 (2015).
40. Loveland, A.B., Demo, G., Grigorieff, N. & Korostelev, A.A. Ensemble cryo-EM elucidates the mechanism of translation fidelity. *Nature* **546**, 113-117 (2017).
41. Shao, S. et al. Decoding Mammalian Ribosome-mRNA States by Translational GTPase Complexes. *Cell* **167**, 1229-1240 e15 (2016).
42. Mohr, D., Wintermeyer, W. & Rodnina, M.V. GTPase activation of elongation factors Tu and G on the ribosome. *Biochemistry* **41**, 12520-12528 (2002).
43. Diaconu, M. et al. Structural basis for the function of the ribosomal L7/12 stalk in factor binding and GTPase activation. *Cell* **121**, 991-1004 (2005).
44. Carlson, M.A. et al. Ribosomal protein L7/L12 is required for GTPase translation factors EF-G, RF3, and IF2 to bind in their GTP state to 70S ribosomes. *FEBS J* **284**, 1631-1643 (2017).

45. Helgstrand, M. et al. The ribosomal stalk binds to translation factors IF2, EF-Tu, EF-G and RF3 via a conserved region of the L12 C-terminal domain. *J. Mol. Biol.* **365**, 468-479 (2007).
46. Savelsbergh, A., Mohr, D., Kothe, U., Wintermeyer, W. & Rodnina, M.V. Control of phosphate release from elongation factor G by ribosomal protein L7/12. *EMBO J.* **24**, 4316–4323 (2005).
47. Kothe, U., Wieden, H.J., Mohr, D. & Rodnina, M.V. Interaction of helix D of elongation factor Tu with helices 4 and 5 of protein L7/12 on the ribosome. *J Mol Biol* **336**, 1011-21 (2004).
48. Shi, X. & Joseph, S. Mechanism of Translation Termination: RF1 Dissociation Follows Dissociation of RF3 from the Ribosome. *Biochemistry* **55**, 6344-6354 (2016).
49. Dunkle, J.A. et al. Structures of the bacterial ribosome in classical and hybrid states of tRNA binding. *Science* **332**, 981-4 (2011).
50. Barat, C. et al. Progression of the ribosome recycling factor through the ribosome dissociates the two ribosomal subunits. *Mol Cell* **27**, 250-61 (2007).
51. Seo, H. et al. Kinetics and thermodynamics of RRF, EF-G, and thiostrepton interaction on the *Escherichia coli* ribosome. *Biochemistry* **43**, 12728-12740 (2004).
52. Borg, A., Pavlov, M. & Ehrenberg, M. Complete kinetic mechanism for recycling of the bacterial ribosome. *RNA* **22**, 10-21 (2016).
53. Savelsbergh, A., Rodnina, M.V. & Wintermeyer, W. Distinct functions of elongation factor G in ribosome recycling and translocation. *RNA* **15**, 772-780 (2009).
54. Milon, P. et al. Transient kinetics, fluorescence, and FRET in studies of initiation of translation in bacteria. *Methods Enzymol* **430**, 1-30 (2007).
55. Rodnina, M.V. & Wintermeyer, W. GTP consumption of elongation factor Tu during translation of heteropolymeric mRNAs. *Proc. Natl. Acad. Sci. USA* **92**, 1945-1949 (1995).
56. Grant, T. & Grigorieff, N. Measuring the optimal exposure for single particle cryo-EM using a 2.6 Å reconstruction of rotavirus VP6. *Elife* **4**, e06980 (2015).
57. Zhang, K. Getf: Real-time CTF determination and correction. *J Struct Biol* **193**, 1-12 (2016).
58. Kucukelbir, A., Sigworth, F.J. & Tagare, H.D. Quantifying the local resolution of cryo-EM density maps. *Nat Methods* **11**, 63-5 (2014).
59. Moriya, T. et al. High-resolution Single Particle Analysis from Electron Cryo-microscopy Images Using SPHIRE. *J Vis Exp* (2017).
60. Rosenthal, P. & Henderson, R. Optimal determination of particle orientation, absolute hand, and control loss in single particle electron microscopy. *J. Mol. Biol.* **333**, 721-745 (2003).
61. Scheres, S.H. & Chen, S. Prevention of overfitting in cryo-EM structure determination. *Nat Methods* **9**, 853-4 (2012).
62. Fischer, N. et al. Structure of the *E. coli* ribosome-EF-Tu complex at <3 Å resolution by C-corrected cryo-EM. *Nature* **520**, 567-570 (2015).
63. Demo, G. et al. Mechanism of ribosome rescue by ArfA and RF2. *Elife* **6**(2017).
64. Pettersen, E.F. et al. UCSF Chimera - A Visualization System for Exploratory Research and Analysis. *J. Comput. Chem.* **25**, 1605-1612 (2004).
65. Emsley, P. & Cowtan, K. Coot: Model-Building Tools for Molecular Graphics. *Acta Crystallographica Section D - Biological Crystallography* **60**, 2126-2132 (2004).
66. Adams, P.D. et al. PHENIX: a comprehensive Python-based system for macromolecular structure solution. *Acta Crystallogr D Biol Crystallogr* **66**, 213-21 (2010).
67. Brown, A. et al. Tools for macromolecular model building and refinement into electron cryo-microscopy reconstructions. *Acta Crystallogr D Biol Crystallogr* **71**, 136-53 (2015).
68. Chen, V.B. et al. MolProbity: all-atom structure validation for macromolecular crystallography. *Acta Crystallogr D Biol Crystallogr* **66**, 12-21 (2010).
69. Sprink, T. et al. Structures of ribosome-bound initiation factor 2 reveal the mechanism of subunit association. *Sci Adv* **2**, e1501502 (2016).

70. Li, W. et al. Activation of GTP hydrolysis in mRNA-tRNA translocation by elongation factor G. *Sci Adv* **1**(2015).

ACKNOWLEDGMENTS

This work has been supported by iNEXT, project number 2992, funded by the Horizon 2020 programme of the European Union. This article reflects only the author's view and the European Commission is not responsible for any use that may be made of the information it contains. CIISB research infrastructure project LM2015043 funded by MEYS CR is gratefully acknowledged for the financial support of the measurements at the CF Cryo-electron Microscopy and Tomography CEITEC MU. This research was supported by grants of the Forschergruppe FOR1805 (to D.N.W. and M.V.R) and WI3285/6-1 (to D.N.W.) from the Deutsche Forschungsgemeinschaft (DFG).

AUTHOR CONTRIBUTIONS

D.N.W and M.V.R. designed the study, M.G. and C.M. prepared the cryo-EM sample, M.P. collected the cryo-EM data, M.G. processed the cryo-EM data, M.G. and P.H. built and refined the molecular models, M.G., P.H. and D.N.W. analyzed the cryo-EM data. C.M. performed L7/L12 experiments. M.G. prepared the figures. M.G. and D.N.W. wrote the paper with help from C.M. and M.V.R.

COMPETING FINANCIAL INTERESTS

The authors declare no competing financial interests.

MATERIALS & CORRESPONDANCE

Please direct any requests for further information or reagents to the lead contact, Daniel N. Wilson (daniel.wilson@chemie.uni-hamburg.de).

ACCESSION NUMBERS

The atomic coordinates and/or the associated maps have been deposited in the PDB and/or EMDB with the accession codes EMD: 1234/PDB: W123 (State I), EMD: 2234/PDB: X123 (State II), EMD: 3234/PDB: Y123 (State III), EMD: 4234/PDB: Z123 (State IV) and EMD: 5234/PDB: A123 (RF3-70S).

FIGURES

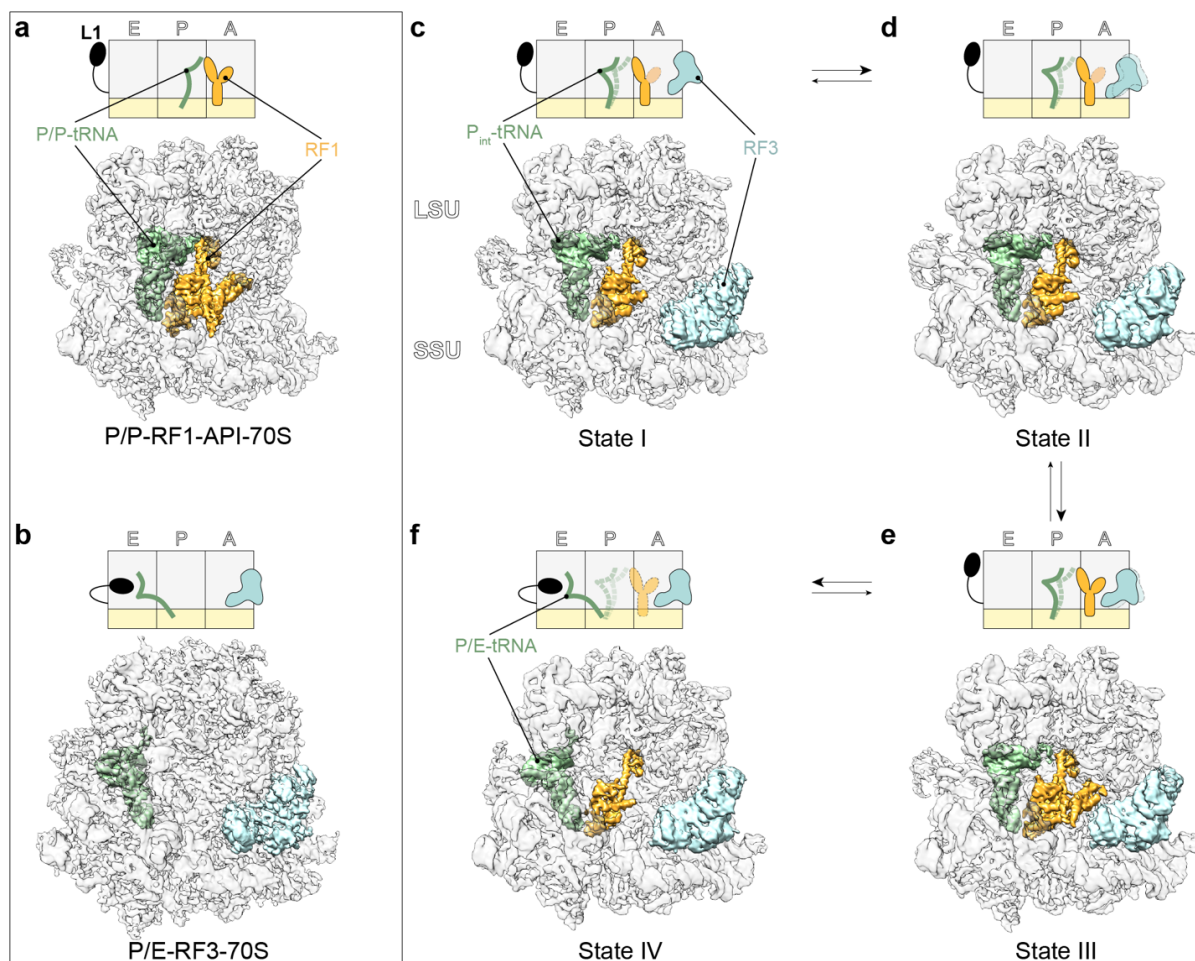


Figure 1 Structures of RF1- and RF3-containing termination complexes. **(a-f)** Schematic representation (above) and electron density (below) for termination complexes containing **(a)** RF1 (orange) stalled by API on a non-rotated ribosome with a classical P/P-site tRNA (green)²⁶, **(b)** RF3 (cyan) trapped by GDPCP on a rotated ribosome with hybrid P/E-site tRNA²⁸, **(c-d)** state I-IV with RF1-GAQ (orange), RF3-GDPCP (cyan) bound to **(c-e)** partially rotated ribosomes with intermediate P-site (P_{int}) tRNA (green) or **(f)** a fully rotated ribosome with a hybrid P/E-site tRNA (green). In the scheme, the SSU and LSU are colored yellow and grey, respectively, with A, P and E-sites and the L1 stalk indicated, whereas flexible regions are indicated by increased transparency. In the map overviews, the electron density for the SSU and LSU has been filtered locally and is shown as a grey transparency so that the ligands can be easily seen within the ribosome.

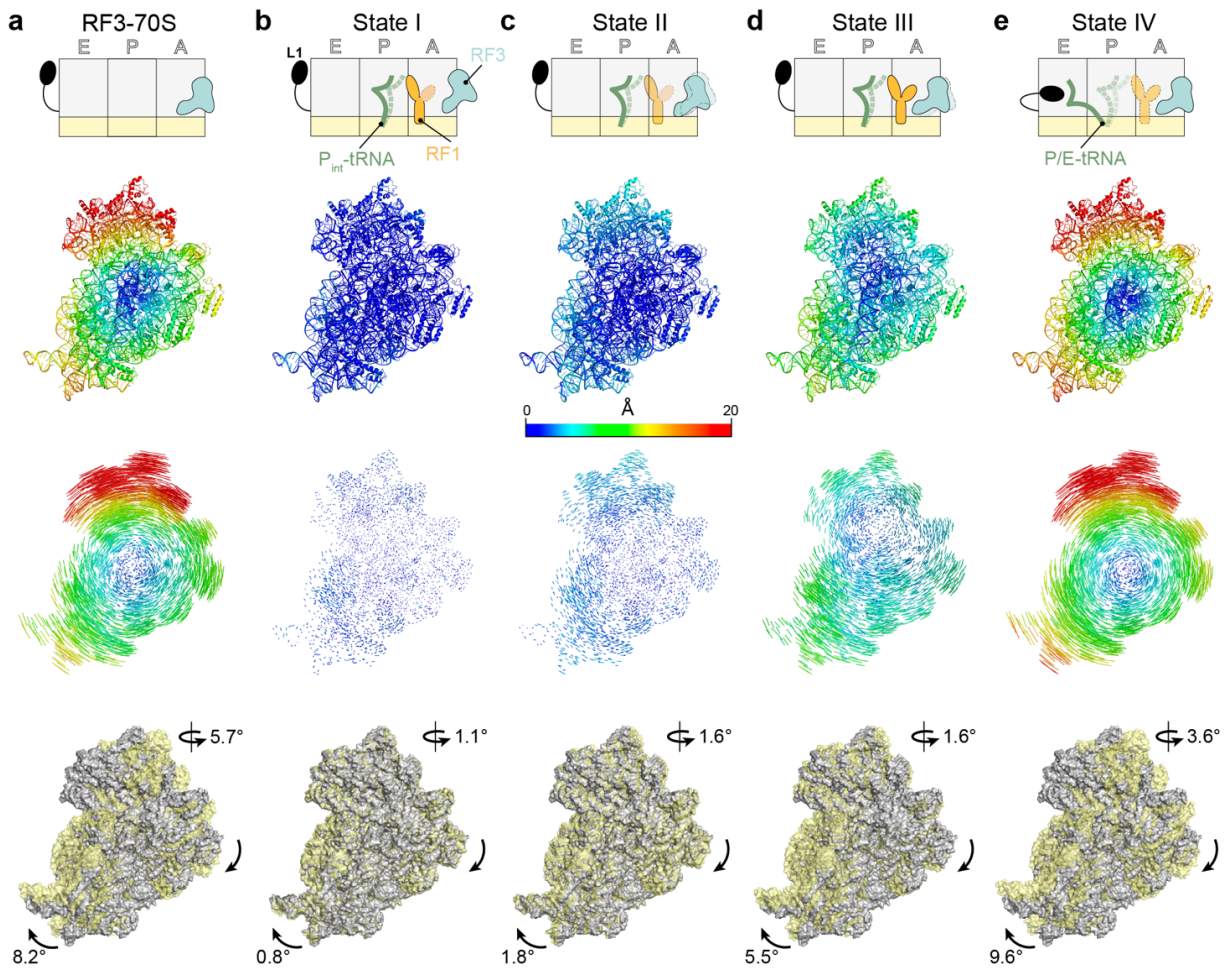


Figure 2 Subunit rotation and head swivel observed in RF3-70S and termination state I-IV complexes. (a-e) Schematic representation (upper row) and SSU structures illustrating the degree of rotation relative to non-rotated RF1-API-70S reference structure²⁶ as shown for (a) RF3-70S, (b) state I, (c) state II, (d) state III and (e) state IV. The distance each atom shifts relative to the reference structure is directly colored on the SSU (second row), shown as colored lines connecting the same atoms between the reference and the shifted structure (third row). Superimposition of cryo-EM maps (row four) of shifted SSU (yellow) relative to reference SSU (grey) based on LSU alignments, with degrees of SSU rotation (clockwise as viewed from intersubunit interface) and head swivel indicated.

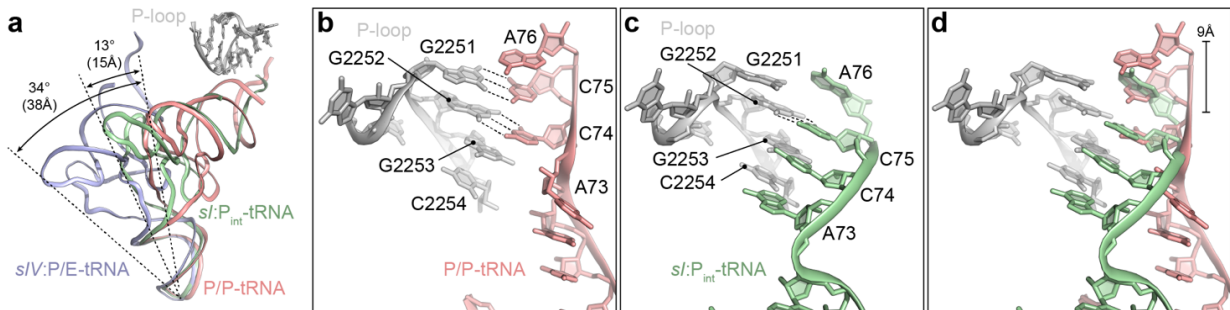


Figure 3 Small subunit rotation induces P-site tRNA rotation. **(a)** Comparison of the relative position of a classical P/P-tRNA (salmon) from the RF1-API-70S complex²⁶ to P_{int} tRNA (green) conformation observed in state I and the hybrid P/E-site tRNA observed in state IV (slate), with the degree of rotation and distance shifted indicated. The P-loop of the 23S rRNA is shown for reference. **(b)** The P/P-site tRNA (salmon) in the RF1-API-70S complex²⁶ and **(c)** the P_{int}-tRNA (green) in state I interact with nucleotides within the P-loop (H80) of the 23S rRNA. Potential hydrogen bonds are indicated with dashed lines. **(d)** Superimposition of **(b)** and **(c)**.

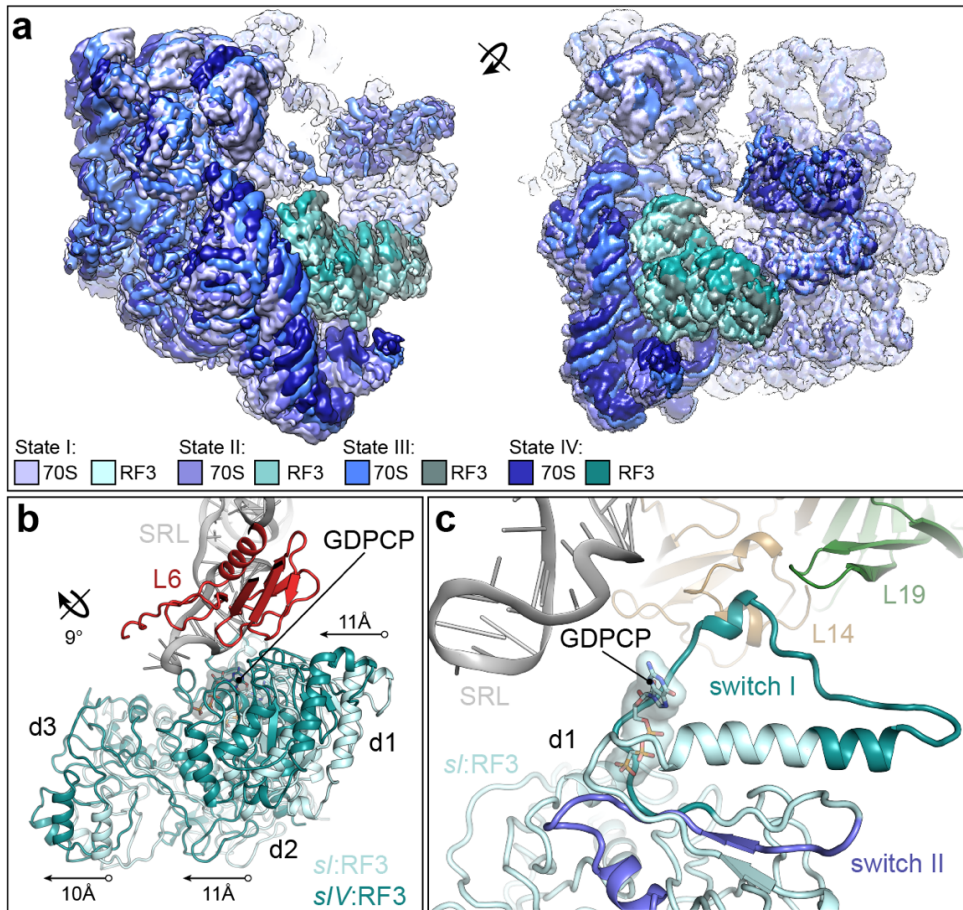
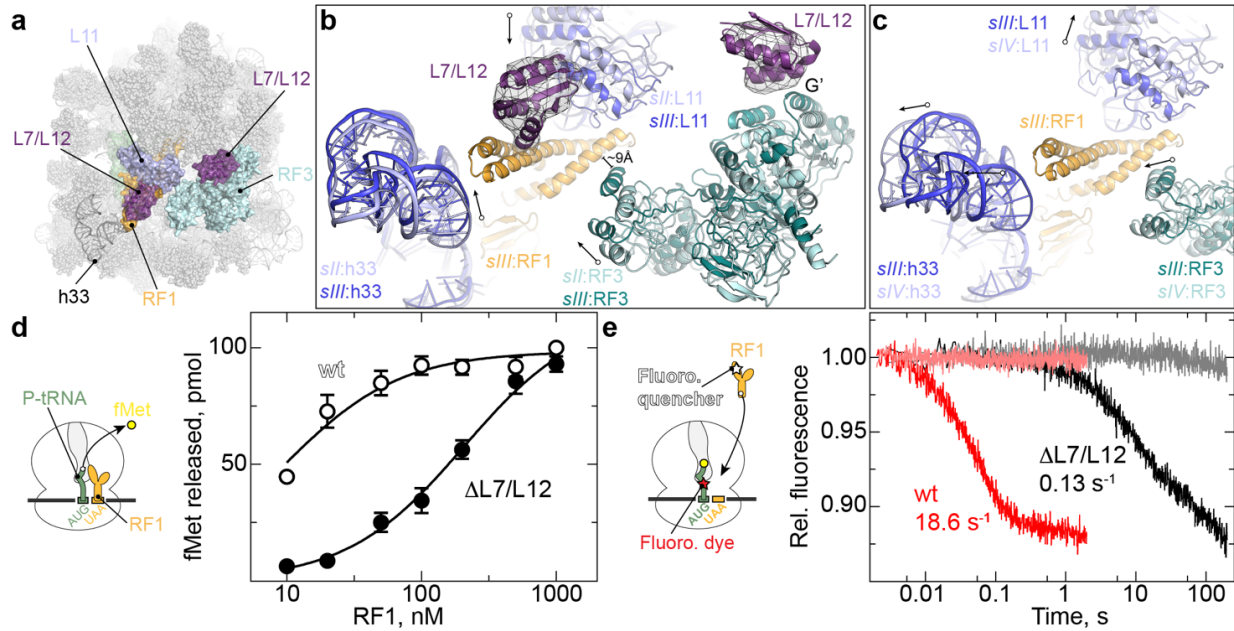


Figure 4 Small subunit rotation leads to RF3 accommodation on the large subunit. **(a)** Two views of the cryo-EM maps of the 70S ribosome (different shades of blue) and RF3 (different shades of green) from states I-IV, illustrating the coupled rotation of the SSU and RF3 relative to the LSU. **(b)** Comparison of the binding site of RF3 in state I (pale cyan, sI:RF3) and state IV (teal, sIV:RF3) relative to ribosomal protein L6 (red) and sarcin-ricin loop (SRL, grey). The distance shifted of each domain (d1-d3) of RF3 between state I and IV is indicated. **(c)** View showing the G domain of RF3 in state I (pale cyan, sI:RF3) with switch I (teal), switch II (slate), GDPCP and proximity to SRL (grey), ribosomal proteins L14 (tan) and L19 (green).



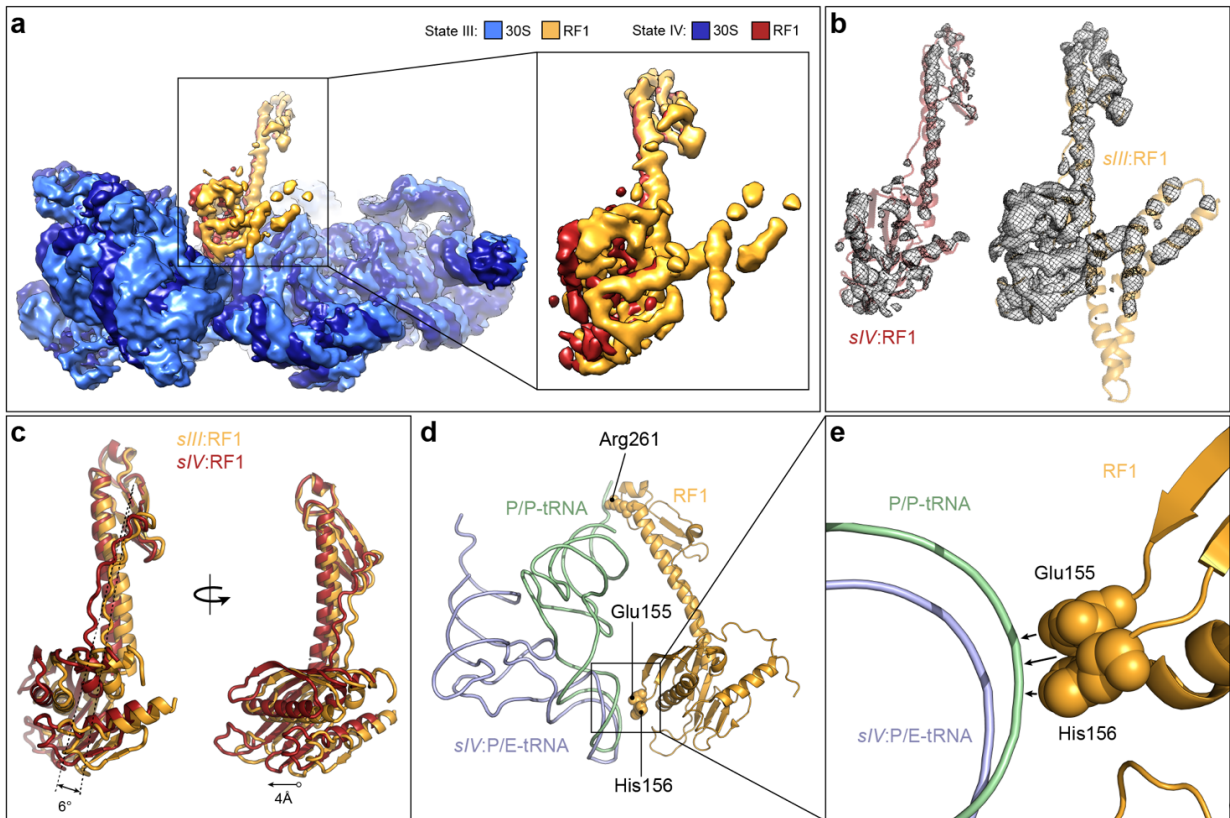


Figure 6 RF3-induced subunit rotation destabilizes RF1 binding. **(a)** Cryo-EM map of SSU (light blue) and RF1 (orange) from state III compared with SSU (dark blue) and RF1 (red) from state IV. **(b)** Isolated cryo-EM electron densities (grey mesh) with molecular models for RF1 from state III (orange) and state IV (red) shown at the same contour level based on comparison with the SSU density. **(c)** Domain 2/4 of RF1 from state III (sIII:RF1, orange) is rotated by 6° and shifted by 4 Å compared to RF1 from state IV (sIV:RF1, red). **(d,e)** Contacts (arrowed) between RF1 (orange) and P/P-tRNA (green) are lost upon formation of the hybrid P/E-tRNA (light blue). Amino acids of RF1 that contact P/P-tRNA are shown as spheres. **(e)** Zoom of **(d)** showing the presence or absence of RF1 contacts with the ASL of P/P- or P/E-tRNA, respectively.

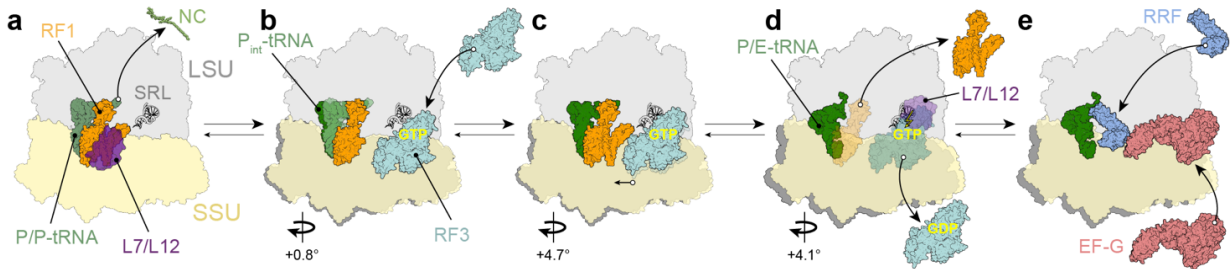


Figure 7 Model for RF3-mediated dissociation of RF1 from the ribosome. **(a)** Binding of decoding release factors, such as RF1 (orange) to the non-rotated termination state ribosome, leads to release of the nascent polypeptide chain (NC) from the P-site tRNA (green). Binding of RF1 to the ribosome is facilitated by interaction of L7/L12 CTD (purple) with domain 1 of RF1. **(b)** RF3 (cyan) in the GTP conformation binds to the ribosome–RF1 complex. RF3 binding induces a slight rotation of the SSU that promotes formation of the partially rotated P-site tRNA conformation (P_{int} -tRNA). **(c)** Additional SSU rotation and head swivel stabilizes domain I of RF1 and induces a closed conformation of L11 (Fig. 5b,c). **(d)** Further SSU rotation leads to destabilization of RF1, promoting its dissociation from the ribosome, as well as accommodation of RF3 on the LSU in close proximity to the sarcin-ricin loop (SRL), thus facilitating hydrolysis of GTP to GDP and dissociation of RF3–GDP from the ribosome. **(e)** The rotated ribosome with a P/E-tRNA is recognized by the ribosome recycling factor (RRF) and EF-G, which recycle the post-termination complex for the next round of translation.

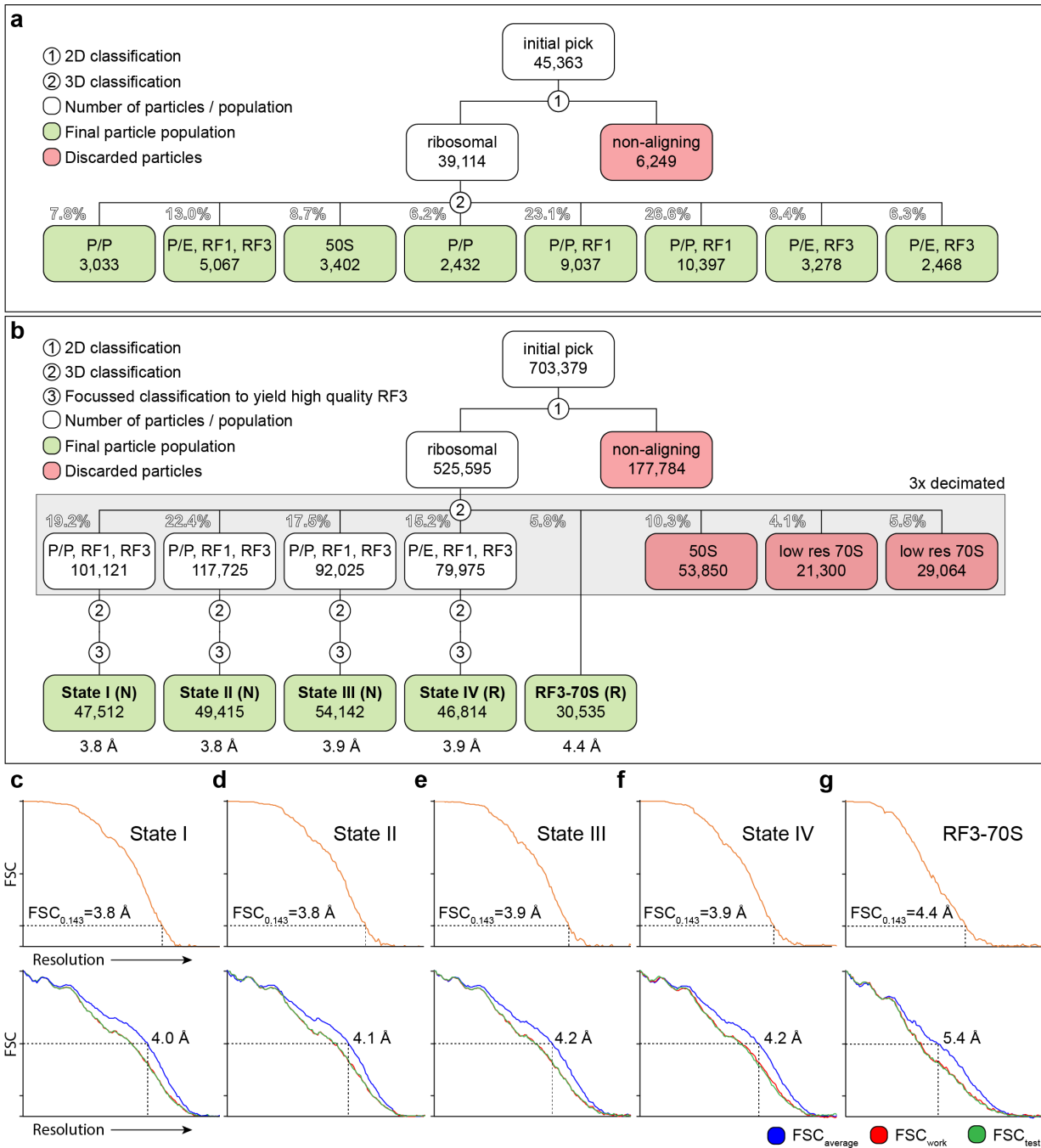
Table 1 Cryo-EM data collection, refinement and validation statistics.

	State I (EMD xxxx, PDB xxxx)	State II (EMD xxxx, PDB xxxx)	State III (EMD xxxx, PDB xxxx)	State IV (EMD xxxx, PDB xxxx)	RF3-70S (EMD xxxx, PDB xxxx)
Data collection					
Microscope	FEI Titan Krios	FEI Titan Krios	FEI Titan Krios	FEI Titan Krios	FEI Titan Krios
Camera	Falcon II	Falcon II	Falcon II	Falcon II	Falcon II
Magnification	131,951	131,951	131,951	131,951	131,951
Voltage (kV)	300	300	300	300	300
Electron dose (e ⁻ / Å ²)	45.9	45.9	45.9	45.9	45.9
Defocus range (μm)	-0.8 to -1.6	-0.8 to -1.6	-0.8 to -1.6	-0.8 to -1.6	-0.8 to -1.6
Pixel size (Å)	1.061	1.061	1.061	1.061	1.061
Initial particles (no.)	525,595	525,595	525,595	525,595	525,595
Final particles (no.)	47,512	49,415	54,142	46,814	30,535
Model composition					
Non-hydrogen atoms	151,484	151,394	151,873	151,479	147,677
Protein residues	6670	6643	6742	6643	6396
RNA bases	4638	4638	4637	4642	4554
Refinement					
Resolution (Å)	3.81	3.85	3.93	3.93	4.44
Mask CC	0.808	0.823	0.819	0.822	0.790
Volume CC	0.798	0.813	0.810	0.812	0.775
Map-sharpening <i>B</i> factor (Å ²)	-125.34	-125.88	-129.42	-126.26	-134.81
Average <i>B</i> factor (Å ²)	187.9	204.3	221.6	206.0	354.1
R.m.s. deviations					
Bond lengths (Å)	0.005	0.004	0.004	0.005	0.008
Bond angles (°)	0.93	0.88	0.86	0.88	0.87
Validation					
MolProbity score*	1.83 (100 th)	1.84 (100 th)	1.80 (100 th)	1.89 (100 th)	1.79 (100 th)
Clashscore**	5.92 (100 th)	5.95 (100 th)	5.51 (100 th)	6.90 (100 th)	5.24 (100 th)
Poor rotamers (%)	0.20%	0.24%	0.20%	0.17%	0.27%
Ramachandran plot					
Favored (%)	91.39%	91.22%	91.47%	91.32%	91.14%
Allowed (%)	8.17%	8.37%	8.09%	8.25%	8.40%
Disallowed (%)	0.44%	0.41%	0.44%	0.43%	0.46%

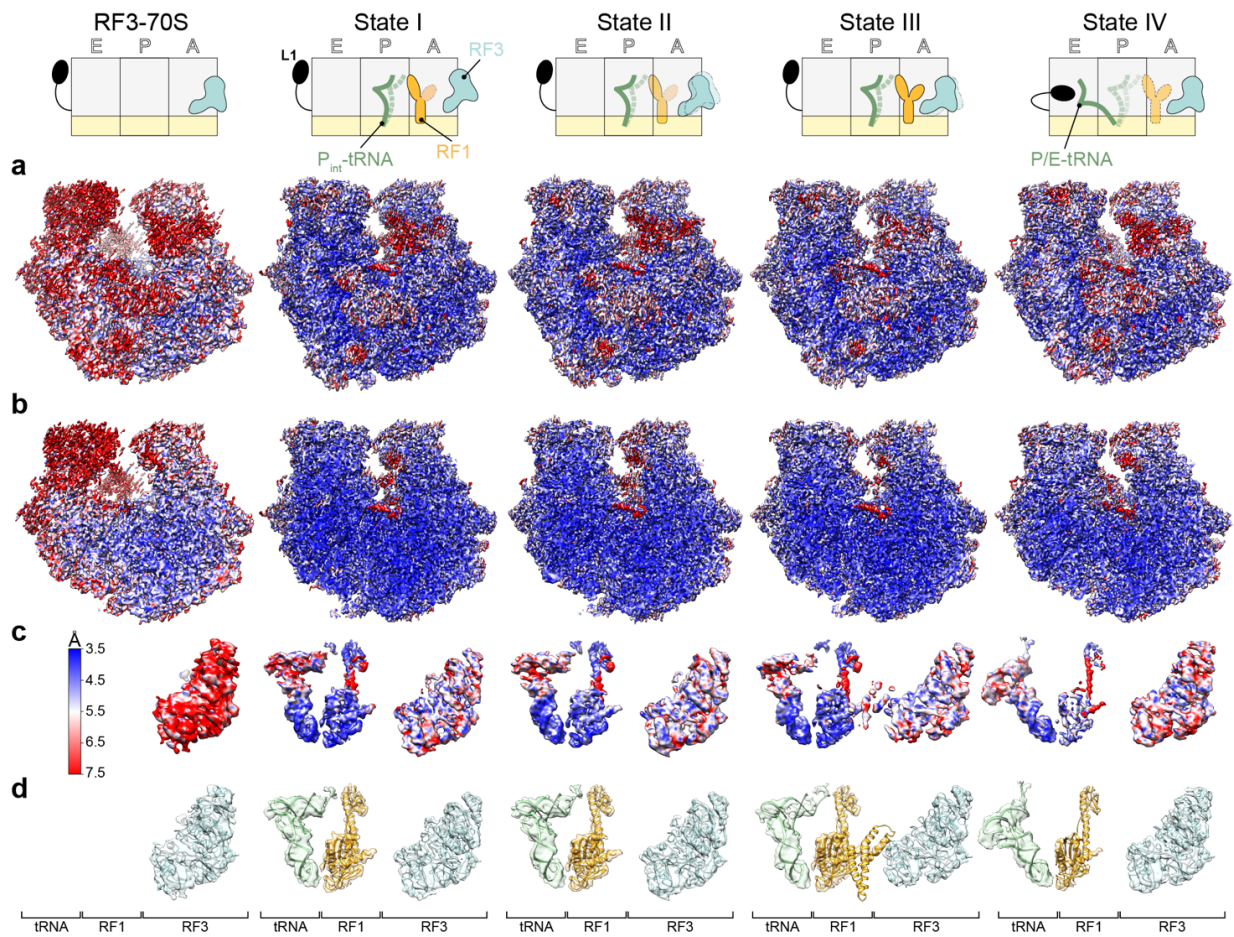
*(3.25Å – 4.05Å)

**(3Å – 9999Å)

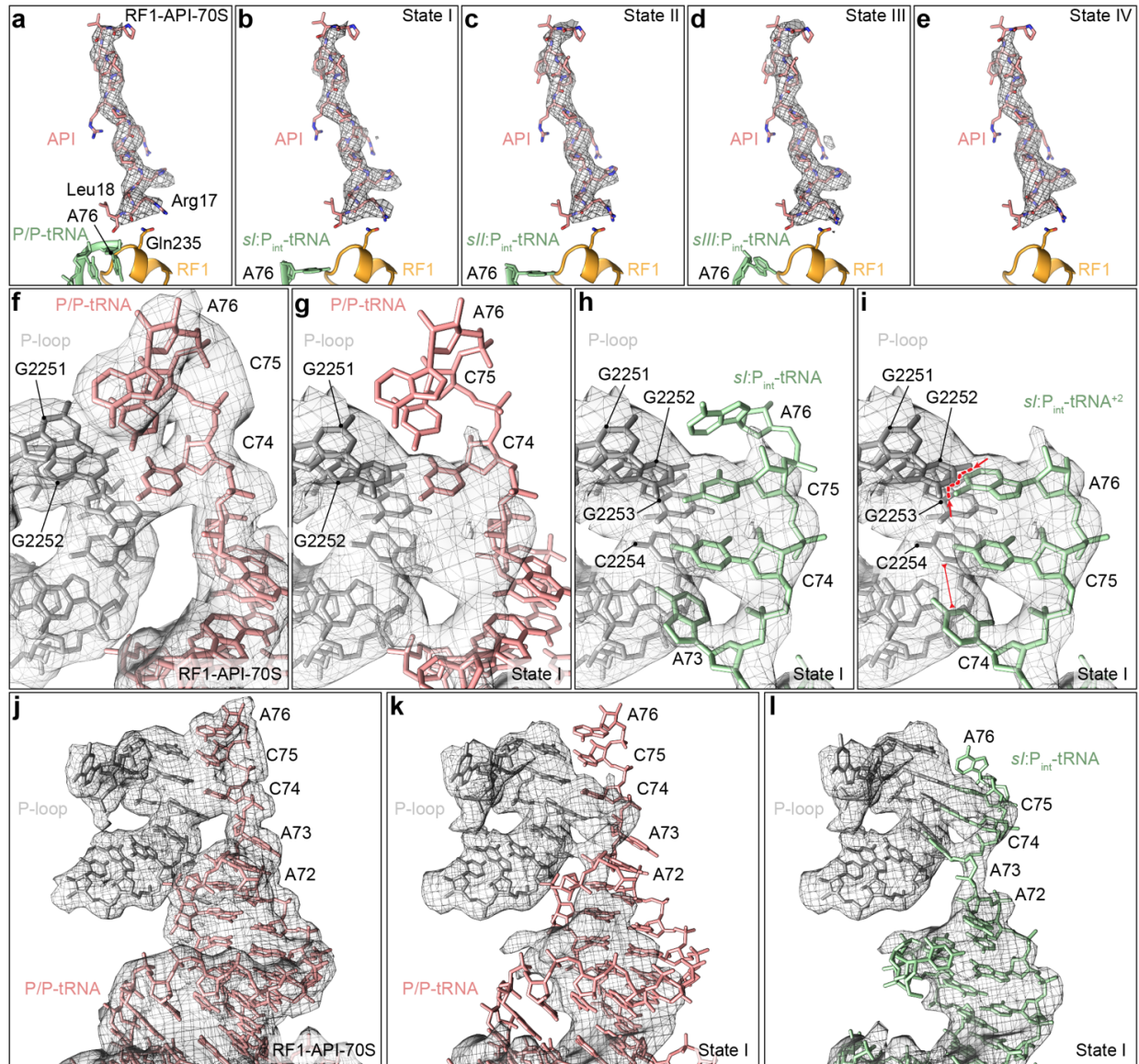
SUPPLEMENTARY FIGURES



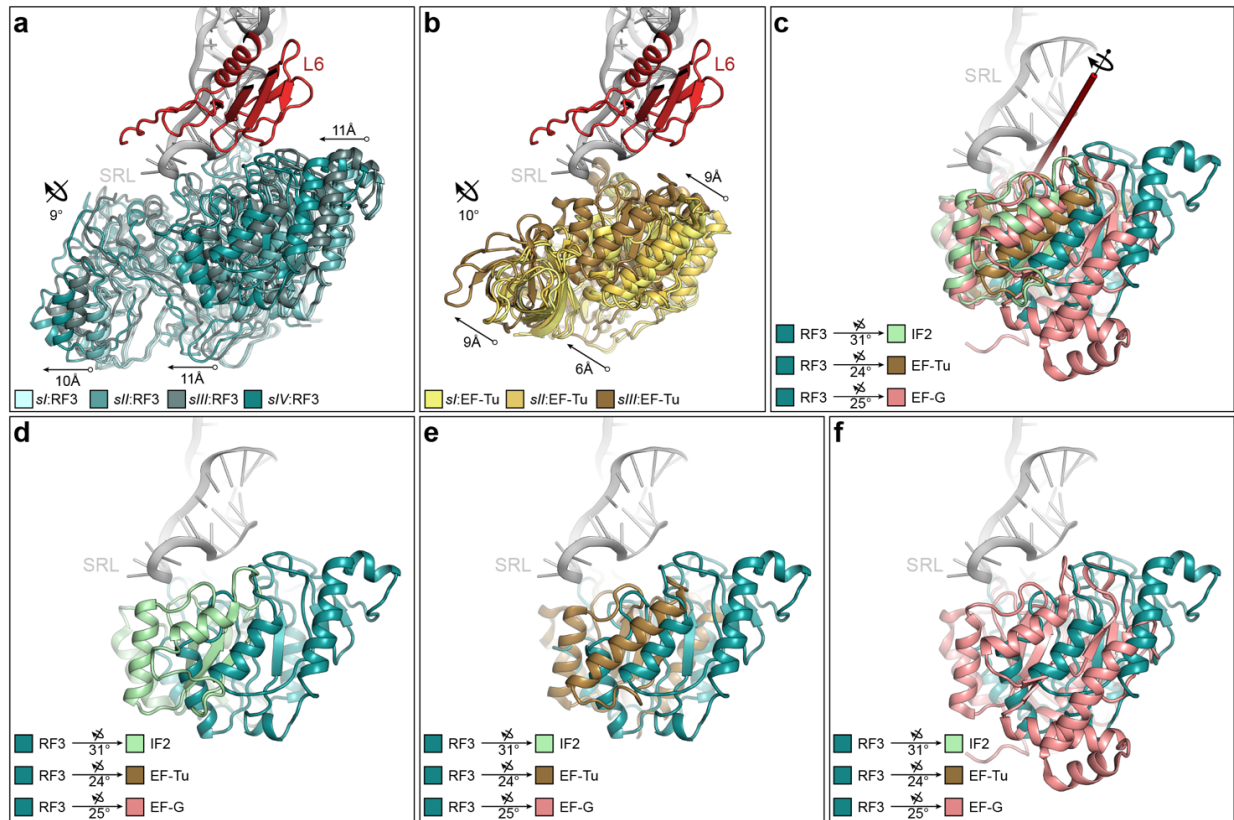
Supplementary Figure 1 Processing of the cryo-EM data of 70S-tRNA-RF1-RF3 complexes. **(a)** Sorting scheme of the cryo-EM data of *in vitro* reconstituted complexes prepared in the absence of API. From a total of 45,363 particles, 6,249 non-aligning particles were discarded after 2D classification. The remaining 39,114 particles were subjected to 3D classification and sorted into 8 different classes. The classes comprise two populations containing only P/P-tRNA, two populations containing P/P-tRNA and RF1, two populations harbouring P/E-tRNA and RF3, one population containing P/E-tRNA, RF1 and RF3, as well as a minor population of 50S subunits. **(b-g)** Processing of 70S-tRNA-RF1-RF3 complexes that were prepared in the presence of API. **(b)** From an initial 703,379 particles, 177,784 non-aligning particles were discarded during 2D classification, yielding 525,595 ribosomal particles. An initial 3D classification was performed sorting the particles into 8 distinct classes, four major populations (states I-IV) containing RF1 and RF3, minor populations containing RF3 only (RF3-70S), vacant 50S subunits or conformational heterogeneous 70S ribosomes. States I to IV were subjected to another round of 3D classification. Moreover, focussed classification was employed to improve density for RF3 in states I-IV. The most stable (sub-)classes were 3D-refined using undecimated particles. **(c-g)** Fourier Shell Correlation (FSC_{0.143}; orange) with the resolution at FSC=0.143 indicated with a dashed line as well as FSC_{average} (blue) and self and cross-validated correlations FSC_{work} (red) and FSC_{test} (green), respectively, shown for **(c)** state I, **(d)** state II, **(e)** state III, **(f)** state IV and **(g)** RF3-70S complex.



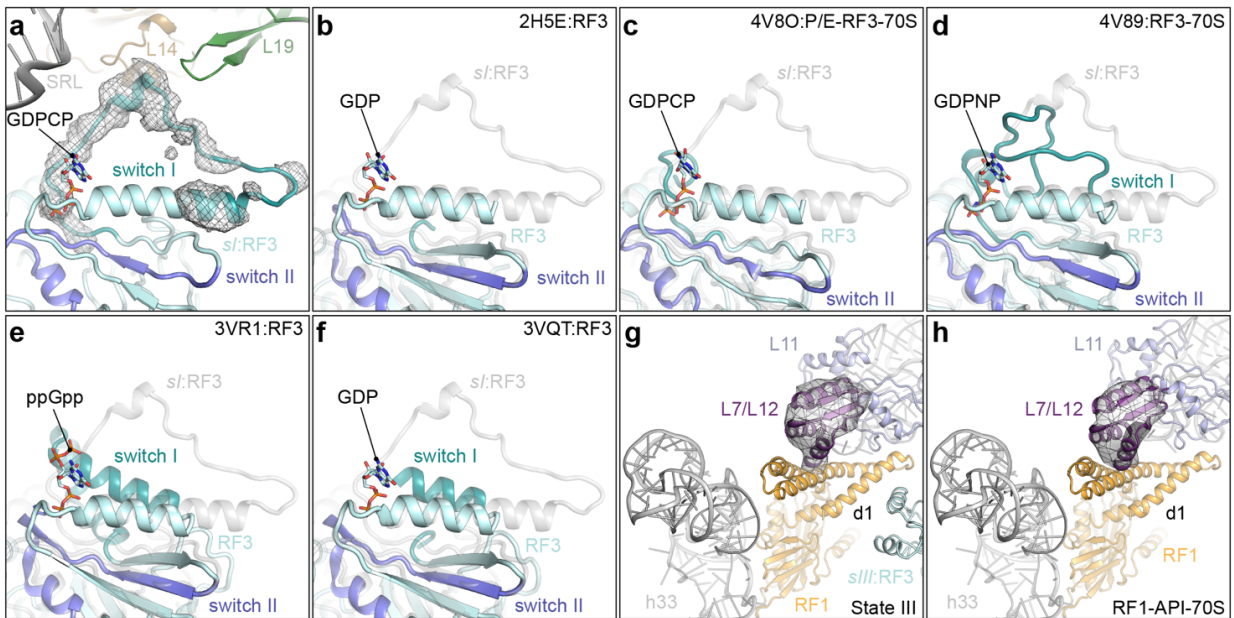
Supplementary Figure 2 Local resolution and molecular models for States I-IV and RF3-70S complex. **(a)** Overview (with schematics shown in first row) and **(b)** transverse section of the cryo-EM maps of the RF3-70S complex and states I-IV colored according to local resolution. Cryo-EM map density for ligands colored according to **(c)** local resolution, or **(d)** with fitted molecular models (displayed as ribbons) and transparent densities for RF3 (cyan), RF1 and tRNA (green).



Supplementary Figure 3 Interactions at the peptidyltransferase center in states I-IV. **(a-e)** The cryo-EM electron density (grey mesh) for API (salmon) bound within the ribosomal tunnel of **(a)** the RF1-API-70S complex²⁶ and **(b-e)** states I-IV. The relative position of the **(a)** P/P-site tRNA (green) and **(b-e)** P_{int}-tRNA are shown with A76 of the CCA-end labelled as well as and Gln235 of the GGQ motif of RF1. **(f-i)** The cryo-EM electron density (grey mesh) for the **(f)** P/P-site tRNA (salmon) in the RF1-API-70S complex²⁶ and **(g-i)** the P_{int}-tRNA (green) in state I with relative position of **(g)** canonical P/P-tRNA (salmon), **(h-i)** P_{int}-RNA (green) with **(h)** one or **(i)** two nucleotide shift in the interaction of the CCA-end with the P-loop. Red dashes in **(i)** indicate steric clashes between A76 and G2252, whereas red line indicates suboptimal distance for basepairing between C74 and C2254. **(j-k)** The cryo-EM electron density (grey mesh) for the **(j)** P/P-site tRNA (salmon) in the RF1-API-70S complex²⁶ and **(k,l)** cryo-EM electron density (grey mesh) for State I with **(k)** superimposition of a canonical P/P-site tRNA (salmon) and **(l)** the P_{int}-tRNA with one nucleotide shift, showing the location of nucleotide A73.



Supplementary Figure 4 Interaction of the G-domain of RF3 with the ribosome. **(a)** Superimposition of RF3 (different shades of green) from states I-IV, relative to the sarcin-ricin loop (SRL, grey) and ribosomal protein L6 (red) of the LSU. **(b)** Same view as **(a)** but with alignment of three different states of EF-Tu (PDB ID 5UYK; 5UYL; 5UYM)⁴⁰. **(c-f)** Superimposition of RF3 from state IV with **(c)** IF2, EF-Tu and EF-G together, or separately with **(d)** IF2 (lime, PDB ID 3JCN)⁶⁹, **(e)** EF-Tu (brown, PDB 5UYM)⁴⁰ and **(f)** EF-G (salmon, PDB 3JA1)⁷⁰. In **(c)**, the axis of rotation that aligns the G-domains of RF3 to the G-domain of the other translational GTPases is shown.



Supplementary Figure 5 Interaction of the switch I loop with large ribosomal subunit. (a) The ordered switch I loop (teal) of RF3 in state I is shown with the electron density (grey mesh) and relative to the SRL (grey) and ribosomal proteins L14 (tan) and L19 (green). (b-f) same view as (a) but with aligned structures showing disordered switch I loop in (B) RF3-GDP crystal structure (PDB ID 2H5E)¹⁷ and (c) RF3-70S complex with P/E-site tRNA (PDB ID 4V8O)²⁸ and ordered switch I loop (teal) in (d) RF3-70S complex without tRNA (PDB ID 4V89)²⁹, (e-f) RF3 crystal structure in complex with (e) ppGpp (PDB ID 3VR1)¹⁸ and (f) GDP (PDB ID 3VQT)¹⁸. In (a-f), the switch II loop (slate) is shown highlighted and in (b-f) the conformation of the switch I loop from (a) is shown in transparent grey for reference. (g-h) Cryo-EM electron density (grey mesh, filtered to 7 Å) for the CTD of L7/L12 (purple) interacting with domain 1 (d1) of RF1 (orange) and ribosomal protein L11 (light blue) in (g) state III and (h) the RF1-API-70S complex²⁶.

Supplementary Table 1 Rotational analysis of the 30S ribosomal subunit.

Complex	Head swivel (°)	Body/platform rotation (°)
State I	1.1	0.8
State II	1.6	1.7
State III	1.6	5.5
State IV	3.6	9.6
RF3-70S complex	5.7*	8.2
4v6r (A-tRNA + P-tRNA)	4.6	8.8
4v9d (P-tRNA only)	-1.2	1.1
4v9d (P/E-tRNA; RRF)	2.6	9.9
4v89 (RF3)	13.6	9.1
4v8o (P/E-tRNA; RF3)	3.6	10.1
5LZF (P/E-tRNA**)	3.2	10.4

*average head swivel; **fMetSec-tRNA^{Sec}

SUPPLEMENTARY VIDEO LEGENDS

Supplementary Video 1 Comparison of movements between state I to IV and RF3-70S. **(a-d)** The structures of state I-IV and the RF3-70S complex shown with view **(a)** into the factor binding site, **(b)** from above with transparent SSU and LSU, and **(c-d)** interface views of the **(c)** LSU and **(d)** SSU. The SSU (yellow), LSU (grey), RF1 (orange), tRNA (green) and RF3 (cyan) are shown as surface representations.

Supplementary Video 2 Comparison of RF3-70S complex with RF3-70S crystal structures. **(a)** The RF3-70S X-ray crystallography structures without tRNA (PDB ID 4V89)²⁹ and with hybrid P/E-site tRNA (PDB ID 4V8O)²⁸. **(b-c)** The RF3-70S complex compared with the RF3-70S X-ray crystallography structures **(b)** without tRNA (PDB ID 4V89)²⁹ and **(c)** with hybrid P/E-site tRNA (PDB ID 4V8O)²⁸.

Cryo-EM structure of the spinach chloroplast ribosome reveals the location of plastid-specific ribosomal proteins and extensions

Michael Graf¹, Stefan Arenz¹, Paul Huter¹, Alexandra Dönhöfer¹, Jiří Nováček² and Daniel N. Wilson^{1,3,*}

¹Gene Center, Department for Biochemistry and Center for integrated Protein Science Munich (CiPSM), University of Munich, 81377 Munich, Germany, ²Central European Institute of Technology (CEITEC), Masaryk University, Kamenice 5, 62500 Brno, Czech Republic and ³Department of Biochemistry and Molecular Biology, University of Hamburg, 20146 Hamburg, Germany

Received October 28, 2016; Revised December 01, 2016; Editorial Decision December 05, 2016; Accepted December 06, 2016

ABSTRACT

Ribosomes are the protein synthesizing machines of the cell. Recent advances in cryo-EM have led to the determination of structures from a variety of species, including bacterial 70S and eukaryotic 80S ribosomes as well as mitoribosomes from eukaryotic mitochondria, however, to date high resolution structures of plastid 70S ribosomes have been lacking. Here we present a cryo-EM structure of the spinach chloroplast 70S ribosome, with an average resolution of 5.4 Å for the small 30S subunit and 3.6 Å for the large 50S ribosomal subunit. The structure reveals the location of the plastid-specific ribosomal proteins (RPs) PSRP1, PSRP4, PSRP5 and PSRP6 as well as the numerous plastid-specific extensions of the RPs. We discover many features by which the plastid-specific extensions stabilize the ribosome via establishing additional interactions with surrounding ribosomal RNA and RPs. Moreover, we identify a large conglomerate of plastid-specific protein mass adjacent to the tunnel exit site that could facilitate interaction of the chloroplast ribosome with the thylakoid membrane and the protein-targeting machinery. Comparing the *Escherichia coli* 70S ribosome with that of the spinach chloroplast ribosome provides detailed insight into the co-evolution of RP and rRNA.

INTRODUCTION

Chloroplasts are organelles found in plant and algal cells, which are responsible for carrying out photosynthesis. The origin of chloroplasts is thought to result from an endosymbiotic event where an early eukaryotic cell engulfed a photo-

tosynthetic cyanobacterium (1). As such chloroplasts possess their own genome, as well as the transcription and translation machinery to convert the genetic information into polypeptides or proteins (2,3). Chloroplast ribosomes, or chlororibosomes, are very specialized since they are only involved in synthesizing the limited number of proteins encoded in the chloroplast genome (2,3). For example, the complete genome sequence of the *Spinacea oleracea* (spinach) chloroplast contains 146 genes encoding protein products and structural RNAs (4). The majority of the chloroplast-encoded proteins are targeted to the chloroplast thylakoid membranes and encompass components of the adenosine triphosphate (ATP) synthase, cytochrome b/f and photosystem I and II complexes (4). In addition, chlororibosomes translate NADH dehydrogenase, the large subunit (LSU) of RuBisCO, RNA polymerase subunits and a distinct subset of ribosomal proteins (RPs), 12 from the small subunit (SSU) and 8 from the LSU. Other proteins essential for chloroplast function are nuclear encoded and must therefore be imported into the chloroplast. This includes the remaining 32 chloroplast RPs (cpRPs), which bear N-terminal chloroplast-targeting sequences that are cleaved off upon import (5,6).

Sequence comparisons indicate that the components of the chloroplast translational machinery are similar to those of eubacteria, especially cyanobacteria, but also γ -proteobacteria, such as *Escherichia coli*. The chloroplast 16S rRNA (cp16S) of the SSU contains 1491 nucleotides (nts) and is therefore only slightly smaller than the *E. coli* 16S rRNA (Ec16S), which has 1542 nts. The *E. coli* LSU contains 2 rRNAs, the 5S (120 nts) and 23S (2904 nts) rRNAs, totaling to 3024 nts. While the chloroplast LSU comprises 3 rRNAs, 5S (121 nts), 4.8S (103 nts) and 23S (2810 nts) rRNAs, the total length of 3034 nts is only slightly larger (10 nts) than in *E. coli*. Similarly, chlororibosomes contain a total of 52 cpRPs (25 in the SSU and 33 in the

*To whom correspondence should be addressed. Tel: +49 89 2180 76903; Fax: +49 89 2180 76945; Email: wilson@lmb.uni-muenchen.de

© The Author(s) 2016. Published by Oxford University Press on behalf of Nucleic Acids Research.
This is an Open Access article distributed under the terms of the Creative Commons Attribution License (<http://creativecommons.org/licenses/by-nc/4.0/>), which permits non-commercial re-use, distribution, and reproduction in any medium, provided the original work is properly cited. For commercial re-use, please contact journals.permissions@oup.com

LSU) and with the exception of L25 and L30, have orthologs in *E. coli* (5,6). However, the cpRPs are generally larger than their *E. coli* counterparts, predominantly due to N- and C-terminal extensions (NTEs and CTEs) (5,6). Proteomic studies also identified six non-orthologous proteins, termed ‘plastid-specific RPs’ (or PSRPs) (5–7). Four PSRPs (PSRP1–4) were found to be associated with the SSU and two (PSRP5 and PSRP6) with the LSU (5–7). A cryo-EM reconstruction of the spinach chlororibosome at 9.4 Å provided first insights into the localization of the PSRPs and cpRP extensions (8), however, higher resolution is required to accurately assign and describe the interactions of the PSRPs and cpRP extensions within the chlororibosome.

Here we present a cryo-EM structure of the spinach chlororibosome, with an average resolution of 5.4 Å for the SSU and 3.6 Å for the LSU, revealing the binding site of the PSRP1, PSRP4, PSRP5 and PSRP6 as well as the conformation of numerous cpRP extensions. The structure illustrates how cpRP extensions and PSRPs wind their way through the core of the chlororibosome establishing interactions with neighboring rRNA and RPs. In many cases, the cpRP extensions interact with RNA or protein features that are specific to the chlororibosome, thus providing insight into their co-evolution. We also identify a large conglomerate of cpRP mass adjacent to the tunnel exit site that we suggest facilitates interaction of the chlororibosome with the thylakoid membrane and the protein-targeting machinery.

MATERIALS AND METHODS

Isolation of chloroplast 70S ribosomes

Chloroplast ribosome isolation was performed as described previously (9). Briefly, 6 kg of spinach leaves were de-veined and washed thoroughly. The leaves were homogenized (21/kg of leaves) using 0.7 M Sorbitol in buffer A (10 mM Tris-HCl pH 7.6, 50 mM KCl, 10 mM MgOAc, 7 mM β -mercaptoethanol). The homogenate was filtered through several layers of cheesecloth and one layer of Miracloth (Calbiochem) before centrifugation at 1200 \times g for 15 min. The pellet was resuspended in 0.4 M Sorbitol in buffer A and re-centrifuged at 1200 \times g for 15 min. The washed chloroplast pellet was resuspended in buffer A supplemented with 2% (v/v) Triton-X100 and incubated on ice for 30 min. The lysed suspension was clarified by centrifugation at 26 000 \times g for 30 min before isolation of crude ribosomes by centrifugation at 50 000 \times g for 24 h through a 1M sucrose (in buffer B: buffer A with 10% glycerol). The greenish pellet was washed and then resuspended in buffer B with gentle agitation. The crude ribosomes were clarified by centrifugation at 26 000 \times g for 15 min before being either snap frozen at –80°C. Alternatively, the clarified supernatant was applied directly onto a 10–30% sucrose gradient (in buffer B) in order to obtain tight-coupled chloroplast 70S ribosomes.

Negative-stain electron microscopy

Ribosomal particles were diluted in buffer A to a final concentration of 5 A₂₆₀/ml. One drop of each sample was deposited on a carbon-coated grid. After 30 s, grids were

washed with distilled water and then stained with 2% aqueous uranyl acetate for 15 s. The remaining liquid was removed by touching the grid with filter paper. Micrographs were taken using a Morgagni transmission electron microscope (FEI), 80 kV, wide angle 8K CCD at direct magnifications of 110K.

Cryo-electron microscopy and single particle reconstruction

A total of 5 A₂₆₀/ml chloroplast ribosome sample was applied to 2 nm pre-coated Quantifoil R3/3 holey carbon supported grids and vitrified using a Vitrobot Mark IV (FEI, Eindhoven). Data collection was performed using an FEI Titan Krios transmission electron microscope equipped with a Falcon II direct electron detector (FEI, Eindhoven), using a pixel size of 1.061 Å and an underfocus range of 1.0–2.3 μm resulting in 2031 micrographs. Each micrograph was recorded as a series of 7 frames (3.9 e[–]/Å² pre-exposure; 5.2 e[–]/Å² dose per frame). All seven frames (accumulated dose of 40.3 e[–]/Å²) were motion-corrected using the Unblur program (10) and power-spectra, defocus values, astigmatism and estimation of micrograph resolution were determined using CTFFIND4 (11). Five hundred and forty-five micrographs showing Thon rings beyond 3.2 Å resolution were manually inspected further for good areas and power-spectra quality. Three times decimated data were pre-processed using the SPIDER software package (12), in combination with an automated workflow as described previously (13). After initial, automated particle selection based on the program SIGNATURE (14), initial alignment was performed with 56 475 particles using *E. coli* LSU as a reference structure (15). The dataset could be sorted into 37 626 (66.6%) ribosomal particles and 18 849 (33.3%) non-aligning particles using an incremental K-means-like method of unsupervised 3D sorting (16) (Supplementary Figure S2). Undecimated ribosomal particles were again initially aligned against an *E. coli* LSU and subsequently refined using FREALIGN (17). Since the SSU of the chlororibosome was flexible, focused alignment and refinement was performed by applying masks either on the SSU or LSU. Due to inherent flexibility, the SSU of the chlororibosome could be refined to an average resolution of 5.4 Å (0.143 FSC) and a local resolution extending to 5.0 Å for the core, whereas the LSU of the chlororibosome could be refined to an average resolution of 3.6 Å (0.143 FSC) and a local resolution extending to <3.5 Å for the core. The local resolution of the final maps was computed using ResMap (18) (Supplementary Figure S2). The final maps were sharpened by dividing the maps by the modulation transfer function of the detector and by applying an automatically determined negative B-factor (–86 for the LSU and –130 for the SSU) to the maps using RELION (19).

Molecular modeling and map-docking procedures

The molecular model of the chloroplast LSU was based on the *E. coli*-70S-EF-Tu structure (20). The 23S rRNA secondary structure was initially generated by manual alignment of the chloroplast 23S rRNA sequence and the secondary structure map (21) to the *E. coli* 23S secondary structure map, which shows high structural similarity. The

16S, 5S and 4.8S rRNA sequences of the chloroplast ribosome were aligned accordingly. The resulting rRNA homology models were rigid-body fitted into the respective chloroplast EM-map using Chimera (22). Subsequently, the models were manually adjusted and refined using Coot (23). *E. coli*-based (20) homology models of the cpRPs were built using SwissModel (24) and HHpred (25) and rigid-body fitted into the map. cpRP-specific extensions were modeled in Coot (23). PSRP5 and PSRP6 were modeled *de novo*, using secondary structure predictions generated by PsiPred (26) as a reference. The complete atomic model of the chloroplast LSU was subsequently refined using *phenix.real_space_refine* (27) with secondary structure restraints calculated by PHENIX. In order to reduce the clashscore, the model was additionally refined in reciprocal space using REFMAC (28) in EM mode. Cross-validation against overfitting was performed as described elsewhere (29,30). The statistics of the refined model were obtained using MolProbity (31).

Figure preparation

All figures showing electron densities and atomic models were generated using UCSF Chimera (22) and PyMol Molecular Graphics Systems (version 1.8 Schrödinger).

RESULTS AND DISCUSSION

Cryo-EM structure of the chloroplast 70S ribosome

Chloroplast 70S ribosomes were isolated from *S. oleracea* (spinach) leaves as described previously (8,9) and subjected to single particle cryo-EM analysis. The cryo-EM data was collected on a Titan Krios transmission electron microscope with a Falcon II direct electron detector. From a total of 56,475 ribosomal particles, *in silico* sorting revealed extreme flexibility of the SSU with respect to the LSU (Supplementary Figure S1). To overcome this conformational heterogeneity, focused alignment was performed independently for each ribosomal subunit using FREALIGN (17). Subsequent refinement yielded cryo-EM reconstructions of the chloroplast SSU and LSU (Figure 1A–D), with an average resolution of 5.4 Å and 3.6 Å, respectively (Supplementary Figure S2 and Table S1).

Analysis of the chloroplast SSU

The resolution of the SSU allowed a homology model of the spinach chloroplast SSU to be rigid body fitted based on the high sequence similarity between the *E. coli* and *S. oleracea* rRNA and RPs (8). As already noted (8), the major difference with respect to the 16S rRNA is the shortening of helices h6, h10 and h17 in the chlororibosome rRNA, leading to a truncated spur (Figure 1A and B) when compared to the *E. coli* SSU. In the previous chlororibosome cryo-EM structure, additional protein density was observed, which was tentatively assigned to PSRP2 and PSRP3, and proposed to compensate for the truncated spur rRNA (8). At higher resolution, this extra spur density was not well-resolved (Figure 1A and B), however, filtering at lower resolution indeed revealed extra density within this region (Supplementary Figure S3). The mass of the extra spur density

could not account fully for either PSRP2 or PSRP3, suggesting that if one of these PSRPs is bound there it is highly flexible.

As mentioned, the *S. oleracea* cpRPs are larger than their respective *E. coli* counterparts due to the presence of NTEs and/or CTEs (6). To ascertain the location of the cpRP extensions, homology models for the *S. oleracea* cpRPs were generated based on *E. coli* templates (20,32), which were then fitted to the cryo-EM map of the chloroplast SSU (Figure 1A and B). In many cases, additional density continuous with the N- or C-termini of the cpRPs could be identified, consistent with the presence of predicted *S. oleracea* cpRP-extensions that are absent in the respective *E. coli* RPs (Figure 1A and B). For example, density was observed for the NTE of cpS5, which is 86 aa longer than *E. coli* S5 (EcS5) (6). In addition, density for the NTEs of cpS9, cpS10 and cpS21 and the CTEs of cpS16 and cpS18 were observed, as well as a rearrangement of the N-terminus of cpS4. The extensions of the cpRPs are located exclusively on the back or cytosolic side of the SSU, but nevertheless encroach on two functional regions related to the path of the mRNA. Specifically, the CTE of cpS18 and the NTE of cpS21 are located at the platform region in vicinity of where the Shine-Dalgarno helix forms between the 5' end of the mRNA and the 3' end of the 16S rRNA (Supplementary Figure S3). The N-terminus of cpS4, and particularly the NTE of cpS5, surround the mRNA entry channel (Figure 1A and B; Supplementary Figure S3). Curiously, we also observed extra density in this region that does not originate from any of the neighboring cpRP extensions. The extra density connects the head and body of the 30S subunit, namely, bridging the tip of helix h16 in the body with cpS3 of the head. This connection is often referred to as the 'latch' because it has been observed to open and close during translation initiation (33,34). Mass spectrometry analysis did not detect additional non-orthologous proteins on the spinach chloroplast SSU (5–7), therefore, the additional density may actually be derived from part of PSRP2 or PSRP3, but we cannot exclude that it is derived from unrelated proteins.

Finally, we identified two additional densities that we assigned to PSRP1 and PSRP4 (Supplementary Figure S4A and B). In agreement with the previous localization (8), we allocated the density within the head of the SSU to PSRP4 (Figure 1A and B) based on its similarity in sequence and binding position with Thx, a small RP identified in the *Thermus thermophilus* SSU (35). Similarly, we assigned the additional density located within the decoding site on the inter-subunit side of the SSU to the N-terminal domain (NTD) of PSRP1, as reported previously (8,36). Sequence alignments indicated that PSRP1 is not a *bona fide* cpRP but rather a homolog of a long form hibernation-promoting factor, which is responsible for 100S formation (70S dimerization) (37). The NTD of PSRP1 is homologous with YfiA and the short form HPF, both of which have also been shown to bind analogously to the SSU of bacterial 70S ribosomes (38,39), overlapping the binding site of the mRNA and tRNAs in the A- and P-sites (Supplementary Figure S4C and D). No density was observed for the C-terminal domain of PSRP1, which has been shown to be responsible for 100S formation in some bacteria (40,41).

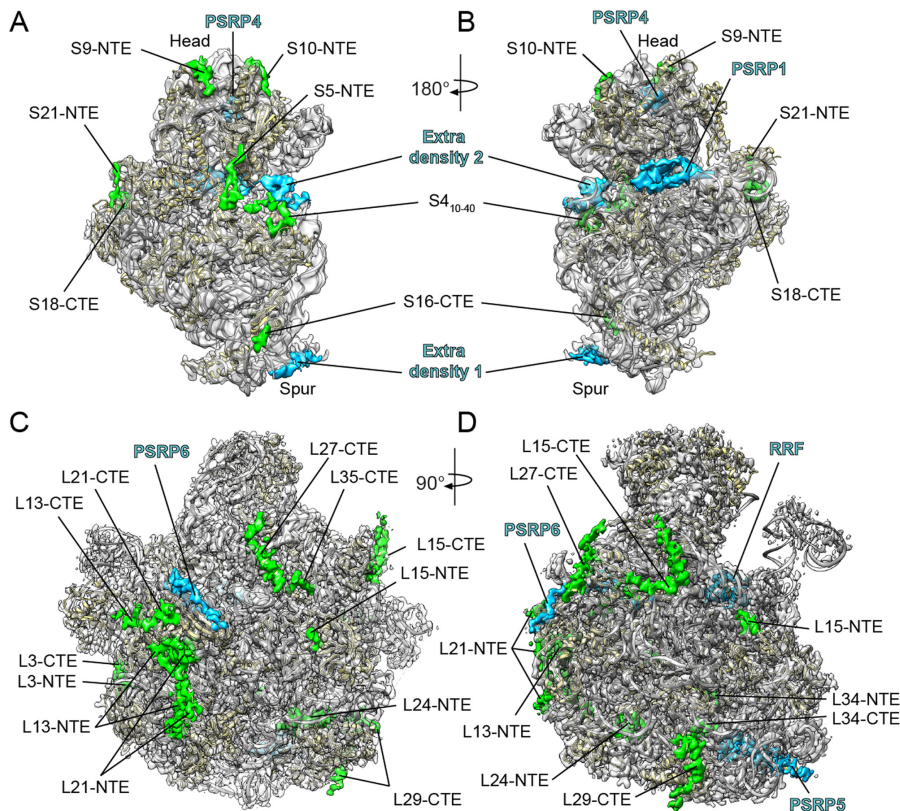


Figure 1. Cryo-EM structure of the chloroplast SSU and LSU. (A–D) Cryo-EM map (transparent gray) of the spinach chloroplast (A and B) SSU and (C and D) LSU, illustrating the additional density for cpRNPs (green) and extra density assigned to PSRPs (blue) and the ribosome recycling factor (RRF). The molecular model for the SSU and LSU includes rRNA (gray) and cpRNPs (yellow).

Molecular model for the chloroplast LSU

Consistent with the local resolution calculations (Supplementary Figure S2), the electron density was particularly well resolved within the core of the LSU, whereas the periphery of the subunit was less defined. We were able to generate molecular models for 28 of the 33 cpRNPs present in the chlororibosome (Figure 2A–C; Supplementary Table S2). cpRNPs L1, L10, L11, L7/L12 and L31 were not modeled due to poor density. The density for cpL5, cpL6 and cpL18 allowed only a rigid body fit of a homology model based on EcL5 and EcL6, and only the NTD of cpL9 was included in the final model. As observed previously (8), density was not observed for L25 and L30, consistent with the absence of genes encoding these cpRNPs in plant and chloroplast genomes (4). We could also model domain I of the chloroplast ribosome recycling factor (cpRRF) (Supplementary Figure S4), which was bound analogously to that reported previously on the chlororibosome at lower resolution (8) as well as on bacterial ribosomes (42,43). Together with cpEF-G, cpRRF has been demonstrated to dissociate PSRP1 from the chlororibosome (36). In addition, molecular models are presented for the complete 5S and 2843 (97.6%) of the 2913 nucleotides that comprise the 4.8S and 23S rRNAs (Figure 3A and B; Supplementary Figure S5).

Features of the chloroplast LSU rRNAs

Unlike the mammalian mitoribosome where a tRNA molecule substitutes for the lack of a 5S rRNA (44,45), the chlororibosome contains a 5S rRNA (Figure 3A and B) that is highly similar in sequence and structure to the bacterial 5S rRNA. As mentioned, the chloroplast 23S rRNA is present in the chlororibosome as two pieces, a 5' fragment representing H1–H97 of domains I–VI (hereafter referred to as cp23S rRNA) and a 3' fragment comprising H99–H101 of domain VII (termed 4.8S rRNA) (Figure 3A and Supplementary Figure S5). This results in the loss of H98 (Δ16 nts) that links domains VI and VII within the *E. coli* 23S (Ec23S) rRNA (Figure 3C). Together with reductions in helices H9 (Δ14 nts), H45, (Δ6 nts), H63 (Δ27 nts) (Figure 3A and B), the cp23S rRNA has a total of 75 nts missing relative to the Ec23S rRNA. While the reductions lead to a shortening in the length of H9 and H45 (Figure 3D and E), the effect on H98 and H63 results in the complete absence of these helices in the chlororibosome (Figure 3C and F). Nevertheless, the combined length of the chloroplast LSU rRNA (3034 nts) is similar to that for *E. coli* (3024 nts) because the four rRNA reductions in the cp23S rRNA are compensated by five rRNA additions (8). This includes additional nucleotides within H15 (+30 nts), H38 (+20 nts), H58 (+23 nts) and H68 (+4 nts) of the cp23S rRNA, as well as +8

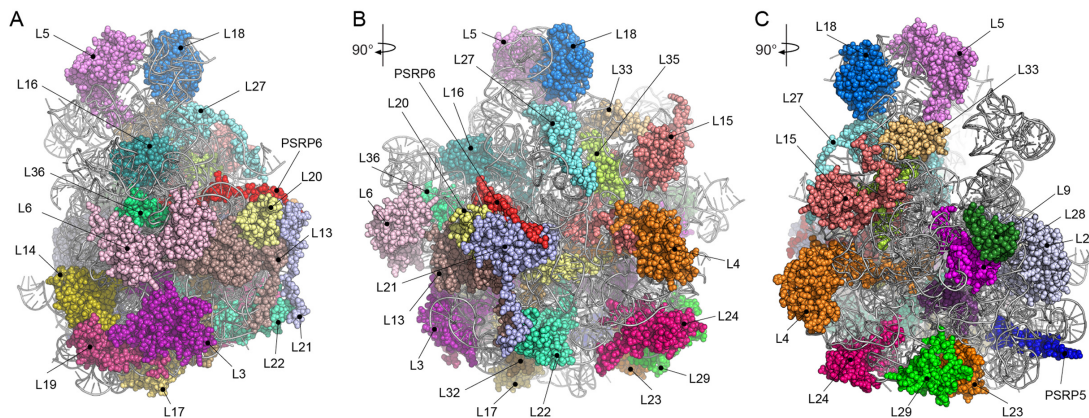


Figure 2. Molecular model for the chloroplast LSU. (A–C) Three overviews of the chloroplast LSU with rRNA (gray ribbons) and modeled cpRPAs and PSRPAs shown with a spacefill representation and colored and labeled individually.

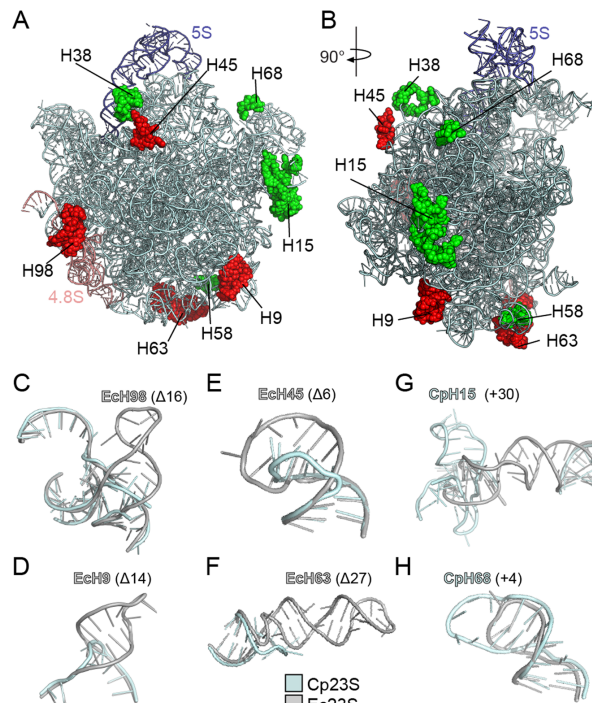


Figure 3. Location of rRNA insertions and deletions in the chlororibosome. (A and B) Two overviews of the chloroplast LSU with 4.8S (teal), 5S (purple) and 23S (cyan) rRNA, highlighting insertions (green) on the cp23S and deletions (red) relative to Ec23S. (C–F) Examples of deletions in the cp23S (cyan) relative to the Ec23S (gray) include deletion of (C) 16 nts in H98, (D) 14 nts in H9, (E) 6 nts in H45 and (F) 27 nts in H63. (G and H) Examples of additions in the cp23S (cyan) relative to the Ec23S (gray) include insertion of (G) 30 nts in H15 and (H) 4 nts in H68.

nt insertion in the linker connecting H100 and H101 of the 4.8S rRNA (Figure 3A and B). The insertions within H15 (Figure 3G) and H68 (Figure 3H) are base-paired and well resolved in the model, whereas the density for the non-base-

paired insertions within H38 and the H100–H101 linker are poorly defined and therefore not included in the final model.

Localization of cpRPAs and extensions

In contrast to the SSU cpRPAs, the LSU cpRPAs are significantly longer than their *E. coli* counterparts due to the presence of NTEs and/or CTEs (5). As expected, additional density continuous with the N- or C-termini of the LSU cpRPAs was observed (Figure 1C and D), allowing 283 amino acids of the cpRP extension to be modeled (Figure 4A; Supplementary Table S2). In particular, cpRPAs L13, L15, L21, L22, L24, L27, L29 and L34 have long NTEs and/or CTEs (Figure 4A). In addition, cpL33 has a β-hairpin with an internal expansion of 13 aa compared to EcL33 (Figure 4A). There are four major exceptions of cpRPAs (L2, L17, L19 and L23) that have significant deletions (>2 aa) compared to their *E. coli* counterparts. In the chlororibosome, cpL17 is C-terminally truncated by 11 aa, although only 4 aa of these are observed in the *E. coli* 70S ribosome structures (20,32). The N-terminus of cpL2 is shorter than EcL2 by only 6 aa, yet we observed no density for the first 25 aa (Figure 4B). Similarly, the CTE of cpL19 is not only 4 aa shorter than EcL19, but the last 11 aa also adopt a distinct conformation (Figure 4B). Lastly, the β-hairpin of EcL23 that reaches into the tunnel lumen in the *E. coli* ribosome (20,32) is significantly shorter in the chlororibosome (Figure 4B), reminiscent of the archaeal/eukaryotic L23 homologs (46,47). However, unlike archaeal/eukaryotic ribosomes that compensate for the truncated L23 with the presence of aeL38 (46,47), the equivalent space remains vacant in the chlororibosome.

Binding sites of PSRP5 and PSRP6 on the LSU

Subsequent to modeling of the LSU rRNAs as well as all the cpRPAs and cpRP extensions, we noticed that two unmodeled regions of electron density were present in the cryo-EM map, which we assigned to PSRP5 and PSRP6 (Figure 1C and D). Due to their buried location within the chlororibosome, the electron density was well resolved (Figure 5A and

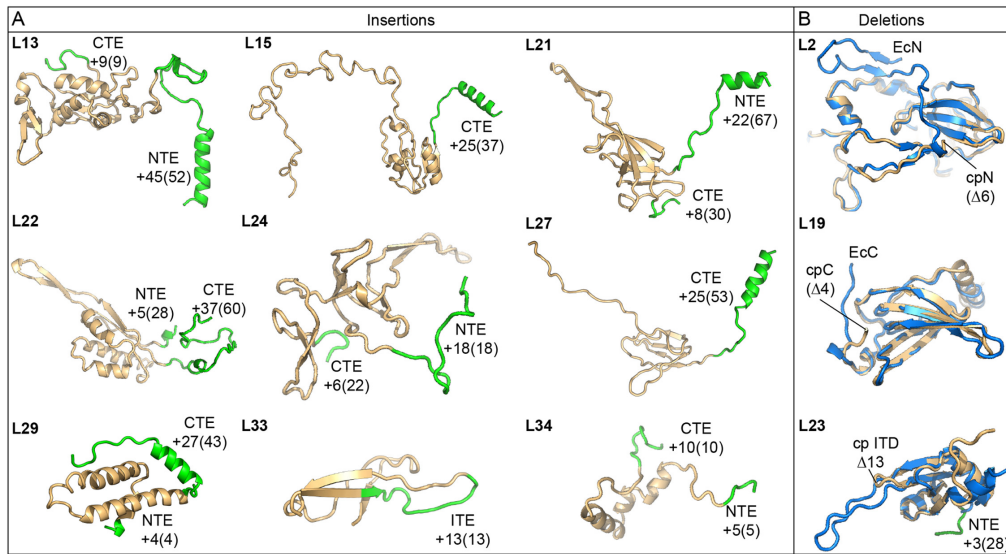


Figure 4. Molecular models indicating cpRP extensions and deletions. (A) Structures of cpRPs showing the core region equivalent to the respective EcRPs (gold) with N-terminal extensions (NTEs), C-terminal extensions (CTEs) or the internal expansion (ITE) highlighted (green). The numbers indicate the modeled residues with the total expansion length indicated in parentheses. (B) Structures of cpRPs (gold) compared with the respective EcRPs (blue) highlighting amino acid deletions (in parentheses) in cpRPs relative to EcRPs.

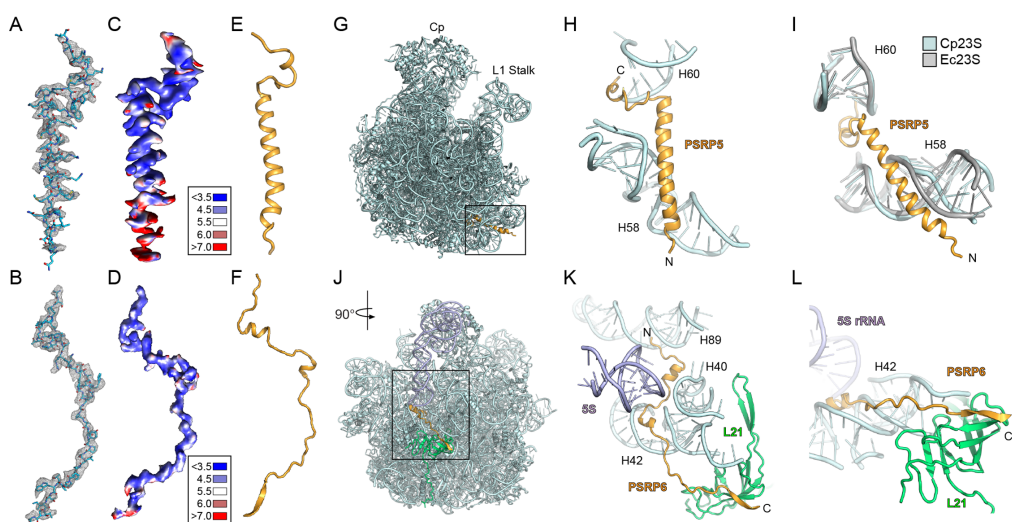


Figure 5. Localization of PSRP5 and PSRP6 on the chlororibosome. (A and B) Cryo-EM electron density (mesh) with molecular models for (A) PSRP5 and (B) PSRP6. (C and D) Cryo-EM electron density for (C) PSRP5 and (D) PSRP6 colored according to local resolution. (E and F) Molecular models showing secondary structure for (E) PSRP5 and (F) PSRP6. (G) Binding site of PSRP5 (gold) on the LSU (cyan). (H and I) Interaction between PSRP5 (gold) and H58 and H60 of the cp23S rRNA (cyan), with (I) comparison of different conformation of H58 from the Ec23S rRNA (gray). (J) Binding site of PSRP6 (gold) on the LSU (cyan). (K and L) Interaction between the N-terminus of PSRP6 (gold) and H40, H42 and H89 of the cp23S rRNA (cyan), and (L) the C-terminus of PSRP6 (gold) with the cpL21 (green).

B), in agreement with local resolution calculations (Figure 5C and D), enabling unambiguous models for both PSRP5 and PSRP6 to be generated (Figure 5E and F; Supplementary Figure S4). Consistent with secondary structure predictions, PSRP5 consists of a short C-terminal α -helix connected by a linker to a long central α -helix (Figure 5E). The binding site of PSRP5 is located at the base of the LSU directly under the L1 stalk, with the N-terminus extending to-

ward the intersubunit interface (Figure 5G). We note that 38 aa are missing from the N-terminus in our model, presumably due to flexibility outside of the ribosome. The surface of the buried regions of PSRP5 is highly positively charged (Supplementary Figure S4F and G), as would be expected from the surrounding negatively charged rRNA environment. The short C-terminal α -helix of PSRP5 inserts into the minor groove of H60, whereas the central α -helix es-

tabishes interactions with H58 (Figure 5H). The specificity of PSRP5 for the chlororibosome may be due to the interaction with H58, since there are significant differences in both the sequence and structural conformation of H58 when comparing with the *E. coli* 70S ribosome (Figure 5I). We note that the position of PSRP5 was mis-assigned in the previous structure of *S. oleracea* chloroplast 70S ribosome (8), probably due to the small size of the protein and the limited resolution of the reconstruction.

PSRP6 adopts a very extended conformation (Figure 5F) that winds its way through the ribosome (Figure 5J–L). The N-terminal half of PSRP6 is predominantly positively charged (Supplementary Figure S4I–K), consistent with the extensive interaction with the negatively charged rRNA (Figure 5K). The N-terminus of PSRP6 interacts with the minor grooves of H89, H40 and H42 as it winds its way out of the ribosomal core (Figure 5K). The two short central α -helices of PSRP6 are positioned within the minor grooves of H40 and H42 and are separated by a linker region that passes near to the 5S rRNA (Figure 5K). The C-terminal half of PSRP6 is less charged (Supplementary Figure S4I), consistent with an interaction with the globular domain of cpL21, rather than with rRNA. The C-terminus of PSRP6 donates a β -strand to augment the β -sheet of cpL21 (Figure 5L) before extending into the solvent where the C-terminal 22 aa are not visualised. The conservation of this region between *S. oleracea* chloroplast and *E. coli* 70S ribosomes suggests that PSRP6 could in principle bind analogously to the *E. coli* 70S ribosome.

cpRP extensions and rRNA stabilization

Generally, the NTE and CTE of cpRPs contain positively charged amino acids that establish additional interactions with the surrounding rRNA, predominantly with the phosphate-oxygens of the backbone. For example, the 10 aa CTE of cpL34 interacts with the loop of helix H8 of the 23S rRNA and forms a potential hydrogen bond from Lys148 with the backbone of U1638 within H51 (Figure 6A). In many cases, the cpRP extensions interact with the minor groove of rRNA helices. Such an interaction is illustrated by the 25 aa CTE of cpL15, which inserts into the minor groove of a helix formed from the loops of H22 and H88 (Figure 6B). Lys243 comes within hydrogen bonding distance of the ribose of A427 and Tyr241 stacks upon A213 that makes an A-minor interaction within the H22/H88 helix (Figure 6B). Similarly, the 18 aa NTE of cpL24 that penetrates deeper into the ribosomal core, approaches the minor groove of an rRNA helix formed from the loops of H6 and H7, before the N-terminus emerges within the tunnel lumen (see later).

We also observed that the cpRP extensions often reinforce interactions with rRNA elements that are already contacted by the core of the cpRP, as illustrated by cpRPs L35 and L13 (Figure 6C and D). Arg140 in the core of cpL35 contacts the phosphate-oxygen of G966 in H38, an interaction also observed for EcL35 (Figure 6C). This contact is reinforced in the chlororibosome by a potential hydrogen bond from Arg157 within the 7 aa CTE of cpL35 to the backbone of C966 within H38 (Figure 6C). Similarly, the interaction from Arg126 in the core of cpL13 with A1170 in H41 is reinforced in the chlororibosome by an additional

hydrogen bond from Arg245 within the NTE of cpL13 to the backbone of A1170 within H41 (Figure 6D).

Three of the cpRP extensions contain α -helical secondary structure, namely within the NTE of cpL13 and the CTEs of cpL15 and cpL27 (Figure 4A). The α -helix within the CTE of cpL15 interacts with H68, which as mentioned is extended in the chlororibosome compared to the *E. coli* 70S (Figure 3H). In the chlororibosome, the NTE of cpL13 forms an α -helix that interacts with the junction where the 5' end of the 4.8S rRNA meets the 3' end of the cp23S rRNA (Figure 6E). Comparison with the *E. coli* 70S ribosome revealed that the N-terminal α -helix of cpL13 occupies the position of H10 of the Ec23S rRNA (Figure 6F), which is absent in the chlororibosome (Figure 6E). The α -helix within the CTE of cpL27 appears to stabilize a three-way junction formed by the insertion of 20 nts within H38 of the cp23S rRNA (Figure 6G), which is lacking in the Ec23S rRNA (Figure 6H). The site of insertion in H38 in the cp23S rRNA correlates with the position of expansion segment 12 (ES12L) in eukaryotic 80S ribosomes (47,48). In the *E. coli* ribosome, EcL30 contacts H38 in the vicinity of the insertion site (Figure 6H). Such an L30-H38 interaction would not be possible in the chlororibosome due to the presence of the additional rRNA helix in H38, thus providing a possible explanation as to why L30 is missing in plant chloroplasts.

Intertwining of cpRP extensions at the tunnel exit

A number of differences with the *E. coli* 70S ribosome were evident when examining the back or cytosolic side of the LSU of the chlororibosome, in particular, the region surrounding the tunnel exit site. As mentioned, the β -hairpin of cpL23 is shorter than EcL23 leading to an enlarged luminal space near the exit site of the chlororibosome (Figure 7A–C). In contrast, the opposite side of the tunnel from cpL23 has extra mass due to the presence of the NTE of cpL24 that penetrates into the ribosomal core from the surface located globular domain (Figure 7B). The 27 aa CTE of cpL29 intertwines with the NTE of cpL23 (Figure 7B), which together occupy the space where 23S rRNA helix H10 is situated in the *E. coli* 70S ribosome (Figure 7C). Comparison with the binding site of *E. coli* SRP on the ribosome (49,50), suggests that the CTE of cpL29 could play a role in recruiting cpSRP54 to the chlororibosome (Figure 7D).

By far the largest conglomerate of cpRP extensions is located at the back of the LSU adjacent to the tunnel exit site (Figure 7E). This conglomerate comprises the 45 aa (of 52 aa) NTE of cpL13, 22 aa (of 67 aa) from the NTE of cpL21 and 37 aa (of 60 aa) CTE of cpL22, which reach out from the respective globular domains to form multiple protein–protein interactions with each other (Figure 7F). The high flexibility of the extensions, and the poor quality of the density at the periphery of the ribosome, enabled only the backbone of the protein extensions to be traced. Moreover, the N-terminal 45 aa of the NTE of cpL21 could not be modeled, although density was observed at lower thresholds suggesting that these residues establish additional interactions with the CTE of cpL22. Collectively, these cpRP extensions expand the area of the LSU and could facilitate interaction with the thylakoid membrane (Figure 7E).

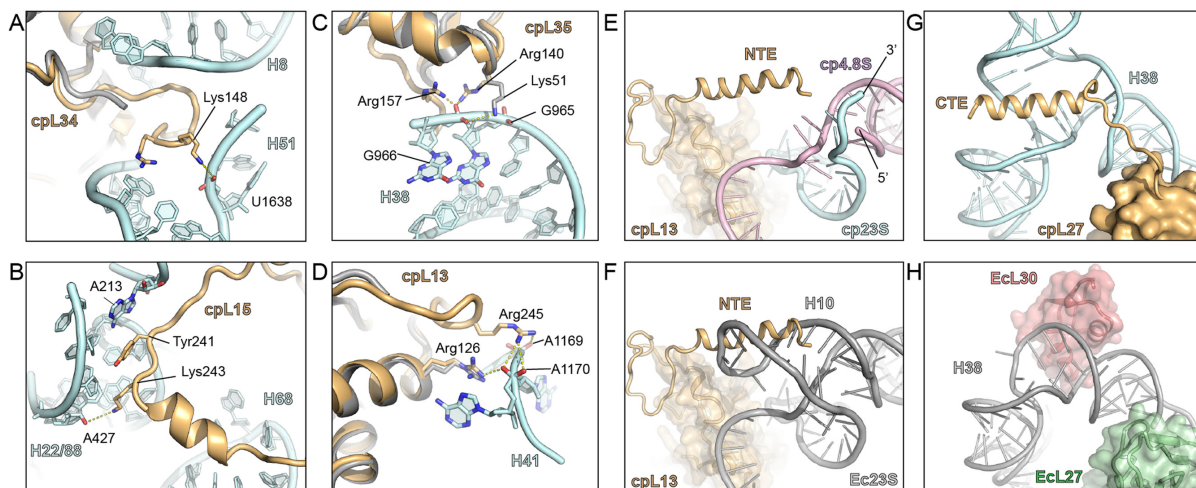


Figure 6. Interaction of cpRP extensions with rRNA. (A–D) Examples of interaction of cpRP extensions (gold) with cp23S rRNA (cyan) include the (A) CTE of cpL34 with H51, (B) CTE of cpL15 with H22/H88, (C) CTE of cpL35 with H38 and (D) NTE of cpL13 with H41. (E) Interaction of NTE of cpL13 (gold) with the 3' end of the cp23S (cyan) and the 5' end of the 4.8S (pink) in the chlororibosome, superimposed with the (F) *Escherichia coli* 70S ribosome showing that H10 of the Ec23S (gray) overlaps with the NTE of cpL13 (gold). (G) Interaction of CTE of cpL27 (gold) with the three-way junction of H38 (cyan) of the chlororibosome, whereas in the (H) *E. coli* 70S ribosome, EcL27 (green) has no extension and H38 (gray) is bound by EcL30 (red).

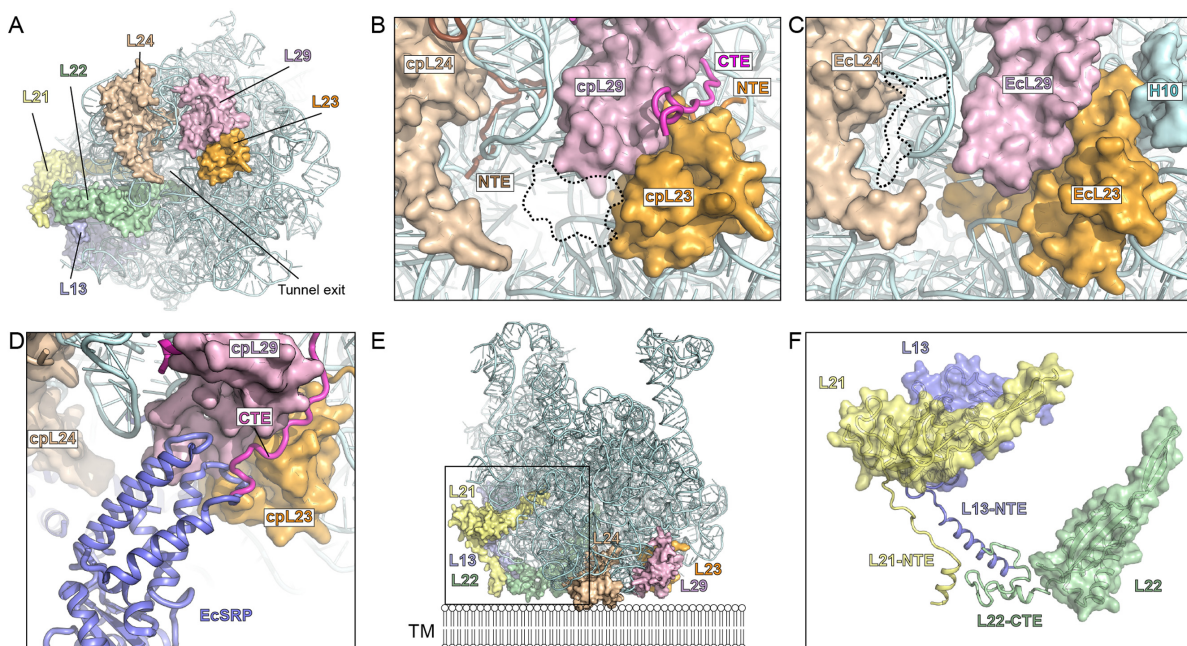


Figure 7. Interaction of cpRP extensions with rRNA. (A) View onto the tunnel exit site of the chloroplast LSU with rRNA (cyan) and highlighting cpRPs L23 (orange), L29 (purple), L24 (tan), L22 (green), L13 (blue) and L21 (yellow). (B) Zoom of (A) highlighting the NTE of cpL24 and cpL23, and the CTE of cpL29 as well as the shorter β -hairpin of cpL23. (C) Equivalent view of (B) but for *Escherichia coli* 70S ribosome, highlighting the absence of EcL24-NTE and the presence of the β -hairpin of EcL23 in the tunnel lumen, as well as H10 of Ec23S rRNA. (D) Superimposition of EcSRP (blue) on chlororibosome illustrating overlap with the CTE of cpL29. (E) Chloroplast LSU, colored as in (A), illustrating additional cpRP protein mass that expands the potential surface area of the LSU and facilitates its possible interaction with the thylakoid membrane (TM). (F) Zoom of boxed region in (E) without rRNA to illustrate the contribution of the cpRP extensions (NTE/CTE) of L21 (yellow), L13 (blue) and L22 (green) to the thylakoid membrane interaction surface.

CONCLUSION

Here we present a near-complete molecular model for the spinach chloroplast LSU, revealing the location of rRNA insertions and deletions, cpRP extensions as well as the binding site of two plastid-specific RPs, PSRP5 and PSRP6. Prior to submission, a cryo-EM structure of the spinach chloroplast 50S subunit was reported by Ahmed and coworkers (51). Generally, the results appear to be in good agreement with our structure, although a careful comparison cannot be undertaken as the cryo-EM map and model were not yet available at the time of submission, nor during the review process. In general, the differences of the chlororibosome with respect to the eubacterial *E. coli* 70S ribosome are localized to peripheral regions of the ribosome and not within core functional regions that would be expected to influence translational activity, such as the sub-unit interface, peptidyl-transferase center or translation factor binding site. One major exception is related to the ribosomal tunnel through which the nascent polypeptide chain passes as it is synthesized. In the chlororibosome, we observed that the lower region of the tunnel differs from bacteria due to a shorter β -hairpin of cpL23 and the additional presence of the NTE of cpL24. Formation of α -helical secondary structure within nascent polypeptides chains has been observed in this region of the ribosomal tunnel (52). Structural changes within this region of the chlororibosome may facilitate targeting and insertion of transmembrane-containing proteins into the thylakoid membrane. In this respect, we also note that the CTE of cpL29 could play a role in recruitment of cpSRP54 to the chlororibosome. Unlike bacterial SRPs, the cpSRP lacks the 4.5S RNA (termed, SRP RNA) and comprises only the SRP54 protein, and therefore the CTE of cpL29 may contribute to stabilization of SRP54 interaction with the chlororibosome. Finally, we observed a large conglomerate of cpRP extensions that expand the surface area at the back of the LSU. We suggest that this may facilitate interaction of the chlororibosome directly with the thylakoid membrane and/or membrane-bound components of the targeting machinery, and thereby increase the efficiency of membrane protein insertion. As mentioned, the majority of the chloroplast-encoded proteins is targeted to the thylakoid membranes, including components of the ATP synthase, cytochrome b/f and especially photosystem I and II complexes (4).

ACCESSION NUMBERS

The coordinates and cryo-EM map for the chlororibosome have been deposited in the Protein Data Bank and EM DataBank under accession codes PDB ID 5MLC and EMD-3525/EMD-3526, respectively.

SUPPLEMENTARY DATA

Supplementary Data are available at NAR Online.

ACKNOWLEDGEMENTS

We would like to thank Heidemarie Sieber, Susi Rieder and Charlotte Ungewickell for expert technical assistance and Sarah Schlaak for help with data analysis. CIISB research

infrastructure project LM2015043 funded by MEYS CR is gratefully acknowledged for the financial support of the measurements at the CF Cryo-electron Microscopy and Tomography CEITEC MU.

FUNDING

Deutsche Forschungsgemeinschaft (DFG) [FOR-1805, SPP-1879, GRK-1721 to D.N.W.]; iNEXT project [653706]; Horizon 2020 program of the European Union; MEYS CR (CIISB research infrastructure project LM2015043. Funding for open access charge: DFG.

Conflict of interest statement. None declared.

REFERENCES

1. Reyes-Prieto,A., Weber,A.P. and Bhattacharya,D. (2007) The origin and establishment of the plastid in algae and plants. *Annu. Rev. Genet.*, **41**, 147–168.
2. Tiller,N. and Bock,R. (2014) The translational apparatus of plastids and its role in plant development. *Mol. Plant*, **7**, 1105–1120.
3. Sun,Y. and Zerges,W. (2015) Translational regulation in chloroplasts for development and homeostasis. *Biochim. Biophys. Acta*, **1847**, 809–820.
4. Schmitz-Linneweber,C., Maier,R.M., Alcaraz,J.P., Cottet,A., Herrmann,R.G. and Mache,R. (2001) The plastid chromosome of spinach (*Spinacia oleracea*): complete nucleotide sequence and gene organization. *Plant Mol. Biol.*, **45**, 307–315.
5. Yamaguchi,K. and Subramanian,A.R. (2000) The plastid ribosomal proteins. Identification of all the proteins in the 50S subunit of an organelle ribosome (chloroplast). *J. Biol. Chem.*, **275**, 28466–28482.
6. Yamaguchi,K., von Knoblauch,K. and Subramanian,A.R. (2000) The plastid ribosomal proteins. Identification of all the proteins in the 30 S subunit of an organelle ribosome (chloroplast). *J. Biol. Chem.*, **275**, 28455–28465.
7. Yamaguchi,K. and Subramanian,A.R. (2003) Proteomic identification of all plastid-specific ribosomal proteins in higher plant chloroplast 30S ribosomal subunit. *Eur. J. Biochem.*, **270**, 190–205.
8. Sharma,M.R., Wilson,D.N., Datta,P.P., Barat,C., Schluenzen,F., Fucini,P. and Agrawal,R.K. (2007) Cryo-EM study of the spinach chloroplast ribosome reveals the structural and functional roles of plastid-specific ribosomal proteins. *Proc. Natl. Acad. Sci. U.S.A.*, **104**, 19315–19320.
9. Bartsch,M., Kimura,M. and Subramanian,A.R. (1982) Purification, primary structure, and homology relationships of a chloroplast ribosomal protein. *Proc. Natl. Acad. Sci. U.S.A.*, **79**, 6871–6875.
10. Grant,T. and Grigorieff,N. (2015) Measuring the optimal exposure for single particle cryo-EM using a 2.6 Å reconstruction of rotavirus VP6. *Elife*, **4**, e06980.
11. Rouhou,A. and Grigorieff,N. (2015) CTFFIND4: fast and accurate defocus estimation from electron micrographs. *J. Struct. Biol.*, **192**, 216–221.
12. Frank,J., Radermacher,M., Penczek,P., Zhu,J., Li,Y., Ladjadj,M. and Leith,A. (1996) SPIDER and WEB: processing and visualization of images in 3D electron microscopy and related fields. *J. Struct. Biol.*, **116**, 190–199.
13. Becker,T., Franckenberg,S., Wickles,S., Shoemaker,C.J., Anger,A.M., Armache,J.P., Sieber,H., Ungewickell,C., Berninghausen,O., Daberkow,I. *et al.* (2012) Structural basis of highly conserved ribosome recycling in eukaryotes and archaea. *Nature*, **482**, 501–506.
14. Chen,J.Z. and Grigorieff,N. (2007) SIGNATURE: a single-particle selection system for molecular electron microscopy. *J. Struct. Biol.*, **157**, 168–173.
15. Arenz,S., Meydan,S., Starosta,A.L., Berninghausen,O., Beckmann,R., Vazquez-Laslop,N. and Wilson,D.N. (2014) Drug sensing by the ribosome induces translational arrest via active site perturbation. *Mol. Cell*, **56**, 446–452.
16. Loerke,J., Giesebricht,J. and Spahn,C.M. (2010) Multiparticle cryo-EM of ribosomes. *Methods Enzymol.*, **483**, 161–177.
17. Grigorieff,N. (2007) FREALIGN: high-resolution refinement of single particle structures. *J. Struct. Biol.*, **157**, 117–125.

18. Kucukelbir,A., Sigworth,F.J. and Tagare,H.D. (2014) Quantifying the local resolution of cryo-EM density maps. *Nat. Methods*, **11**, 63–65.
19. Scheres,S.H. (2012) RELION: implementation of a Bayesian approach to cryo-EM structure determination. *J. Struct. Biol.*, **180**, 519–530.
20. Fischer,N., Neumann,P., Konevega,A.L., Bock,L.V., Ficner,R., Rodnina,M.V. and Stark,H. (2015) Structure of the *E. coli* ribosome-EF-Tu complex at <3 Å resolution by C-corrected cryo-EM. *Nature*, **520**, 567–570.
21. Cannone,J.J., Subramanian,S., Schnare,M.N., Collett,J.R., D’Souza,L.M., Du,Y., Feng,B., Lin,N., Madabusi,L.V., Muller,K.M. et al. (2002) The comparative RNA web (CRW) site: an online database of comparative sequence and structure information for ribosomal, intron, and other RNAs. *Biomed Central Bioinformatics*, **3**, 2.
22. Pettersen,E.F., Goddard,T.D., Huang,C.C., Couch,G.S., Greenblatt,D.M., Meng,E.C. and Ferrin,T.E. (2004) UCSF chimera—a visualization system for exploratory research and analysis. *J. Comput. Chem.*, **25**, 1605–1612.
23. Emsley,P. and Cowtan,K. (2004) Coot: model-building tools for molecular graphics. *Acta Crystallogr. D Biol. Crystallogr.*, **60**, 2126–2132.
24. Guex,N. and Peitsch,M.C. (1997) SWISS-MODEL and the Swiss-PdbViewer: an environment for comparative protein modeling. *Electrophoresis*, **18**, 2714–2723.
25. Soding,J., Biegert,A. and Lupas,A.N. (2005) The HHpred interactive server for protein homology detection and structure prediction. *Nucleic Acids Res.*, **33**, W244–W248.
26. Buchan,D., Minneci,F., Nugent,T., Bryson,K. and Jones,D. (2013) Scalable web services for the PSIPRED Protein Analysis Workbench. *Nucleic Acids Res.*, **41** W340–W348.
27. Adams,P.D., Afonine,P.V., Bunkoczi,G., Chen,V.B., Davis,I.W., Echols,N., Headd,J.J., Hung,L.W., Kapral,G.J., Grosse-Kunstleve,R.W. et al. (2010) PHENIX: a comprehensive Python-based system for macromolecular structure solution. *Acta Crystallogr. D Biol. Crystallogr.*, **66**, 213–221.
28. Vagin,A.A., Steiner,R.A., Lebedev,A.A., Potterton,L., McNicholas,S., Long,F. and Murshudov,G.N. (2004) REFMAC5 dictionary: organization of prior chemical knowledge and guidelines for its use. *Acta Crystallogr. D Biol. Crystallogr.*, **60**, 2184–2195.
29. Brown,A., Long,F., Nicholls,R.A., Toots,J., Emsley,P. and Murshudov,G. (2015) Tools for macromolecular model building and refinement into electron cryo-microscopy reconstructions. *Acta Crystallogr. D Biol. Crystallogr.*, **71**, 136–153.
30. Amunts,A., Brown,A., Bai,X.C., Llacer,J.L., Hussain,T., Emsley,P., Long,F., Murshudov,G., Scheres,S.H. and Ramakrishnan,V. (2014) Structure of the yeast mitochondrial large ribosomal subunit. *Science*, **343**, 1485–1489.
31. Chen,V.B., Arendall,W.B. 3rd, Headd,J.J., Keedy,D.A., Immormino,R.M., Kapral,G.J., Murray,L.W., Richardson,J.S. and Richardson,D.C. (2010) MolProbity: all-atom structure validation for macromolecular crystallography. *Acta Crystallogr. D Biol. Crystallogr.*, **66**, 12–21.
32. Noeske,J., Wasserman,M.R., Terry,D.S., Altman,R.B., Blanchard,S.C. and Cate,J.H. (2015) High-resolution structure of the *Escherichia coli* ribosome. *Nat. Struct. Mol. Biol.*, **22**, 336–341.
33. Llacer,J.L., Hussain,T., Marler,L., Aitken,C.E., Thakur,A., Lorsch,J.R., Hinnebusch,A.G. and Ramakrishnan,V. (2015) Conformational differences between open and closed states of the eukaryotic translation initiation complex. *Mol. Cell*, **59**, 399–412.
34. Hussain,T., Llacer,J.L., Wimberly,B.T., Kieft,J.S. and Ramakrishnan,V. (2016) Large-scale movements of IF3 and tRNA during bacterial translation initiation. *Cell*, **167**, 133–144.
35. Wimberly,B.T., Brodersen,D.E., Clemons,W.M., Morgan-Warren,R.J., Carter,A.P., Vonrhein,C., Hartsch,T. and Ramakrishnan,V. (2000) Structure of the 30S ribosomal subunit. *Nature*, **407**, 327–339.
36. Sharma,M.R., Donhofer,A., Barat,C., Marquez,V., Datta,P.P., Fucini,P., Wilson,D.N. and Agrawal,R.K. (2010) PSRP1 is not a ribosomal protein, but a ribosome-binding factor that is recycled by the ribosome-recycling factor (RRF) and elongation factor G (EF-G). *J. Biol. Chem.*, **285**, 4006–4014.
37. Yoshida,H. and Wada,A. (2014) The 100S ribosome: ribosomal hibernation induced by stress. *Wiley interdisciplin. Rev. RNA*, **5**, 723–732.
38. Vila-Sanjurjo,A., Schuwirth,B.S., Hau,C.W. and Cate,J.H.D. (2004) Structural basis for the control of translational initiation during stress. *Nat. Struct. Mol. Biol.*, **11**, 1054–1059.
39. Polikanov,Y.S., Blaha,G.M. and Steitz,T.A. (2012) How hibernation factors RMF, HPF, and YfA turn off protein synthesis. *Science*, **336**, 915–918.
40. Puri,P., Eckhardt,T.H., Franken,L.E., Fusetti,F., Stuart,M.C., Boekema,E.J., Kuipers,O.P., Kok,J. and Poolman,B. (2014) *Lactococcus lactis* YfA is necessary and sufficient for ribosome dimerization. *Mol. Microbiol.*, **91**, 394–407.
41. Basu,A. and Yap,M.N. (2016) Ribosome hibernation factor promotes Staphylococcal survival and differentially represses translation. *Nucleic Acids Res.*, **44**, 4881–4893.
42. Wilson,D.N., Schlunzen,F., Harms,J.M., Yoshida,T., Ohkubo,T., Albrecht,R., Buerger,J., Kobayashi,Y. and Fucini,P. (2005) X-ray crystallography study on ribosome recycling: the mechanism of binding and action of RRF on the 50S ribosomal subunit. *EMBO J.*, **24**, 251–260.
43. Weixlbaumer,A., Petry,S., Dunham,C.M., Selmer,M., Kelley,A.C. and Ramakrishnan,V. (2007) Crystal structure of the ribosome recycling factor bound to the ribosome. *Nat. Struct. Mol. Biol.*, **14**, 733–737.
44. Amunts,A., Brown,A., Toots,J., Scheres,S.H. and Ramakrishnan,V. (2015) Ribosome. The structure of the human mitochondrial ribosome. *Science*, **348**, 95–98.
45. Greber,B.J., Bieri,P., Leibundgut,M., Leitner,A., Aebersold,R., Boehringer,D. and Ban,N. (2015) Ribosome. The complete structure of the 55S mammalian mitochondrial ribosome. *Science*, **348**, 303–308.
46. Ban,N., Nissen,P., Hansen,J., Moore,P.B. and Steitz,T.A. (2000) The complete atomic structure of the large ribosomal subunit at 2.4 Å resolution. *Science*, **289**, 905–920.
47. Ben-Shem,A., Garreau de Loubresse,N., Melnikov,S., Jenner,L., Yusupova,G. and Yusupov,M. (2011) The structure of the eukaryotic ribosome at 3.0 Å resolution. *Science*, **334**, 1524–1529.
48. Anger,A.M., Armache,J.P., Berninghausen,O., Habeck,M., Subklewe,M., Wilson,D.N. and Beckmann,R. (2013) Structures of the human and *Drosophila* 80S ribosome. *Nature*, **497**, 80–85.
49. Halic,M., Blau,M., Becker,T., Mielke,T., Pool,M.R., Wild,K., Sinning,I. and Beckmann,R. (2006) Following the signal sequence from ribosomal tunnel exit to signal recognition particle. *Nature*, **444**, 507–511.
50. Jomaa,A., Boehringer,D., Leibundgut,M. and Ban,N. (2016) Structures of the *E. coli* translating ribosome with SRP and its receptor and with the translocon. *Nat. Commun.*, **7**, 10471.
51. Ahmed,T., Yin,Z. and Bhushan,S. (2016) Cryo-EM structure of the large subunit of the spinach chloroplast ribosome. *Sci. Rep.*, **6**, 35793.
52. Wilson,D.N. and Beckmann,R. (2011) The ribosomal tunnel as a functional environment for nascent polypeptide folding and translational stalling. *Curr. Opin. Struct. Biol.*, **21**, 1–10.

SUPPLEMENTARY ONLINE MATERIALS

for

Cryo-EM structure of the spinach chloroplast ribosome reveals the location of plastid-specific ribosomal proteins and extensions

Michael Graf¹, Stefan Arenz¹, Paul Huter¹, Alexandra Dönhöfer¹, Jiří Nováček², Daniel N. Wilson^{1,3,*}

¹ Gene Center, Department for Biochemistry and Center for integrated Protein Science Munich (CiPSM), University of Munich, 81377 Munich, Germany

² Central European Institute of Technology (CEITEC), Masaryk University, Kamenice 5, 62500 Brno, Czech Republic.

³ Department of Biochemistry and Molecular Biology, University of Hamburg, 20146 Hamburg, Germany.

* To whom correspondence should be addressed. Tel: +49 89 2180 76903; Fax: +49 89 2180 76945; Email: wilson@lmb.uni-muenchen.de.

SUPPLEMENTARY FIGURES

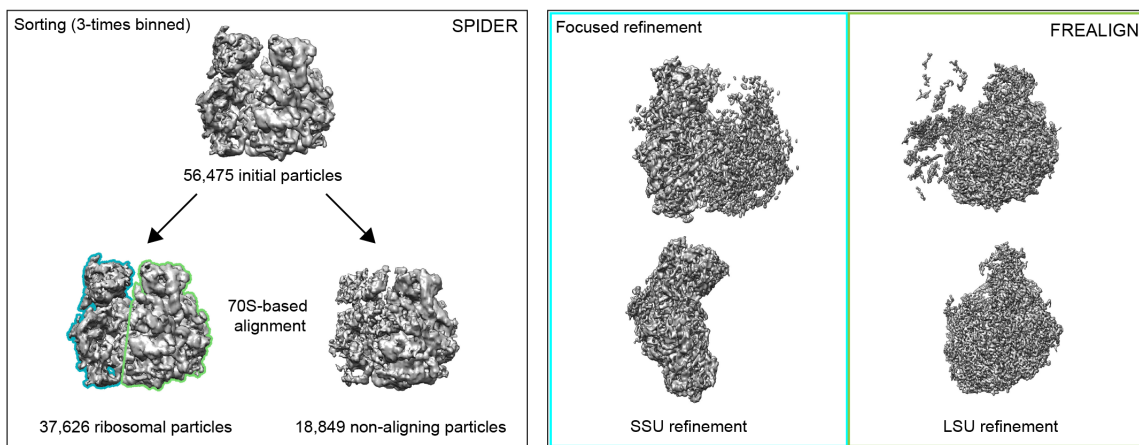


Figure S1: *In silico* sorting and refinement of the chloroplast SSU and LSU. (A) *In silico* sorting was performed using SPIDER (2), starting with an initial 56,475 particles that yielded after removal of non-aligning particles (18,849), a dataset of 37,626 ribosomal particles. (B) Subsequently, focused alignment and refinement of the SSU and LSU was performed in FREALIGN (3).

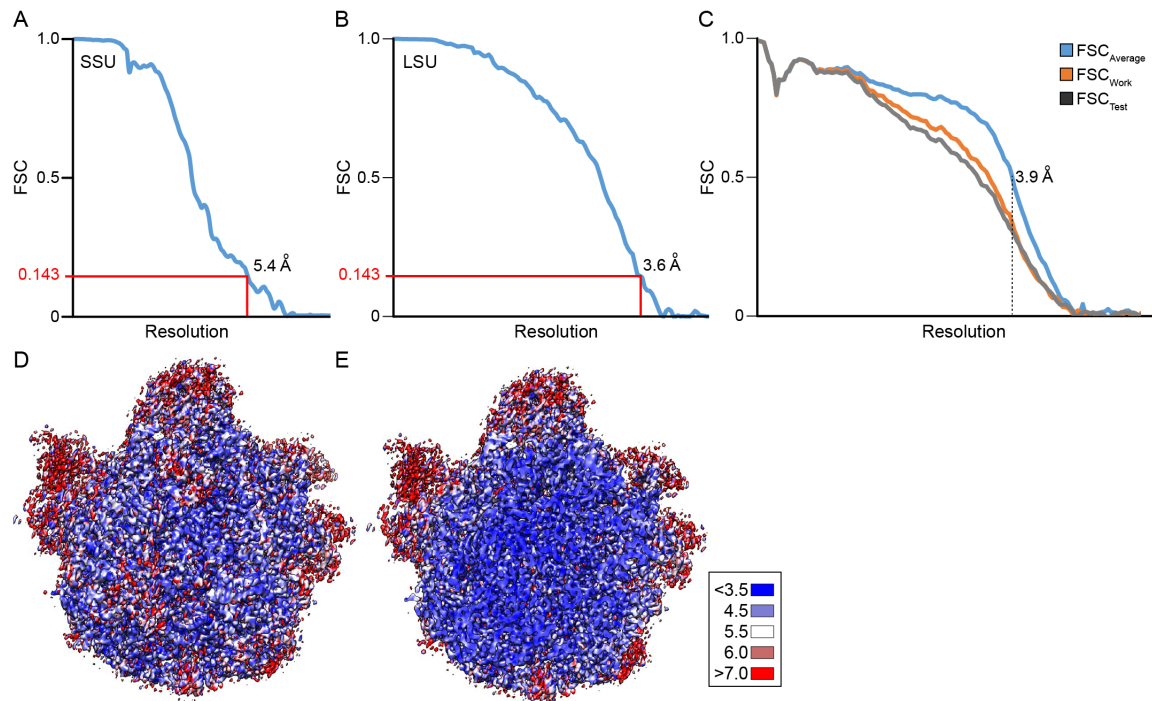


Figure S2: Resolution of the cryo-EM reconstruction of the chloroplast SSU and LSU. (A,B) Fourier-shell correlation curve (FSC) of the refined final map of the chloroplast (A) SSU and (B) LSU, indicating the average resolution is 5.4 Å and 3.6 Å, respectively. (C) Fit of models to maps. FSC curves calculated between the refined model and the final map (blue), with the self- and cross-validated correlations in orange and black, respectively. Information beyond 3.6 Å was not used during refinement and preserved for validation. (D) Overview and (E) transverse section through the chloroplast LSU colored according to the local resolution as calculated using ResMap (1).

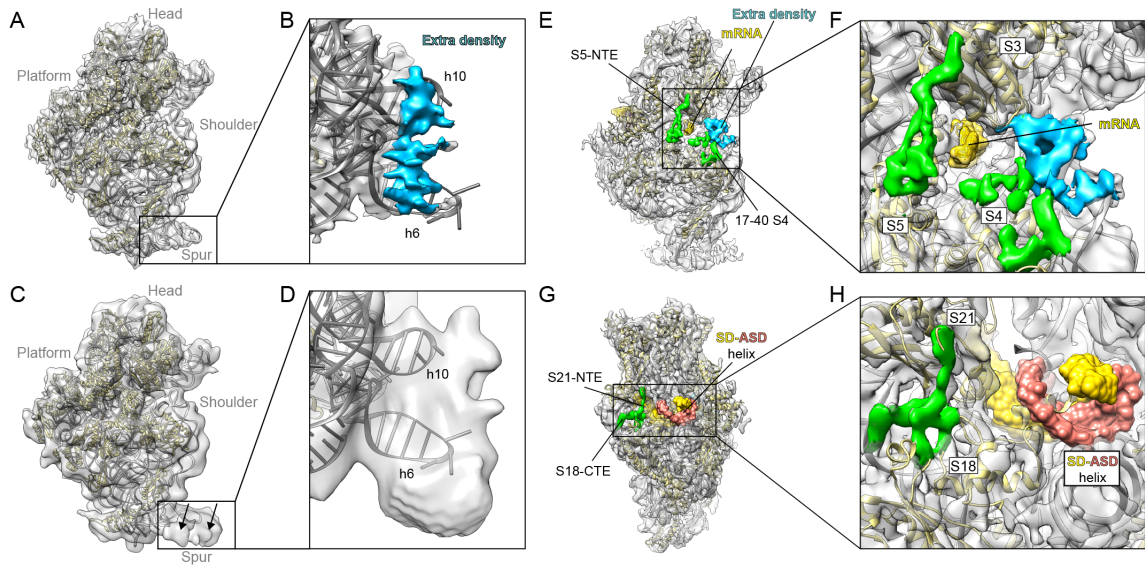


Figure S3: Localization of extra density on the SSU. **(A)** Overview of the back of the cryo-EM map (grey) of the chloroplast SSU with molecular model (rRNA, grey; RPs, yellow), and with **(B)** zoom onto the spur region, showing extra density (blue). **(C)** Overview of the back of the cryo-EM map (grey) of the chloroplast SSU from Sharma and coworkers (4) with molecular model (rRNA, grey; RPs, yellow), and with **(D)** zoom onto the spur region, showing additional density that was assigned to PSRP2/3. **(E)** Overview and **(F)** zoom onto the back of the cryo-EM map (grey) of the chloroplast SSU with molecular model (rRNA, grey; RPs, yellow), with cpRP densities (green) and unassigned extra density (blue) shown relative to the position of mRNA (yellow; superimposed from PDB ID 3I8G (5)). **(G)** Overview and **(H)** zoom onto the platform of the cryo-EM map (grey) of the chloroplast SSU with molecular model (rRNA, grey; RPs, yellow) and cpRP densities (green) shown relative to the position of SD-aSD helix (yellow/red; superimposed from PDB ID 3I8G (5)).

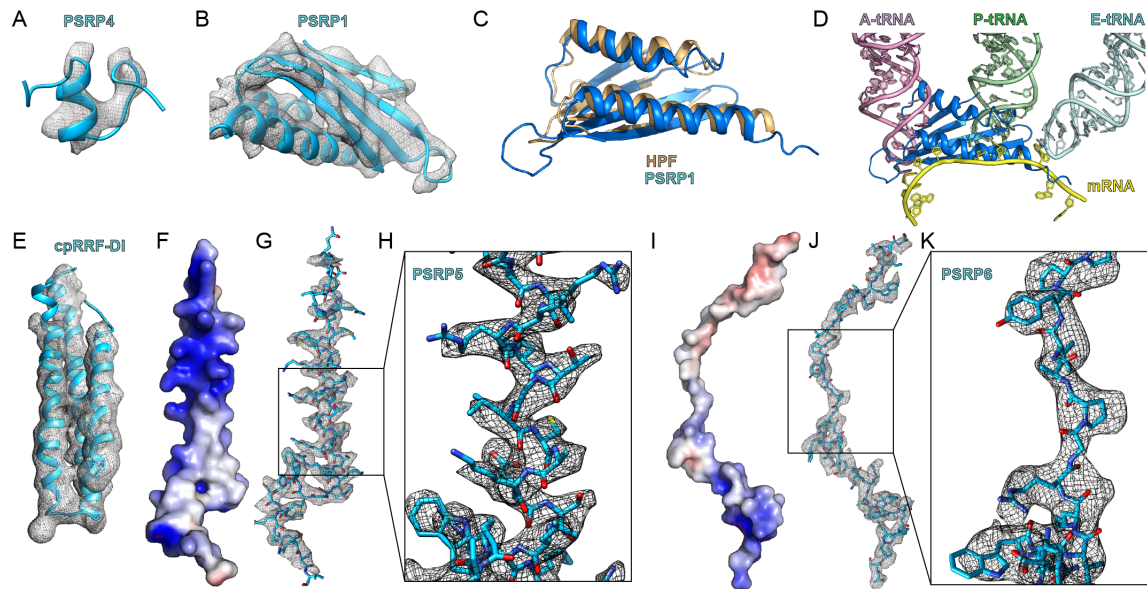


Figure S4: Localization of PSRPs on the chlororibosome. (A,B) Cryo-EM electron density (grey mesh) for (A) PSRP4 and (B) PSRP1. (C,D) Superimposition of the binding site of PSRP1 (blue) on the chlororibosome relative to (C) *E. coli* HPF (orange) bound to the *Thermus thermophilus* 70S ribosome (PDB ID 4V8H, (6)) and (D) mRNA (yellow) and A-site (pink), P-site (green) and E-site (cyan) tRNAs (PDB ID 3I8G, (5)). (E) Cryo-EM electron density (grey mesh) for domain I of the cpRRF (blue, cpRRF-DI). (F-H) Molecular model for PSRP5 shown as (F) surface charge (blue, positive) and (G) with electron density (grey mesh) and (H) zoom of the boxed region in (G). (I-K) Molecular model for PSRP6 shown as (I) surface charge (blue, positive, white neutral, red, negative) and (J) with electron density (grey mesh) and (K) zoom of the boxed region in (J).

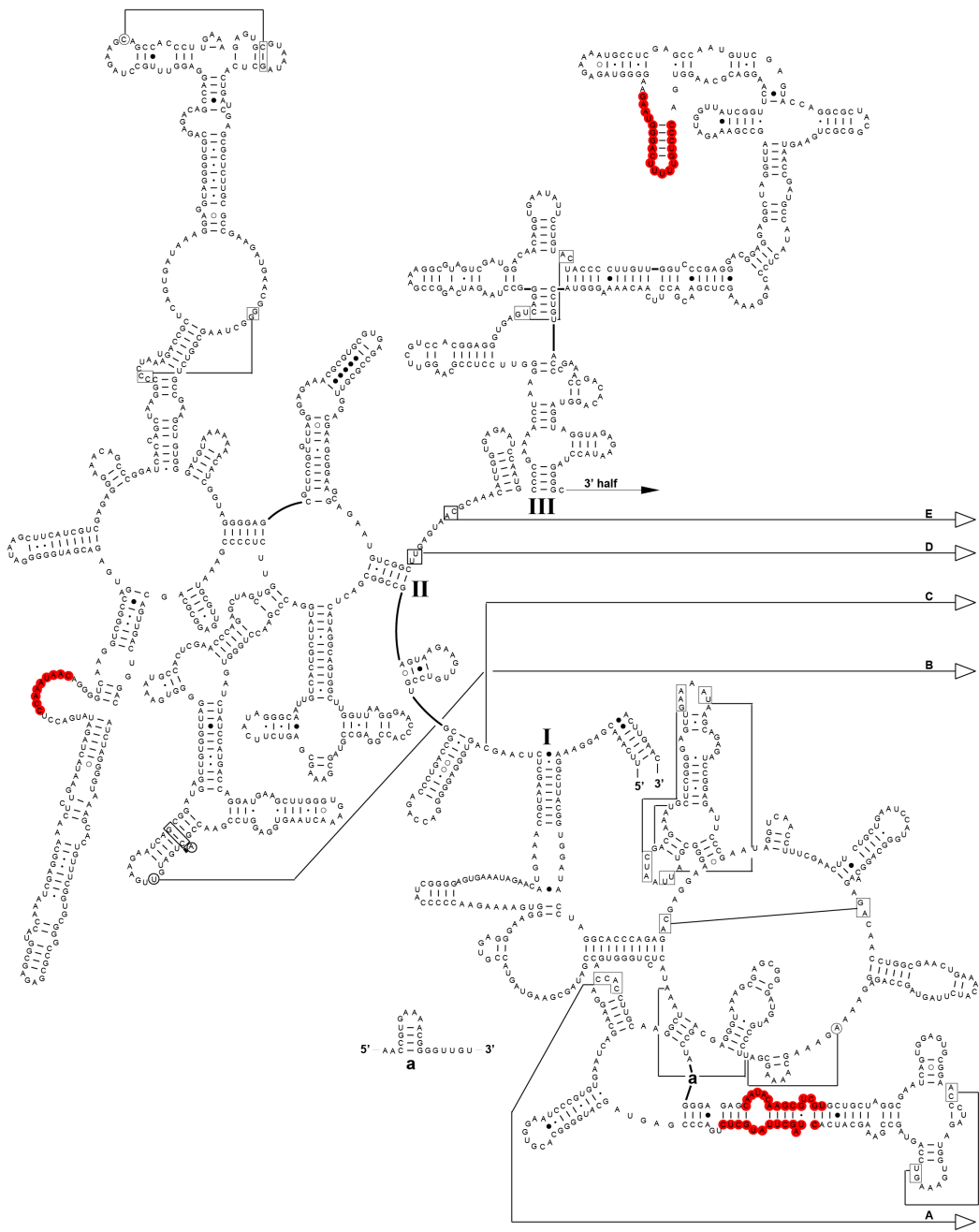


Figure S5: Modelled nucleotides of the chloroplast 4.8S and 23S rRNAs. (A) Secondary structure of the 5' portion of the cp23S rRNA, with nucleotides highlighted in red that were not modelled. The secondary structure diagram was taken from the Comparative RNA Web (CRW) Site (www.rna.ccbb.utexas.edu) (7).

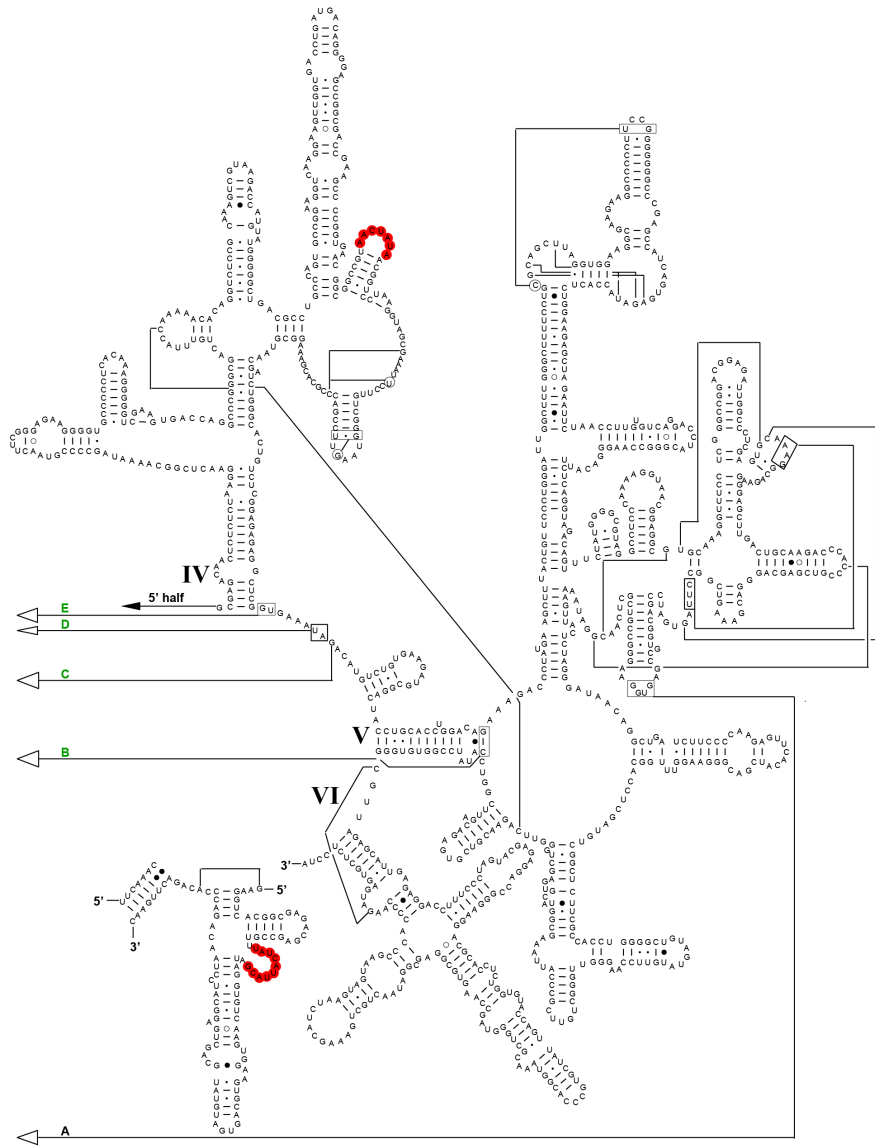


Figure S5: Modelled nucleotides of the chloroplast 4.8S and 23S rRNAs. (B)
 Secondary structure of the 3' portion of the cp23S rRNA and 4.8S rRNA, with nucleotides highlighted in red that were not modelled. The secondary structure diagram was taken from the Comparative RNA Web (CRW) Site (www.rna.ccbb.utexas.edu) (7).

SUPPLEMENTARY TABLES

Supplementary Table S1. Data collection and refinement statistics

Data Collection and Refinement	Cp50S
Particles	37,636
Pixel size (Å)	1.061
Defocus range (μm)	-1.0-2.3
Voltage (kV)	300
Electron dose (e ⁻ /Å ⁻²)	40.3
Map sharpening B factor (Å ²)	-84.98
Resolution (Å, 0.143 FSC)	3.6
FSC _{Average}	0.88
<hr/>	
Model Composition	
Protein residues	3,392
RNA bases	2,963
<hr/>	
Validation (proteins)	
Poor rotamers (%)	7.11
Ramachandran outliers (%)	2.94
Ramachandran favored (%)	85.51
Bad backbone bonds (%)	0.04
Bad backbone angles	0.01
MolProbity score	2.48 (99 th percentile)
<hr/>	
Validation (nucleic acids)	
Correct sugar puckers (%)	96.39
Good backbone conformations (%)	69.83
Bad bonds (%)	0.01
Bad angles	0.21
Clash score, all atoms	3.96 (100 th percentile)
<hr/>	

Supplementary Table S2 Modeled proteins of the chloroplast LSU

Protein	UniProtKB	Preprotein	Mature Length	Modeled Residues
uL01c	Q9LE95	1-352	73-352	
uL02c	P06509		2-272	26-271
uL03c	A0A0K9QEC7	1-305	85-305	85-303
uL04c	O49937	1-293	51-293	56-260
uL05c	P82192		1-220	16-194
uL06c	A0A0K9R4N9	1-220	39-220	40-217
bL09c	A0A0K9RQ91	1-196	42-196	43-87
uL10c	A0A0K9R3N5	1-232	53-232	
uL11c	P31164	1-224	67-224	
bL12c	P02398	1-189	57-189	
uL13c	P12629	1-250	48-250	55-250
uL14c	P09596		1-121	1-120
uL15c	A0A0K9QHT0	1-271	61-271	78-259
uL16c	P17353		1-135	1-135
bL17c	A0A0K9RLJ4	1-126	11-126	11-126
uL18c	A0A0K9QQ60	1-166	45-166	49-166
bL19c	P82413	1-233	78-233	117-230
bL20c	P28803		2-128	2-117
bL21c	P24613	1-256	56-256	101-234
uL22c	P09594		2-199	25-176
uL23c	Q9LWB5	1-198	77-198	104-194
uL24c	P27683	1-191	47-191	47-175
bL27c	A0A0K9R4I2	1-194	57-194	59-166
bL28c	A0A0K9RD02	1-148	72-148	72-146
uL29c	A0A0K9R7W8	1-168	59-168	59-152
bL31c	A0A0K9R0R6	1-130	37-130	
bL32c	P28804	1-57	2-57	2-43
bL33c	P28805		1-66	6-65
bL34c	P82244	1-152	92-152	92-152
bL35c	P23326	1-159	87-159	90-159
bL36c	P12230		1-37	1-37
PSRP5	P27684	1-142	59-142	97-142
PSRP6	P82411	1-116	48-116	48-94
RRF	P82231		1-271	89-114;191-271

SUPPLEMENTARY REFERENCES

1. Kucukelbir, A., Sigworth, F.J. and Tagare, H.D. (2014) Quantifying the local resolution of cryo-EM density maps. *Nat. Methods*, **11**, 63-65.
2. Frank, J., Radermacher, M., Penczek, P., Zhu, J., Li, Y., Ladjadj, M. and Leith, A. (1996) SPIDER and WEB: processing and visualization of images in 3D electron microscopy and related fields. *J. Struct. Biol.*, **116**, 190-199.
3. Grigorieff, N. (2007) FREALIGN: high-resolution refinement of single particle structures. *J. Struct. Biol.*, **157**, 117-125.
4. Sharma, M.R., Wilson, D.N., Datta, P.P., Barat, C., Schluenzen, F., Fucini, P. and Agrawal, R.K. (2007) Cryo-EM study of the spinach chloroplast ribosome reveals the structural and functional roles of plastid-specific ribosomal proteins. *Proc. Natl. Acad. Sci. USA*, **104**, 19315-19320.
5. Jenner, L.B., Demeshkina, N., Yusupova, G. and Yusupov, M. (2010) Structural aspects of messenger RNA reading frame maintenance by the ribosome. *Nat. Struct. Mol. Biol.*, **17**, 555-560.
6. Polikanov, Y.S., Blaha, G.M. and Steitz, T.A. (2012) How hibernation factors RMF, HPF, and YfiA turn off protein synthesis. *Science*, **336**, 915-918.
7. Cannone, J.J., Subramanian, S., Schnare, M.N., Collett, J.R., D'Souza, L.M., Du, Y., Feng, B., Lin, N., Madabusi, L.V., Muller, K.M. *et al.* (2002) The comparative RNA web (CRW) site: an online database of comparative sequence and structure information for ribosomal, intron, and other RNAs. *BioMed Central Bioinformatics*, **3**, 2.

The proline-rich antimicrobial peptide Onc112 inhibits translation by blocking and destabilizing the initiation complex

A Carolin Seefeldt^{1,2,6}, Fabian Nguyen^{3,6}, Stéphanie Antunes^{1,4,6}, Natacha Pérébaskine^{1,2}, Michael Graf³, Stefan Arenz³, K Kishore Inampudi^{1,2}, Céline Douat^{1,4}, Gilles Guichard^{1,4}, Daniel N Wilson^{3,5} & C Axel Innis^{1,2}

The increasing prevalence of multidrug-resistant pathogenic bacteria is making current antibiotics obsolete. Proline-rich antimicrobial peptides (PrAMPs) display potent activity against Gram-negative bacteria and thus represent an avenue for antibiotic development. PrAMPs from the oncocin family interact with the ribosome to inhibit translation, but their mode of action has remained unclear. Here we have determined a structure of the Onc112 peptide in complex with the *Thermus thermophilus* 70S ribosome at a resolution of 3.1 Å by X-ray crystallography. The Onc112 peptide binds within the ribosomal exit tunnel and extends toward the peptidyl transferase center, where it overlaps with the binding site for an aminoacyl-tRNA. We show biochemically that the binding of Onc112 blocks and destabilizes the initiation complex, thus preventing entry into the elongation phase. Our findings provide a basis for the future development of this class of potent antimicrobial agents.

Antimicrobial peptides form a diverse group of molecules that are produced as part of the innate immune response of all multicellular organisms¹. Among these, PrAMPs have garnered considerable attention as a possible means of countering the rapid increase in bacterial resistance to classical antibiotics^{2,3}. Unlike many peptides that kill bacteria by disrupting their cell membrane, PrAMPs are transported into the cytoplasm by specialized transporters, such as SbmA in Gram-negative bacteria^{4,5}, where they inhibit specific intracellular targets. Given that such transport mechanisms are absent in mammalian cells, and only limited interactions with intracellular eukaryotic proteins have been detected, PrAMPs are generally considered to be nontoxic⁶ and therefore an attractive alternative to existing antimicrobials. Interestingly, some PrAMPs can cross the blood-brain barrier to selectively target brain cells, thus further highlighting their potential for the treatment of cerebral infections or for brain-specific drug delivery⁷.

Initial efforts to locate bacterial targets for PrAMPs led to the identification of the heat-shock protein DnaK as the prime candidate for inhibition⁸. Short proline-rich peptides (of 18–20 amino acids (aa)) such as oncocin, drosocin, pyrrhocoricin or apidaecin were previously shown to bind to this bacterial chaperone in a stereospecific manner, thus leading to the development of improved PrAMP derivatives with increased affinity for DnaK^{9–12}. However, subsequent studies into the antimicrobial properties of PrAMPs¹³ have suggested that these peptides are likely to use additional modes of action to inhibit growth. For example, a C-terminally truncated version of the apidaecin 1b peptide results in a loss of antimicrobial activity but no observable decrease

in DnaK binding or cellular uptake¹³. Similarly, oncocin (Onc72 and Onc112) and apidaecin (Api88 and Api137) derivatives were found to inhibit the growth of a *dnaK*-deletion strain as efficiently as that of the *dnaK*-containing parental strain¹⁴. Further investigation revealed that these PrAMPs have an additional target within the bacterial cell, namely the ribosome¹⁴. Although such PrAMPs have been shown to bind to the ribosome and inhibit translation¹⁴, the mechanism by which they inhibit translation has so far not been determined.

Here, we set out to address this issue by obtaining a 3.1-Å-resolution X-ray crystallography structure of the *Thermus thermophilus* 70S ribosome (Tth70S) in complex with a peptidyl (P)-site-bound deacylated tRNA_i^{Met} and Onc112, a representative of the oncocin family of PrAMPs produced by the milkweed bug (*Oncopeltus fasciatus*)¹⁵. The structure reveals that the N-terminal residues 1–12 of Onc112 bind to the upper region of the ribosomal exit tunnel, overlapping the binding site for the CCA end of an aminoacyl (A)-site tRNA at the peptidyl transferase center. Consistently with this, we showed biochemically that Onc112 allows translation to initiate but destabilizes the initiation complex and thus prevents subsequent entry of affected ribosomes into the translation-elongation phase. Moreover, we demonstrated that although truncation of the C-terminal portion of Onc112 is dispensable for ribosome binding, it is essential for antimicrobial activity. We believe that these findings will provide an excellent basis for the design of improved antibacterial compounds, either peptidic or peptidomimetic, that inhibit translation by targeting the ribosomal exit tunnel.

¹Institut Européen de Chimie et Biologie, Université de Bordeaux, Pessac, France. ²INSERM U869, Bordeaux, France. ³Gene Center, Department of Biochemistry, University of Munich, Munich, Germany. ⁴Université de Bordeaux, CNRS, Institut Polytechnique de Bordeaux, UMR 5248, Institut de Chimie et Biologie des Membranes et des Nano-objets (CBMN), Pessac, France. ⁵Center for Integrated Protein Science Munich (CiPSM), University of Munich, Munich, Germany. ⁶These authors contributed equally to this work. Correspondence should be addressed to C.A.I. (axel.innis@inserm.fr) or D.N.W. (wilson@lmb.uni-muenchen.de).

Received 26 February; accepted 22 April; published online 18 May 2015; doi:10.1038/nsmb.3034

RESULTS

Onc112 binds in a reverse orientation within the exit tunnel

We obtained the structure herein referred to as *Tth*70S–Onc112 by soaking the 19-aa Onc112 peptide (VDKPPYLPRPRPPRrIYNr-NH₂, in which r denotes D-arginine) into crystals of *Tth*70S ribosomes in complex with a P-site-bound deacylated tRNA_i^{Met} and a short mRNA (Table 1). Using a minimally biased $F_o - F_c$ map calculated after refinement of a model comprising *Tth*70S ribosomes, tRNA_i^{Met} and mRNA but lacking Onc112, we could see clear density that could be attributed to the N-terminal two-thirds of the Onc112 peptide (Fig. 1). Interestingly, the peptide is bound inside the tunnel with a reversed orientation relative to the growing polypeptide chain during protein synthesis, i.e., with its N terminus located near the peptidyl transferase center and its C terminus extending into the exit tunnel toward the constriction formed by ribosomal proteins L4 and L22. Despite the reversed orientation, the location of the Onc112 peptide overlaps to varying extents with the path of nascent polypeptide chains that have been visualized within the ribosomal tunnel^{16–18} (Supplementary Fig. 1). The conformation of Onc112 bound to the ribosome is extended, in a manner similar to but distinct from that observed previously for oncocin in complex with DnaK¹⁰ (Supplementary Fig. 2). Our CD studies suggest that, in solution, the Onc112 peptide adopts an essentially random conformation, with short stretches of poly(Pro)II helix, specifically, 6% α -helix, 54% random coil, 30% PPII and 6% β -sheet (Supplementary Fig. 3).

Interaction between Onc112 and 23S rRNA of the exit tunnel

Comparison of the *Tth*70S–Onc112 structure with that of a *Tth*70S ribosome featuring tRNA_i^{Met} bound to the P site¹⁹ reveals that several nucleotides of the 23S rRNA undergo a conformational change upon binding of Onc112 to the ribosome (Fig. 2a). U2506 shifts to occupy a position similar to that observed upon binding of aminoacyl-tRNA to the A site of the ribosome^{20,21}. In the presence of Onc112, U2585, which is very flexible in many crystal structures, adopts a defined position similar to that modeled in the structure of a vacant *Escherichia coli* 70S ribosome²². In addition, A2062 shifts to provide space for Onc112, adopting a similar conformation to that observed previously in the presence of the ErmBL nascent chain²³. Thus, binding of Onc112 to the ribosome is accompanied by an induced fit involving several 23S rRNA nucleotides that are generally known for their dynamic behavior within the peptidyl transferase center and ribosomal tunnel.

Electron density for the Onc112 peptide was strongest for residues Val1–Pro8 and became weaker after Pro10, thus making it difficult to model the peptide beyond Pro12 (Fig. 1). We observed three sets of interactions between the N-terminal 10 aa of Onc112 and nucleotides of the 23S rRNA (Fig. 2b). The first set involves aa 1–3 of Onc112 and encompasses eight potential hydrogen-bond interactions (Fig. 2b,c). Val1 of Onc112 can form three hydrogen bonds with nucleotides of the 23S rRNA; two via its α -amine to the N3 atom of C2573 and the O3' atom of C2507; and one via its carbonyl oxygen to the N4 atom of C2573. Three additional hydrogen bonds are possible between the side chain carboxylic acid of Asp2 and the N1 and N2 atoms of G2553 or the 2'-OH of C2507. The positively charged side chain of Lys3 extends into a negatively charged cavity, displacing a hydrated magnesium ion that is present at this site in other *Tth*70S ribosome structures²⁰, and it interacts with the backbone phosphates of A2453 (Fig. 2c) and U2493 (not shown). Substitution of Val1, Asp2 and especially Lys3 by alanine in Onc72 leads to a loss of antimicrobial activity¹⁰, whereas, as expected, a D2E mutant of Onc112 retained both *in vitro* and *in vivo* activity (Supplementary Fig. 4). The K3A

Table 1 Data collection and refinement statistics

	<i>Tth</i> 70S–Onc112 ^a
Data collection	
Space group	<i>P</i> 2 ₁ 2 ₁ 2 ₁
Cell dimensions	
<i>a</i> , <i>b</i> , <i>c</i> (Å)	209.30, 452.29, 624.12
α , β , γ (°)	90.0, 90.0, 90.0
Resolution (Å)	50 (3.1)
<i>R</i> _{merge}	25.5% (166.4%)
<i>I</i> / σ <i>I</i>	5.47 (0.95)
Completeness (%)	99.1 (98.8)
Redundancy	3.8 (3.6)
Refinement	
Resolution (Å)	3.1
No. reflections	3,999,403
<i>R</i> _{work} / <i>R</i> _{free}	23.08 / 27.13
No. atoms	
Protein / RNA	91,758 / 195,737
Ligand/ion	2,333
<i>B</i> factors	
Protein / RNA	64.81 / 63.15
Ligand/ion	51.31
r.m.s. deviations	
Bond lengths (Å)	0.015
Bond angles (°)	0.809

^aStructure determined from a single crystal.

substitution in Onc72 reduced its ribosome binding affinity by a factor of 4.3 and lowered the half-maximal inhibitory concentration (IC₅₀) for *in vitro* translation more than 18-fold¹⁴.

The second set of interactions involves the side chains of Tyr6 and Leu7 of Onc112 (Fig. 2b,d). The aromatic side chain of Tyr6 establishes a π -stacking interaction with C2452 of the 23S rRNA (Fig. 2d). In addition, the side chain hydroxyl of Tyr6 hydrogen-bonds with an undetermined ion that is coordinated by the backbone phosphate of U2506 and the O2 atoms of C2452 and U2504. The hydrophobic cavity occupied by the Tyr6 side chain also accommodates the side chain of Leu7 of Onc112, which packs against the phenol moiety of Tyr6, whereas the backbone of Leu7 forms two hydrogen bonds with U2506 (Fig. 2b,d). The compact hydrophobic core formed by Tyr6 and Leu7 is likely to be key in anchoring the Onc112 peptide to the tunnel because mutagenesis experiments have shown that alanine substitution of either residue in Onc72 reduces the ribosome binding affinity by a factor of 7 and results in a complete loss of inhibitory activity on translation *in vitro*¹⁴. In contrast, mutation of Leu7 in Onc112 to cyclohexylalanine, which would preserve the hydrophobic environment, resulted in retention of inhibitory activity on translation *in vitro* but unexpectedly led to a loss of antimicrobial activity (Supplementary Fig. 4).

Additional interactions with the ribosome encompass the PRPRP motif of Onc112 (Fig. 2b) and include a π -stacking interaction between the guanidino group of Arg9 of Onc112 and the base of C2610 (Fig. 2e). Although substitution of Arg11 with alanine in Onc72 also reduces the ribosome binding affinity and inhibitory properties of the peptide¹⁴, we observed very little density for the side chain of this residue, thus suggesting that it could be important for the overall electrostatic properties of the peptide rather than for a defined interaction with the ribosome (Fig. 1). The high conservation of the 23S rRNA nucleotides that comprise the ribosome-binding site of Onc112 is consistent with the broad spectrum of antimicrobial

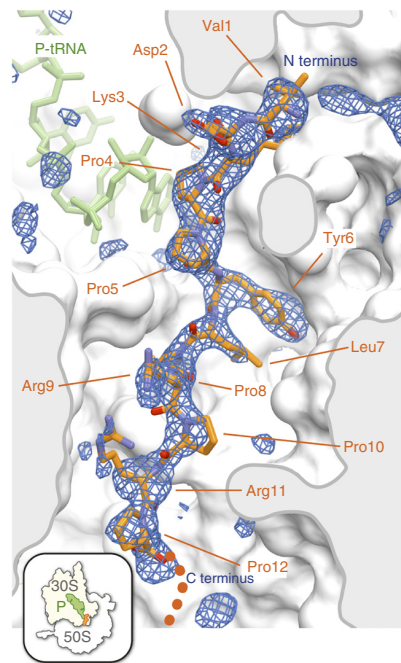
Figure 1 Onc112-binding site within the exit tunnel of the ribosome. Transverse section of the exit tunnel of the *Tth*70S ribosome showing the binding site for the Onc112 peptide (orange). Minimally biased $F_0 - F_c$ difference map contoured at $+3.0\sigma$ (blue) is observable for the first 12 amino acids of Onc112 (**VDKPPYLPRPRPPR**PRIYNr-NH₂; residues 1–12 are bold and underlined). Initiator tRNA_i^{Met} bound at the P site is shown in green. Inset shows the view chosen to display the Onc112 peptide relative to the complete 70S ribosome.

activity displayed by this and related PrAMPs against a range of Gram-negative bacteria^{10,24}.

Onc112 allows translation to initiate but blocks elongation

Comparison of the *Tth*70S-Onc112 structure with that of the *Tth*70S ribosome in the preattack state of peptide-bond formation²⁰ indicated that the binding of Onc112 to the ribosome would prevent accommodation of the CCA end of an incoming aminoacyl-tRNA via steric occlusion of the ribosomal A site at the peptidyl transferase center (Fig. 3a). Indeed, Asp2 of Onc112 directly interacts with G2553, a residue located within helix H92 of the 23S rRNA, termed the A loop, that normally stabilizes the A site tRNA at the peptidyl transferase center via Watson-Crick base-pairing with nucleotide C75 of its CCA end.

In order to determine the step of translation that Onc112 inhibits, we performed cell-free protein synthesis and monitored the location of the ribosomes on the mRNA (Fig. 3b and Supplementary Data Set 1), by using toe-printing assays^{25,26}. In the absence of Onc112 or antibiotic, ribosomes were able to initiate at the AUG start codon and translate through the open reading frame, but they became trapped on the downstream isoleucine codon because isoleucine was omitted from the translation mix. In the presence of the antibiotics clindamycin or thiostrepton, ribosomes accumulated at the start codon and could not translate down to the isoleucine codon because these antibiotics prevent delivery and/or accommodation of the first aminoacyl-tRNA directly following the initiation codon²⁷. We observed similar results when performing the toe-printing assay with increasing concentrations of the Onc112 peptide, namely a loss



of the band corresponding to ribosomes stalled at the isoleucine codon and an increase in the band corresponding to the ribosomes accumulating at the start codon. These findings indicate that Onc112 allows subunit joining and formation of the 70S initiation complex but prevents accommodation of the first aminoacyl-tRNA at the A site, as suggested by steric overlap between Onc112 and an A-site tRNA (Fig. 3a). This contrasts with a bona fide translation-initiation inhibitor, such as edeine, which interferes with the stable binding of fMet-tRNA_i^{Met} to the 30S subunit and thus prevents 70S initiation-complex formation²⁸, in agreement with the lack of a toe-print band at the start codon in the presence of edeine (Fig. 3b).

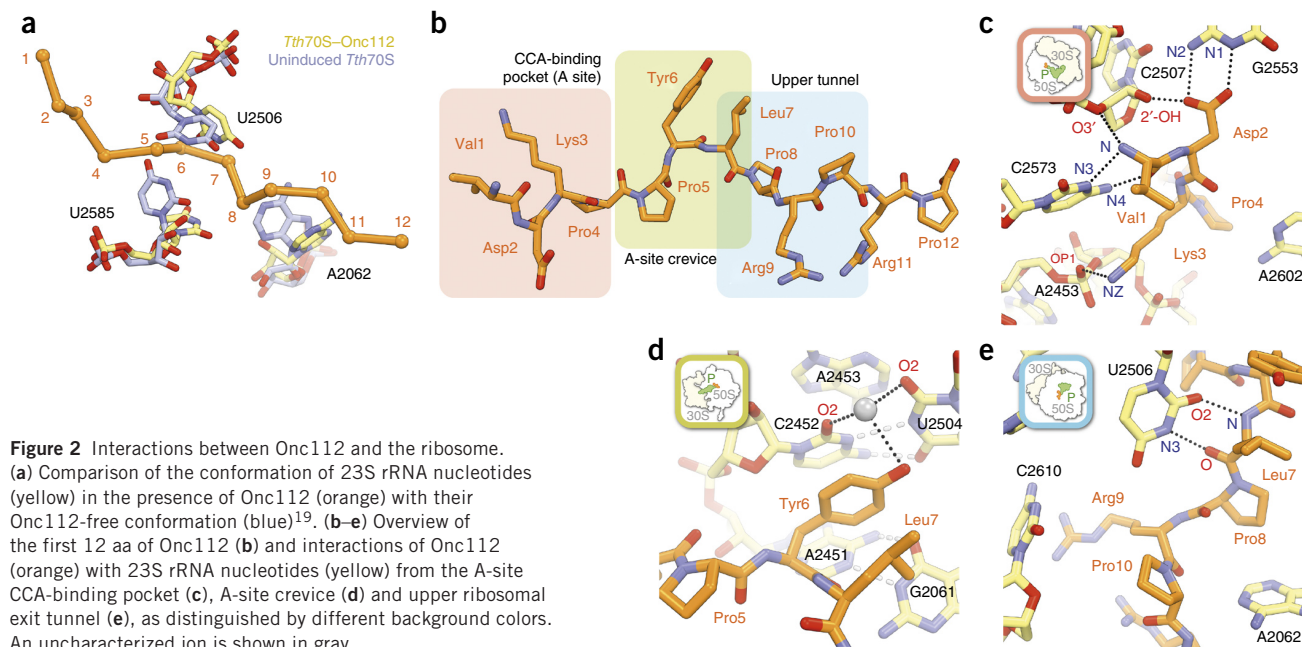
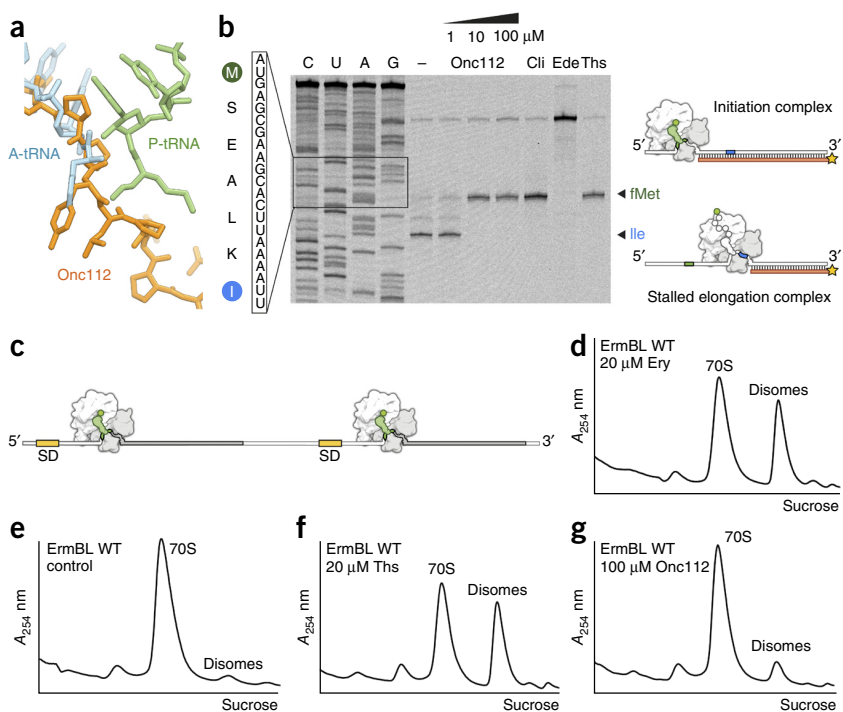


Figure 3 Onc112 blocks and destabilizes the initiation complex. **(a)** Structural comparison of Phe-tRNA^{phe} (blue) in the A site and fMet-tRNA_i^{Met} in the P site²⁰ with the binding site of Onc112 (orange). **(b)** Toe-printing assay performed in the absence (–) or presence of increasing concentrations (1 μ M, 10 μ M and 100 μ M) of Onc112, 50 μ M clindamycin (Cli), 50 μ M edeine (Ede) or 100 μ M thiostrepton (Ths). Sequencing lanes for C, U, A and G and the sequence surrounding the toe-print bands (arrows) when ribosomes accumulate at the AUG start codon (green, initiation complex) or the isoleucine codon (blue, stalled elongation complex) are included for reference, as illustrated graphically. The uncropped gel image for the toe-printing assay is in **Supplementary Data Set 1**. **(c–g)** Schematic (**c**) showing the dicistronic ErmBL mRNA that was used to monitor disome formation with sucrose gradients in the presence (**d**) or absence (**e**) of 20 μ M erythromycin (Ery) or the presence of 20 μ M thiostrepton (**f**) or 100 μ M Onc112 (**g**). In **c**, SD denotes the Shine-Dalgarno sequence. **A**, absorbance.

Onc112 destabilizes the translation-initiation complex

We noticed that the toe-print bands at the start codon in the presence of Onc112 were consistently weaker than those observed in the presence of clindamycin or thiostrepton (Fig. 3b and data not shown), thus suggesting that Onc112 may also perturb the placement of fMet-tRNA_i^{Met} at the P site. In the *Tth*70S–Onc112 structure, the P-site tRNA is uncharged, and its terminal A76 residue undergoes a conformational change that positions it \sim 3.4 Å away from the Onc112 peptide. *In vivo*, however, we would expect fMet-tRNA_i^{Met} to bind to the peptidyl transferase center in the same manner as in the *Tth*70S ribosome preattack complexes²⁰, such that the formyl group of the fMet moiety would sterically clash with residues Tyr6 and Leu7 of the Onc112 peptide (Fig. 3a). Consequently, we used sucrose gradients to monitor disome formation upon translating a dicistronic ErmBL mRNA *in vitro*, in order to investigate the stability of the translation-initiation complex formed in the presence of Onc112 (Fig. 3c–g). As a positive control, we performed translation in the presence of the macrolide antibiotic erythromycin, which acts synergistically with the ErmBL polypeptide



chain within the ribosomal tunnel to stall translation at a specific site on the mRNA²⁹. Because the mRNA was dicistronic, two stalled ribosomes on a single mRNA led to the formation of disomes that could be visualized on a sucrose gradient (Fig. 3d), as shown previously^{16,23}. We observed negligible disome formation in the absence of erythromycin because the ribosomes rapidly translated the short ORF and were released from the mRNA (Fig. 3e). As expected, thiostrepton, which allows 70S initiation-complex formation but prevents elongation (Fig. 3b), also led to efficient disome formation (Fig. 3f). In contrast, the presence of Onc112, even at concentrations as high as 100 μ M, resulted in only a small increase in disomes (Fig. 3g). This leads us to suggest that the 70S initiation complexes formed in the presence of Onc112 are unstable, presumably because the Onc112 peptide encroaches onto fMet-tRNA_i^{Met}, thus causing it to dissociate from the ribosome under the nonequilibrium conditions (centrifugation and sucrose density) used in the disome assay.

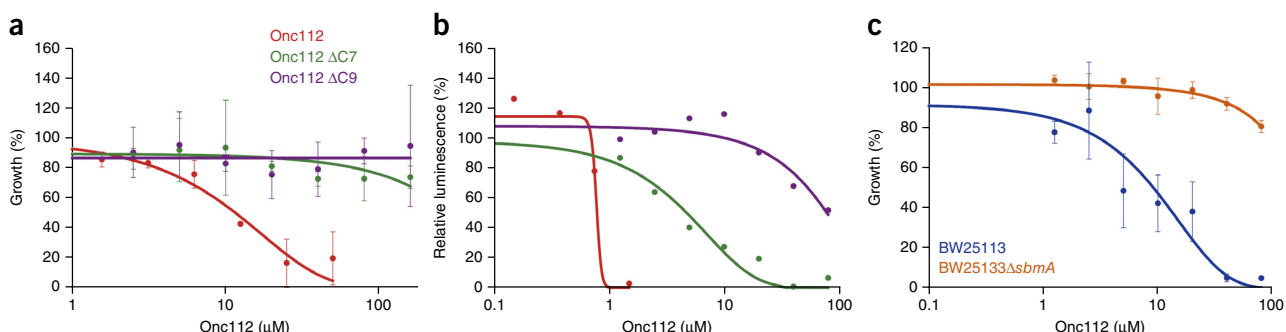
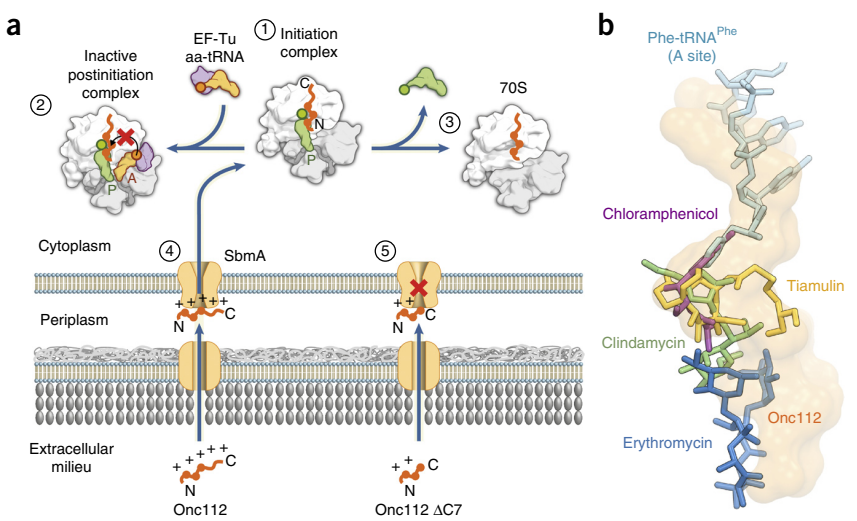


Figure 4 Characterization of Onc112, its C-terminally truncated derivatives and its membrane transporter in Gram-negative bacteria. **(a,b)** Effect of Onc112 (red) and C-terminally truncated Onc112 derivatives Onc112 Δ C7 (green) and Onc112 Δ C9 (purple) on overnight growth of *E. coli* strain BL21(DE3) (**a**) and the luminescence resulting from the *in vitro* translation of Fluc (**b**). **(c)** Effect of Onc112 on overnight growth of *E. coli* strain BW25113 (blue) or BW25113 Δ sbmA (orange). In **a** and **c**, error bars represent mean \pm s.d. for triplicate experiments, whereas the experiment in **b** was performed in duplicate, with the plotted points representing the mean value. The growth or luminescence measured in the absence of peptide was assigned as 100% in all cases.

Figure 5 Mechanism of action and overlap of Onc112 with antibiotics that target the large subunit of the ribosome. (a) Model for the mechanism of action of Onc112. (1) Onc112 binds within the exit tunnel of the ribosome with a reverse orientation relative to a nascent polypeptide chain. (2) Onc112 allows formation of a translation-initiation complex but prevents accommodation of the aminoacyl-tRNA (aa-tRNA) at the A site of the peptidyl transferase center. (3) The initiation complex is destabilized, thus leading to dissociation of the fMet-tRNA_i^{Met} from the P site. Although full-length Onc112 can efficiently penetrate the bacterial cell membrane by using the SbmA transporter (4), C-terminal truncation of Onc112 reduces its antimicrobial activity (5), presumably owing to impaired uptake. (b) Relative binding position of Onc112 (orange) on the ribosome, compared with those of well-characterized translation inhibitors chloramphenicol (purple)^{32,33}, clindamycin (green)³³, tiamulin (yellow)³⁴ and erythromycin (blue)^{32,33} as well as an A site-bound Phe-tRNA^{Phe} (ref. 20).



Onc112 C terminus is needed for uptake, not ribosome binding

The lack of density for the C terminus of Onc112 (residues 13–19) hinted that this region is dispensable for ribosome binding, yet its high degree of conservation suggested that it may nevertheless be necessary for antimicrobial activity. In order to assess the role of the C-terminal region of Onc112, we prepared truncated versions of this peptide, Onc112 ΔC7 and Onc112 ΔC9, which lacked the last 7 and 9 aa, respectively. We then determined the half-minimal inhibitory concentration (MIC₅₀) for the growth of *E. coli* strain BL21(DE3) in the presence of full-length Onc112 and compared it with those of the truncated Onc112 ΔC7 and Onc112 ΔC9 derivatives (Fig. 4a). As expected, the full-length Onc112 displayed good activity, inhibiting growth with an MIC₅₀ of 10 µM, a value similar to that reported previously¹⁴. In contrast, truncation of 7 or 9 aa from the C terminus of Onc112 led to a complete loss of inhibitory activity, even at concentrations above 100 µM (Fig. 4a). To ascertain whether the truncated Onc112 peptides could still bind to the ribosome and inhibit translation, we monitored *in vitro* translation of firefly luciferase (Fluc) by measuring luminescence after 60 min of translation in the presence of increasing concentrations of either full-length Onc112 or the truncated Onc112 ΔC7 and Onc112 ΔC9 derivatives (Fig. 4b). As expected, the full-length peptide displayed excellent activity, inhibiting translation of Fluc with an IC₅₀ of 0.8 µM (Fig. 4b), a value similar to that reported when the same system was used for well-characterized translation inhibitors such as chloramphenicol³⁰. In contrast to their lack of antimicrobial activity (Fig. 4a), both truncated Onc112 peptides displayed some inhibitory activity with the *in vitro* translation system (Fig. 4b), albeit with a reduced efficiency relative to that of full-length Onc112. Specifically, the Onc112 ΔC7 peptide consisting of residues 1–12 of Onc112 had an IC₅₀ of 5 µM, which was only six times greater than that of full-length Onc112, a result consistent with our structure-based prediction that these residues comprise the major ribosome binding determinants. In contrast, the Onc112 ΔC9 peptide consisting of aa 1–10 of Onc112 had an IC₅₀ of 80 µM, which was 16 times greater than that of Onc112 ΔC7 and two orders of magnitude greater than that of full-length Onc112. These results illustrate the contribution of Arg11 to efficient ribosome binding and translation inhibition, as reported previously¹⁴.

Although the inner-membrane protein SbmA has been shown to be responsible for the uptake of the eukaryotic PrAMPs Bac7 and PR39 (refs. 4,5), the only insect PrAMP tested so far was apidaecin Ib⁴. In order to assess the role of SbmA in the uptake of Onc112, we compared the growth of an *E. coli* strain lacking the *sbmA* gene (Δ *sbmA*) with the parental strain BW25113 in the presence of increasing concentrations of Onc112 (Fig. 4c). As expected, the full-length Onc112 displayed excellent activity against the susceptible SbmA-containing parental strain, inhibiting growth with an MIC₅₀ of 8 µM (Fig. 4c), a value similar to that observed with the BL21(DE3) strain (Fig. 4a). In contrast, the Δ *sbmA* strain displayed increased resistance to Onc112, such that even with 100 µM Onc112, growth was reduced by only 20% (Fig. 4c). These findings indicate that SbmA is indeed necessary for the uptake of Onc112 into Gram-negative bacteria, such as *E. coli*, and provide further support for the proposition that the SbmA transporter is involved in the mechanism of action of the entire group of the PrAMPs⁴.

DISCUSSION

From our structural and biochemical data, we propose a model to explain the mechanism by which PrAMPs such as oncocin inhibit translation (Fig. 5a). We have shown that the binding of Onc112 to the ribosomal exit tunnel allows formation of the 70S initiation complex but prevents accommodation of the aminoacyl-tRNA into the A site (Fig. 5a, steps 1 and 2). Additionally, we propose that Onc112 destabilizes the postinitiation complex by inducing dissociation of fMet-tRNA_i^{Met} from the P site (Fig. 5a, step 3). Finally, our data also suggest that positively charged residues distributed along the entire length of the Onc112 sequence are necessary for ensuring the efficient SbmA-mediated uptake of Onc112 into the cell, whereas residues from the N-terminal moiety of Onc112 are responsible for targeting this peptide to the ribosome (Fig. 5a, steps 4 and 5). We believe that this mechanism of action is likely to be the same for other PrAMPs, such as drosocin, pyrrhocoricin and apidaecin, which share many of the residues of Onc112 that are important for its ribosome binding and antimicrobial function.

The binding site for Onc112 within the ribosomal exit tunnel overlaps with the binding sites for a majority of the antibiotics that target the large subunit of the ribosome (Fig. 5b), such as the

chloramphenicols, pleuromutilins (for example, tiamulin) and lincosamides (for example, clindamycin), which inhibit peptide-bond formation by preventing the correct positioning of the tRNA substrates, as well as the macrolides (for example, erythromycin), which abort translation by interfering with the movement of the nascent polypeptide chain through the ribosomal exit tunnel²⁷. Given the substantial spatial overlap that exists between the binding sites for these antibiotics and the regions of the tunnel that interact with Onc112 (Fig. 5b) and presumably with several other PrAMPs, it appears likely that such antimicrobial peptides represent a vast, untapped resource for the development of new therapeutics. Several strategies have been pursued to design improved or entirely new antimicrobials that target the exit tunnel of the ribosome³¹. One approach consists of modifying existing antibiotics to create semisynthetic compounds that possess enhanced antimicrobial properties, including better affinity for mutated or modified ribosomes, the ability to evade drug modification or degradation pathways, increased solubility, improved uptake and reduced efflux. Other strategies involve designing chimeric antibiotics from drugs with adjacent binding sites (for example, macrolide-chloramphenicol or linezolid-sparsomycin) or developing entirely new scaffolds, as exemplified by the oxazolidinone linezolid. The ability to produce new scaffolds based on peptides, such as Onc112, that display potent activity against a diverse range of Gram-negative bacteria represents an exciting avenue for the development of future antimicrobials.

METHODS

Methods and any associated references are available in the [online version of the paper](#).

Accession codes. Coordinates and structure factors have been deposited in the Protein Data Bank under accession code [4ZER](#).

Note: Any Supplementary Information and Source Data files are available in the [online version of the paper](#).

ACKNOWLEDGMENTS

We thank the staff at the European Synchrotron Radiation Facility (beamline ID-29) for help during data collection and B. Kauffmann and S. Massip at the Institut Européen de Chimie et Biologie for help with crystal freezing and screening. We also thank C. Mackereth for discussions and advice. This research was supported by grants from the Agence Nationale pour la Recherche (ANR-14-CE09-0001 to C.A.I., G.G. and D.N.W.), Région Aquitaine (2012-13-01-009 to C.A.I.), the Fondation pour la Recherche Médicale (AJE201133 to C.A.I.), the European Union (PCIG14-GA-2013-631479 to C.A.I.), the CNRS (C.D.) and the Deutsche Forschungsgemeinschaft (FOR1805, WI3285/4-1 and GRK1721 to D.N.W.). Predoctoral fellowships from the Direction Générale de l'Armement and Région Aquitaine (S. Antunes) and INSERM and Région Aquitaine (A.C.S.) are gratefully acknowledged.

AUTHOR CONTRIBUTIONS

A.C.S. performed structure solution, model building and analysis. N.P. prepared and crystallized ribosomes. N.P. and C.A.I. collected X-ray crystallography data. F.N. performed growth and *in vitro*-translation inhibition assays. S. Antunes and C.D. synthesized the peptides and performed NMR, CD and electrospray ionization high-resolution MS experiments. M.G. performed toe-printing assays. S. Arenz performed disome assays. K.K.I. prepared tRNA_i^{Met}. G.G., D.N.W. and C.A.I. designed experiments, interpreted data and wrote the manuscript.

COMPETING FINANCIAL INTERESTS

The authors declare no competing financial interests.

Reprints and permissions information is available online at <http://www.nature.com/reprints/index.html>.

1. Wang, G. *et al.* Antimicrobial peptides in 2014. *Pharmaceuticals (Basel)* **8**, 123–150 (2015).

2. Casteels, P., Ampe, C., Jacobs, F., Vaeck, M. & Tempst, P. Apidaecins: antibacterial peptides from honeybees. *EMBO J.* **8**, 2387–2391 (1989).
3. Li, W. *et al.* Proline-rich antimicrobial peptides: potential therapeutics against antibiotic-resistant bacteria. *Amino Acids* **46**, 2287–2294 (2014).
4. Mattiuzzo, M. *et al.* Role of the *Escherichia coli* SbmA in the antimicrobial activity of proline-rich peptides. *Mol. Microbiol.* **66**, 151–163 (2007).
5. Runti, G. *et al.* Functional characterization of SbmA, a bacterial inner membrane transporter required for importing the antimicrobial peptide Bac7 (1–35). *J. Bacteriol.* **195**, 5343–5351 (2013).
6. Hansen, A., Schäfer, I., Knappe, D., Seibel, P. & Hoffmann, R. Intracellular toxicity of proline-rich antimicrobial peptides shuttled into mammalian cells by the cell-penetrating peptide penetratin. *Antimicrob. Agents Chemother.* **56**, 5194–5201 (2012).
7. Stalmans, S. *et al.* Blood-brain barrier transport of short proline-rich antimicrobial peptides. *Protein Pept. Lett.* **21**, 399–406 (2014).
8. Otvos, L. *et al.* Interaction between heat shock proteins and antimicrobial peptides. *Biochemistry* **39**, 14150–14159 (2000).
9. Czihal, P. *et al.* Api88 is a novel antibacterial designer peptide to treat systemic infections with multidrug-resistant Gram-negative pathogens. *ACS Chem. Biol.* **7**, 1281–1291 (2012).
10. Knappe, D. *et al.* Rational design of oncocin derivatives with superior protease stabilities and antibacterial activities based on the high-resolution structure of the oncocin-DnaK complex. *ChemBioChem* **12**, 874–876 (2011).
11. Zahn, M. *et al.* Structural studies on the forward and reverse binding modes of peptides to the chaperone DnaK. *J. Mol. Biol.* **425**, 2463–2479 (2013).
12. Zahn, M. *et al.* Structural identification of DnaK binding sites within bovine and sheep bactenecin Bac7. *Protein Pept. Lett.* **21**, 407–412 (2014).
13. Berthold, N. & Hoffmann, R. Cellular uptake of apidaecin 1b and related analogs in Gram-negative bacteria reveals novel antibacterial mechanism for proline-rich antimicrobial peptides. *Protein Pept. Lett.* **21**, 391–398 (2014).
14. Krizsan, A. *et al.* Insect-derived proline-rich antimicrobial peptides kill bacteria by inhibiting bacterial protein translation at the 70 S ribosome. *Angew. Chem. Int. Ed. Engl.* **53**, 12236–12239 (2014).
15. Schneider, M. & Dorn, A. Differential infectivity of two *Pseudomonas* species and the immune response in the milkweed bug, *Oncopeltus fasciatus* (Insecta: Hemiptera). *J. Invertebr. Pathol.* **78**, 135–140 (2001).
16. Arenz, S. *et al.* Drug sensing by the ribosome induces translational arrest via active site perturbation. *Mol. Cell* **56**, 446–452 (2014).
17. Bischoff, L., Berninghausen, O. & Beckmann, R. Molecular basis for the ribosome functioning as an L-tryptophan sensor. *Cell Reports* **9**, 469–475 (2014).
18. Shao, S. & Hegde, R.S. Reconstitution of a minimal ribosome-associated ubiquitination pathway with purified factors. *Mol. Cell* **55**, 880–890 (2014).
19. Jenner, L. *et al.* Structural basis for potent inhibitory activity of the antibiotic tigecycline during protein synthesis. *Proc. Natl. Acad. Sci. USA* **110**, 3812–3816 (2013).
20. Polikanov, Y.S., Steitz, T.A. & Innis, C.A. A proton wire to couple aminoacyl-tRNA accommodation and peptide-bond formation on the ribosome. *Nat. Struct. Mol. Biol.* **21**, 787–793 (2014).
21. Schmeing, T.M., Huang, K.S., Strobel, S.A. & Steitz, T.A. An induced-fit mechanism to promote peptide bond formation and exclude hydrolysis of peptidyl-tRNA. *Nature* **438**, 520–524 (2005).
22. Schuwirth, B.S. *et al.* Structures of the bacterial ribosome at 3.5 Å resolution. *Science* **310**, 827–834 (2005).
23. Arenz, S. *et al.* Molecular basis for erythromycin-dependent ribosome stalling during translation of the ErmBL leader peptide. *Nat. Commun.* **5**, 3501 (2014).
24. Knappe, D. *et al.* Oncocin (VDKPPYLPRLPRPRPPRRIYRN-NH2): a novel antibacterial peptide optimized against Gram-negative human pathogens. *J. Med. Chem.* **53**, 5240–5247 (2010).
25. Hartz, D., McPhee, D.S., Traut, R. & Gold, L. Extension inhibition analysis of translation initiation complexes. *Methods Enzymol.* **164**, 419–425 (1988).
26. Starosta, A.L. *et al.* Translational stalling at polyproline stretches is modulated by the sequence context upstream of the stall site. *Nucleic Acids Res.* **42**, 10711–10719 (2014).
27. Wilson, D.N. The A-Z of bacterial translation inhibitors. *Crit. Rev. Biochem. Mol. Biol.* **44**, 393–433 (2009).
28. Dinos, G. *et al.* Dissecting the ribosomal inhibition mechanisms of edeine and pactamycin: the universally conserved residues G693 and C795 regulate P-site RNA binding. *Mol. Cell* **13**, 113–124 (2004).
29. Vázquez-Laslop, N., Ramu, H., Klepacki, D., Kannan, K. & Mankin, A.S. The key function of a conserved and modified tRNA residue in the ribosomal response to the nascent peptide. *EMBO J.* **29**, 3108–3117 (2010).
30. Starosta, A.L. *et al.* Interplay between the ribosomal tunnel, nascent chain, and macrolides influences drug inhibition. *Chem. Biol.* **17**, 504–514 (2010).
31. Wilson, D.N. Ribosome-targeting antibiotics and mechanisms of bacterial resistance. *Nat. Rev. Microbiol.* **12**, 35–48 (2014).
32. Bulkley, D., Innis, C.A., Blaha, G. & Steitz, T.A. Revisiting the structures of several antibiotics bound to the bacterial ribosome. *Proc. Natl. Acad. Sci. USA* **107**, 17158–17163 (2010).
33. Dunkle, J.A., Xiong, L., Mankin, A.S. & Cate, J.H. Structures of the *Escherichia coli* ribosome with antibiotics bound near the peptidyl transferase center explain spectra of drug action. *Proc. Natl. Acad. Sci. USA* **107**, 17152–17157 (2010).
34. Schlünzen, F., Pyetan, E., Fucini, P., Yonath, A. & Harms, J.M. Inhibition of peptide bond formation by pleuromutilins: the structure of the 50S ribosomal subunit from *Deinococcus radiodurans* in complex with tiamulin. *Mol. Microbiol.* **54**, 1287–1294 (2004).

ONLINE METHODS

Peptide synthesis. Commercially available reagents were used throughout without purification. *N,N*-dimethylformamide (DMF, peptide synthesis-quality grade) was purchased from Carlo Erba, and piperidine and trifluoroacetic acid (TFA) were purchased from Alfa Aesar. Rink amide PS resin was purchased from PolyPeptide Laboratories. *N,N'*-diisopropylcarbodiimide (DIC), Oxyma and all standard *N*-Fmoc-protected L and D amino acids were purchased from Iris Biotech. *N*-Fmoc-cyclohexylalanine-OH (Fmoc-Cha-OH) was purchased from PolyPeptide laboratories. RP-HPLC-quality acetonitrile (CH₃CN, Sigma-Aldrich) and MilliQ water were used for RP-HPLC analyses and purification. Analytical RP-HPLC analyses were performed on a Dionex U3000SD with a Macherey-Nagel Nucleodur column (4.6 × 100 mm, 3 μm) at a flow rate of 1 ml min⁻¹ at 50 °C. The mobile phase was composed of 0.1% (v/v) TFA-H₂O (solvent A) and 0.1% TFA-CH₃CN (solvent B). Purification was performed on a Gilson GX-281 with a Macherey-Nagel Nucleodur VP250/21 100–5 C18ec column (21 × 250 mm, 5 μm) at a flow rate of 20 mL min⁻¹. The solid-phase syntheses of peptides were conducted on an automated Liberty Blue System synthesizer (CEM μWaves S.A.S.). ¹H NMR spectra were recorded on a DPX-400 NMR spectrometer (Bruker Biospin) with a vertical 9.4T narrow-bore/ultrashield magnet operating at 400 MHz for ¹H observation by means of a 5-mm direct QNP ¹H/¹³C/³¹P/¹⁹F probe with gradient capabilities (Supplementary Fig. 5). ESI-MS analyses were carried out on a Thermo Exactive from the Mass Spectrometry Laboratory at the European Institute of Chemistry and Biology (UMS 3033—IECB), Pessac, France (Supplementary Fig. 5).

All peptides were synthesized on Rink Amide PS resin (0.79 mmol/g) with a five-fold excess of reagents for the coupling step (0.2 M *N*-Fmoc-amino acid solution (in DMF) with 0.5 M DIC (in DMF) and 1.0 M Oxyma (in DMF)). Coupling of *N*-Fmoc-protected L- and D-arginine-OH was performed twice at 25 °C without microwaves for 1,500 s. Other amino acid couplings were performed first at 90 °C, 170 W, 115 s then at 90 °C, 30 W, 110 s. Fmoc removal was performed with a solution of 20% piperidine in DMF at 75 °C with 155 W for 15 s then 90 °C, 35 W, 50 s. After completion of the synthesis, the peptide resin was washed three times with DCM. Cleavage was performed by treatment with 5 mL of a freshly prepared TFA/TIS/H₂O solution for 240 min at room temperature. The resin was then filtered off, and the TFA solution was concentrated under reduced pressure. The crude products were precipitated as TFA salts in the presence of Et₂O and purified with the appropriate gradient (10–30% of B in 20 min) by semipreparative RP-HPLC. The compounds were freeze dried, and TFA was exchanged with HCl by two repetitive freeze-drying cycles in 0.1 N HCl solution³⁵.

The list of peptides prepared for this study and details concerning their synthesis is as follows:

Onc112. H-Val-Asp-Lys-Pro-Pro-Tyr-Leu-Pro-Arg-Pro-Arg-Pro-Pro-(D-Arg)-Ile-Tyr-Asn-(D-Arg)-NH₂ (2,389.85 g mol⁻¹). Synthesis of Onc112 (0.1-mmol scale): 24 mg (10% yield); RP HPLC *t*_R 4.11 min (gradient 10–50% of B in 10 min); ESI HRMS (*m/z*): found 1,195.70 [M + 2H]²⁺, 797.47 [M + 3H]³⁺, 598.35 [M + 4H]⁴⁺, and 478.88 [M + 5H]⁵⁺.

Onc112 ΔC7. H-Val-Asp-Lys-Pro-Pro-Tyr-Leu-Pro-Arg-Pro-Arg-NH₂ (1,433.73 g mol⁻¹). Synthesis of Onc112 ΔC7 (0.15-mmol scale): 79.4 mg (37% yield); RP HPLC *t*_R 3.54 min (gradient 10–50% of B in 10 min); ESI HRMS (*m/z*): [M + H]⁺ calcd for C₆H₁₀W₂O₁₅, 1,433.83758 found 1,433.84017, with 717.42 [M + 2H]²⁺ and 478.61 [M + 3H]³⁺.

Onc112 ΔC9. H-Val-Asp-Lys-Pro-Pro-Tyr-Leu-Pro-Arg-Pro-NH₂ (1,180.42 g mol⁻¹). Synthesis of Onc112 ΔC9. (0.1-mmol scale): 22.6 mg (19% yield); RP HPLC *t*_R 4.78 min (gradient 10–50% of B in 10 min); ESI HRMS (*m/z*): [M + H]⁺ calcd for C₅₆H₈₉W₁₅O₁₃, 1,180.63370 found 1,180.68368, with [M + 2H]²⁺ 590.84 and [M + 3H]³⁺ 394.23.

Onc112 D2E. H-Val-Glu-Lys-Pro-Pro-Tyr-Leu-Pro-Arg-Pro-Arg-Pro-(D-Arg)-Ile-Tyr-Asn-(D-Arg)-NH₂ (2,403.88 g mol⁻¹). Synthesis of Onc112 D2E (0.05-mmol scale): 11.6 mg (10% yield); RP HPLC *t*_R 5.75 min (gradient 10–50% of B in 10 min); ESI HRMS (*m/z*): found 1316.70 [M + 2H]²⁺, 840.14 [M + 3H]³⁺ and 601.86 [M + 4H]⁴⁺.

Onc112 L7Cha. H-Val-Asp-Lys-Pro-Pro-Tyr-Cha-Pro-Arg-Pro-Arg-(D-Arg)-Ile-Tyr-Asn-(D-Arg)-NH₂ (2,429.92 g mol⁻¹). Synthesis of Onc112 L7Cha (0.05-mmol scale): 6.9 mg (6% yield); RP HPLC *t*_R 5.28 min (gradient 10–50% of B in 10 min); ESI HRMS (*m/z*): found 1,252.18 [M + 2H]²⁺, 822.80 [M + 3H]³⁺ and 608.36 [M + 4H]⁴⁺.

CD spectroscopy. CD spectra of peptides were recorded on a J-815 Jasco spectropolarimeter (Jasco France). Data are expressed in terms of total molar ellipticity in deg cm² dmol⁻¹. CD spectra for the Onc112 peptide were acquired at four different concentrations in phosphate buffer (pH 7.6, 10 mM) between 180 and 280 nm with a rectangular quartz cell with a path length of 1 mm (Hellma 110-QS 1 mm) averaging over two runs. Secondary-structure proportion was estimated from the CD spectra with the deconvolution program CDFriend (S. Buchoux (Unité de Génie Enzymatique et Cellulaire, UMR 6022 CNRS—Université de Picardie Jules Verne) and E. Dufourc (Université de Bordeaux, CNRS, Institut Polytechnique de Bordeaux, UMR 5248 Institut de Chimie et Biologie des Membranes et des Nano-objets (CBMN); available upon request), unpublished). This program uses standard curves obtained for each canonical structure (α -helix, β -sheet, helix-polyproline type II and random coil) with L_iK_j (alternated hydrophobic leucine and hydrophilic/charged lysine residues) peptides of known length, secondary structure and CD spectra. The program implements a simulated annealing algorithm to get the best combination of α -helix, β -sheet, helix-II and random coil that exhibits the lowest normalized r.m.s. deviation with respect to the experimental spectrum^{36–38}. The algorithm yielded the following assessment for the Onc112 peptide: 54% random coil, 30% helix-PPII, 6% α -helix and 6% β -sheet content.

Purification of *T. thermophilus* 70S ribosomes. *Tth*70S ribosomes were purified as described previously³⁹ and resuspended in buffer containing 5 mM HEPES-KOH, pH 7.5, 50 mM KCl, 10 mM NH₄Cl, and 10 mM Mg(CH₃COO)₂ to yield a final concentration of 26–32 mg/mL. For storage, *Tth*70S ribosomes were flash frozen in liquid nitrogen and kept at -80 °C.

Preparation of mRNA and tRNA_i^{Met}. Synthetic mRNA with the sequence 5'-GGC AAG GAG GUA AAA AUG CGU UUU CGU-3' was obtained from Eurogentec. This mRNA contains a Shine-Dalgarno sequence and an AUG start codon followed by several additional codons. *E. coli* tRNA_i^{Met} was overexpressed in *E. coli* HB101 cells and purified as described previously⁴⁰.

Complex formation. A ternary complex containing *Tth*70S ribosomes, mRNA and deacylated tRNA_i^{Met} was formed by mixing of 5 μM *Tth*70S ribosomes with 10 μM mRNA and incubating at 55 °C for 10 min. For the next step, 20 μM tRNA_i^{Met} was added, and the mixture was incubated at 37 °C for 10 min. Before the complexes for crystallization were used, the sample was incubated at room temperature for at least 15 min. All complexes were centrifuged briefly before use for crystallization. The final buffer conditions were 5 mM HEPES-KOH, pH 7.6, 50 mM KCl, 10 mM NH₄Cl and 10 mM Mg(CH₃COO)₂.

Crystallization. Published conditions were used as a starting point for screening crystallization conditions by vapor diffusion in sitting-drop trays at 20 °C (refs. 20,39). Crystallization drops consisted of 3 μl of ternary complex and 3–4 μl of reservoir solution containing 100 mM Tris-HCl, pH 7.6, 2.9% (v/v) PEG 20000, 7–10% (v/v) MPD and 175 mM arginine. Crystals appeared within 2–3 d and grew to ~1,000 × 100 × 100 μm within 7–8 d. For cryoprotection, the concentration of MPD was increased in a stepwise manner to yield a final concentration of 40% (v/v). The ionic composition during cryoprotection was 100 mM Tris-HCl, pH 7.6, 2.9% (v/v) PEG 20000, 50 mM KCl, 10 mM NH₄Cl and 10 mM Mg(CH₃COO)₂. *Tth*70S-Onc112 complexes were obtained by soaking 10–20 μM of Onc112 dissolved in the final cryoprotection solution overnight at 20 °C. Crystals were then flash frozen in a nitrogen cryostream at 80 K for subsequent data collection.

Data collection and processing. Diffraction data were collected at beamline ID29 of the European Synchrotron Radiation Facility (ESRF) in Grenoble, France. A complete data set was obtained by merging 0.1° oscillation data collected at 100 K with a wavelength of 0.97625 Å from multiple regions of the same crystal. Initial data processing, including integration and scaling, were performed with XDS⁴¹. All of the data collected could be indexed in the P2₁2₁ space group, with unit-cell dimensions around 210 Å × 450 Å × 625 Å and an asymmetric unit containing two copies of the *Tth*70S ribosome.

Model building and refinement. Initial phases were obtained by molecular replacement performed with Phaser⁴². The search model was obtained from

a high-resolution structure of the *Tth*70S ribosome (PDB 4Y4O). Restrained crystallographic refinement was carried out with Phenix⁴³ and consisted of a single cycle of rigid-body refinement followed by multiple cycles of positional and individual *B*-factor refinement. Rigid bodies comprised four domains from the small 30S subunit (head, body, spur and helix h44) and three domains from the large 50S subunit (body, L1 stalk and the C terminus of ribosomal protein L9). Noncrystallographic symmetry restraints between the two copies of the *Tth*70S ribosome in the asymmetric unit were also applied during refinement. After confirming that a single tRNA was bound to the P site and that additional density corresponding to the Onc112 peptide was visible inside the exit tunnel in a minimally biased $F_o - F_c$ map, a model for Onc112 was built with Rapper⁴⁴ and Coot⁴⁵. The models for the tRNA and mRNA were obtained from a high-resolution structure of the *Tth*70S ribosome preattack complex (PDB 1VY4). Further refinement and model validation were carried out in Phenix and on the MolProbity server⁴⁶, respectively. In the final model, 0.65% of protein residues were classified as Ramachandran outliers, and 94.38% had favorable backbone conformations.

In vitro–translation assay. The inhibition of firefly luciferase (Fluc) synthesis by Onc112 was assessed with an *E. coli* lysate–based transcription–translation coupled assay (RTS100, 5Prime) as described previously for other translational inhibitors³⁰. Briefly, 6-μL reactions, with or without Onc112/antibiotic were mixed according to the manufacturer's description and incubated for 1 h at 30 °C with shaking (1,000 r.p.m.). 1 μL of each reaction was stopped with 7 μL kanamycin (50 μg/μL) and then diluted with 40 μL of luciferase assay substrate (Promega) into a white 96-well chimney flat-bottom microtiter plate (Greiner). The luminescence was then measured with a Tecan Infinite M1000 plate reader. Relative values were determined by defining the luminescence value of the sample without inhibitor as 100%.

Growth inhibition assays. Determination of the minimal inhibitory concentration (MIC) of Onc112 was performed as described previously for other antibiotics³⁰. Specifically, an overnight culture of *E. coli* strain BL21(DE3) (Invitrogen), BW25113 or Keio deletion strain BW25113ΔsmbA (plate 61, well 10E)⁴⁷ was diluted 1:100 to an OD₆₀₀ of ~0.02, and 200 μL of the diluted cells was then transferred into individual wells of a 96-well plate (Sarstedt). Either 10 μL of Onc112, Onc112 derivative peptide or water was added to each well. Plates were then incubated overnight in a thermomixer (Eppendorf) at 37 °C/350 r.p.m. The OD₆₀₀ was measured in a Tecan Infinite M1000 plate reader, and the relative growth was calculated by defining the growth of samples without antibiotic as 100%.

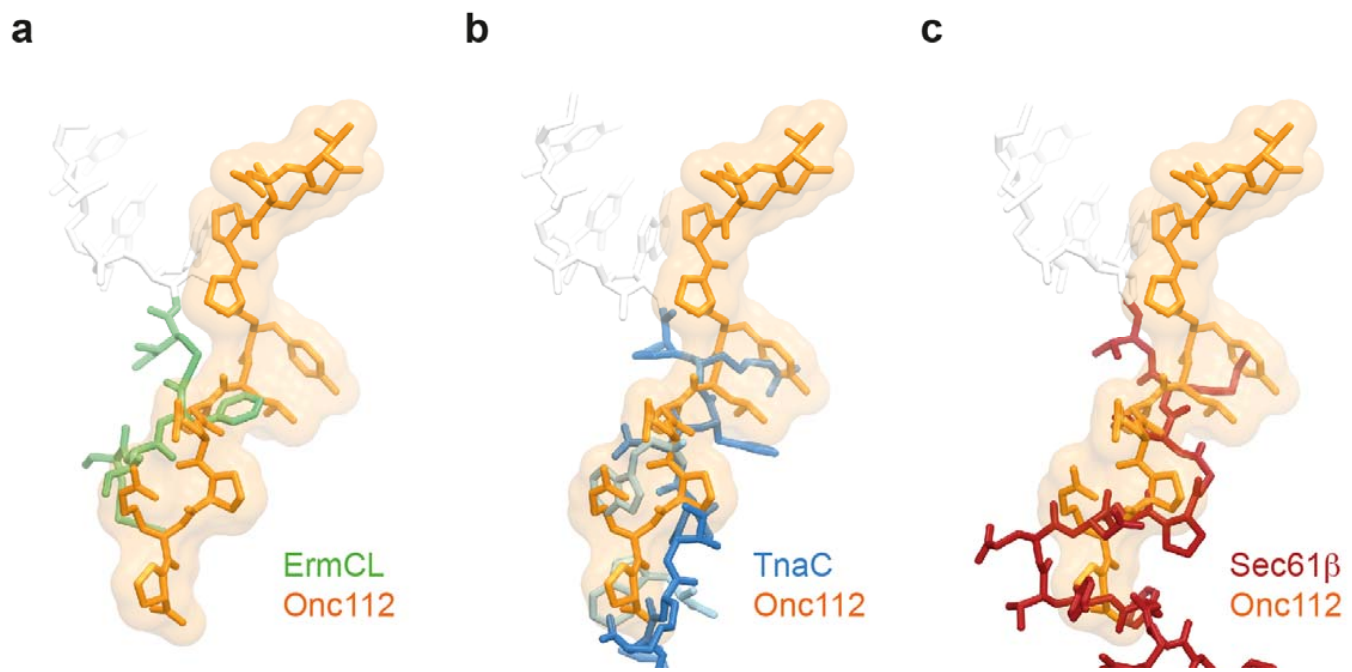
Toe-printing assay. The position of the ribosome on the mRNA was monitored with a toe-printing assay based on an *in vitro*–coupled transcription–translation system with the PURExpress *in vitro* protein synthesis kit (NEB)²⁶. Briefly, each translation reaction consisted of 1 μL solution A, 0.5 μL *l*-isoleucine + tryptophan amino acid mixture, 0.5 μL tRNA mixture, 1.5 μL solution B, 1 μL (0.5 pmol) hns40aa template: (5'-ATTAATACGACTCACTATAGGGATATAAGGAGGA AAACATATGAGCGAAGCACTTAAATTCTGAACACATCCGTACTC TTCGTGCGCAGGCAAGAGAATGTACACTTGAACACGCTGGAAAGAAAT GCTGGAAAAATTAGAAGTTGTTAACGAAACGTTGGATTGTAA GTGATAGAATTCTATCGTTAATAAGCAAATTCAATTATAACC 3', with start codon ATG, catch isoleucine codon ATT and stop codon TAA in bold, the hns40aa ORF underlined and primer-binding sites in italics) and 0.5 μL additional agents (nuclease-free water, Onc112 or antibiotics). Translation was performed in the absence of isoleucine at 37 °C for 15 min at 500 r.p.m. in 1.5-mL reaction tubes. Ile-tRNA aminoacylation was further prevented by the use of the

Ile-tRNA synthetase inhibitor mupirocin. After translation, 2 pmol Alexa647-labeled NV-1 toe-print primer (5'-GGTTATAATGAATTTGCTTATTAAC-3') was added to each reaction and incubated at 37 °C without shaking for 5 min. Reverse transcription was performed with 0.5 μL of AMV RT (NEB), 0.1 μL dNTP mix (10 mM) and 0.4 μL Pure System Buffer and incubated at 37 °C for 20 min. Reverse transcription was quenched and RNA degraded by addition of 1 μL 10 M NaOH and incubation for at least 15 min at 37 °C and then was neutralized with 0.82 μL of 12 M HCl. 20 μL toe-print resuspension buffer and 200 μL PN1 buffer were added to each reaction before treatment with a QIAquick Nucleotide Removal Kit (Qiagen). The Alexa647-labeled DNA was then eluted from the QIAquick columns with 80 μL of nuclease-free water. A vacuum concentrator was used to vaporize the solvent, and the Alexa647-labeled DNA was then dissolved into 3.5 μL of formamide dye. The samples were heated to 95 °C for 5 min before being applied onto a 6% polyacrylamide (19:1) sequencing gel containing 7 M urea. Gel electrophoresis was performed at 40 W and 2,000 V for 2 h. The GE Typhoon FLA9500 imaging system was subsequently used to scan the polyacrylamide gel.

Disome formation assay. The disome formation assay was performed as described previously^{16,23}. Briefly, *in vitro* translation of the 2xermBL construct was performed with the Rapid Translation System RTS 100 *E. coli* HY Kit (Roche). Translations were carried out for 1 h at 30 °C and then analyzed on 10–55% sucrose-density gradients (in a buffer containing 50 mM HEPES-KOH, pH 7.4, 100 mM KOAc, 25 mM Mg(OAc)₂ and 6 mM β-mercaptoethanol) by centrifugation at 154,693g (SW-40 Ti, Beckman Coulter) for 2.5 h at 4 °C.

Figure preparation. Figures showing electron density and atomic models were generated with PyMOL (<http://www.pymol.org/>).

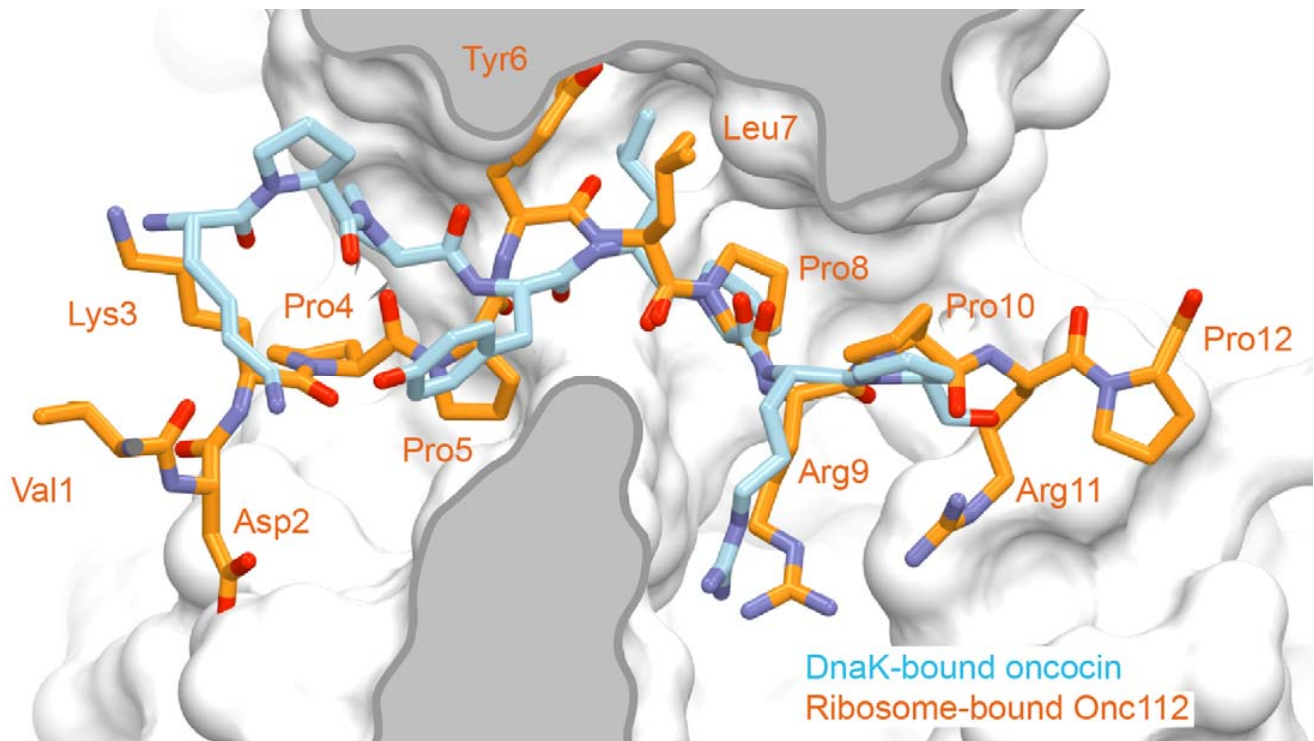
35. Brazier, S.P., Ramesh, B., Haris, P.I., Lee, D.C. & Srai, S.K. Secondary structure analysis of the putative membrane-associated domains of the inward rectifier K⁺ channel ROMK1. *Biochem. J.* **335**, 375–380 (1998).
36. Jean-François, F. *et al.* Variability in secondary structure of the antimicrobial peptide Cateslytin in powder, solution, DPC micelles and at the air–water interface. *Eur. Biophys. J.* **36**, 1019–1027 (2007).
37. Jobin, M.L. *et al.* The enhanced membrane interaction and perturbation of a cell penetrating peptide in the presence of anionic lipids: toward an understanding of its selectivity for cancer cells. *Biochim. Biophys. Acta* **1828**, 1457–1470 (2013).
38. Khemtémourian, L., Buchoux, S., Aussenac, F. & Dufourc, E.J. Dimerization of Neu/Erb2 transmembrane domain is controlled by membrane curvature. *Eur. Biophys. J.* **36**, 107–112 (2007).
39. Selmer, M. *et al.* Structure of the 70S ribosome complexed with mRNA and tRNA. *Science* **313**, 1935–1942 (2006).
40. Schmitt, E., Blanquet, S. & Mechulam, Y. Crystallization and preliminary X-ray analysis of *Escherichia coli* methionyl-tRNAMetf formyltransferase complexed with formyl-methionyl-tRNAMetf. *Acta Crystallogr. D Biol. Crystallogr.* **55**, 332–334 (1999).
41. Kabsch, W. Xds. *Acta Crystallogr. D Biol. Crystallogr.* **66**, 125–132 (2010).
42. McCoy, A.J. *et al.* Phaser crystallographic software. *J. Appl. Crystallogr.* **40**, 658–674 (2007).
43. Adams, P.D. *et al.* PHENIX: a comprehensive Python-based system for macromolecular structure solution. *Acta Crystallogr. D Biol. Crystallogr.* **66**, 213–221 (2010).
44. de Bakker, P.I., DePristo, M.A., Burke, D.F. & Blundell, T.L. *Ab initio* construction of polypeptide fragments: accuracy of loop decoy discrimination by an all-atom statistical potential and the AMBER force field with the Generalized Born solvation model. *Proteins* **51**, 21–40 (2003).
45. Emsley, P. & Cowtan, K. Coot: model-building tools for molecular graphics. *Acta Crystallogr. D Biol. Crystallogr.* **60**, 2126–2132 (2004).
46. Chen, V.B. *et al.* MolProbity: all-atom structure validation for macromolecular crystallography. *Acta Crystallogr. D Biol. Crystallogr.* **66**, 12–21 (2010).
47. Baba, T. *et al.* Construction of *Escherichia coli* K-12 in-frame, single-gene knockout mutants: the Keio collection. *Mol. Syst. Biol.* **2**, 2006.0008 (2006).



Supplementary Figure 1

Overlap of Onc112 with nascent polypeptide chains in the ribosome exit tunnel.

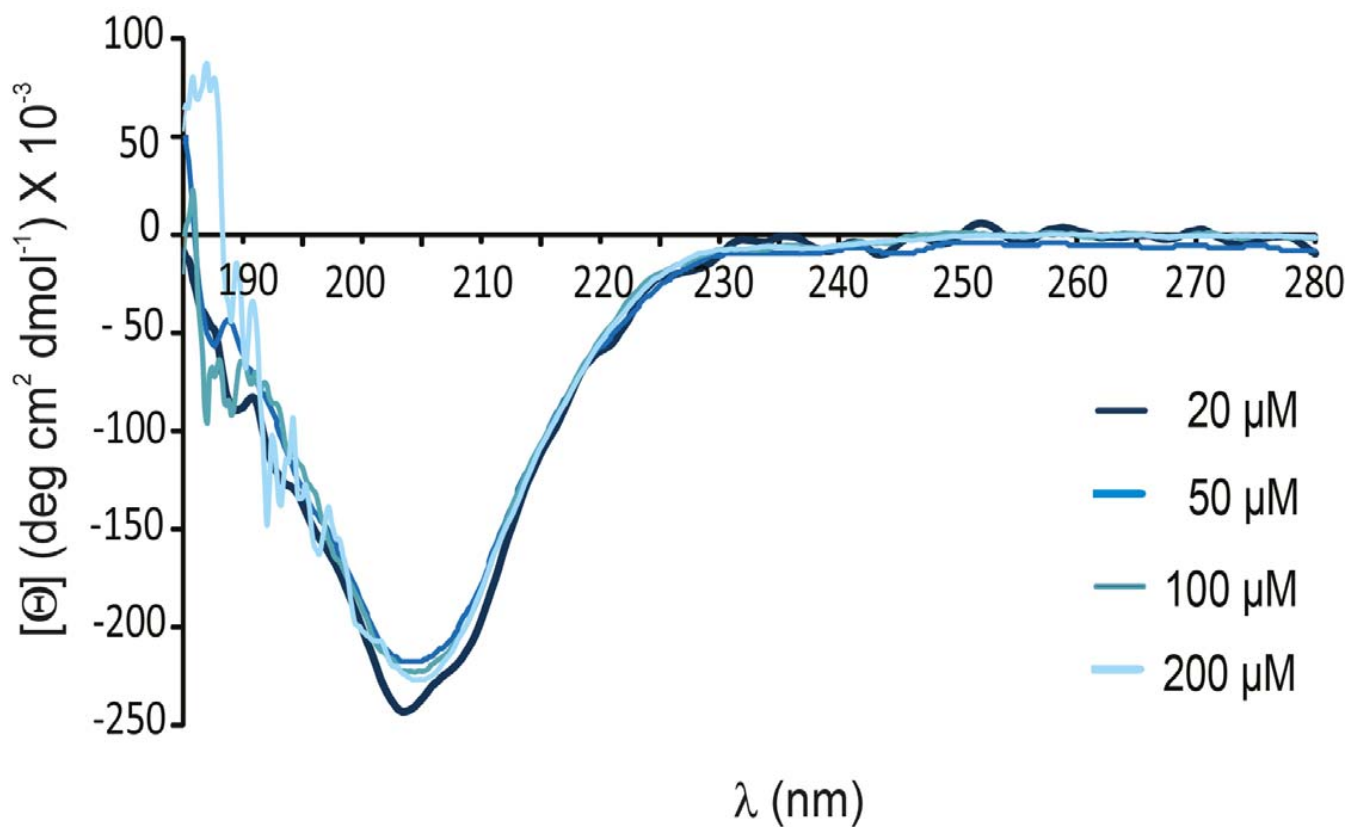
Comparison of the binding position of Onc112 (orange) with (a) ErmCL (green), (b) TnaC (blue) and Sec61 β (red) nascent chains. In (a)-(c), the CCA-end of the P-tRNA is shown in white and in (b) the two tryptophan molecules are in cyan.



Supplementary Figure 2

Comparison of *Tth*70S–Onc112 with the DnaK–oncocin complex.

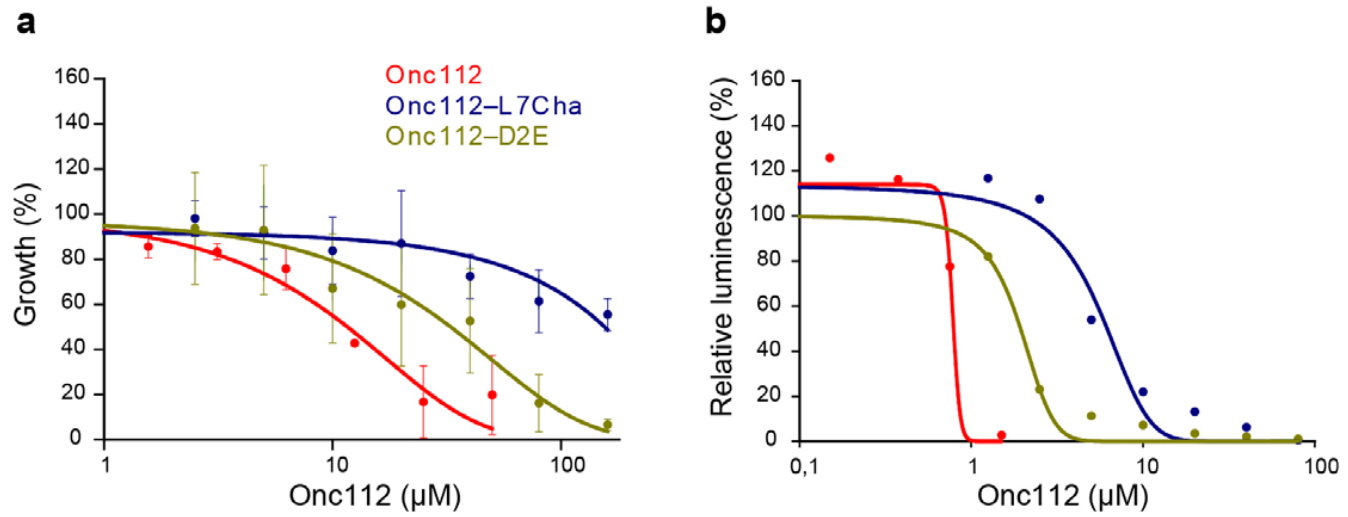
The conformation of residues Lys3–Pro10 of the Oncocin peptide O2 (cyan, VDKPPYLPRPRPPROIYNO–NH₂, where O represents ornithine) in complex with DnaK (white surface representation) was compared with residues Val1–Pro12 of Onc112 (orange) from the ribosome-bound Onc112 structure.



Supplementary Figure 3

Conformation of the Onc112 peptide in solution.

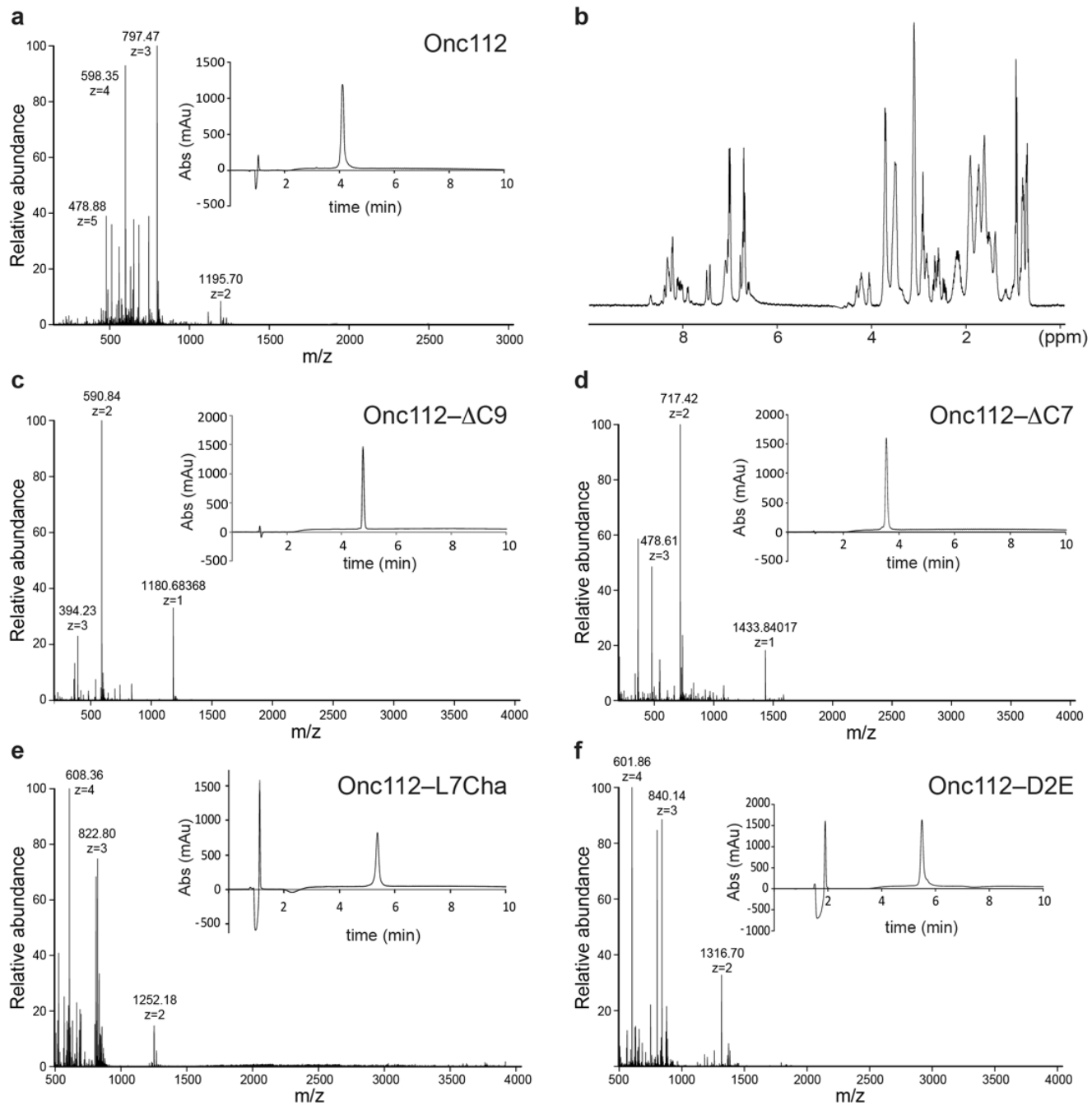
Far-UV circular dichroism (CD) spectra of the Onc112 peptide at concentrations ranging from 20 to 200 μM .



Supplementary Figure 4

Inhibitory activity of Onc112 peptide derivatives.

(a-b) Effect of Onc112 (red) and Onc112 derivatives Onc112-L7Cha (blue) and Onc112-D2E (olive) on (a) the overnight growth of *E. coli* strain BL21(DE3) and (b) the luminescence resulting from the *in vitro* translation of firefly luciferase (Fluc). In (a), the error bars represent the standard deviation (s.d.) from the mean for a triplicate experiment ($n=3$). In (b), the experiment was performed in duplicate ($n=2$). The growth or luminescence measured in the absence of peptide was assigned as 100%.



Supplementary Figure 5

Validation of Onc112 and derivatives.

(a) Electrospray ionization high resolution mass spectrometry (ESI-HRMS) and reverse phase (RP) high performance liquid chromatography (HPLC), and (b) ¹H nuclear magnetic resonance (NMR) spectra of the Onc112 peptide. (c-f) ESI-HRMS and RP HPLC of the (c) Onc112-ΔC9, (d) Onc112-ΔC7, (e) Onc112-L7Cha and (f) Onc112-D2E peptides.

Structure of the mammalian antimicrobial peptide Bac7(1–16) bound within the exit tunnel of a bacterial ribosome

A. Carolin Seefeldt^{1,2,3,†}, Michael Graf^{4,†}, Natacha Pérébaskine^{1,2,3}, Fabian Nguyen⁴, Stefan Arenz⁴, Mario Mardirossian⁵, Marco Scocchi⁵, Daniel N. Wilson^{4,6,*} and C. Axel Innis^{1,2,3,*}

¹Institut Européen de Chimie et Biologie, University of Bordeaux, Pessac 33607, France, ²U1212, Inserm, Bordeaux 33076, France, ³UMR 5320, CNRS, Bordeaux 33076, France, ⁴Gene Center and Department for Biochemistry, University of Munich, Munich 81377, Germany, ⁵Department of Life Sciences, University of Trieste, Trieste 34127, Italy and ⁶Center for integrated Protein Science Munich (CiPSM), University of Munich, Munich 81377, Germany

Received October 13, 2015; Revised December 22, 2015; Accepted December 28, 2015

ABSTRACT

Proline-rich antimicrobial peptides (PrAMPs) produced as part of the innate immune response of animals, insects and plants represent a vast, untapped resource for the treatment of multidrug-resistant bacterial infections. PrAMPs such as oncacin or bactenecin-7 (Bac7) interact with the bacterial ribosome to inhibit translation, but their supposed specificity as inhibitors of bacterial rather than mammalian protein synthesis remains unclear, despite being key to developing drugs with low toxicity. Here, we present crystal structures of the *Thermus thermophilus* 70S ribosome in complex with the first 16 residues of mammalian Bac7, as well as the insect-derived PrAMPs metalnikowin I and pyrrhocoricin. The structures reveal that the mammalian Bac7 interacts with a similar region of the ribosome as insect-derived PrAMPs. Consistently, Bac7 and the oncacin derivative Onc112 compete effectively with antibiotics, such as erythromycin, which target the ribosomal exit tunnel. Moreover, we demonstrate that Bac7 allows initiation complex formation but prevents entry into the elongation phase of translation, and show that it inhibits translation on both mammalian and bacterial ribosomes, explaining why this peptide needs to be stored as an inactive pro-peptide. These findings highlight the need to consider the specificity of PrAMP derivatives for the bacterial ribosome in future drug development efforts.

INTRODUCTION

Antimicrobial peptides (AMPs) represent a large and diverse group of molecules that form part of the innate immune response of a variety of invertebrate, plant and animal species (1). While many AMPs kill bacteria by disrupting the bacterial cell membrane, there is growing evidence that some AMPs have intracellular targets (1). Members of one such class of non-membranolytic peptides are referred to as proline-rich AMPs (PrAMPs) and are present in the hemolymph of several species of insects and crustaceans, as well as in the neutrophils of many mammals (2). PrAMPs exhibit potent antimicrobial activity against a broad range of bacteria, especially Gram-negative, and are therefore considered as potential lead candidates for the development of therapeutic antimicrobial agents (3). Well-characterized insect PrAMPs include the apidaecins produced by bees (*Apis mellifera*) and wasps (*Apis Vespidae*), pyrrhocoricin from firebugs (*Pyrrhocoris apterus*), drosocins from fruit flies (*Drosophila*), metalnikowins from the green shield bug (*Palomena prasina*) and the milkweed bug (*Oncopeltus fasciatus*) oncocins (2,4,5). PrAMPs are synthesized as inactive precursors, which undergo proteolysis to release the active peptide. In contrast to the active insect peptides, which are generally <21 amino acids in length, the active mammalian mature forms tend to be much longer; for example, the porcine PR-39 is 39 residues long, whereas the bovine bactenecin-7 (Bac7), which is also found in sheep and goats, is 60 residues long (2). Nevertheless, C-terminally truncated versions of the mammalian PrAMPs retain antimicrobial activity (6–9) and exhibit high sequence similarity with the insect PrAMPs. Indeed, the Bac7(1–16) and Bac7(1–35) derivatives corresponding to the first 16 and

*To whom correspondence should be addressed. Tel: +33 540 006 149; Fax: +33 540 002 215; Email: axel.innis@inserm.fr

Correspondence may also be addressed to Daniel N. Wilson. Tel: +49 89 2180 76903; Fax: +49 89 2180 76945; Email: wilson@lmb.uni-muenchen.de

†These authors contributed equally to the paper as first authors.

© The Author(s) 2016. Published by Oxford University Press on behalf of Nucleic Acids Research.

This is an Open Access article distributed under the terms of the Creative Commons Attribution License (<http://creativecommons.org/licenses/by-nc/4.0/>), which permits non-commercial re-use, distribution, and reproduction in any medium, provided the original work is properly cited. For commercial re-use, please contact journals.permissions@oup.com

35 residues of Bac7, respectively, display similar, if not improved, antimicrobial activities compared to the full-length processed Bac7 peptide (6,10,11). For instance, Bac7(1–35) reduces mortality from *Salmonella typhimurium* in a mouse model of infection (12) as well as in a rat model for septic shock (13).

The insect-derived PrAMPs apidaecin and oncocin, as well as the mammalian Bac7, penetrate the bacterial cell membrane mainly via the SbmA transporter present in many Gram-negative bacteria (10,14). Early studies identified interactions between both insect and mammalian PrAMPs and DnaK, suggesting that this molecular chaperone was the common intracellular target (2,15). However, subsequent studies questioned the relevance of this interaction by demonstrating that these PrAMPs also display an equally potent antimicrobial activity against bacterial strains lacking the *dnaK* gene (16–18). Instead, apidaecin, oncocin and Bac7 were shown to bind to the ribosome and inhibit translation (17,19). Subsequent crystal structures of the oncocin derivative Onc112 in complex with the bacterial 70S ribosome revealed that this peptide binds with a reverse orientation in the ribosomal tunnel and blocks binding of the aminoacyl-tRNA to the A-site (20,21). However, there are no crystal structures to date of a mammalian PrAMP in complex with the ribosome.

Here we present 2.8–2.9 Å resolution X-ray structures of the *Thermus thermophilus* 70S (*Tth*70S) ribosome in complex with either the mammalian Bac7 derivative Bac7(1–16) or the insect-derived PrAMPs metalnikowin I or pyrrhocoricin. The structures reveal that Bac7(1–16), metalnikowin I and pyrrhocoricin bind within the ribosomal tunnel with a reverse orientation compared to a nascent polypeptide chain, as observed previously for oncocin (20,21). In contrast to the insect PrAMPs oncocin, metalnikowin I and pyrrhocoricin, the mammalian Bac7(1–16) utilizes multiple arginine side chains to establish stacking interactions with exposed nucleotide bases of the rRNA, and we show that its unique N-terminal RIRR motif is critical for inhibiting translation. Like oncocin, metalnikowin I and pyrrhocoricin, the binding site of Bac7 overlaps with that of the A-tRNA, consistent with our biochemical studies indicating that Bac7(1–16) allows 70S initiation complex formation, but prevents subsequent rounds of translation elongation. Furthermore, we demonstrate that Bac7(1–35) displays activity in a mammalian *in vitro* translation system, providing a possible explanation for why Bac7 is produced as a pre-pro-peptide that is targeted to large granules and phagosomes, thus avoiding direct contact between the active peptide and the mammalian ribosome.

MATERIALS AND METHODS

Peptide synthesis and purification

The Bac7 N-terminal fragments Bac7(1–16; RRIR-PRPPRLPRPRPR), Bac7(1–35; RRIRPRPPRL-PRPRPRLPFPRLPGPRPIPRPLPFP) and Bac7(5–35; PRPPRLPRPRPRLPFPRLPGPRPIPRPLPFP) were synthesized on solid phase and purified by reversed-phase HPLC as described previously (22). Their concentrations were determined as reported previously (4). All peptides, with a purity of at least 95%, were stored in

milliQ water at –80°C until use. The Onc112 peptide was obtained from an earlier study (21). Metalnikowin I (VDKPDYRPRPRPPNM) and pyrrhocoricin (VDKG-SYLPRTPPRPIYNRN) were synthesized to 97.5 and 98.1% purity by NovoPro Bioscience (China).

Purification of *T. thermophilus* 70S ribosomes

*Tth*70S ribosomes were purified as described earlier (23) and resuspended in buffer containing 5 mM HEPES-KOH, pH 7.5, 50 mM KCl, 10 mM NH₄Cl and 10 mM Mg(CH₃COO)₂ to yield a final concentration of ~30 mg/ml. *Tth*70S ribosomes were flash frozen in liquid nitrogen and kept at –80°C for storage.

Preparation of mRNA, tRNA_i^{Met} and YfiA

Synthetic mRNA containing a Shine-Dalgarno sequence and an AUG start codon followed by a phenylalanine codon (5'-GGC AAG GAG GUA AAA AUG UUC UAA -3') was purchased from Eurogentec. *Escherichia coli* tRNA_i^{Met} was overexpressed in *E. coli* HB101 cells and purified as described previously (24). YfiA was overexpressed in BL21 Star cells and purified as described previously (25).

Complex formation

A quaternary complex containing *Tth*70S ribosomes, mRNA, deacylated tRNA_i^{Met} and Bac7(1–16) peptide was prepared by mixing of 5 μM *Tth*70S ribosomes with 10 μM mRNA and 50 μM Bac7(1–16), and incubating at 55°C for 10 min. After addition of 20 μM tRNA_i^{Met}, the mixture was incubated at 37°C for 10 min. The sample was then incubated at room temperature for at least 15 min and centrifuged briefly prior to use. Ternary complexes containing 50 μM metalnikowin I or pyrrhocoricin, 5 μM *Tth*70S ribosomes and 50 μM YfiA were formed by incubation for 30 min at room temperature. The final buffer conditions were 5 mM HEPES-KOH, pH 7.6, 50 mM KCl, 10 mM NH₄Cl and 10 mM Mg(CH₃COO)₂.

Crystallization

Published conditions were used as a starting point for screening crystallization conditions by vapour diffusion in sitting-drop trays at 20°C (23,26). Crystallization drops consisted of 3 μl of quaternary or ternary complexes and 3–4 μl of reservoir solution containing 100 mM Tris-HCl, pH 7.6, 2.9% (v/v) PEG 20,000, 7–10% (v/v) 2-methyl-2,4-petanediol (MPD) and 175 mM arginine. Crystals appeared within 2–3 days and grew to ~1000 × 100 × 100 μm within 7–8 days. For cryoprotection, the concentration of MPD was increased in a stepwise manner to yield a final concentration of 40% (v/v). The ionic composition during cryoprotection was 100 mM Tris-HCl, pH 7.6, 2.9% (v/v) PEG 20,000, 50 mM KCl, 10 mM NH₄Cl and 10 mM Mg(CH₃COO)₂. Crystals were flash frozen in a nitrogen cryostream at 80 K for subsequent data collection.

Data collection and processing

Diffraction data for Bac7(1–16) were collected at PROXIMA-2A, a beamline at the SOLEIL synchrotron (Saclay, France) equipped with an ADSC Q315 detector. A complete dataset was obtained by merging 0.25° oscillation data collected at 100 K with a wavelength of 0.98011 Å from multiple regions of the same crystal. Diffraction data for mettalnikowin I and pyrrhocoricin were collected at PROXIMA-1, a beamline at the SOLEIL synchrotron equipped with a DECTRIS PILATUS 6M detector. Complete datasets were obtained by merging 0.1° oscillation data collected at 100 K with a wavelength of 0.97857 Å from multiple regions of the crystal. Initial data processing, including integration and scaling, was performed with X-ray Detector Software (XDS) (27). The data could be indexed in the $P2_12_12_1$ space group, with unit-cell dimensions approximating 210 × 450 × 625 Å and an asymmetric unit containing two copies of the *Tth*70S ribosome.

Model building and refinement

Initial phases were obtained by molecular replacement performed with Phaser (28). The search model was obtained from a high-resolution structure of the *Tth*70S ribosome (PDB ID: 4Y4O) (29) where the RNA backbone had been further improved with the ERRASER-Phenix pipeline (30), using the deposited structure factors. Restrained crystallographic refinement was carried out with Phenix (31) and consisted of a single cycle of rigid-body refinement followed by multiple cycles of positional and individual *B*-factor refinement. Rigid bodies comprised four domains from the small 30S subunit (head, body, spur and helix h44) and three domains from the large 50S subunit (body, L1 stalk and the C terminus of ribosomal protein L9). Non-crystallographic symmetry restraints between the two copies of the *Tth*70S ribosome in the asymmetric unit were also applied during refinement. After confirming that a single tRNA was bound to the P site or that YfiA was present at the decoding center, and that additional density corresponding to the PrAMPs was visible within the exit tunnel in a minimally biased F_O – F_C map, models of the corresponding PrAMPs were built in Coot (32). The models for the tRNA and mRNA were obtained from a high-resolution structure of the *Tth*70S ribosome pre-attack complex (PDB ID: 1VY4). The model for YfiA was obtained from a high resolution *Tth*70S ribosome structure (PDB ID: 4Y4O). Further refinement and model validation was carried out in Phenix (31) and on the MolProbity server (33), respectively. In the final models, 0.56–0.95% of protein residues were classified as Ramachandran outliers, and 92.4–94.3% had favourable backbone conformations (Supplementary Table S1). Coordinates and structure factors have been deposited in the Protein Data Bank under accession codes 5F8K (Bac7(1–16)), 5FDU (Mettalnikowin I) and 5FDV (Pyrrhocoricin).

In vitro translation assays

Escherichia coli lysate-based transcription-translation coupled assay (RTS100, 5Prime) were performed as described previously for other translational inhibitors (34). Briefly,

μl reactions, with or without PrAMP were mixed according to the manufacturer's description and incubated for 1 h at 30°C with shaking (750 rpm). A total of 0.5 μl of each reaction were stopped with 7.5 μl kanamycin (50 μg/μl). The effect of Bac7(1–35) on eukaryotic translation was determined using Rabbit Reticulocyte Lysate System (Promega). A total of 6 μl reactions, with or without Bac7(1–35) were mixed according to the manufacturer's description and incubated for 1 h at 30°C with shaking (300 rpm). A total of 5 μl of each reaction were stopped in 5 μl kanamycin (50 μg/μl). All samples were diluted with 40 μl of Luciferase assays substrate (Promega) into a white 96-well chimney flat bottom microtiter plate (Greiner). The luminescence was then measured using a Tecan Infinite M1000 plate reader. Relative values were determined by defining the luminescence value of the sample without inhibitor as 100%.

Toe-printing assay

The position of the ribosome on the mRNA was monitored with a toe-printing assay (35) based on an *in vitro*-coupled transcription-translation system with the PURExpress *in vitro* protein synthesis kit (NEB), as described previously (21,36). Briefly, each translation reaction consisted of 1 μl solution A, 0.5 μl Δisoleucine amino acid mixture, 0.5 μl tRNA mixture, 1.5 μl solution B, 0.5 μl (0.5 pmol) hns37aa template: (5'-ATTAAT ACGACTCACTATAGGGATATAAGGAGGAAAC AT~~atg~~*AGCGAAGCACTTAA*~~att~~*CTGAACAAACCTGC* GTACTCTCGTGC~~G~~CAGGCAAGACC~~G~~CCGCC~~G~~ TTGAAACGCTGGAAGAAATGCTGGAAAAATT~~A~~ GAAGTTGTT~~G~~Taa~~G~~TGATAGAATTCTATC~~G~~TTA ATAAGCAAAATT~~C~~ATTATAAC-3', with start codon ATG, catch isoleucine codon ATT and stop codon TAA in bold, the hns37aa ORF underlined and toe-print primer binding site in italics) and 0.5 μl additional agents (nuclease-free water, water dissolved Bac7(1–35) Bac7(1–16), Bac7(5–35) (1, 10 or 100 μM final concentration) or antibiotics (100 μM thiostrepton, 50 μM edeine, 50 μM clindamycin final concentration)). Translation was performed in the absence of isoleucine at 37°C for 15 min at 500 rpm in 1.5 ml reaction tubes. After translation, 2 pmol Alexa647-labelled NV-1 toe-print primer (5'-GGTTATAATGAATTTC~~G~~TATTAAAC-3') was added to each reaction. Reverse transcription was performed with 0.5 μl of AMV RT (NEB), 0.1 μl dNTP mix (10 mM) and 0.4 μl Pure System Buffer and incubated at 37°C for 20 min. Reverse transcription was quenched and RNA degraded by addition of 1 μl 10 M NaOH and incubation for at least 15 min at 37°C and then was neutralized with 0.82 μl of 12 M HCl. 20 μl toe-print resuspension buffer and 200 μl PN1 buffer were added to each reaction before treatment with a QIAquick Nucleotide Removal Kit (Qiagen). The Alexa647-labelled DNA was then eluted from the QIAquick columns with 80 μl of nuclease-free water. A vacuum concentrator was used to vaporize the solvent and the Alexa647-labelled DNA was then dissolved into 3.5 μl of formamide dye. The samples were heated to 95°C for 5 min before being applied onto a 6% polyacrylamide (19:1) sequencing gel containing 7 M urea. Gel electrophoresis was performed at 40 W and 2000 V for 2 h. The GE

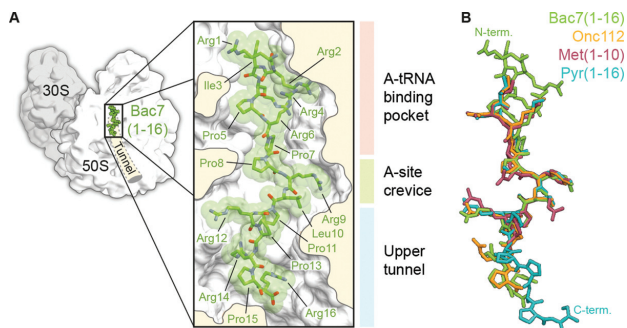


Figure 1. Binding site of Bac7(1–16) on the ribosome and comparison with Onc112. (A) Overview and closeup view of a cross-section of the *Tth*70S ribosomal exit tunnel showing the Bac7(1–16) peptide (RRIR-PRPPRPLRPRPR) in green and highlighting the three regions of interaction with the ribosome: the A-tRNA binding pocket (light pink), the A-site crevice (light green) and the upper section of the exit tunnel (light blue). (B) Structural comparison of Bac7(1–16) (green) with Onc112 (orange) (20,21), Met1(1–10) (burgundy) and Pyr(1–16) (cyan), highlighting the distinct structure of the Bac7 N-terminus (N-term) and the Pyr C-terminus (C-term).

Typhoon FLA9500 imaging system was subsequently used to scan the polyacrylamide gel.

Filter binding assay

Filter binding assays were performed as described previously (34,37). Briefly, 3 pmol of 70S ribosomes purified from BL21 *E. coli* strain were exposed to 30 pmol of radiolabelled [¹⁴C]-Erythromycin (Perkin Elmer; 110 dpm/pmol) in presence of 1x filter binding buffer (10 mM HEPES/KOH [pH 7.4], 30 mM MgCl₂, 150 mM NH₄Cl and 6 mM β-mercaptoethanol) for 15 min at 37°C. Our controls indicated that approximately 65% of the 70S ribosomes (2 pmol) contained [¹⁴C]-Erythromycin previous to the addition of the different PrAMPs. The PrAMPs were diluted in nuclease-free water to a concentration of 1 mM, 100 μM and 10 μM. 2 μl of each PrAMP stock dilution (Onc112, Bac7(1–35), Bac7(1–16) and Bac7(5–35)) were transferred to the respective tube resulting in final concentrations of 100, 10 and 1 μM. Reactions were incubated for an additional 25 min at 37°C. Afterwards the 20 μl samples were passed through a HA-type nitrocellulose filter from Millipore (0.45 μm pore size) and the filter subsequently washed three times with 1 ml 1x filter binding buffer. Scintillation counting was performed in the presence of Rotiszint® eco plus Scintillant. All reactions were performed in duplicate and results were analysed using GraphPad Prism 5. Error bars represent the standard deviation from the mean.

Disome formation assay

The disome formation assay was performed as described previously (38,39). Briefly, *in vitro* translation of the 2xermBL construct was performed using the Rapid Translation System RTS 100 *E. coli* HY Kit (Roche). Translations were carried-out for 1 h at 30°C and then analysed on 10–55% sucrose density gradients (in a buffer containing 50 mM HEPES-KOH, pH 7.4, 100 mM KOAc, 25 mM

Mg(OAc)₂, 6 mM β-mercaptoethanol) by centrifugation at 154 693 × g (SW-40 Ti, Beckman Coulter) for 2.5 h at 4°C.

RESULTS

The N-terminus of Bac7 adopts a compact conformation

We obtained a structure referred to here as *Tth*70S-Bac7 from co-crystals of *Tth*70S ribosomes in complex with deacylated tRNA_i^{Met}, a short mRNA and Bac7(1–16) (Supplementary Table S1). In addition, we obtained two additional structures, *Tth*70S-MetI and *Tth*70S-Pyr, from co-crystals of *Tth*70S ribosomes in complex with YfiA and either metalnikowin I or pyrrhocoricin, respectively (Supplementary Table S1). The quality of the electron density in the minimally biased F_O–F_C difference maps calculated after refinement of a model comprising *Tth*70S ribosomes and tRNA_i^{Met}/mRNA or YfiA, made it possible to build a model for the entire Bac7(1–16; RRIRPRPPRL-PRPRPR), the first 10 (of 15; VDKPDYRPRPRPPNM) residues of metalnikowin I (MetI) and the first 16 (of 20; VDKGSYLPRLPPTPPRPIYNRN) residues of pyrrhocoricin (Pyr), as well as to position several neighbouring solvent molecules (Supplementary Figure S1). Like the insect-derived Onc112 peptide (20,21), MetI, Pyr and Bac7(1–16) all bind to the ribosomal exit tunnel in a reverse orientation relative to the nascent polypeptide chain and make extensive interactions with three distinct regions of the large 50S ribosomal subunit: the A-tRNA binding pocket, the A-site crevice and the upper section of the nascent polypeptide exit tunnel (Figure 1A, B and Supplementary Figure S1). A nearly identical, extended backbone conformation is seen for residues 7–13 of Bac7(1–16) and residues 4–10 of Onc112, MetI and Pyr, with Arg9 of Bac7(1–16) substituting for Tyr6 of Onc112, MetI and Pyr (Figure 1B). The structural similarity however does not extend to the N-terminus of Bac7(1–16), where the first six residues adopt a structure that deviates substantially from that of the shorter N-terminus of the insert-derived PrAMPs. Indeed, arginine residues within this region are arranged such that the side chain of Arg6 is sandwiched between the side chains of Arg2 and Arg4 to form a compact, positively charged structure (Figure 1A and B). The binding site of Bac7(1–16) suggests that the additional C-terminal residues of Bac7(1–35) and of the full-length Bac7 (60 residues) would occupy the entire length of the ribosomal tunnel. Consistently, a photocrosslinkable derivative of Bac7(1–35) has been cross-linked to two ribosomal proteins of ~16 and 25 kDa (19), which we suggest to be L22 and L4, respectively, based on their size and close proximity to the Bac7(1–16) binding site (Supplementary Figure S2). Compared to Onc112 and MetI, additional density for the C-terminal PRPR motif (residues 13–16) of Pyr is observed extending deeper into the tunnel (Figure 1 and Supplementary Figure S1). With the exception of Arg14 for which no density is observed, the PRPR motif is quite well ordered despite not forming any obvious direct interactions with the ribosome.

Bac7 makes extensive interactions with the 50S ribosomal subunit

As with Onc112 (20,21), binding of Bac7(1–16) to the ribosome is accompanied by an induced fit involving 23S rRNA residues A2062, U2506 and U2585 (Supplementary Figure S3A; *E. coli* numbering is used throughout this work for the 23S rRNA), such that the base of this last nucleotide occupies a position that would normally clash with the formyl-methionyl moiety of fMet-tRNA_i^{Met} bound to the P-site of an initiation complex (Supplementary Figure S3B). Three modes of interaction are observed between Bac7(1–16) and the large 50S ribosomal subunit (Figure 2A–E).

First, the N-terminal region of Bac7(1–16) forms multiple hydrogen bonds and salt bridges with the A-tRNA binding pocket of the ribosome (Figure 2A and B). In particular, the compact structure formed by Arg2, Arg4 and Arg6 provides a positively charged N-terminal anchor that displaces two magnesium ions from a deep groove lined by 23S rRNA residues C2452, A2453 and G2454 on one side, and residues U2493 and G2494 on the other (Figure 2B). This groove differs from the standard A-form RNA major groove in that it occurs between two unpaired, antiparallel strands of the 23S rRNA. Consequently, the compact arginine structure at the N-terminus of Bac7(1–16) is ideally sized and shaped to fit into this groove and the resulting interaction is likely to be specific in spite of its simple electrostatic nature. Further contacts in this region are likely to increase the specificity of Bac7(1–16) for the ribosome, such as the two hydrogen bonds between the side chain of Arg1 and 23S rRNA residues U2555 and C2556, and four hydrogen bonds between the backbone of Bac7(1–16) residues Arg2–Arg4 and 23 rRNA residues U2492, U2493 and C2573 (Figure 2A).

Second, the unusually high arginine (50%) and proline (37.5%) content of Bac7(1–16) restricts the types of contacts that this peptide can establish with the ribosome. This results in π -stacking interactions between the side chains of Arg2, Arg9, Arg12, Arg14 and Arg16 and exposed bases of 23S rRNA residues C2573, C2452/U2504, C2610, C2586 and A2062, respectively. Additional rigidity within the peptide is provided through the packing of Arg1 against Ile3 and Arg9 against Leu10, and through the compact arginine stack described above (Figure 2C).

Third, numerous possible hydrogen bonds can be established between the backbone of Bac7(1–16) and the ribosome (Figure 2A, D and E), including many indirect interactions via ordered solvent molecules (Figure 2D and E). Many of the water-mediated contacts suggested for *Tth*70S–Bac7 are likely to occur with oncocin, even though the lower resolution of the earlier *Tth*70S–Onc112 structures precluded the modelling of any water molecules (20,21). In addition, interactions such as those between 23S rRNA residue U2506 and the backbone of Bac7(1–16) residues Arg9 and Leu10 were also proposed to occur between the Onc112 peptide and the ribosome (20,21).

Bac7 and Onc112 compete with erythromycin for ribosome binding

The C-terminal residues 12–16 of Bac7(1–16) overlap with the binding site of the macrolide antibiotic erythromycin

on the bacterial ribosome (40,41), in particular with the region occupied by the cladinose sugar and part of the lactone ring (Figure 3A). Consistently, we could demonstrate that Bac7(1–16) and Bac7(1–35) efficiently compete with the binding of radiolabelled erythromycin to the 70S ribosome (Figure 3B). Similarly, Onc112 also efficiently competed with erythromycin (Figure 3B), as expected based on the similarity in binding mode with the ribosome for these regions of Onc112 and Bac7 (Figure 1B). In contrast, Bac7(5–35) was a poor competitor of erythromycin (Figure 3B), indicating that the highly cationic N-terminus of Bac7 and its interaction with the A-tRNA binding pocket (Figure 2B) are important for high affinity binding of Bac7 to the ribosome. Indeed, Bac7 derivatives lacking the first four N-terminal residues (RRIR), Bac7(5–35) and Bac7(5–23), exhibit dramatically reduced minimal inhibitory concentrations (MIC) against Gram-negative strains, such as *E. coli*, as well as *Salmonella typhimurium* (6). We note, however, that the internalization of Bac7(5–35) into bacteria is reduced, indicating that the N-terminal RRIR motif also plays an important role for cell penetration (11).

Bac7 allows initiation, but prevents translation elongation

Consistent with the erythromycin binding assays and in agreement with previous results (Figure 4A) (19), we observed that Bac7(1–35) inhibits the production of luciferase with an IC₅₀ of 1 μ M in an *E. coli* *in vitro* translation system, similar to MetI and Pyr (Supplementary Figure S1), as well as that observed previously for Onc112 (20,21). Bac7(1–16) was an equally potent inhibitor as Bac7(1–35), consistent with the similar MICs observed for these two derivatives (6,10,11). In contrast, Bac7(5–35) inhibited *in vitro* translation with an IC₅₀ of 10 μ M, i.e. 10-fold higher than observed for Bac7(1–16) or Bac7(1–35), indicating that the reduced affinity for the ribosome, together with reduced cellular uptake (11), results in the higher MIC of the Bac7(5–35) derivative (6,42).

Next we investigated the mechanism of inhibition by Bac7 using two *in vitro* translation assays. First, we compared the effect of Bac7(1–35) and Bac7(5–35) on the stabilization of disomes formed upon the stalling of ribosomes on a dicistronic mRNA (in this case 2XErmBL mRNA), as measured by sucrose gradient centrifugation (21,38,39). In the absence of inhibitor, the majority of ribosomes are present as 70S monosomes (control in Figure 4B), whereas the presence of erythromycin leads to translational arrest of the ribosomes on both cistrons of the 2XErmBL mRNA, thereby generating the expected disome peaks (Ery in Figure 4B). Consistent with the *in vitro* translation assays (Figure 4A), translation inhibition and thus disome formation was observed in the presence of 10 μ M Bac7(1–35), whereas even 100 μ M of Bac7(5–35) did not produce significant disomes (Figure 4B). These findings suggest that Bac7(1–35) but not Bac7(5–35) stabilizes an arrested ribosome complex, as observed previously for Onc112 (21).

Second, to monitor the exact site of translation inhibition of the Bac7 derivatives, we employed a toeprinting assay, which uses reverse transcription from the 3' end of an mRNA to determine the exact location of the ribosomes that are translating it (35). In the absence of in-

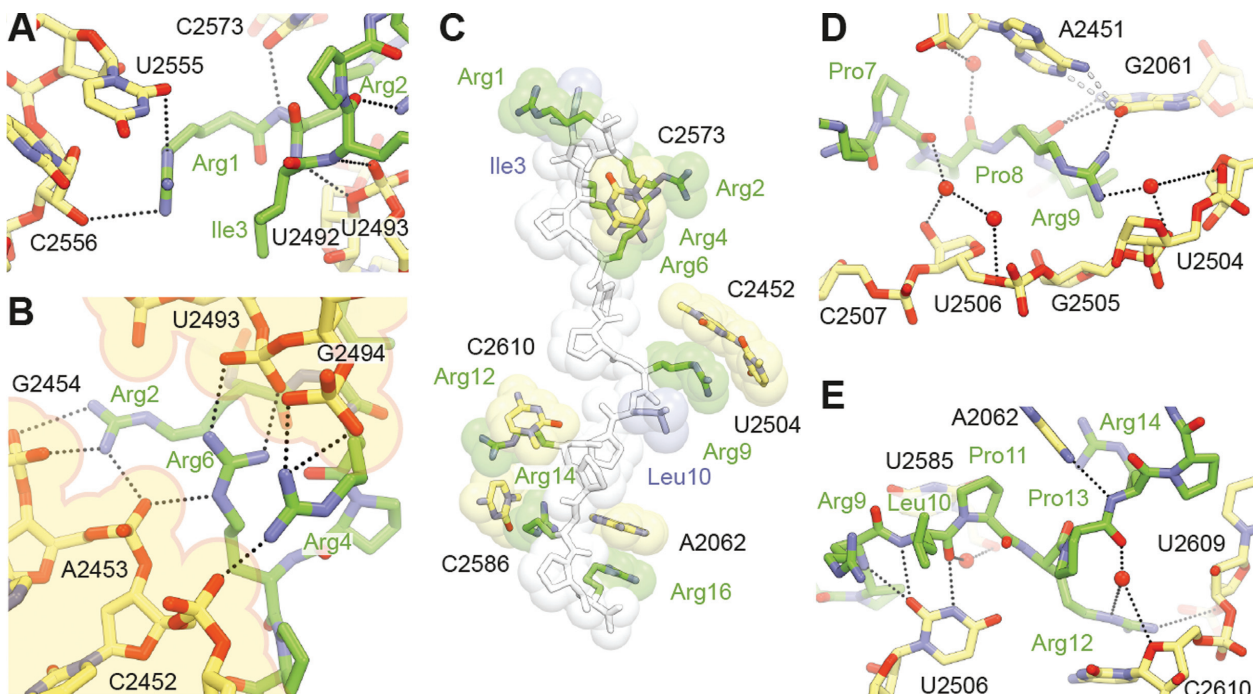


Figure 2. Interactions between Bac7(1–16) and the ribosome. (A) Bac7(1–16) (green) makes extensive contacts with the A-site tRNA binding region of the ribosome, in particular (B) electrostatic interactions between its N-terminal arginine stack and a deep groove lined by phosphate groups from the 23S rRNA (B). (C) π -stacking interactions between arginine side chains (green) of Bac7(1–16) and 23S rRNA bases contribute to much of the binding and are reinforced through further packing against aliphatic side chains (blue). (D and E) Water-mediated contacts between the peptide and the ribosome are also proposed to occur further down the exit tunnel, in addition to direct hydrogen bonding interactions between the two.

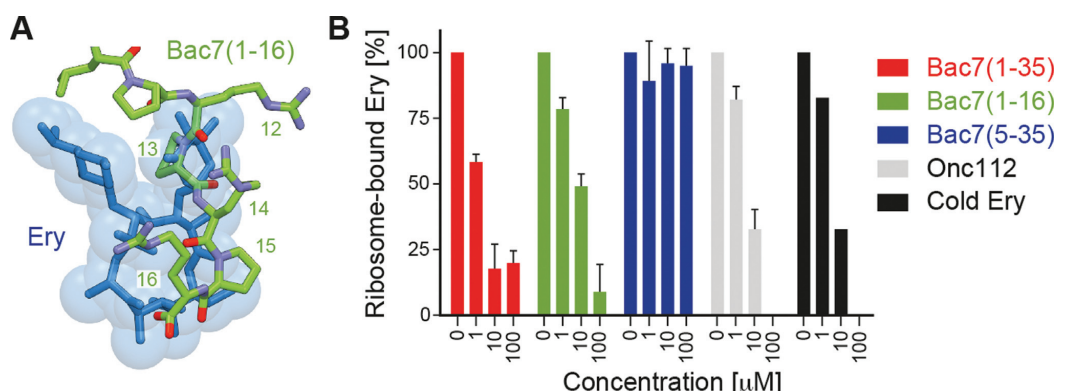


Figure 3. Competition between Bac7 derivatives and erythromycin. (A) Superimposition of the binding site of erythromycin (blue) (40,41) with residues 11–16 of Bac7(1–16) (green). (B) A filter binding assay was used to monitor competition between radiolabelled [14 C]-erythromycin and increasing concentrations (1–100 μ M) of Bac7(1–35) (red), Bac7(1–16) (green), Bac7(5–35) (blue), Onc112 (grey) and cold (non-radioactive) erythromycin (ery, black).

hibitor, ribosomes initiated at the AUG start codon of the mRNA, translated through the open reading frame and ultimately became stalled on an isoleucine codon (Figure 4C) due to the omission of isoleucine from the translation mix. In the presence of thiostrepton or clindamycin, ribosomes accumulated at the AUG codon (Figure 4C), since these antibiotics prevent delivery and/or accommodation of aminoacyl-tRNA at the A-site directly following initiation (43). Similar results were observed when using the Bac7(1–35) and Bac7(1–16) derivatives, such that complete

inhibition of translation elongation was observed at a peptide concentration of 10 μ M (Figure 4C). These findings suggest that like Onc112 (21), Bac7 allows subunit joining and fMet-tRNA_i^{Met} binding, but prevents accommodation of the first aminoacyl-tRNA at the A-site, as suggested by the overlap in the binding site of Bac7 and the CCA-end of an A-tRNA (Figure 4D). Curiously, the toeprint for ribosomes stalled during initiation became weaker at 100 μ M of Bac7(1–16) and Bac7(1–35) and the signal for the full-length mRNA became stronger, similar to the effect ob-

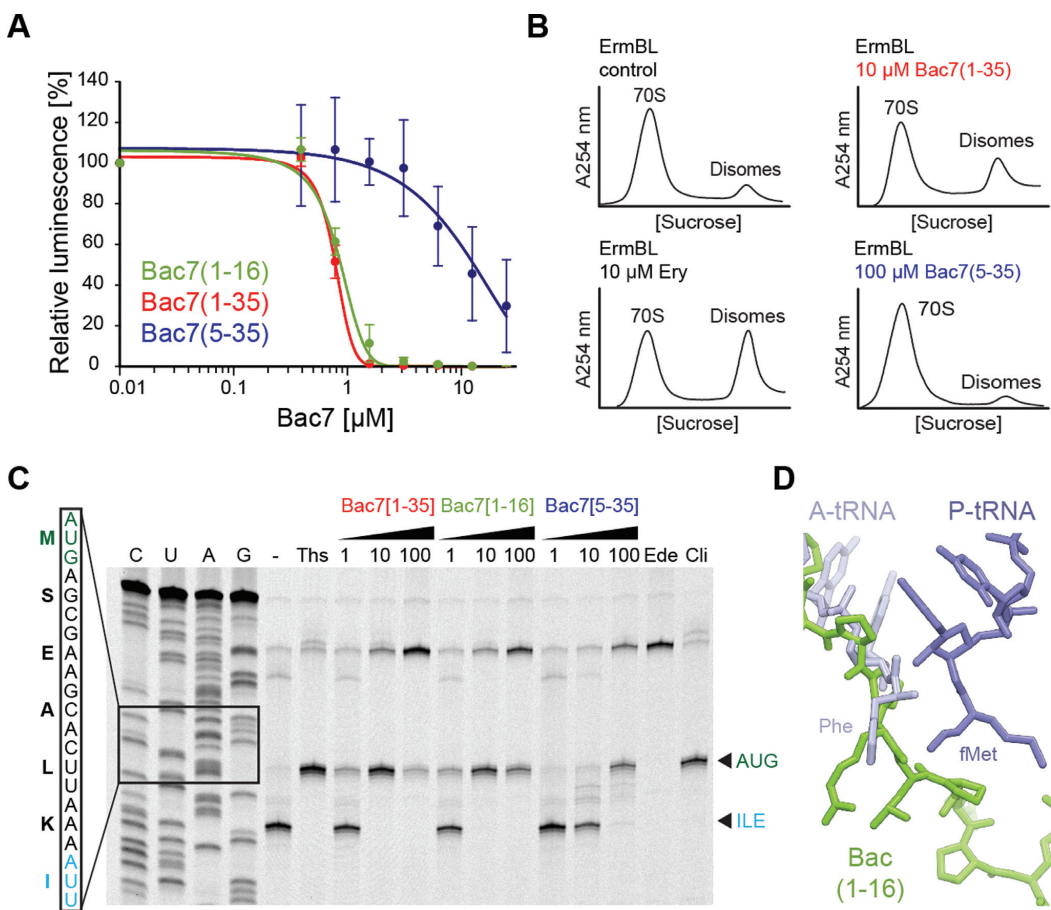


Figure 4. Mechanism of action of Bac7 on the ribosome. (A) Effects of increasing concentrations of Bac7 derivatives Bac7(1–16) (green), Bac7(1–35) (red) and Bac7(5–35) (blue) on the luminescence resulting from the *in vitro* translation of firefly luciferase (Fluc) using an *Escherichia coli* lysate-based system. The error bars represent the standard deviation from the mean for triplicate experiments and the luminescence is normalized relative to that measured in the absence of peptide, which was assigned as 100%. (B) Sucrose gradient profiles to monitor disome formation from *in vitro* translation of the 2XErmBL mRNA in the absence (control) or presence of 20 μM erythromycin (Ery), 10 μM Bac7(1–35) (red) or 100 μM Bac7(5–35) (blue). (C) Toe-printing assay performed in the absence (–) or presence of increasing concentrations (1, 10, 100 μM) of Bac7(1–35), Bac7(1–16) or Bac7(5–35), or 100 μM thiostrepton (Ths), 50 μM edeine (Ede) or 50 μM clindamycin (Cli). Sequencing lanes for C, U, A and G and the sequence surrounding the toe-print bands (arrowed) when ribosomes accumulate at the AUG start codon (green, initiation complex) or the isoleucine codon (blue, stalled elongation complex) are included for reference. (D) Structural comparison of Phe-tRNA^{Phe} (slate) in the A-site and fMet-tRNA_i^{Met} in the P-site (blue) (26) with the binding site of Bac7(1–16) (green).

served when the antibiotic edeine was used (Figure 4C). Edeine prevents 70S initiation complex formation by destabilizing fMet-tRNA_i^{Met} binding to the 30S subunit (43). Thus, Bac7 may have a similar effect when high cytosolic concentrations are achieved through active uptake into the cell, possibly due to the presence of non-specific interactions with the ribosome. In contrast to Bac7(1–16) and Bac7(1–35), Bac7(5–35) only stabilized the initiation complex at a much higher concentration (100 μM) (Figure 4C). This is consistent with a reduced affinity of Bac7(5–35) for the ribosome and reinforces the critical role played by the first four residues of Bac7 in its inhibitory activity (Figure 1A) (6,42).

Bac7 inhibits eukaryotic translation *in vitro*

Bac7(1–35) is internalized by mammalian cells (42,44), yet no toxicity has been observed, even at concentrations well above those effective against microbes (12,13,42), raising the question as to whether Bac7 binds to eukaryotic cytosolic ribosomes. A comparison of the binding site of Bac7(1–16) on the bacterial 70S ribosome with the equivalent region of a mammalian 80S ribosome reveals that the rRNA nucleotide sequence is highly conserved. Structurally, the conformation of three 25S rRNA nucleotides, C4519 (C2573), U4452 (U2506) and A3908 (A2602), would be expected to preclude Bac7(1–16) from binding to the mammalian ribosome (Figure 5A). Nevertheless, these nucleotides are highly mobile and adopt different conformations depending on the functional state of the ribosome (26,39,45,46), suggesting that conformational rearrangements of these nu-

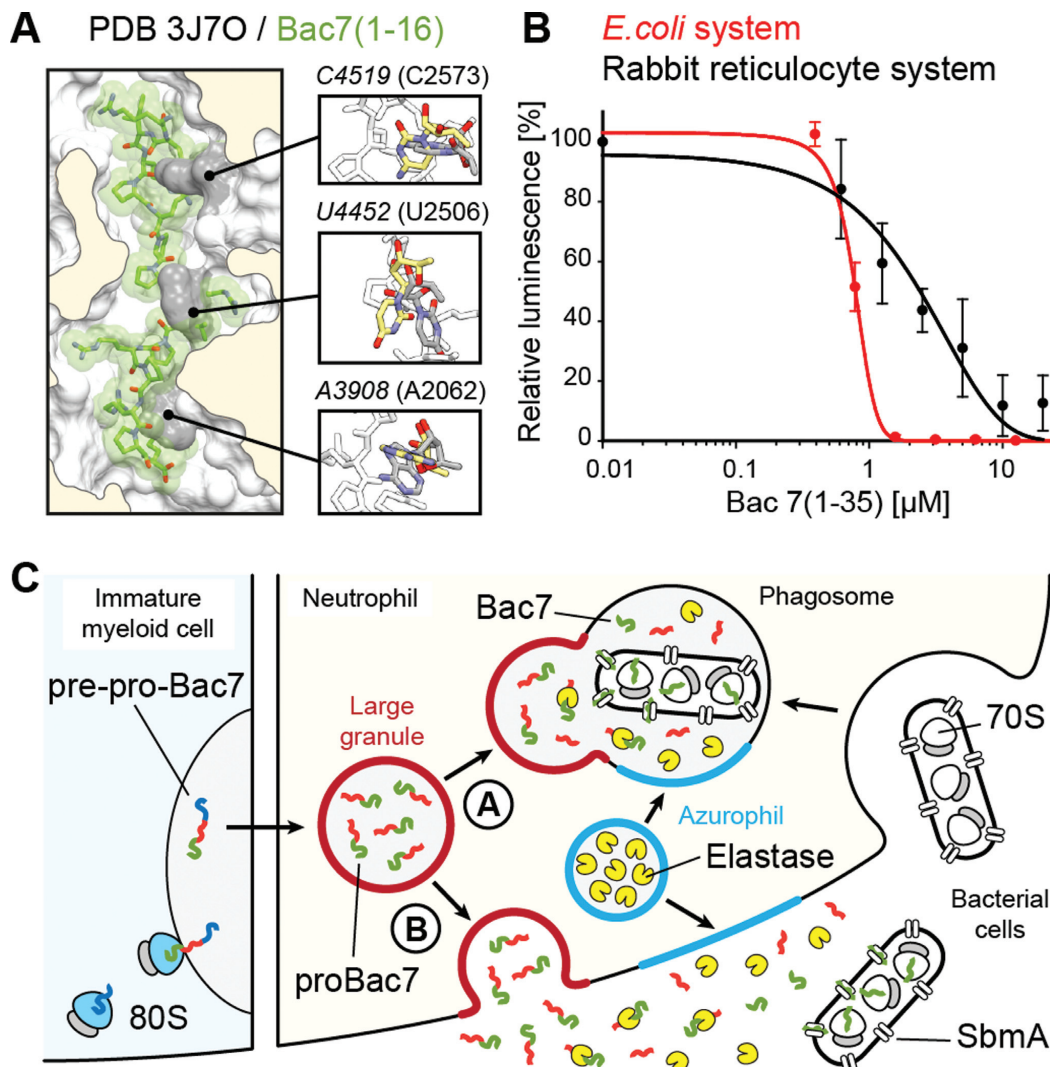


Figure 5. Specificity of Bac7 for bacterial and eukaryotic ribosomes. (A) Superimposition of Bac7(1–16) (green) onto a mammalian 80S ribosome (PDB ID: 3J7O) (47) on the basis of the 23S and 25S rRNA chains in the corresponding structures, with inset illustrating three rRNA nucleotides whose conformation differs in the 80S (grey) and *Tth*70S-Bac7 (yellow) structures. (B) Effect of increasing concentrations of Bac7(1–35) on the luminescence resulting from the *in vitro* translation of firefly luciferase (Fluc) using an *Escherichia coli* lysate-based system (red) or rabbit reticulocyte-based system (black). The error bars represent the standard deviation from the mean for triplicate experiments and the fluorescence is normalized relative to that measured in the absence of peptide, which was assigned as 100%. (C) Model for the targeting of proBac7 to large granules and its processing by elastase to yield active Bac7 peptide. The latter is transported through the bacterial inner membrane by the SbmA transporter and binds within the tunnel of bacterial ribosomes to inhibit translation.

cleotides could allow Bac7(1–16) binding. Indeed, we observed that increasing concentrations of Bac7(1–35) inhibited *in vitro* translation using a rabbit reticulocyte system (Figure 5B). Bac7(1–35) exhibited an IC₅₀ of 2.5 μM, only 2.5-fold higher than that observed in the *E. coli* *in vitro* translation system (Figure 5B). The excellent inhibitory activity of Bac7(1–35) on mammalian ribosomes, combined with its lack of toxicity on mammalian cells (42), would be consistent with a mechanism of internalization via an endocytic process (42) to ensure that Bac7 minimizes contact with the mammalian cytosolic ribosomes.

DISCUSSION

Our finding that Bac7 is active against eukaryotic translation, together with the current literature, allows us to present a model that explains how and why the mammalian cell prevents the active Bac7 peptide from being present in the cytoplasm (Figure 5C). Bac7 is produced by immature myeloid cells as a pre-pro-Bac7 precursor that is targeted to large granules, where it is stored as pro-Bac7 in differentiated neutrophils (48). The inactive proBac7 is cleaved by elastase, a serine protease that is present in azurophil granules, either upon (A) fusion with the phagosome, or (B) exocytosis and release into the extracellular matrix (Figure

5C) (48,49). The resulting activated Bac7 peptide can then enter into the bacterial cell through the SbmA transporter (10), where it subsequently binds to the ribosome to inhibit translation (Figure 5C) (19). Our structure of the *Tth70S*-Bac7 complex reveals specifically how Bac7 interacts with the bacterial ribosome (Figures 1 and 2) and inhibits translation by allowing initiation but preventing translation elongation (Figure 3). Although the overall mechanism of action of Bac7 is similar to that of insect-derived AMPs like oncocin (20,21), the high arginine content of Bac7 leads to a distinct mode of binding to the ribosome, namely through electrostatic and stacking interactions with the backbone and bases of 23S rRNA nucleotides, respectively (Figure 2C). It will be interesting to see whether such interactions are the basis for the translational arrest that has been observed when the ribosome translates a nascent polypeptide chain bearing positively charged arginine residues (50,51).

ACCESSION NUMBERS

PDB IDs: 5F8K, 5FDU, 5FDV.

SUPPLEMENTARY DATA

Supplementary Data are available at NAR Online.

ACKNOWLEDGEMENT

We thank the staff at the SOLEIL synchrotron (beamlines PROXIMA-2A and PROXIMA-1) for help during data collection and B. Kauffmann and S. Massip at the Institut Européen de Chimie et Biologie for help with crystal freezing and screening.

FUNDING

Agence Nationale pour la Recherche [ANR-14-CE09-0001 to C.A.I., D.N.W.]; Conseil Régional d'Aquitaine [2012-13-01-009 to C.A.I.]; European Union [PCIG14-GA-2013-631479 to C.A.I.]; Deutsche Forschungsgemeinschaft [FOR1805, WI3285/4-1, GRK1721 to D.N.W.]; Fondo Ricerca di Ateneo [FRA2014 to M.S.]; Institut National de la Santé et de la Recherche Médicale Pre-doctoral Fellowship (to A.C.S.); Conseil Régional d'Aquitaine Pre-doctoral Fellowship (to A.C.S.). Funding for open access charge: Institut National de la Santé et de la Recherche Médicale [PCIG14-GA-2013-631479 to C.A.I.].

Conflict of interest statement. None declared.

REFERENCES

1. Brogden,K.A. (2005) Antimicrobial peptides: pore formers or metabolic inhibitors in bacteria? *Nat. Rev. Microbiol.*, **3**, 238–250.
2. Scocchi,M., Tossi,A. and Gennaro,R. (2011) Proline-rich antimicrobial peptides: converging to a non-lytic mechanism of action. *Cell. Mol. Life Sci.*, **68**, 2317–2330.
3. Li,W., Tailhades,J., O'Brien-Simpson,N.M., Separovic,F., Otvos,L. Jr, Hossain,M.A. and Wade,J.D. (2014) Proline-rich antimicrobial peptides: potential therapeutics against antibiotic-resistant bacteria. *Amino Acids*, **46**, 2287–2294.
4. Ebbensgaard,A., Mordhorst,H., Overgaard,M.T., Nielsen,C.G., Aarestrup,F.M. and Hansen,E.B. (2015) Comparative evaluation of the antimicrobial activity of different antimicrobial peptides against a range of pathogenic bacteria. *PLoS One*, **10**, e0144611.
5. Chernysh,S., Cocianich,S., Briand,J.P., Hetru,C. and Bulet,P. (1996) The inducible antibacterial peptides of the Hemipteran insect *Palomena prasina*: identification of a unique family of proline rich peptides and of a novel insect defensin. *J. Insect. Physiol.*, **42**, 81–89.
6. Benincasa,M., Scocchi,M., Podda,E., Skerlavaj,B., Dolzani,L. and Gennaro,R. (2004) Antimicrobial activity of Bac7 fragments against drug-resistant clinical isolates. *Peptides*, **25**, 2055–2061.
7. Chan,Y.R., Zanetti,M., Gennaro,R. and Gallo,R.L. (2001) Anti-microbial activity and cell binding are controlled by sequence determinants in the anti-microbial peptide PR-39. *J. Invest. Dermatol.*, **116**, 230–235.
8. Frank,R.W., Gennaro,R., Schneider,K., Przybylski,M. and Romeo,D. (1990) Amino acid sequences of two proline-rich bactenecins. Antimicrobial peptides of bovine neutrophils. *J. Biol. Chem.*, **265**, 18871–18874.
9. Tokunaga,Y., Niidome,T., Hatakeyama,T. and Aoyagi,H. (2001) Antibacterial activity of bactenecin 5 fragments and their interaction with phospholipid membranes. *J. Pept. Sci.*, **7**, 297–304.
10. Mattiuzzo,M., Bandiera,A., Gennaro,R., Benincasa,M., Pacor,S., Antcheva,N. and Scocchi,M. (2007) Role of the *Escherichia coli* SbmA in the antimicrobial activity of proline-rich peptides. *Mol. Microbiol.*, **66**, 151–163.
11. Podda,E., Benincasa,M., Pacor,S., Micali,F., Mattiuzzo,M., Gennaro,R. and Scocchi,M. (2006) Dual mode of action of Bac7, a proline-rich antibacterial peptide. *Biochim. Biophys. Acta*, **1760**, 1732–1740.
12. Benincasa,M., Pelillo,C., Zorzet,S., Garrovo,C., Biffi,S., Gennaro,R. and Scocchi,M. (2010) The proline-rich peptide Bac7 (1–35) reduces mortality from *Salmonella typhimurium* in a mouse model of infection. *BMC Microbiol.*, **10**, 178.
13. Ghiselli,R., Giacometti,A., Cirioni,O., Circo,R., Moccagiani,F., Skerlavaj,B., D'Amato,G., Scalise,G., Zanetti,M. and Saba,V. (2003) Neutralization of endotoxin *in vitro* and *in vivo* by Bac7(1–35), a proline-rich antibacterial peptide. *Shock*, **19**, 577–581.
14. Krizsan,A., Knappe,D. and Hoffmann,R. (2015) Influence of yjl and upstream genes on the antibacterial activity of proline-rich antimicrobial peptides overcoming *Escherichia coli* resistance induced by the missing SbmA transporter system. *Antimicrob. Agents Chemother.*, **59**, 5992–5998.
15. Otvos,L., O.I., Rogers,M.E., Consolvo,P.J., Condie,B.A., Lovas,S., Bulet,P. and Blaszczyk-Thurin,M. (2000) Interaction between heat shock proteins and antimicrobial peptides. *Biochemistry*, **39**, 14150–14159.
16. Czihal,P., Knappe,D., Fritsche,S., Zahn,M., Berthold,N., Piantavigna,S., Müller,U., Van Dorpe,S., Herth,N., Binas,A. *et al.* (2012) Api88 is a novel antibacterial designer peptide to treat systemic infections with multidrug-resistant gram-negative pathogens. *ACS Chem. Biol.*, **7**, 1281–1291.
17. Krizsan,A., Volke,D., Weinert,S., Sträter,N., Knappe,D. and Hoffmann,R. (2014) Insect-derived proline-rich antimicrobial peptides kill bacteria by inhibiting bacterial protein translation at the 70S ribosome. *Angew. Chem. Int. Ed.*, **53**, 12236–12239.
18. Scocchi,M., Lüthy,C., Decarli,P., Mignogna,G., Christen,P. and Gennaro,R. (2009) The proline-rich antibacterial peptide Bac7 binds to and inhibits *in vitro* the molecular chaperone DnaK. *Int. J. Pept. Res. Therapeut.*, **15**, 147–155.
19. Mardirossian,M., Grzela,R., Giglione,C., Meinnel,T., Gennaro,R., Mergaert,P. and Scocchi,M. (2014) The host antimicrobial peptide Bac71–35 binds to bacterial ribosomal proteins and inhibits protein synthesis. *Chem. Biol.*, **21**, 1639–1647.
20. Roy,R.N., Lomakin,I.B., Gagnon,M.G. and Steitz,T.A. (2015) The mechanism of inhibition of protein synthesis by the proline-rich peptide oncocin. *Nat. Struct. Mol. Biol.*, **22**, 466–469.
21. Seefeldt,A.C., Nguyen,F., Antunes,S., Perebaskine,N., Graf,M., Arenz,S., Inampudi,K.K., Douat,C., Guichard,G., Wilson,D.N. *et al.* (2015) The proline-rich antimicrobial peptide Onc112 inhibits translation by blocking and destabilizing the initiation complex. *Nat. Struct. Mol. Biol.*, **22**, 470–475.
22. Guida,F., Benincasa,M., Zahariev,S., Scocchi,M., Berti,F., Gennaro,R. and Tossi,A. (2015) Effect of size and N-terminal residue characteristics on bacterial cell penetration and antibacterial activity of the proline-rich peptide Bac7. *J. Med. Chem.*, **58**, 1195–1204.
23. Selmer,M., Dunham,C.M., Murphy,F.V., Weixlbaumer,A., Petry,S., Kelley,A.C., Weir,J.R. and Ramakrishnan,V. (2006) Structure of the

- 70S ribosome complexed with mRNA and tRNA. *Science*, **313**, 1935–1942.
24. Schmitt,E., Blanquet,S. and Mechulam,Y. (1999) Crystallization and preliminary X-ray analysis of Escherichia coli methionyl-tRNAMetf formyltransferase complexed with formyl-methionyl-tRNAMetf. *Acta Crystallogr. D*, **55**, 332–334.
25. Polikanov,Y.S., Blaha,G.M. and Steitz,T.A. (2012) How hibernation factors RMF, HPF, and YfiA turn off protein synthesis. *Science*, **336**, 915–918.
26. Polikanov,Y.S., Steitz,T.A. and Innis,C.A. (2014) A proton wire to couple aminoacyl-tRNA accommodation and peptide-bond formation on the ribosome. *Nat. Struct. Mol. Biol.*, **21**, 787–793.
27. Kabsch,W. (2010) Xds. *Acta Crystallogr. D Biol. Crystallogr.*, **66**, 125–132.
28. McCoy,A.J., Grosse-Kunstleve,R.W., Adams,P.D., Winn,M.D., Storoni,L.C. and Read,R.J. (2007) Phaser crystallographic software. *J. Appl. Crystallogr.*, **40**, 658–674.
29. Polikanov,Y.S., Melnikov,S.V., Soll,D. and Steitz,T.A. (2015) Structural insights into the role of rRNA modifications in protein synthesis and ribosome assembly. *Nat. Struct. Mol. Biol.*, **22**, 342–344.
30. Chou,F.C., Echols,N., Terwilliger,T.C. and Das,R. (2016) RNA structure refinement using the ERRASER-phenix pipeline. *Methods Mol. Biol.*, **1320**, 269–282.
31. Adams,P.D., Afonine,P.V., Bunkoczi,G., Chen,V.B., Davis,I.W., Echols,N., Headd,J.J., Hung,L.W., Kapral,G.J., Grosse-Kunstleve,R.W. *et al.* (2010) PHENIX: a comprehensive Python-based system for macromolecular structure solution. *Acta Crystallogr. D Biol. Crystallogr.*, **66**, 213–221.
32. Emsley,P. and Cowtan,K. (2004) Coot: model-building tools for molecular graphics. *Acta Crystallogr. D Biol. Crystallogr.*, **60**, 2126–2132.
33. Chen,V.B., Arendall,W.B. 3rd, Headd,J.J., Keedy,D.A., Immormino,R.M., Kapral,G.J., Murray,L.W., Richardson,J.S. and Richardson,D.C. (2010) MolProbity: all-atom structure validation for macromolecular crystallography. *Acta Crystallogr. D Biol. Crystallogr.*, **66**, 12–21.
34. Starosta,A.L., Karpenko,V.V., Shishkina,A.V., Mikolajka,A., Sumbatyan,N.V., Schluzen,F., Korshunova,G.A., Bogdanov,A.A. and Wilson,D.N. (2010) Interplay between the ribosomal tunnel, nascent chain, and macrolides influences drug inhibition. *Chem. Biol.*, **17**, 504–514.
35. Hartz,D., McPheeters,D.S., Traut,R. and Gold,L. (1988) Extension inhibition analysis of translation initiation complexes. *Methods Enzymol.*, **164**, 419–425.
36. Starosta,A.L., Lassak,J., Peil,L., Atkinson,G.C., Virumäe,K., Tenson,T., Remme,J., Jung,K. and Wilson,D.N. (2014) Translational stalling at proline stretches is modulated by the sequence context upstream of the stall site. *Nucleic Acids Res.*, **42**, 10711–10719.
37. Polikanov,Y.S., Starosta,A.L., Juette,M.F., Altman,R.B., Terry,D.S., Lu,W., Burnett,B.J., Dinos,G., Reynolds,K.A., Blanchard,S.C. *et al.* (2015) Distinct tRNA accommodation intermediates observed on the ribosome with the antibiotics hygromycin A and A201A. *Mol. Cell*, **58**, 832–844.
38. Arenz,S., Meydan,S., Starosta,A.L., Berninghausen,O., Beckmann,R., Vazquez-Laslop,N. and Wilson,D.N. (2014) Drug sensing by the ribosome induces translational arrest via active site perturbation. *Mol. Cell*, **56**, 446–452.
39. Arenz,S., Ramu,H., Gupta,P., Berninghausen,O., Beckmann,R., Vazquez-Laslop,N., Mankin,A.S. and Wilson,D.N. (2014) Molecular basis for erythromycin-dependent ribosome stalling during translation of the ErmBL leader peptide. *Nat. Commun.*, **5**, 3501.
40. Bulkley,D., Innis,C.A., Blaha,G. and Steitz,T.A. (2010) Revisiting the structures of several antibiotics bound to the bacterial ribosome. *Proc. Natl. Acad. Sci.*, **107**, 17158–17163.
41. Dunkle,J.A., Xiong,L., Mankin,A.S. and Cate,J.H. (2010) Structures of the Escherichia coli ribosome with antibiotics bound near the peptidyl transferase center explain spectra of drug action. *Proc. Natl. Acad. Sci. U.S.A.*, **107**, 17152–17157.
42. Tomasinig,L., Skerlavaj,B., Papo,N., Giabbai,B., Shai,Y. and Zanetti,M. (2006) Mechanistic and functional studies of the interaction of a proline-rich antimicrobial peptide with mammalian cells. *J. Biol. Chem.*, **281**, 383–391.
43. Wilson,D.N. (2009) The A-Z of bacterial translation inhibitors. *Crit. Rev. Biochem. Mol. Biol.*, **44**, 393–433.
44. Sadler,K., Eom,K.D., Yang,J.L., Dimitrova,Y. and Tam,J.P. (2002) Translocating proline-rich peptides from the antimicrobial peptide bactenecin 7. *Biochemistry*, **41**, 14150–14157.
45. Schmeing,T.M., Huang,K.S., Strobel,S.A. and Steitz,T.A. (2005) An induced-fit mechanism to promote peptide bond formation and exclude hydrolysis of peptidyl-tRNA. *Nature*, **438**, 520–524.
46. Schuwirth,B.S., Borovinskaya,M.A., Hau,C.W., Zhang,W., Vila-Sanjurjo,A., Holton,J.M. and Cate,J.H. (2005) Structures of the bacterial ribosome at 3.5 Å resolution. *Science*, **310**, 827–834.
47. Voorhees,R.M., Fernandez,I.S., Scheres,S.H. and Hegde,R.S. (2014) Structure of the mammalian ribosome-Sec61 complex to 3.4 Å resolution. *Cell*, **157**, 1632–1643.
48. Zanetti,M., Litteri,L., Gennaro,R., Horstmann,H. and Romeo,D. (1990) Bactenecins, defense polypeptides of bovine neutrophils, are generated from precursor molecules stored in the large granules. *J. Cell Biol.*, **111**, 1363–1371.
49. Scocchi,M., Skerlavaj,B., Romeo,D. and Gennaro,R. (1992) Proteolytic cleavage by neutrophil elastase converts inactive storage proforms to antibacterial bactenecins. *Eur. J. Biochem.*, **209**, 589–595.
50. Dimitrova,L.N., Kuroha,K., Tatematsu,T. and Inada,T. (2009) Nascent peptide-dependent translation arrest leads to Not4p-mediated protein degradation by the proteasome. *J. Biol. Chem.*, **284**, 10343–10352.
51. Lu,J. and Deutsch,C. (2008) Electrostatics in the ribosomal tunnel modulate chain elongation rates. *J. Mol. Biol.*, **384**, 73–86.

SUPPLEMENTARY ONLINE MATERIALS
for

**Structure of the mammalian antimicrobial peptide Bac7(1-16) bound
within the exit tunnel of a bacterial ribosome**

A. Carolin Seefeldt^{1,2,3}, Michael Graf⁴, Natacha Pérébaskine^{1,2,3}, Fabian Nguyen⁴, Stefan Arenz⁴,
Mario Mardirossian⁵, Marco Scocchi⁵, Daniel N. Wilson^{4,6,*} and C. Axel Innis^{1,2,3,*}

¹ Institut Européen de Chimie et Biologie, University of Bordeaux, Pessac, 33607, France

² U1212, Inserm, Bordeaux, 33076, France

³ UMR[---], CNRS, Bordeaux, 33076, France

⁴ Gene Center and Department for Biochemistry, University of Munich, Munich, 81377, Germany

⁵ Department of Life Sciences, University of Trieste, Trieste, 34127, Italy

⁶ Center for integrated Protein Science Munich (CiPSM), University of Munich, Munich, 81377, Germany

* To whom correspondence should be addressed. Tel: +33 540006149; Fax: +33 540002215; Email: axel.innis@inserm.fr. Correspondence may also be addressed to: wilson@lmb.uni-muenchen.de.

The authors wish it to be known that, in their opinion, the first two authors should be regarded as joint First Authors.

Table S1. X-ray data processing and crystallographic refinement statistics

	Bac7(1-16)	Metl	Pyr
PDB code	5F8K	5FDU	5FDV
Space group	P2 ₁ 2 ₁ 2 ₁	P2 ₁ 2 ₁ 2 ₁	P2 ₁ 2 ₁ 2 ₁
Unit cell dimensions			
a	209.8 Å	209.7 Å	209.9 Å
b	450.3 Å	448.1 Å	450.1 Å
c	622.2 Å	623.4 Å	622.9 Å
α	90.0°	90.0°	90.0°
β	90.0°	90.0°	90.0°
γ	90.0°	90.0°	90.0°
Data processing			
Resolution	50 Å – 2.8 Å	50 Å – 2.9 Å	50 Å – 2.8 Å
R _{Merge}	51.3% (233.9%)	17.0% (181.0%)	17.8% (229.7%)
I/σI	5.71 (0.95)	11.61 (1.10)	15.99 (1.29)
CC 1/2	95.7 (16.1)	99.7 (34.9)	99.9 (41.1)
Completeness	99.6% (97.6%)	99.6% (99.5%)	100% (100%)
Redundancy	8.3 (8.1)	6.9 (6.7)	13.8 (13.4)
Refinement			
R _{work} /R _{free}	24.8% / 29.2%	18.3% / 23.4%	18.9% / 24.0%
Bond deviations	0.018 Å	0.030 Å	0.029 Å
Angle deviations	1.083°	1.976°	1.942°
Figure of merit	0.80	0.84	0.83
Ramachandran outliers	0.56%	0.95%	0.87%
Favorable backbone	94.3%	92.4%	93.3%

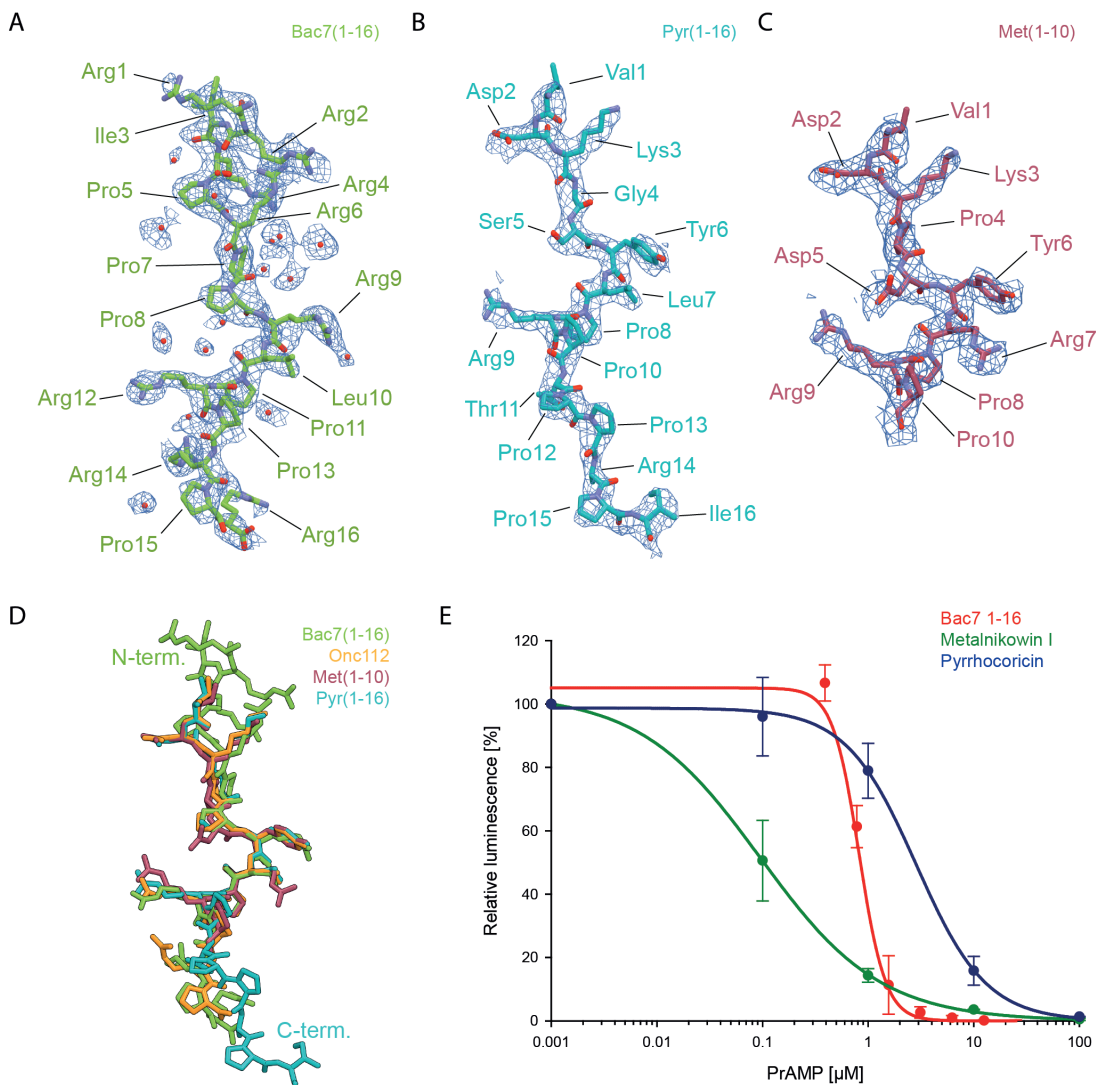


Figure S1. Minimally biased electron density for (A) the Bac7(1-16) peptide (green) and surrounding solvent molecules, as well as the (B) Pyr(1-16) (cyan) and (C) Metl(1-10) (burgundy) peptides. The peptides are shown in the same orientation as in Figure 1A and solvent molecules are displayed as spheres (red). Continuous density for the entire peptide and clear density for the solvent molecules are observed in a minimally biased $F_o - F_c$ difference map contoured at $+2.0\sigma$ (blue mesh). (D) Superimposition of the Bac7(1-16), Onc112(1-12) (orange), Pyr(1-16) and Metl(1-10) peptides. (E) Effects of increasing concentrations of Bac7(1-16) (red), Metalnikowin I (green) and Pyrrhocoricin (green) on the luminescence resulting from the *in vitro* translation of firefly luciferase (Fluc) using an *E. coli* lysate-based system. The error bars represent the standard deviation from the mean for triplicate experiments and the luminescence is normalized relative to that measured in the absence of peptide, which was assigned as 100%.

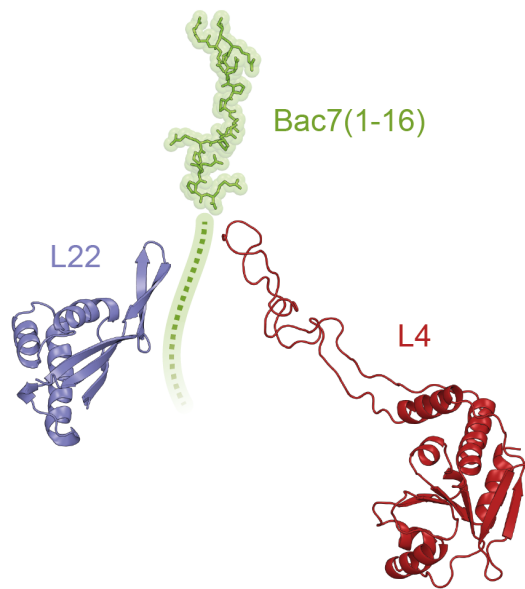


Figure S2. Relative position of the ribosome-bound Bac7(1-16) peptide (green) to the ribosomal proteins L4 (red) and L22 (blue) that reach into the lumen of the ribosomal tunnel. The proposed path for the full-length Bac7 peptide is shown as a dotted green line.

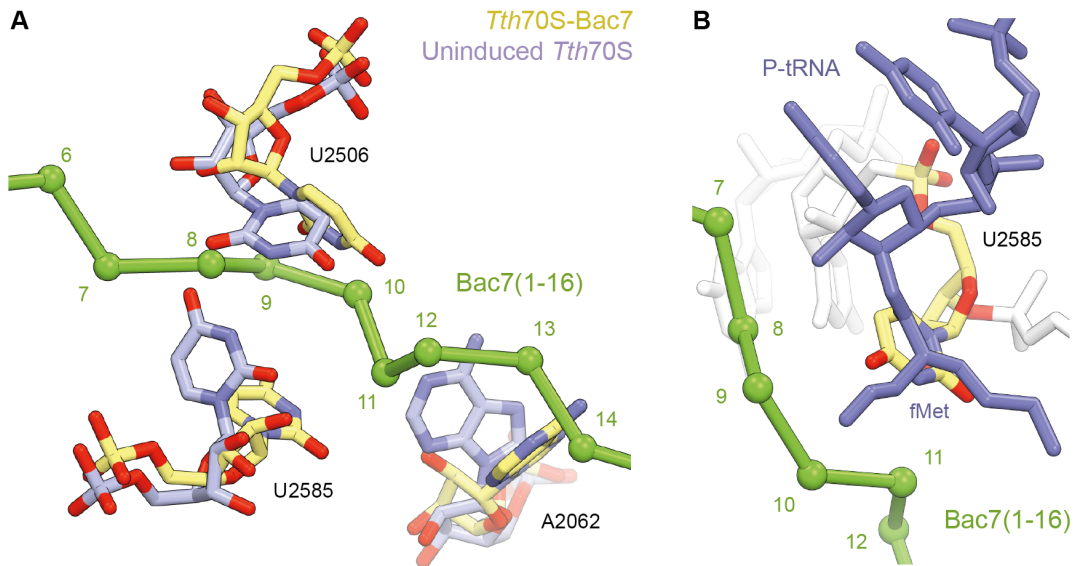
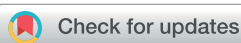


Figure S3. (A) Conformational changes in 23S rRNA nucleotides A2062, U2506 and U2585 that take place upon binding of Bac7(1-16) to the ribosome. Nucleotides from the *Tth70S-Bac7* structure are shown in yellow, while nucleotides in the Bac7-free or “uninduced” conformation are in blue (1). (B) Clash between the formyl-methionyl moiety of a P-site bound fMet-tRNA^{Met} (blue) and 23S rRNA residue U2585 in its Bac7-bound conformation (yellow). Bac7(1-16) is shown as a green C_α-trace in both panels.

SUPPLEMENTARY REFERENCES

1. Jenner, L., Starosta, A.L., Terry, D.S., Mikolajka, A., Filonava, L., Yusupov, M., Blanchard, S.C., Wilson, D.N. and Yusupova, G. (2013) Structural basis for potent inhibitory activity of the antibiotic tigecycline during protein synthesis. *Proceedings of the National Academy of Sciences of the United States of America*, **110**, 3812-3816.



Cite this: *Nat. Prod. Rep.*, 2017, **34**, 702

Proline-rich antimicrobial peptides targeting protein synthesis

Michael Graf, †^a Mario Mardirossian, †^a Fabian Nguyen, †^a A. Carolin Seefeldt, ^b Gilles Guichard, ^c Marco Scocchi, ^d C. Axel Innis, ^b and Daniel N. Wilson, *^{ae}

Covering: up to 2017

The innate immune system employs a broad array of antimicrobial peptides (AMPs) to attack invading microorganisms. While most AMPs act by permeabilizing the bacterial membrane, specific subclasses of AMPs have been identified that pass through membranes and inhibit bacterial growth by targeting fundamental intracellular processes. One such subclass is the proline-rich antimicrobial peptides (PrAMPs) that bind to the ribosome and interfere with the process of protein synthesis. A diverse range of PrAMPs have been identified in insects, such as bees, wasps and beetles, and crustaceans, such as crabs, as well as in mammals, such as cows, sheep, goats and pigs. Mechanistically, the best-characterized PrAMPs are the insect oncocsins, such as Onc112, and bovine bactenecins, such as Bac7. Biochemical and structural studies have revealed that these PrAMPs bind within the ribosomal exit tunnel with a reverse orientation compared to a nascent polypeptide chain. The PrAMPs allow initiation but prevent the transition into the elongation phase of translation. Insight into the interactions of PrAMPs with their ribosomal target provides the opportunity to further develop these peptides as novel antimicrobial agents.

Received 24th March 2017

DOI: 10.1039/c7np00020k

rsc.li/npr

1 Discovery of PrAMPs

The innate immune system uses a broad range of antimicrobial peptides (AMP) as the first line of defense to kill invading microorganisms. AMPs inhibit the proliferation of bacteria and therefore can prevent the establishment of an infection. They can either be induced through pathogen sensing receptors or are continuously secreted into body fluids.¹ Based on their nature and composition they can be divided into amphiphilic peptides, with two to four β -strands, amphipathic α -helices, loop structures and extended structures.² Although most of these five classes inhibit bacterial cells by permeabilizing the membrane, the action of AMPs is not limited to the surface of pathogens.³ Some AMPs have intracellular targets which affect the metabolism of the invading organism,⁴ such as the subclass of Proline-rich Antimicrobial

Peptides (PrAMPs).⁵⁻⁷ PrAMPs belong to the group of cationic peptides that are enriched in proline residues and are often arranged in conserved patterns together with arginine residues (Fig. 1A and B). PrAMPs appear to be irregularly dispersed amongst animals, being so far only identified in some arthropods (insects and crustaceans) and mammals (Fig. 1A). The discovery of the first PrAMP started with apidaecin in the late 1980s.⁸ Casteels and coworkers injected a sub-lethal dose of *Escherichia coli* cells into the body cavity of adult bees and subsequently monitored the appearance of AMPs by HPLC.⁸ This led to the identification of three active forms of apidaecin which were further characterized with respect to their molecular mass and amino acid sequence.⁸ The discovery of apidaecins was quickly followed by the identification of other insect and mammalian PrAMPs. Insect PrAMPs include abaecin from the honey bee *Apis mellifera*,⁹ drosocin from the fruit fly *Drosophila melanogaster*,¹⁰ pyrrhocoricin from the firebeetle *Pyrrhocoris apterus*,¹¹ metalnikowin-1 from the green shield bug *Palomena prasina*¹² and oncocin from the milkweed bug *Oncopeltus fasciatus*^{13,14} (Fig. 1A). In crustaceans, the PrAMP Arasin 1 has been isolated from the spider crab *Hyas araneus*¹⁹ as well as a PrAMP with similarity to Bac7 from the shore crab *Carcinus maenas*.²⁰ Two distinct mammalian PrAMPs have been identified in ruminant species, such as cows (e.g. *Bos taurus*),¹⁵ sheep (e.g. *Ovis aries*)^{16,17} and goats (e.g. *Capra hircus*) (Fig. 1A).^{16,17} These PrAMPs were named bactenecin 5 and 7 (Bac5 and Bac7) due

^aGene Center, Department for Biochemistry and Center for Integrated Protein Sciences Munich (CiPS-M), University of Munich, 81377 Munich, Germany

^bUniv. Bordeaux, ARNA Laboratory, Inserm U1212, CNRS UMR 5320, IECB, 33607 Pessac, France

^cUniversité de Bordeaux, CNRS, Institut Polytechnique de Bordeaux, UMR 5248, Institut de Chimie et Biologie des Mémoires et des Nano-objets (CBMN), IECB, 33607 Pessac, France

^dDepartment of Life Sciences, University of Trieste, Trieste, 34127, Italy

^eInstitute for Biochemistry and Molecular Biology, University of Hamburg, 20146 Hamburg, Germany. E-mail: Daniel.Wilson@chemie.uni-hamburg.de; Fax: +49 40 4283 82848; Tel: +49 40 4283 82841

† These authors contributed equally.

Highlight

to the molecular weight of the mature peptides being 5 and 7 kDa, respectively.¹⁵ In pigs the corresponding PrAMP homolog to Bac7 has been called PR-39 due to its length of 39 amino acids.¹⁸ Additional bactenecin-like PrAMPs, such as Bac4, Bac6.5 and Bac11, were identified in the sheep genome,¹⁶ but remain to be characterized.

2 Synthesis of PrAMPs

The synthesis of AMPs, including PrAMPs, occurs mainly in response to invading bacteria.¹ While most of the PrAMPs characterized to date are synthesized by the ribosome as inactive precursors, interestingly, their paths of activation differ significantly between species.

Mammalian Bac5/Bac7 peptides are produced, as other non-proline-rich mammalian AMPs, by immature myeloid cells as pre-pro-peptide precursors (Fig. 2A). The Bac5 and Bac7 pre-pro-

peptides comprise a 29 aa pre-signal followed by a 101 aa pro-region. Bac5/Bac7 are targeted to large granules, where the targeting signals are cleaved upon import to yield pro-peptides in differentiated neutrophils.²¹ When the immune system recognizes invading bacteria, the maturation of pro-Bacs is triggered by secretion and mixing of the contents of large and azurophil granules.²² The inactive pro-Bacs are then cleaved by elastase, a serine protease that is present in azurophils, either upon (i) fusion with the phagosome, or (ii) exocytosis and release into the extracellular matrix (Fig. 2A).^{22,23} The mature Bac5 (43 aa) and Bac7 (60 aa) peptides can then pass through the bacterial cell membrane *via* the SbmA transporter (see next section), where they can subsequently interact with their intracellular target (Fig. 2A).^{24,25} Similarly, cDNA analysis showed that the pig PR-39 is synthesized as a 172 aa pre-pro-PR-39 peptide, which is comprised of a 29 aa signal sequence, a 101 aa pro-region and a 42 aa N-terminal PR-39-containing region.



Michael Graf initially studied Biology at the Technical University Aachen, Germany from 2009 until 2011. Subsequently, Michael studied Biochemistry from 2012 until 2014 at the Ludwig Maximilian University (LMU) in Munich, Germany. His Master thesis was conducted at the University of Illinois at Chicago in the group of Prof. Alexander Mankin. Currently, Michael is a Ph.D. student in the Wilson group at the Gene Center, LMU.



Fabian Nguyen received his master degree in Biochemistry at the Ludwig Maximilian University, Munich in 2013. Currently, he is pursuing his Ph.D. in Biochemistry in the group of Daniel Wilson at the Gene Center, LMU. His main fields of interest are the characterization of novel antibiotics and resistance mechanisms.



Mario Mardirossian studied Biology obtaining a Master Degree in Functional Genomics at the University of Trieste, Italy, and a Master of Genetics at the University Diderot-Paris 7, Paris, France. He received a Ph.D. in Molecular Biomedicine in 2012 at the University of Trieste where he worked as a post-doc until 2015. In 2015, Mario obtained a Talent mobility grant to work in the group of Prof. Wilson at the Ludwig Maximilian University, Munich, Germany. Mario is currently working at the University of Trieste with a research focus on antimicrobial peptides, particularly on the proline-rich peptides, their molecular mode of action and their optimization.



Daniel Wilson studied Biochemistry in Wellington, New Zealand from 1989–1992 and received his PhD from Otago University, Dunedin, New Zealand in 1999. Daniel was awarded an Alexander von Humboldt fellowship and was post-doc at the Max-Planck Institute for Molecular Genetics in Berlin from 2001–2006. In 2007, Daniel established an independent research group at the Gene Center, Ludwig Maximilian University of Munich. Daniel was awarded an EMBO young investigator program (YIP) fellowship in 2010 and the GlaxoSmithKline (GSK) Medical Research Award in 2011. Since October 2016, Daniel holds a Chair as Professor for Biochemistry at the University of Hamburg. Daniel's research is focused on regulation of protein synthesis in general and with an emphasis on ribosome-targeting antibiotics and bacterial resistance mechanisms.

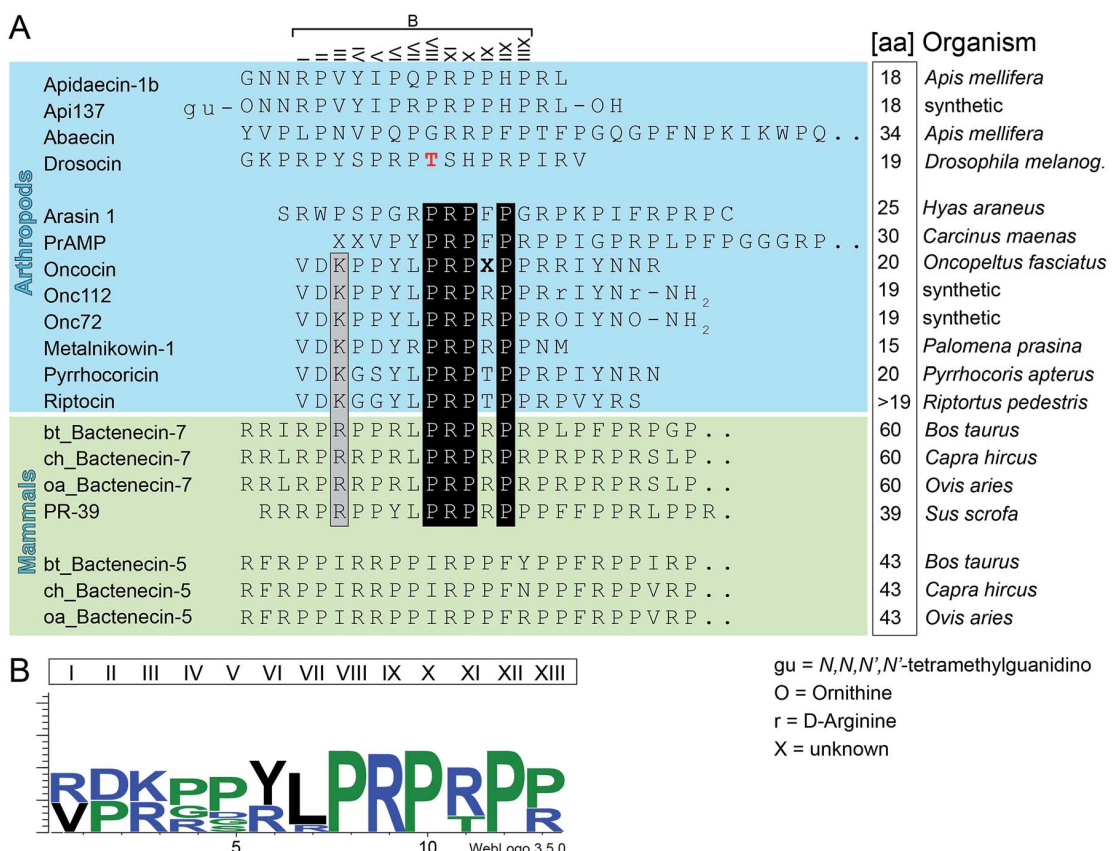


Fig. 1 Sequence alignments of PrAMPs. (A) Sequences of naturally occurring and synthetic PrAMPs derived from arthropods (insects and crustaceans, blue) and mammals (green). The central PrAMPs were aligned first based on ribosome-bound structures of Onc112, Pyr, Met and Bac7 and then on sequence similarity. Similar and identical residues are shown in grey and black, respectively. The *O*-glycosylation (Thr11) of drosocin indicated (red) and position 11 of oncocin is unknown and indicated with an "X". The number of amino acids (aa) comprising the mature peptide is also indicated for each PrAMP. (B) Sequence conservation of the core residues I to XIII of the natural PrAMPs listed in the central region of (A) between oncocin and PR-39 is shown using a WebLogo⁶² representation.

The last 3 aa are removed post-translationally to generate the 39 aa active PR-39 peptide.²⁶

PrAMPs have been found in many insect species. In *Drosophila melanogaster* one gene encoding the PrAMP drosocin has been identified.²⁷ The gene encodes a 21 aa N-terminal signal sequence (pre-sequence), the 19 aa PrAMP and a 24 aa inactivating pro-sequence that lies behind the PrAMP.¹⁰ In contrast, some PrAMPs are synthesized as multiple copy peptides encoded within a single ORF, conferring the advantage of a fast signal amplification in response to a bacterial infection (Fig. 2B).²⁸ Examples include the PrAMPs riptocin [Genebank AB842297.1] and apidaecin.²⁸ The multiple copy product of apidaecin contains a single pre-signal sequence of 16 or 19 aa followed by a pro-fragment of 13–16 aa in length (Fig. 2B).²⁸ The mature 18 aa long apidaecin peptide sequence follows in multiple copies containing different isoforms (Fig. 2B).^{28,29} In *Apis mellifera* individual apidaecin peptide sequences are separated by an inactivating RR-EAEPEAEP spacer sequence (Fig. 2B).²⁸ Upon activation amino-, endo- and carboxypeptidases process the linker and liberate the multiple copies of mature apidaecin (Fig. 2A and B). Strikingly, apidaecin is not just encoded as multiple copies within one gene, it is also encoded in several genes containing different isoforms.^{28,29} In the

Asian honey bee *Apis cerana*, multiple genes encoding four different apidaecin isoforms are evident.²⁹ Each gene contains a single pre-pro-region that is followed by a variable number of 84 nt repeats containing a linker sequence, a RR or CR dipeptide and a mature isoform of apidaecin.²⁹

3 Membrane permeability and uptake of PrAMPs

The majority of AMPs act by damaging bacterial membranes and causing thereby metabolite efflux and cell destruction. However, PrAMPs primarily kill bacteria using a non-lytic mechanism *i.e.* without significantly affecting membrane integrity. The first indications for this mode of action came from studies on apidaecin and PR-39, both of which were shown to inhibit bacterial growth without causing cell lysis.^{5,30} Moreover, it was shown that apidaecin was internalized by bacteria, indicating that such PrAMPs do not lyse microorganisms but rather kill them from within by inhibiting important metabolic pathways.⁶ By contrast, previous investigations indicated that Bac7 permeabilizes the envelope of Gram-negative bacteria

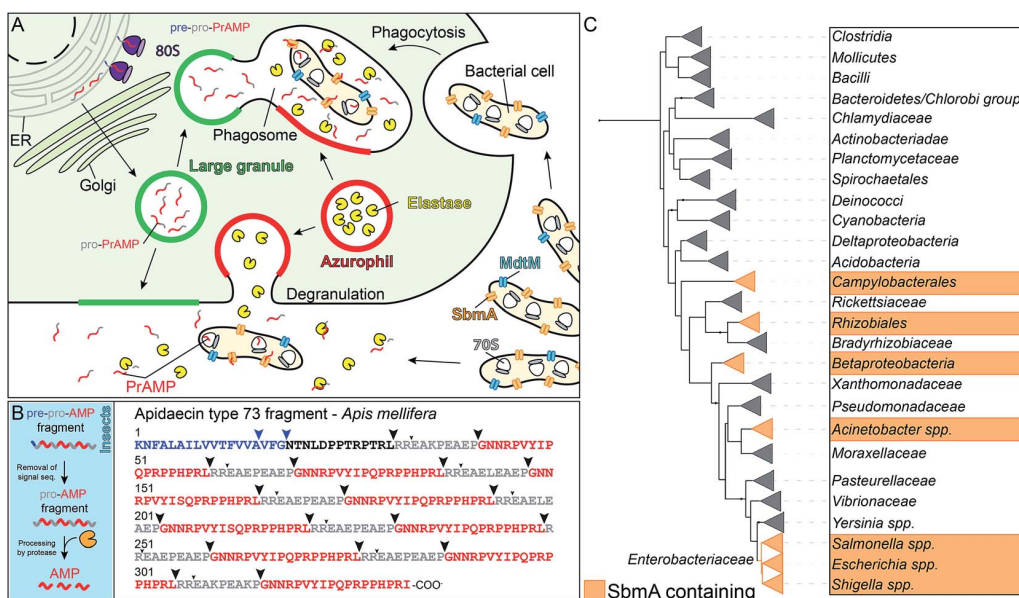


Fig. 2 Synthesis of PrAMPs. (A) Mammalian PrAMPs are synthesized as pre-pro-sequences and targeted to large granules. The PrAMPs are activated upon bacterial infection by fusion of pro-PrAMP containing large granules with the elastase-containing azurophil granules and either the plasmamembrane or the phagosome. Elastase activates the mature PrAMP by removal of the pro-sequence. The activated PrAMP is transported via SbmA (or to a lesser extent MdtM) into the bacterial cell. (B) Schematic (left) illustrating the activation of insect PrAMPs synthesized as multiple copies within one open reading frame. Liberation of the mature peptide involves the processing of a pre-pro-AMP by amino-, carboxy- and endoproteases. An example for a pre-pro form (right) of apidaecin type 73 fragment from *Apis mellifera*, which contains several isoforms of mature apidaecin. Putative cleavage sites are highlighted with arrows. (C) Phylogenetic tree showing distribution of SbmA (orange) across Eubacteria. Bacterial groups that have some members carrying SbmA have been highlighted in orange. The iTOL software was used to draw the tree.³⁷

under restrictive conditions, with a higher permeabilizing activity correlating with longer and more hydrophobic peptides.³¹ This contradiction was resolved when a dual mode of action was demonstrated for shorter fragments of Bac7, such as Bac7(1-35), against *Enterobacteriaceae*.³² The lytic mode of action was relegated to a secondary effect of this molecule, observable only in the presence of high peptide concentrations (starting from 16 μ M), much above the bacteriostatic and bactericidal levels (0.5 μ M and 1 μ M respectively).³²

The non-lytic mode of action of PrAMPs implies the presence of one or more transporters for cellular uptake into bacteria. The principal “Trojan horse” exploited by insect and mammalian PrAMPs was shown to be the inner membrane protein SbmA.²⁴ The SbmA transporter is also involved in uptake of the microcins B17,³³ J25,³⁴ and of the non-ribosomal peptide antibiotic bleomycin.³⁵ SbmA transports PrAMPs inside the bacterial cytosol exploiting the electrochemical proton gradient across the inner membrane³⁶ and is the major transporter responsible for their uptake.²⁴ The physiological role of SbmA still remains unclear, but this protein can be found in phylogenetically distant species of Gram-negative bacteria (Fig. 2C).³⁷ Evidence for SbmA homologs can be found amongst *Gamma-proteobacteria*, in particular, the *Enterobacteriaceae* (e.g. *E. coli*, *S. dysenteriae*, *S. enterica*, and *Klebsiella pneumoniae*) and *Pseudomonadales* (*A. baumannii*), but also amongst *Alpha-proteobacteria* such as *Rhizobiales* (e.g. *S. meliloti*, *A. tumefaciens* and *B. abortus*), *Beta-proteobacteria* (e.g. *Neisseria meningitidis*), and *Epsilon-proteobacteria* (*Campylobacter* spp.) (Fig. 2C). The

deletion of the *sbmA* gene in bacteria did not fully confer resistance towards PrAMPs, but significantly reduced their sensitivity.²⁴ This is likely due to a decrease but not abolishment of peptide internalization in bacteria in the absence of SbmA (or presence of non-functional SbmA),²⁴ indicating that SbmA is not the only transporter for uptake of PrAMPs. Indeed, a second transport mechanism for PrAMP uptake was recently discovered, namely, the inner membrane protein MdtM.³⁸ MdtM is an efflux pump that extrudes antibiotics from the bacterial cytosol.^{39,40} Simultaneous deletions of MdtM and SbmA in *E. coli* further decreased the susceptibility of bacteria to some PrAMPs, but not to all of them.³⁸ For PrAMPs with a dual mode of action, such as Bac7 or the synthetic A3-APO, the lytic mode of action becomes dominant at high concentrations, thus obliterating the advantage that the deletion mutants have over wild-type bacteria.³⁸

Interestingly, there is a link between the presence of transporters for PrAMPs in the membrane of a bacterial species and the mode of action of the PrAMP towards a specific microorganism. For example, *Pseudomonas aeruginosa* does not have SbmA, therefore PrAMPs cannot easily reach the cytosol to inhibit bacterial growth by targeting specific intracellular pathways. The antimicrobial effect of Bac7 fragments is indeed lower on *Pseudomonas* sp. if compared with other bacterial species in which an *sbmA* gene is present.⁴¹ Similarly, insect PrAMPs are also less active toward *P. aeruginosa* strains, and studies optimizing apidaecins with improved antimicrobial activity toward this pathogen, ended up selecting for derivatives

with more membranolytic capabilities.⁴² However, if the exogenous *E. coli* SbmA is expressed in *P. aeruginosa* PA01, an increase in internalization and antimicrobial activity was observed.⁴³ On the other hand, the PrAMP becomes less permeabilizing toward the bacterial cell. SbmA seems therefore to drain Bac7 from the membrane, keeping the local concentration lower and thereby as a consequence reducing membrane damage by the PrAMP.⁴³

4 Intracellular targets of PrAMPs

Despite the identification of several PrAMPs, the exact target of these peptides remained elusive for a long time and in the beginning it was even unclear whether PrAMPs were lytic, like most other AMPs, or whether they utilize a completely different mode of action. Five years after the initial discovery of apidaecin, permeabilization assays suggested that the PrAMP apidaecin utilizes a non-lytic mechanism⁵ and inhibits bacteria by targeting intracellular components.⁶ *In vivo* metabolic labeling assays monitoring the incorporation of radioactive methionine indicated that protein synthesis may be the intracellular target of apidaecin,⁶ however, these findings were initially not investigated further. The second target suggested for PrAMP interaction were the chaperones of the Hsp70 family.⁴⁴ In co-immunoprecipitation assays the DnaK chaperone was shown to co-purify with PrAMPs, such as drosocin, pyrrhocoricin, apidaecin 1a⁴⁴ and Bac7(1-35).⁴⁵ Subsequent structural studies visualized the interactions of PrAMPs with DnaK and revealed that PrAMPs bind within the same pocket as natural DnaK substrates.⁴⁶⁻⁴⁸ The hypothesis that DnaK is the primary target for PrAMP action was challenged when studies reported that DnaK-deficient strains still remained susceptible to Bac7(1-35) treatment.⁴⁵ Subsequently, similar results were also obtained for the insect PrAMPs oncocin and apidaecin.⁴⁹ Thus, the interaction of PrAMPs with DnaK appeared to be a secondary effect, suggesting the existence of another intracellular target for PrAMP action.

To identify the physiological target of PrAMPs, synthetic derivatives of the insect PrAMP oncocin and apidaecin were biotin-labeled and used to “fish” for interactors within bacterial extracts.⁴⁹ This led to the identification of ribosomal proteins, suggesting that ribosomes may be the major target of PrAMPs.⁴⁹ Consistently, oncocins and apidaecins derivatives were shown to bind to *E. coli* 70S ribosomes and inhibit *E. coli* protein synthesis using *in vitro* transcription/translation assays.⁴⁹ A second independent study reached the same conclusion, demonstrating that the mammalian PrAMP Bac7 co-sedimented with bacterial ribosomes, inhibited *in vitro* transcription/translation reactions using bacterial lysates and blocked protein synthesis in living bacteria.²⁵ Recently, apidaecin was proposed to have a distinct mechanism of action compared to other insect PrAMPs, such as oncocin, namely, by interfering with the assembly of the large ribosomal subunit.⁵⁰ However, it remains to be determined whether this is a direct effect on assembly or an indirect effect resulting from inhibition of translation. Nevertheless, competition assays with other translation inhibitors indicate that the apidaecin binding site

on the ribosome may differ somewhat from that of oncocin.⁵⁰ A distinct mechanism of action for apidaecins compared to oncocins is also supported by differences in the importance of their C- and N-terminal residues, respectively,^{6,41,49,51} as discussed in the following section.

5 Structure activity relationships of PrAMPs

The antimicrobial potency of PrAMPs is most effective against Gram-negative bacteria, especially *Enterobacteriaceae* such as *E. coli*, whereas Gram-positive bacteria are generally less susceptible to PrAMPs, presumably due to the absence of specific transporters, such as SbmA.⁷ Given the potential of native PrAMPs for development as antibacterial compounds against Gram-negative bacteria, efforts have been made to identify which residues are crucial or dispensable for their inhibitory activity. The best-characterized PrAMP derivatives are those related to the insect oncocins and apidaecins, as well as the bovine Bac7.

The original sequencing analysis of oncocin did not reveal the nature of the residue at position 11 (see Fig. 1A),¹³ yet further mutagenesis studies indicated that the antimicrobial efficiency of oncocin derivatives strongly depends on this position.⁴⁴ For example, oncocin derivatives containing Pro11 or Thr11 displayed significantly worse MICs ($128 \mu\text{g mL}^{-1}$) against *E. coli* compared to derivatives with Arg11 ($8 \mu\text{g mL}^{-1}$). Subsequent removal of Asn18 and addition of an amino group to the C-terminus, coupled with the additional replacement of both Arg15 and Arg19 with either D-arginine or L-ornithine, led to the development of Onc112 and Onc72 derivatives, respectively, both of which displayed increased serum stability without loss in antimicrobial activity against *E. coli* and *Micrococcus luteus* strains.^{14,52} Onc72 showed moderate activity against different *E. coli* strains with MICs ranging from $18-44 \mu\text{g mL}^{-1}$, whereas Onc112 was more active against *E. coli* in diluted tryptic broth media with MICs of $2.5-6.8 \mu\text{g mL}^{-1}$.⁵³ Alanine-scanning mutagenesis of oncocin revealed that replacement of Tyr6 or Leu7 with Ala led to a 32-fold increase of MIC against *E. coli*,⁴⁸ whereas these mutations had little effect on the MIC against *P. aeruginosa*.⁵⁴ Onc112 and Onc72 both display potent inhibitory activity in *E. coli* *in vitro* translation systems.⁴⁹ While Onc112 derivatives lacking the last seven C-terminal residues (Onc112Δ7) retained some translation inhibition activity, truncation of an additional two residues (Onc112Δ9) led to complete loss of activity.⁵⁵ Both derivatives were unable to inhibit the growth of *E. coli* BL21(DE3) in undiluted LB medium at concentrations up to $383 \mu\text{g mL}^{-1}$, while full-length Onc112 inhibited the growth at $60 \mu\text{g mL}^{-1}$ indicating that the very C-terminus of oncocin is more important for cellular uptake than for ribosome binding and inhibition.⁵⁵ An oncocin derivative lacking the first two N-terminal residues (Onc112ΔVD) had reduced capacity to inhibit bacterial growth *in vivo* and protein synthesis *in vitro*,⁵¹ illustrating the significance of N-terminal residues for activity.

Given the increased length (60 aa) of Bac7 compared to insect PrAMPs (<20 aa), structure-activity studies on Bac7 have

so far focussed mainly on analyzing activity of truncated Bac7 derivatives, rather than specific amino acid substitutions.⁴¹ These studies demonstrated that the first 35 N-terminal residues of Bac7 are necessary and sufficient to inhibit bacterial growth with the same efficacy as the full-length native peptide. Bac7(1-35) was shown to display excellent activity (MIC $\leq 8.4 \mu\text{g mL}^{-1}$) against a range of clinically relevant Gram-negative pathogens, such as *E. coli*, *A. baumannii*, *K. pneumoniae* and *Salmonella enterica*.⁴¹ The Bac7 peptide can be further shortened to encompass only the first 16 N-terminal residues (Bac7(1-16)), sacrificing only partially its antimicrobial potency, whereas further truncation of even one amino acid (Bac7(1-15)) leads to a complete loss of antimicrobial activity.⁴¹ The loss of activity of Bac7(1-15) results from impaired transport into the cytosol, indicating that Bac7(1-16) is the shortest Bac7 PrAMP that is efficiently taken up by bacterial cells.⁵⁶ Unlike the C-terminal truncations, removal of the two N-terminal arginine residues of Bac7(1-23) increases the MIC by 8-fold⁵⁶ and truncation of the first four N-terminal residues basically inactivated Bac7(1-35).⁴¹ Thus, only the first 16 amino acids of the full 60 of the native Bac7 are crucial for its killing activity. Similarly, N-terminally truncated Bac7(5-35) was shown to have reduced inhibitory activity compared to both Bac7(1-16) and Bac7(1-35) when analyzed using *E. coli* *in vitro* translation assays.⁵⁷ This indicates that the first 16 amino acids of Bac7 are necessary to inhibit bacterial growth, and are also necessary to efficiently block protein synthesis.

The first insights into which apidaecin residues are critical for its inhibitory activity came from a comparative analysis of natural apidaecin-type peptides from a diverse range of insects.⁵⁸ Comparison of these peptides revealed a conserved core containing the sequence R/KPxxxPxxPRPPHPRI/L. Deviations from the C-terminal consensus severely reduced the antimicrobial activity of apidaecins, for example, an exchange of penultimate Arg by Ala in hornet apidaecin resulted in an 2500-fold increase in MIC (from $0.01 \mu\text{g mL}^{-1}$ for the wildtype to $25 \mu\text{g mL}^{-1}$).⁶ In contrast, substitutions within the middle or N-terminal part of hornet apidaecin produced milder effects.⁶ The promising MIC values made apidaecin a potential candidate for the development of new antimicrobial agents, however, apidaecin displayed low stability in mouse serum.⁵⁹ In order to improve serum stability, the honey bee apidaecin 1b was modified with an N-terminal tetramethylguanidino-L-ornithine group instead of a glycine, yielding the apidaecin derivative Api137.⁵⁹ In addition to increased serum stability, Api137 also exhibited a slightly improved MIC against *E. coli* strains.⁵⁹ In accordance with previous studies,⁶ the C-terminal of Api137 was shown to be crucial for activity *in vivo*.⁴⁹ In the absence of the last C-terminal Leu18 residue, the MIC of Api137 increased by 16-fold (from $4 \mu\text{g mL}^{-1}$ to $66 \mu\text{g mL}^{-1}$),⁴⁹ whereas removal of the last two residues (Arg17-Leu18), increased the MIC towards *E. coli* ~ 140 -fold (to $578 \mu\text{g mL}^{-1}$). By contrast, mutations within the N-terminal region, for example the Arg4Ala mutation, did not significantly alter the MIC.⁴⁹ Thus, unlike oncocin and Bac7 where the N-terminal terminus is critical for antimicrobial activity and the C-terminus is to a large extent dispensable, it is

the C-terminus of apidaecins that is important for activity whereas the N-terminus appears to be less critical.

6 Interaction of PrAMPs with the 70S ribosome

The reports that PrAMPs bind to ribosomes and inhibit protein synthesis^{25,49} prompted two independent studies to determine structures of the oncocin derivative Onc112 in complex with the bacterial 70S ribosome.^{55,60} Subsequently, structures were also reported for the insect PrAMPs pyrrhocoricin (Pyr) and metalnikowin-1 (Met) as well as mammalian Bac7 bound to the ribosome.^{51,57} These structures revealed that these PrAMPs all interact with the large (50S) subunit of the ribosome, specifically, binding within the ribosomal exit tunnel (Fig. 3A and B). The binding site of the PrAMPs was visualized within the upper region of the exit tunnel, adjacent to the binding site of a peptidyl-tRNA and overlaps with the path of the nascent polypeptide through the tunnel (Fig. 3C).

Within the tunnel, the PrAMPs adopt an elongated conformation, predominantly consisting of random coil interspersed with stretches of *trans*-polyproline helices (type II). The PrAMPs bind with an opposite orientation compared to a nascent polypeptide chain (for example MifM), namely, with the N-terminus located at the tunnel entry and the C-terminus extending deeper into the tunnel (Fig. 3C). For each of the insect PrAMPs, the C-terminal residues (4 aa, 5 aa and 6 aa of Pyr, Met and Onc112, respectively) were not visualized in the structure (Fig. 3B), suggesting that they are not crucial for stabilizing the interaction with the ribosome.^{51,55,57,60} Similarly, while all 16 residues of Bac7(1-16) were observed,⁵⁷ only 19 residues of Bac7(1-35) were visible with the C-terminal 16 residues being disordered. Consistently, the native Bac7 is 60 aa long however the C-terminus of Bac7 is less crucial for activity and C-terminal truncated derivatives of native Bac7, such as Bac7(1-16), have been shown to retain activity.⁴¹

PrAMP interaction with the 70S ribosome is facilitated by a multitude of hydrogen bonds and stacking interactions (Fig. 3D-F).^{51,55,57,60} The majority of hydrogen bonds are formed between the peptide backbone of PrAMP with the nucleobases of the 23S rRNA. The high content of *trans*-proline residues within PrAMPs seems to be important for maintaining the elongated structure that maximizes the interaction of the peptide backbone with the surrounding rRNA. For insect PrAMPs, such as Onc112, Pyr and Met, additional hydrogen bond interactions are established by amino acid sidechains within the N-terminus of the PrAMP, specifically, Asp2 (D2) interacts with the nucleobase of G2553 and Lys3 (K3) with the phosphate-oxygen rRNA of A2453 (Fig. 3D). Two conserved stacking interactions are observed for the insect PrAMPs Onc112, Pyr and Met, namely, Arg9 (R9) stacks upon 23S rRNA nucleotide C2610 whereas Tyr6 is stacked between C2452 and the neighboring Leu7/Asp7 sidechain of the PrAMP.^{51,55,57,60} These stacking interactions are likely to be important, since exchange of Arg9 by Ala leads to a loss of activity when tested in *P. aeruginosa*,⁵⁴ and substitutions of Tyr6 or Leu7 with Ala in

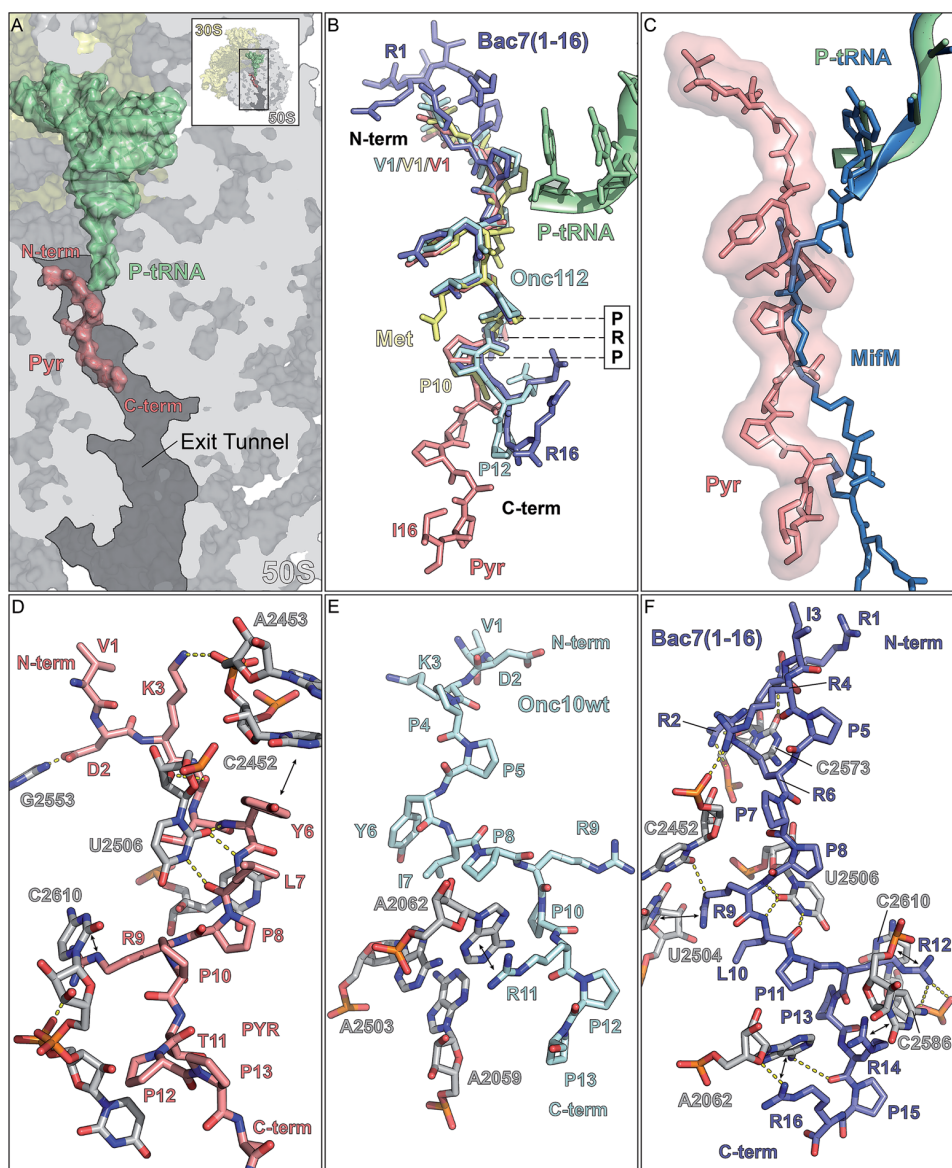


Fig. 3 Binding site of PrAMP within the ribosomal exit tunnel. (A) Overview showing the binding site of pyrrhocoricin (Pyr, salmon) within the exit tunnel of the 50S subunit (grey) with P-site tRNA (green). (B) Superimposition of mammalian Bac7(1-16) (light blue) and insect derived PrAMPs Onc112 (cyan), metalnikowin-1 (Met, yellow) and Pyr (salmon), with the conserved PRP motif highlighted. (C) Binding position of Pyr (salmon) relative to the MifM polypeptide chain (dark blue). (D–F) Interactions of (D) insect Pyr (salmon), (E) Onc112 (cyan) and (F) mammalian Bac7(1-16) with nucleotides situated within the polypeptide exit tunnel. Hydrogen bonds are indicated as dashed yellow lines and stacking interactions with arrows.

oncocin reduce the inhibitory activity in *E. coli* by 32-fold.⁴⁸ Mutations within the ribosomal tunnel, namely, A2503C or A2059C, increased resistance against Onc112 by about 4-fold, and the double mutation by more than 15-fold.⁵¹ While neither of these rRNA nucleotides directly contacts Onc112, both residues interact with A2062, which in turn forms stacking interaction with the peptide (Fig. 3E).⁵¹ In addition to revealing the importance of A2062 for Onc112 activity, the mutagenesis data establishes the ribosome as the immediate cellular target of Onc112 and probably other PrAMPs.⁵¹

Compared to insect PrAMPs, the mammalian Bac7(1-16) contains many more arginine residues. In fact, half (8) of the 16 residues are arginines, which establish multiple hydrogen bonding and stacking interactions with the 23S rRNA (Fig. 3F). The two stacking interactions observed in the insect PrAMPs from Tyr6 and Arg9 have equivalents in Bac7(1-16), namely, Arg9 in Bac7(1-16), which occupies the position of Tyr6, and Arg12, which aligns with Arg9 of insect PrAMPs within the conserved core PRP motif (Fig. 1A and B). This centrally conserved core region is the most structurally conserved region

between PrAMPs, with diverse conformations being observed for the N- and C-terminally flanking regions of the various PrAMPs. Bac7(1-16) establishes another three stacking interactions involving the sidechains of Arg2, Arg14 and Arg16 with 23S rRNA nucleotides C2573, C2586 and A2062, respectively (Fig. 3F).^{51,57} The N-terminus of Bac7(1-16) is particularly arginine-rich, comprising Arg1, Arg2, Arg4 and Arg6, which generate a positively charged compacted structure that anchors the N-terminus of the PrAMP to the negatively charged cleft created by the surrounding rRNA. Truncations of four N-terminal residues of Bac7(1-35) inactivated the PrAMP indicating that these interactions are also likely to be critical for Bac7 activity.⁴¹

7 Mechanism of action of PrAMPs

The outcome of initiation of translation is the presence of the initiator fMet-tRNA interacting with the AUG start codon of the mRNA located within the P-site of the ribosome (Fig. 4A). Translation elongation ensues with the delivery of an aminoacylated tRNA (aa-tRNA) to the ribosomal A-site of the ribosome by the elongation factor EF-Tu (Fig. 4B). Correct recognition of the codon of the mRNA by the anticodon of the aa-tRNA leads to dissociation of EF-Tu from the ribosome and accommodation of the aa-tRNA on the large subunit (Fig. 4C). The binding position of PrAMPs, such as Onc112 and Bac7(1-35), on the ribosome indicates that they would allow delivery of the aa-tRNA by EF-Tu to the ribosome, but would prevent accommodation of the aa-tRNA on the large subunit (Fig. 4D). Specifically, overlapping the structure of an accommodated aa-tRNA shows a steric clash between the aminoacylated CCA-end of the A-tRNA and the N-terminal residues of these PrAMPs (Fig. 4E and F).^{51,55,57,60} Bac7 shows the largest extension into the A-site, surpassing Onc112, Pyr (Fig. 4E) and Met by four amino acids at the N-terminus (Fig. 4F).^{51,57} This is consistent with the loss of

activity of Onc112 derivatives lacking the first two N-terminal residues and the reduced activity and binding affinity of N-terminal truncated Bac7 derivatives.^{51,57} In contrast, the N-terminus of the PrAMPs does not significantly overlap with the binding position of the P-tRNA, which is in agreement with biochemical assays demonstrating that these PrAMPs allow binding of the initiator tRNA at the P-site during translation initiation but prevent the transition from initiation into the elongation cycle to occur.^{51,55,57} Presumably, once ribosomes are translating, they are immune to the effects of PrAMPs, such as oncocin, since the binding position of PrAMPs within the ribosomal exit tunnel is likely to be incompatible with the presence of a nascent polypeptide chain (Fig. 3C). Thus, PrAMPs are likely to bind to ribosomes following termination of translation when the polypeptide chain has been released from the ribosome. Additionally, PrAMPs could bind during the late stages of ribosome biogenesis when the binding pocket has formed on the large ribosomal particle.

8 Outlook

A structural understanding of how different PrAMPs interact with components of the ribosome provides further insight into which residues of the PrAMPs as well as which interactions are critical for their inhibitory activity. Importantly, the structures also reveal which regions of the PrAMPs are less important and can be further modified to increase stability and solubility as well as establish additional interactions with the ribosome to increase the binding affinity. This latter point may become important since the binding site of PrAMPs overlaps with many known translation inhibitors, such as chloramphenicol, clindamycin and erythromycin (Fig. 4G).^{55,60,61} Therefore, it will be important to assess cross-resistance between such antibiotics and PrAMPs, especially since initial reports reveal some ribosomal mutations that confer erythromycin resistance also

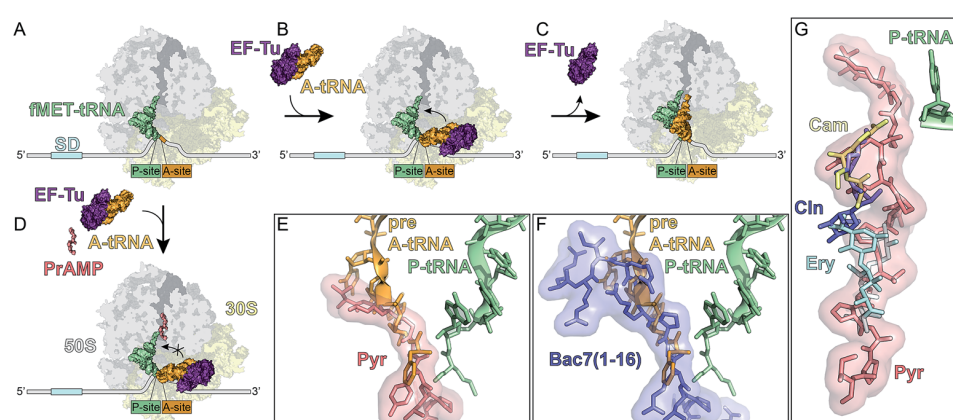


Fig. 4 Inhibition of protein synthesis by PrAMPs. (A–C) Canonical translation in absence of protein synthesis inhibitors, showing (A) translation initiation with initiator P-tRNA (green) bound to the ribosomal P-site. (B) Delivery of aa-tRNA by EF-Tu to the A-site, followed by (C) tRNA accommodation into the A-site on the large subunit and subsequent departure of EF-Tu. (D) In the presence of PrAMPs, such as oncocin, aa-tRNA delivery can occur however the aa-tRNA accommodation is blocked. (E and F) Superimposition of (E) insect Pyr (salmon) and (F) mammalian Bac7(1-16) with accommodated aa-tRNA (bright orange). (G) Superimposition of antibiotics chloramphenicol (Cam; yellow), clindamycin (Cln; slate) and erythromycin (Ery; cyan) with the binding position of the insect PrAMP Pyr (salmon).

reduce PrAMP inhibition.⁵¹ PrAMPs, such as Bac7, also bind to and inhibit translation on eukaryotic ribosomes, albeit less efficiently than on bacterial ribosomes,⁵⁷ thus raising issues of toxicity. Fortunately, it seems that most PrAMPs do not penetrate eukaryotic membranes, however, maintaining the non-lytic mechanism of the PrAMPs during optimization will be critical to avoid disrupting the eukaryotic cell membranes. One major concern for development of PrAMPs as an antimicrobial is the ease with which resistance arises in bacteria *via* mutation of the SbmA transporter. Whether these resistant strains can be overcome by the next generation PrAMPs remains to be seen. Lastly, it is unclear as to the full scope of PrAMPs across different species and, in particular, as to the conservation in terms of mechanism of action. Initial indications suggest that PrAMPs such as drosocin and apidaecin may differ from those of well-characterized PrAMPs such as oncocin and Bac7.

9 Acknowledgements

We would like to thank funding agencies for enabling work in our laboratories related to this topic: Agence Nationale pour la Recherche [ANR-14-CE09-0001 to C. A. I., G. G. and D. N. W.]; Deutsche Forschungsgemeinschaft [FOR1805, WI3285/4-1, GRK1721 to D. N. W.]; European Union [PCIG14-GA-2013-631479 to C. A. I.]; Fondo Ricerca di Ateneo [FRA2014 to M. S.]. Joint Inserm and Conseil Régional d'Aquitaine pre-doctoral fellowship awarded to A. C. S. and Talent³ fellowship awarded to M. M.

10 References

- 1 M. Zasloff, *N. Engl. J. Med.*, 2002, **347**, 1199–1200.
- 2 H. Jenssen, P. Hamill and R. E. Hancock, *Clin. Microbiol. Rev.*, 2006, **19**, 491–511.
- 3 K. A. Brogden, *Nat. Rev. Microbiol.*, 2005, **3**, 238–250.
- 4 P. Nicolas, *FEBS J.*, 2009, **276**, 6483–6496.
- 5 P. Casteels and P. Tempst, *Biochem. Biophys. Res. Commun.*, 1994, **199**, 339–345.
- 6 M. Castle, A. Nazarian, S. S. Yi and P. Tempst, *J. Biol. Chem.*, 1999, **274**, 32555–32564.
- 7 M. Scocchi, A. Tossi and R. Gennaro, *Cell. Mol. Life Sci.*, 2011, **68**, 2317–2330.
- 8 P. Casteels, C. Ampe, F. Jacobs, M. Vaeck and P. Tempst, *EMBO J.*, 1989, **8**, 2387–2391.
- 9 P. Casteels, C. Ampe, L. Riviere, J. Van Damme, C. Elicone, M. Fleming, F. Jacobs and P. Tempst, *Eur. J. Biochem.*, 1990, **187**, 381–386.
- 10 P. Bulet, J. L. Dimarcq, C. Hetru, M. Lagueux, M. Charlet, G. Hegy, A. Van Dorsselaer and J. A. Hoffmann, *J. Biol. Chem.*, 1993, **268**, 14893–14897.
- 11 S. Cociancich, A. Dupont, G. Hegy, R. Lanot, F. Holder, C. Hetru, J. A. Hoffmann and P. Bulet, *Biochem. J.*, 1994, **300**(Pt 2), 567–575.
- 12 S. Chernysh, S. Cociancich, J. P. Briand, C. Hetru and P. Bulet, *J. Insect Physiol.*, 1996, **42**, 81–89.
- 13 M. Schneider and A. Dorn, *J. Invertebr. Pathol.*, 2001, **78**, 135–140.
- 14 D. Knappe, S. Piantavigna, A. Hansen, A. Mechler, A. Binas, O. Nolte, L. L. Martin and R. Hoffmann, *J. Med. Chem.*, 2010, **53**, 5240–5247.
- 15 R. Gennaro, B. Skerlavaj and D. Romeo, *Infect. Immun.*, 1989, **57**, 3142–3146.
- 16 K. M. Huttner, M. R. Lambeth, H. R. Burkin, D. J. Burkin and T. E. Broad, *Gene*, 1998, **206**, 85–91.
- 17 O. Shamova, K. A. Brogden, C. Zhao, T. Nguyen, V. N. Kokryakov and R. I. Lehrer, *Infect. Immun.*, 1999, **67**, 4106–4111.
- 18 B. Agerberth, J. Y. Lee, T. Bergman, M. Carlquist, H. G. Boman, V. Mutt and H. Jornvall, *Eur. J. Biochem.*, 1991, **202**, 849–854.
- 19 K. Stensvag, T. Haug, S. V. Sperstad, O. Rekdal, B. Indrevoll and O. B. Styrvold, *Dev. Comp. Immunol.*, 2008, **32**, 275–285.
- 20 D. Schnapp, G. D. Kemp and V. J. Smith, *Eur. J. Biochem.*, 1996, **240**, 532–539.
- 21 M. Zanetti, L. Litteri, R. Gennaro, H. Horstmann and D. Romeo, *J. Cell Biol.*, 1990, **111**, 1363–1371.
- 22 M. Zanetti, L. Litteri, G. Griffiths, R. Gennaro and D. Romeo, *J. Immunol.*, 1991, **146**, 4295–4300.
- 23 M. Scocchi, B. Skerlavaj, D. Romeo and R. Gennaro, *Eur. J. Biochem.*, 1992, **209**, 589–595.
- 24 M. Mattiuzzo, A. Bandiera, R. Gennaro, M. Benincasa, S. Pacor, N. Antcheva and M. Scocchi, *Mol. Microbiol.*, 2007, **66**, 151–163.
- 25 M. Mardirossian, R. Grzela, C. Giglione, T. Meinnel, R. Gennaro, P. Mergaert and M. Scocchi, *Chem. Biol.*, 2014, **21**, 1639–1647.
- 26 P. Storici and M. Zanetti, *Biochem. Biophys. Res. Commun.*, 1993, **196**, 1058–1065.
- 27 M. Charlet, M. Lagueux, J. M. Reichhart, D. Hoffmann, A. Braun and M. Meister, *Eur. J. Biochem.*, 1996, **241**, 699–706.
- 28 K. Casteels-Josson, T. Capaci, P. Casteels and P. Tempst, *EMBO J.*, 1993, **12**, 1569–1578.
- 29 P. Xu, M. Shi and X. X. Chen, *PLoS One*, 2009, **4**, e4239.
- 30 H. G. Boman, B. Agerberth and A. Boman, *Infect. Immun.*, 1993, **61**, 2978–2984.
- 31 B. Skerlavaj, D. Romeo and R. Gennaro, *Infect. Immun.*, 1990, **58**, 3724–3730.
- 32 E. Podda, M. Benincasa, S. Pacor, F. Micali, M. Mattiuzzo, R. Gennaro and M. Scocchi, *Biochim. Biophys. Acta*, 2006, **1760**, 1732–1740.
- 33 M. Lavina, A. P. Pugsley and F. Moreno, *J. Gen. Microbiol.*, 1986, **132**, 1685–1693.
- 34 R. E. de Cristobal, J. O. Solbiati, A. M. Zenoff, P. A. Vincent, R. A. Salomon, J. Yuzenkova, K. Severinov and R. N. Farias, *J. Bacteriol.*, 2006, **188**, 3324–3328.
- 35 P. Yorkey, J. Lee, J. Kordel, E. Vivas, P. Warner, D. Jebaratnam and R. Kolter, *Proc. Natl. Acad. Sci. U. S. A.*, 1994, **91**, 4519–4523.
- 36 G. Runti, C. Lopez Ruiz Mdel, T. Stoilova, R. Hussain, M. Jennions, H. G. Choudhury, M. Benincasa, R. Gennaro, K. Beis and M. Scocchi, *J. Bacteriol.*, 2013, **195**, 5343–5351.
- 37 I. Letunic and P. Bork, *Nucleic Acids Res.*, 2016, **44**, W242–W245.

Highlight

- 38 A. Krizsan, D. Knappe and R. Hoffmann, *Antimicrob. Agents Chemother.*, 2015, **59**, 5992–5998.
- 39 I. T. Paulsen, L. Nguyen, M. K. Sliwinski, R. Rabus and M. H. Saier Jr, *J. Mol. Biol.*, 2000, **301**, 75–100.
- 40 S. R. Holdsworth and C. J. Law, *Biochimie*, 2012, **94**, 1334–1346.
- 41 M. Benincasa, M. Scocchi, E. Podda, B. Skerlavaj, L. Dolzani and R. Gennaro, *Peptides*, 2004, **25**, 2055–2061.
- 42 M. E. Bluhm, V. A. Schneider, I. Schafer, S. Piantavigna, T. Goldbach, D. Knappe, P. Seibel, L. L. Martin, E. J. Veldhuizen and R. Hoffmann, *Front Cell Dev. Biol.*, 2016, **4**, 39.
- 43 G. Runti, M. Benincasa, G. Giuffrida, G. Devescovì, V. Venturi, R. Gennaro and M. Scocchi, *Antimicrob. Agents Chemother.*, 2017, **61**, e01660.
- 44 L. Ottos Jr, I. O. M. E. Rogers, P. J. Consolvo, B. A. Condie, S. Lovas, P. Bulet and M. Blaszczyk-Thurin, *Biochemistry*, 2000, **39**, 14150–14159.
- 45 M. Scocchi, C. Lüthy, P. Decarli, G. Mignogna, P. Christen and R. Gennaro, *Int. J. Pept. Res. Ther.*, 2009, **15**, 147–155.
- 46 M. Zahn, B. Kieslich, N. Berthold, D. Knappe, R. Hoffmann and N. Strater, *Protein Pept. Lett.*, 2014, **21**, 407–412.
- 47 M. Zahn, N. Berthold, B. Kieslich, D. Knappe, R. Hoffmann and N. Strater, *J. Mol. Biol.*, 2013, **425**, 2463–2479.
- 48 D. Knappe, M. Zahn, U. Sauer, G. Schiffer, N. Strater and R. Hoffmann, *ChemBioChem*, 2011, **12**, 874–876.
- 49 A. Krizsan, D. Volke, S. Weinert, N. Strater, D. Knappe and R. Hoffmann, *Angew. Chem., Int. Ed. Engl.*, 2014, **53**, 12236–12239.
- 50 A. Krizsan, C. Prahl, T. Goldbach, D. Knappe and R. Hoffmann, *ChemBioChem*, 2015, **16**, 2304–2308.
- 51 M. G. Gagnon, R. N. Roy, I. B. Lomakin, T. Florin, A. S. Mankin and T. A. Steitz, *Nucleic Acids Res.*, 2016, **44**, 2439–2450.
- 52 D. Knappe, N. Kabankov and R. Hoffmann, *Int. J. Antimicrob. Agents*, 2011, **37**, 166–170.
- 53 D. Knappe, N. Kabankov, N. Herth and R. Hoffmann, *Future Med. Chem.*, 2016, **8**, 1035–1045.
- 54 D. Knappe, S. Ruden, S. Langanke, T. Tikkoo, J. Ritzer, R. Mikut, L. L. Martin, R. Hoffmann and K. Hilpert, *Amino Acids*, 2016, **48**, 269–280.
- 55 A. C. Seefeldt, F. Nguyen, S. Antunes, N. Perebaskine, M. Graf, S. Arenz, K. K. Inampudi, C. Douat, G. Guichard, D. N. Wilson and C. A. Innis, *Nat. Struct. Mol. Biol.*, 2015, **22**, 470–475.
- 56 F. Guida, M. Benincasa, S. Zahariev, M. Scocchi, F. Berti, R. Gennaro and A. Tossi, *J. Med. Chem.*, 2015, **58**, 1195–1204.
- 57 A. C. Seefeldt, M. Graf, N. Perebaskine, F. Nguyen, S. Arenz, M. Mardirossian, M. Scocchi, D. N. Wilson and C. A. Innis, *Nucleic Acids Res.*, 2016, **44**, 2429–2438.
- 58 P. Casteels, J. Romagnolo, M. Castle, K. Casteels-Josson, H. Erdjument-Bromage and P. Tempst, *J. Biol. Chem.*, 1994, **269**, 26107–26115.
- 59 N. Berthold, P. Czihal, S. Fritsche, U. Sauer, G. Schiffer, D. Knappe, G. Alber and R. Hoffmann, *Antimicrob. Agents Chemother.*, 2013, **57**, 402–409.
- 60 R. N. Roy, I. B. Lomakin, M. G. Gagnon and T. A. Steitz, *Nat. Struct. Mol. Biol.*, 2015, **22**, 466–469.
- 61 J. A. Dunkle, L. Xiong, A. S. Mankin and J. H. Cate, *Proc. Natl. Acad. Sci. U. S. A.*, 2010, **107**, 17152–17157.
- 62 G. E. Crooks, G. Hon, J. M. Chandonia and S. E. Brenner, *Genome Res.*, 2004, **14**, 1188–1190.

An antimicrobial peptide that inhibits translation by trapping release factors on the ribosome

Tanja Florin^{1,5}, Cristina Maracci^{2,5}, Michael Graf^{3,5}, Prajwal Karki², Dorota Klepacki¹, Otto Berninghausen³, Roland Beckmann³, Nora Vázquez-Laslop¹, Daniel N Wilson^{3,4}, Marina V Rodnina² & Alexander S Mankin¹

Many antibiotics stop bacterial growth by inhibiting different steps of protein synthesis. However, no specific inhibitors of translation termination are known. Proline-rich antimicrobial peptides, a component of the antibacterial defense system of multicellular organisms, interfere with bacterial growth by inhibiting translation. Here we show that Api137, a derivative of the insect-produced antimicrobial peptide apidaecin, arrests terminating ribosomes using a unique mechanism of action. Api137 binds to the *Escherichia coli* ribosome and traps release factor (RF) RF1 or RF2 subsequent to the release of the nascent polypeptide chain. A high-resolution cryo-EM structure of the ribosome complexed with RF1 and Api137 reveals the molecular interactions that lead to RF trapping. Api137-mediated depletion of the cellular pool of free release factors causes the majority of ribosomes to stall at stop codons before polypeptide release, thereby resulting in a global shutdown of translation termination.

The release of the polypeptide from the ribosome is an essential step of protein synthesis. When the translating ribosome reaches the end of an open reading frame (ORF), it carries the completed protein chain attached to the P-site tRNA and has a stop codon in the A site. In bacteria, termination requires the action of three release factors, RF1, RF2 and RF3. RF1 or RF2 recognize the stop codon in the A site of the small (30S) subunit while their conserved GGQ motif is placed in the active site of the peptidyl transferase center (PTC) of the large (50S) subunit where it facilitates the hydrolysis of the peptidyl-tRNA ester bond, releasing the completed protein (reviewed in ref. 1). Because the number of ribosomes in the cell greatly exceeds the number of RF1 and RF2 molecules^{2,3}, continuous translation relies upon the rapid turnover of these factors in order to serve the needs of all the cellular ribosomes. RF3 is a GTPase that facilitates recycling of RF1 and RF2 subsequent to polypeptide release^{4,5}. Finally, the ribosome-recycling factor together with the elongation factor G dislodges the ribosome from the mRNA and splits it into subunits⁶. Inhibition of any of these reactions should reduce fitness and viability of the bacterial cell. Strikingly, in spite of the complexity and importance of translation termination, no specific inhibitors of this key step in protein synthesis have so far been identified.

Antimicrobial peptides constitute an important component of the innate immune defense system of multicellular organisms against bacterial infection⁷. While many antibacterial peptides lyse cells by disrupting their membrane, a specific class of nonlytic peptides, called proline-rich antimicrobial peptides (PrAMPs), act upon the intracellular target, the ribosome^{8–13}. Several investigated PrAMPs, such as oncocin 112 (Onc112) and others, whose sizes range from 15 to 20 amino acids, bind

to the nascent peptide exit tunnel of the ribosome and, by encroaching upon the A site of the PTC, prevent binding of aminoacyl-tRNA^{10–13}. This mode of action results in the arrest of the ribosome at the mRNA start codon before the first peptide bond can be formed^{10–13}.

Among PrAMPs, the 18–20-amino-acid long antimicrobial peptides called apidaecins, which are produced by bees, hornets and wasps, remain outliers. Compared to other PrAMPs, they compete with a different subset of ribosomal antibiotics for binding¹⁴. Furthermore, whereas Onc112 and other PrAMPs readily inhibit protein synthesis *in vivo* and *in vitro*, apidaecins efficiently interfere with protein synthesis in living cells but are poor inhibitors of *in vitro* translation^{14–16}. We sought to understand the mechanism of action of apidaecins using Api137 (Fig. 1a), an 18-amino-acid derivative of the natural apidaecin 1b, which was optimized to have improved antibacterial properties and serum stability¹⁷.

RESULTS

Api137 arrests translation at the stop codon of mRNAs

To identify the stage of translation inhibited by Api137, we used *in vitro* toeprinting analysis, which determines the location of stalled ribosomes on mRNA¹⁸. In contrast to Onc112, which arrests translation at the start codon^{12,13} (Fig. 1a), Api137 arrested translation when the stop codon entered the A site of the ribosome (Fig. 1b). Similar stalling at the stop codon was obtained with other tested mRNAs when translation was carried out in the presence of Api137 or the unmodified natural apidaecin 1a (Supplementary Fig. 1). These results show that Api137, unlike other ribosome-targeting PrAMPs or any other known antibiotic, has the unique ability to specifically arrest the terminating ribosome.

¹Center for Biomolecular Sciences, University of Illinois at Chicago, Chicago, Illinois, USA. ²Department of Physical Biochemistry, Max Planck Institute for Biophysical Chemistry, Göttingen, Germany. ³Gene Center, Department for Biochemistry and Center for Protein Science Munich (CiPSM), University of Munich, Munich, Germany. ⁴Institute for Biochemistry and Molecular Biology, University of Hamburg, Hamburg, Germany. ⁵These authors contributed equally to this work. Correspondence should be addressed to A.S.M. (shura@uic.edu), M.V.R. (rodnina@mpibpc.mpg.de), D.N.W. (daniel.wilson@chemie.uni-hamburg.de) or N.V.-L. (nvazquez@uic.edu).

Received 6 April; accepted 21 June; published online 24 July 2017; doi:10.1038/nsmb.3439

Mutations in RF1, RF2 and the ribosome confer resistance to Api137

In order to identify the components of the translation apparatus that are involved in the mechanism of Api137 action, we carried out an unbiased selection of spontaneous Api137-resistant mutants in two *E. coli* strains. We isolated three types of mutants. The resistance in the first type of mutant was caused by nonsense mutations in the *sbmA* gene (Supplementary Fig. 2a) encoding the transporter responsible for importing PrAMPs into the cell¹⁹.

Resistant mutants of the second type carried mutations in the *prfA* or *prfB* genes encoding RF1 and RF2, respectively. RF1 and RF2 recognize the stop codon of the mRNA and facilitate hydrolysis of the peptidyl-tRNA ester bond, releasing the completed protein (reviewed in ref. 1). Mutants isolated using *E. coli* strain SQ110 carried a mutation in the *prfA* gene, which resulted in the replacement of Asp241 of the encoded RF1 with a glycine residue (Supplementary Fig. 2). The Api137-resistant mutant isolated with the *E. coli* strain BL21 had mutations in the *prfB* gene, resulting in substitutions R262C or Q280L in RF2 (Supplementary Fig. 2). The difference in the results obtained using these two strains probably reflects the fact that SQ110, as a derivative of the K12 strain, carries an alteration in the *prfB* gene that results in the replacement of Ala246 of RF2 with a threonine²⁰ (Supplementary Fig. 2d). This mutation affects the properties of RF2 (ref. 21) and could conceivably alter the interactions of the K12-type RF2 with Api137. The RF1 and RF2 mutations found in Api137-resistant strains are located in proximity to the catalytically important GGQ motif (Supplementary Fig. 2b,c), suggesting that Api137 interferes with the function of RF1 and RF2.

The third type of Api137-resistant mutants had a mutation in the gene *rplP* encoding ribosomal protein uL16 (Supplementary Fig. 2). Subsequent testing of other ribosomal-protein mutants showed that mutations in the proteins uL22 and uL4, which are located in

the nascent peptide exit tunnel, also increased resistance to Api137 (Supplementary Fig. 2). In agreement with this observation, mutations of nearby 23S rRNA nucleotides A2059 and A2503 rendered cells resistant to Api137 (Supplementary Fig. 2). Consistently, Api137 did not induce pronounced arrest of the A2059C or A2503G mutant ribosomes at the stop codons *in vitro* (Fig. 1c). Taken together, these results indicate that Api137 interferes with translation termination by influencing functional interactions between RF1 or RF2 and the ribosome.

Api137 inhibits turnover of RF1 and RF2

To understand the mode of inhibition of translation termination by Api137, we used a fully reconstituted *in vitro* translation system. We prepared a model termination complex corresponding to the state of the ribosome before hydrolysis of peptidyl-tRNA (prehydrolysis complex, PreHC)^{4,22} (Fig. 2a). Mixing the PreHC with RF1 or RF2 results in the hydrolysis of the ester bond linking fMet to the P-site tRNA, emulating the polypeptide-release reaction. At a high concentration of RF1 or RF2, when recycling of the factors was not required for the reaction to progress to completion, rapid and complete hydrolysis of peptidyl-tRNA was observed even in the presence of high Api137 concentrations (Fig. 2b), suggesting that Api137 does not inhibit peptidyl-tRNA hydrolysis. In contrast, at limiting concentrations of RF1 or RF2, when multiple rounds of binding and dissociation of the factors from PreHC were needed to achieve termination on all PreHCs, the reaction was dramatically inhibited in the presence of as little as 1 μM Api137 (Fig. 2c). This result suggested that Api137 either competes with the RFs for binding to the PreHC or traps the RFs in the posthydrolysis (PostHC) complex, abolishing recycling of the factor.

To distinguish between these scenarios, we directly examined the effect of Api137 on RF1 binding or dissociation using a fluorescent derivative of fMet-tRNA^{fMet} (PreHC_{Flu}) and a quencher-dye-labeled

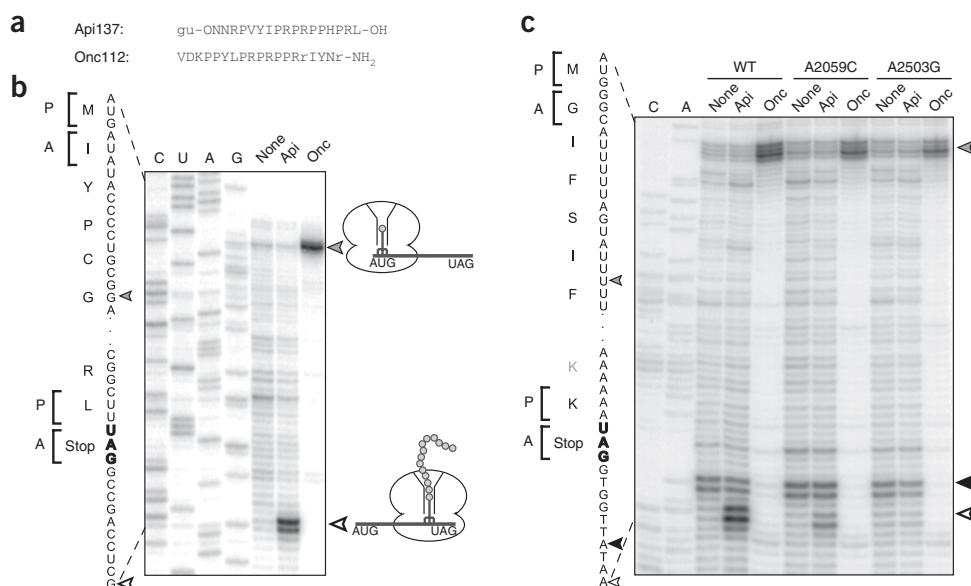


Figure 1 Api137 stalls ribosomes at the termination step of translation. **(a)** Amino acid sequences of PrAMPs Api137 and Onc112. gu, *N,N,N',N'-*tetramethylguanidino; OH, hydroxyl; O, L-ornithine; r = D-arginine. **(b,c)** *In vitro* toeprinting analysis comparing the Onc112- or Api137-mediated (labeled Onc and Api, respectively) translation arrest on model mRNA templates derived from the *yrbA* **(b)** or *ermCL* **(c)** genes. Positions of the toeprint bands (indicated by arrowheads on the gene sequence) are 16–17 nt downstream from the first nucleotide of the P-site codon. The P- and A-site codons of the stalled ribosomes are indicated by brackets. Toeprints in **b** were produced by wild-type ribosomes (WT) or by ribosomes with mutations in specific rRNA nucleotides (Supplementary Fig. 2a). Gray arrowheads indicate toeprint bands in **b** and **c** generated by Onc112-arrested ribosomes at the initiation codon; white arrowheads indicate bands from ribosomes arrested by Api137 at termination. The similar intensities of the PrAMP-independent toeprint bands marked with a black arrowhead in **c** shows that WT and mutant ribosomes translate with comparable efficiencies. Sequencing reactions are marked. The gels are representatives of six **(b)** and two **(c)** independent biological replicates.

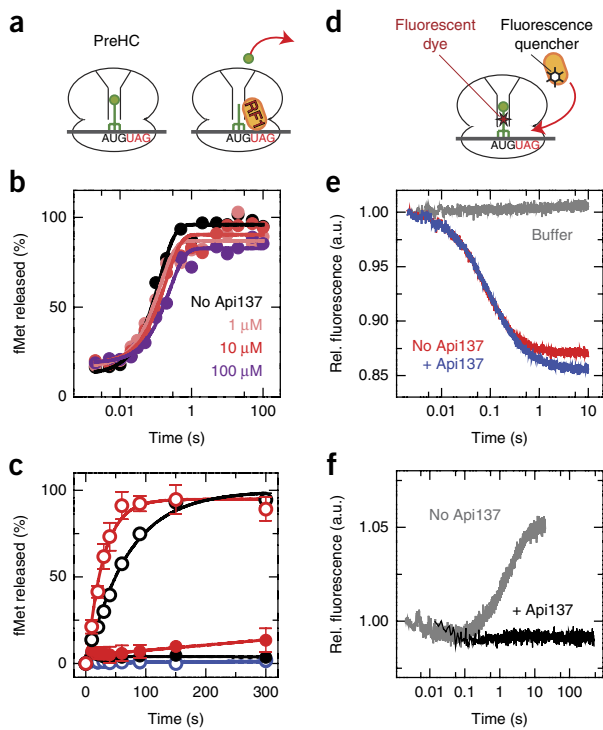


Figure 2 Api137 allows peptide hydrolysis but inhibits turnover of RF1 and RF2. (a) Schematics of the peptidyl-tRNA hydrolysis experiments. PreHC carrying f³H]Met-tRNA^{fMet} is reacted with RF1 (shown) or RF2, and the release of ff³H]Met is measured. (b) Time courses of peptide hydrolysis in PreHC in the presence of excess RF1 without (black) or with the indicated concentrations of Api137 (colored traces). (c) Time courses of peptide hydrolysis in PreHC by RF1 (black) and RF2 (red) under turnover conditions in the absence (open circles) or presence (closed circles) of 1 μ M Api137. RF3-GTP was present in all reactions. Control experiments (blue) lacked RF1 and RF2 in the absence (open circles) or presence (closed circles) of Api137. 100% corresponds to ten cycles of RF binding, catalysis and dissociation. Error bars represent the range of two independent replicates. (d) Schematics of the RF1-binding experiments. PreHC carries fluorescein-labeled fMet-tRNA^{fMet} (PreHC_{Flu}) and RF1 carries fluorescence quencher dye (RF1_{QSY}). (e) Time courses of binding of RF1_{QSY} to PreHC_{Flu} in the absence (red) or presence (blue) of Api137. Gray trace, no RF1. The fluorescence traces represent the average of five to seven technical replicates. a.u., arbitrary units. (f) Time course of RF1 dissociation. RF1_{QSY} was incubated with PreHC_{Flu} to generate PostHC_{Flu} and then mixed with a ten-fold excess of unlabeled RF1 and RF3-GTP in the absence (gray) or in the presence (black) of Api137. The traces represent the average of up to seven technical replicates. Details in Online Methods.

RF1 (RF1_{QSY}) and following changes in fluorescence resonance energy transfer (Fig. 2d). Though Api137 did not affect binding of RF1 (Fig. 2e), it entirely blocked RF1 dissociation (Fig. 2f), demonstrating that Api137 prevents turnover of RF1 and RF2 by trapping them on the ribosome. When similar experiments were carried out with the Api137-resistant mutant of RF1 (Supplementary Fig. 2a), Api137 was unable to abolish RF1 dissociation (Supplementary Fig. 3a), indicating that the mutation allowed RF1 to escape Api137-mediated trapping in the PostHC complex. Similarly, the RF2 A246T mutation endemic in the K12 *E. coli* strain and located in the vicinity of the selected Api137-resistance mutations (Supplementary Fig. 2d) showed considerably increased tolerance of Api137 inhibition compared to the unaltered RF2 (Supplementary Fig. 3b). Collectively, these

Table 1 Cryo-EM data collection, refinement and validation statistics
RF1-API (EMD 3730, PDB 502R)

Data collection	
Microscope	FEI Titan Krios
Camera	Falcon II
Magnification	129,151
Voltage (kV)	300
Electron dose (e ⁻ /Å ²)	28
Defocus range (μm)	-0.7 to -2.5
Pixel size (Å)	1.084
Initial particles (no.)	116,212
Final particles (no.)	36,826
Model composition	
Nonhydrogen atoms	147,985
Protein residues	6,205
RNA residues	4,643
Refinement	
Resolution (Å)	3.4
Map CC (around atoms)	0.78
Map CC (whole unit cell)	0.76
Map-sharpening <i>B</i> factor (Å ²)	-73.07
Average <i>B</i> factor (Å ²)	52.5
R.m.s. deviations	
Bond lengths (Å)	0.0110
Bond angles (°)	1.30
Validation	
MolProbity score	1.99
Clashscore	7.00
Poor rotamers (%)	1.01
Ramachandran plot	
Favored (%)	87.90
Allowed (%)	11.58
Disallowed (%)	0.52

results showed that Api137 traps RF1 and RF2 on the ribosome after the release of the nascent protein, abolishes RF turnover and prevents disassembly of the termination complex and recycling of the ribosome for new rounds of translation.

Interactions of Api137 with the ribosome and RF1 illuminate molecular mechanisms of RF trapping

To obtain insights into the molecular mechanism of RF trapping, we determined a cryo-EM structure of Api137 bound to a terminating ribosome (Fig. 3). The ribosome–nascent chain complex bearing a UAG stop codon in the A site was prepared by translating *in vitro* the model *ermCL* ORF in the presence of Api137 and then purified and subjected to cryo-EM analysis. *In silico* sorting of the cryo-EM data revealed a major subpopulation of ribosomes bearing a tRNA in the P site and RF1 bound in the A site (Supplementary Fig. 4 and Table 1). A final cryo-EM reconstruction with an average resolution of 3.4 Å enabled the generation of a molecular model for the entire complex (Fig. 3a). In the Api137-stalled complex, the conformation of RF1 is similar to that observed previously in the PostHC during canonical termination^{23,24} (Supplementary Fig. 5a–c). Consistent with our kinetics data, the P-site tRNA is deacylated, showing that RF1 has catalyzed hydrolysis of the polypeptide chain in the presence of Api137. A distinct electron density observed within the ribosomal exit tunnel could be unambiguously assigned to residues 5–18 of Api137 bound in an extended conformation (Fig. 3b and Supplementary Fig. 4g,h). The orientation of Api137 within the tunnel matches that of a nascent

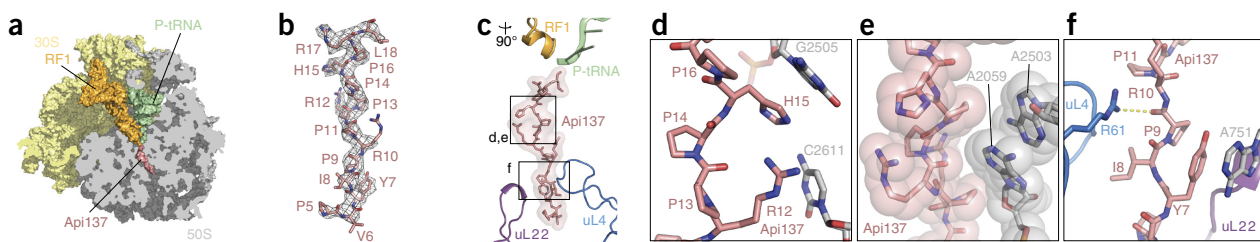


Figure 3 Binding of Api137 to the terminating ribosome and its interactions with the exit tunnel. **(a)** Transverse section of the 50S subunit (gray) showing the binding site of Api137 (salmon) on the 70S ribosome (30S subunit in yellow) within the polypeptide exit tunnel relative to RF1 (orange) and the P-site tRNA (green). **(b)** Cryo-EM density (mesh) and molecular model (salmon) for residues 5–18 of Api137. **(c)** Placement of Api137 in the exit tunnel relative to RF1, P-site tRNA and ribosomal proteins uL4 and uL22. **(d–f)** Enlargement of boxed regions from **b** showing interactions of Api137 with components of the exit tunnel, including **(d,e)** nucleotides of the 23S rRNA (gray) and **(f)** ribosomal protein uL4. In **e**, sphere representation is used to approximate van der Waals interactions, and in **f**, a dashed yellow line indicates a hydrogen bond.

peptide (Supplementary Fig. 5d) but is opposite from that observed for other investigated PrAMPs^{10–13} (Supplementary Fig. 5e). The C-terminal Arg17 and Leu18, which are critical for the activity of Api137 (ref. 16), are positioned close to the PTC (Fig. 4a). However, in contrast to other PrAMPs that encroach upon the PTC A site, Api137 is positioned entirely within the exit tunnel, allowing it to bind when the A site is occupied by RF1 or RF2 (Supplementary Fig. 5e).

Api137 makes multiple interactions with the exit tunnel, including stacking and van der Waals interactions with the 23S rRNA nucleotides (Fig. 3d,e) and a potential hydrogen bond with the ribosomal protein uL4 (Fig. 3f), clarifying how rRNA and ribosomal protein mutations could confer resistance (Supplementary Figs. 2 and 6).

The interactions of the central and N-terminal segments of Api137 with the tunnel elements help to place the functionally critical C-terminal amino acids of Api137 in the vicinity of the GGQ motif of RF1 in the PTC (Fig. 4a–c). The side chain of the penultimate residue Arg17 of Api137 is fixed in place by hydrogen bonding with the 2' hydroxyl of the G2505 ribose and the O2 of the C2452 base (Fig. 4b). This network of hydrogen bonds with the nucleotides of the 23S rRNA positions Arg17 for interaction with RF1. The Gln235 side chain carbonyl of RF1 is within hydrogen bond distance from the terminal nitrogen of the Arg17 guanidinium group (Fig. 4b). The contact between the Arg17 side chain and RF1 is likely to be critical, because mutations of the penultimate residue of Api137 decrease the affinity of the PrAMP for the ribosome and reduce its inhibitory activity¹⁶. Additionally, the backbone carboxyl of Arg17 of Api137 is also within hydrogen bond distance of the Gln235 side chain amine of RF1 (Fig. 4b). Interaction between Api137 and RF1 not only helps to trap the RF on the ribosome but also stabilizes binding of Api137 itself. RNA probing experiments showed that in the absence of RF1, Api137 only minimally shielded A2058, A2059 and A2062 from modification, whereas the PrAMP readily protected these nucleotides when RF1 was present (Fig. 4d). The C-terminal hydroxyl of Api137 is within hydrogen bond distance from the ribose hydroxyls of A76 of the deacylated P-site tRNA (Fig. 4c). These interactions could further contribute to RF1 or RF2 trapping by preventing the ribosome from undergoing the RF3-stimulated transition into the rotated state required for RF1 or RF2 dissociation^{5,25}.

The results of the structural analysis not only corroborate the findings of biochemical and genetic experiments but also illuminate the possible molecular mechanism of trapping RF1 and RF2 on the terminating ribosome after the release of the nascent peptide.

Api137-mediated RF depletion inhibits nascent peptide release

The number of ribosomes in the bacterial (*E. coli*) cell exceeds the number of RF2 and RF1 molecules by ~25-fold and ~200-fold, respectively^{2,3}.

Api137-mediated trapping of RF1 or RF2 on a relatively small number of ribosomes should lead to a rapid depletion of the RFs. As a consequence, there would be no RF1 or RF2 available to facilitate the peptide release when the remaining translating ribosomes reach a stop codon. Therefore, although Api137 arrests the ribosome in a prehydrolysis state, in the cells treated with Api137, most of the ribosomes should stall at stop codons in a prehydrolysis state carrying an intact peptidyl-tRNA.

We first tested this hypothesis in a cell-free translation system using the TnaC stalling peptide as a model. At high tryptophan concentrations (5 mM), the RF2-mediated release of TnaC peptide is impeded, leading to a well-documented accumulation of TnaC-tRNA²⁶ (Fig. 5a). By contrast, at low concentrations of tryptophan (0.3 mM), the TnaC peptide is rapidly released at the RF2-specific UGA stop codon. Strikingly, when Api137 was present, TnaC-tRNA also accumulated at low tryptophan concentrations. A similar result was obtained with the *tnaC* template carrying an RF1-specific UAG stop codon (Fig. 5a). These results demonstrated that as a consequence of RF1 or RF2 depletion due to Api137-mediated trapping on a fraction of ribosomes, the majority of ribosomes are unable to release the TnaC peptide. Consistent with this conclusion, the Api137-induced accumulation of TnaC-tRNA was largely rescued by supplementing the reaction with a five-fold molar excess of RF1 over the ribosomes (Fig. 5b).

When the translating ribosome reaches a stop codon, the occasional binding of a near-cognate aminoacyl-tRNA instead of the RFs may promote a stop codon readthrough event. The Api137-induced depletion of the pools of free RF1 and RF2 is expected to bias this competition in favor of aminoacyl-tRNA binding. Indeed, Api137 dramatically increased the readthrough frequency in a reporter *E. coli* strain carrying a mutant *lacZ* allele with a premature UAG stop codon (Fig. 5c). Notably, the efficiency of Api137-induced readthrough was considerably higher than that induced by the miscoding antibiotic streptomycin (Fig. 5c). These results confirm that while Api137 traps RF1 and RF2 on the ribosome after the nascent protein release, the main downstream effect of Api137 action is the arrest of the ribosomes in the prehydrolysis state (Fig. 5d,e).

DISCUSSION

Our biochemical, genetic and structural data reveal Api137 as the first known inhibitor that is specific for translation termination. Though several inhibitors can potentially interfere with polypeptide release^{27,28}, these antibiotics also target other steps of protein synthesis; in these cases, inhibition of termination is just a collateral effect of the antibiotic binding to the ribosomal centers critical for various ribosomal activities. In contrast, Api137 does not inhibit initiation or elongation of translation but specifically arrests the ribosome at the stop codons. Api137 achieves

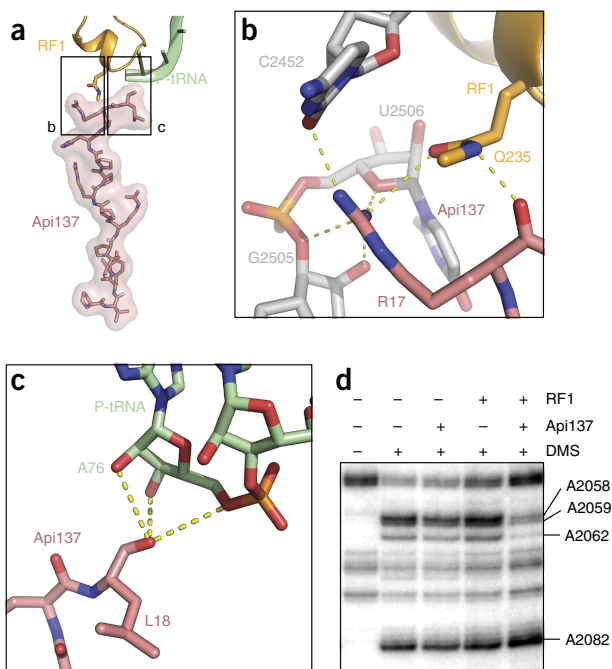


Figure 4 Inhibitory action of Api137 is mediated by its interactions with RF1 and P-site tRNA. (a) Position of Api137 (salmon) relative to RF1 (orange) and P-site tRNA (green). The boxed regions are enlarged in b and c. (b) Interactions of Api137 with RF1. Arg17 of Api137 is coordinated by bonding with 23S rRNA nucleotides C2452, G2505 and U2506 (gray) to form direct contacts with Gln235 of the GGQ motif of RF1 (orange). (c) The C-terminal hydroxyl of Leu18 of Api137 interacts with the ribose of A76 of deacylated P-site tRNA (green). (d) Dimethylsulfate (DMS) probing of Api137 interaction with PostHC 23S rRNA in the absence or presence of RF1. The gel is representative of two independent experiments.

its inhibitory action in two related but functionally distinct ways. The primary effect of Api137 is to trap RF1 and RF2 on the ribosomes after the release of the nascent peptide (Fig. 5d). This leads to depletion of the free RF pool and, as a result, the majority of cellular ribosomes are arrested at the stop codons in the prehydrolysis state (Fig. 5e). The arrested ribosome may additionally block other ribosomes on the same ORF from completing translation. Thus, treatment of cells with Api137 results in the formation of two populations of ribosomes stalled at the stop codons: a small fraction is arrested in a posthydrolysis state, whereas the majority carries unhydrolyzed peptidyl-tRNA.

Although Api137 belongs to the broad group of ribosome-targeting PrAMPs, its mode of binding is fundamentally different from those of the previously studied derivatives of oncocin, bactenecin, pyrrhocoricin and metalnikowin^{10–14}. Whereas the binding sites of all PrAMPs overlap, the orientation of Api137 is opposite to that observed for other PrAMPs. Furthermore, the N termini of other PrAMPs encroach upon the A site of the PTC, completely blocking it and hindering binding of any A-site substrates^{10–13}, whereas Api137 binds entirely within the exit tunnel. Therefore, the binding of RF1 or RF2 to the A site is incompatible with the placement of oncocin and similar PrAMPs, whereas Api137 actually requires RF1 or RF2 for efficient binding.

Due to the spatial constraints of the tunnel, direct binding of Api137 promoted by its interactions with RF1 or RF2 is likely to occur only after the peptidyl-tRNA ester bond has been hydrolyzed and the newly synthesized protein has vacated the ribosome. Therefore, apidaecins have a rather narrow time window to exert their inhibitory action: namely, after the departure of the newly made protein but before RF1

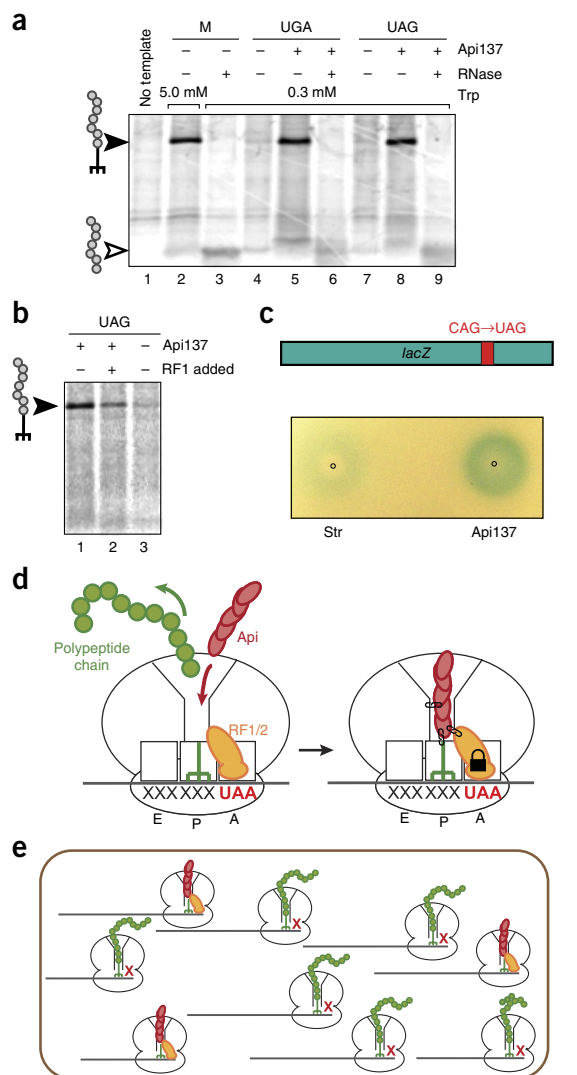


Figure 5 Api137 induces accumulation of peptidyl-tRNA and stop codon readthrough. (a) Gel electrophoresis analysis of the ^{35}S -labeled products of the *in vitro* translation of the *tnaC* gene with its original UGA stop codon (lanes 1–6) or with the UAG stop codon (lanes 7–9), in the absence or presence of Api137. Lane 1, control reaction without mRNA. Lane 2 (M, marker) shows RNase-sensitive TnaC-tRNA accumulated at high concentration of tryptophan (Trp). Lanes 5 and 8 show Api137-induced accumulation of TnaC-tRNA at low concentration of tryptophan. The bands corresponding to TnaC-tRNA and the released TnaC peptide are indicated with filled and open arrowheads, respectively. The gel is representative of five independent biological replicates. (b) Excess of RF1 rescues Api137-induced accumulation of peptidyl-tRNA. Cell-free translation with a low tryptophan concentration was carried out in standard conditions (lanes 1 and 3) or with five-fold molar excess of RF1 over the ribosomes (lane 2). The gel is representative of two independent biological replicates. (c) Expression of the chromosomal mutant *lacZ* with a premature stop codon, mediated by stop codon readthrough stimulated by the miscoding antibiotic streptomycin (Str) or by Api137. The central circles indicate where droplets of Str or Api137 were placed on a lawn of *E. coli* cells grown on an LB-agar plate supplemented with ampicillin, IPTG and X-Gal. This plate represents one of three independent experiments. (d,e) The dual mode of Api137 action. (d) Api137 binds to the ribosome after RF1 or RF2 catalyzes the release of the complete protein and traps RF1 or RF2, thereby preventing their turnover. (e) Trapping of RF1 or RF2 depletes their available pool, causing the stalling of most of the ribosomes at the stop codons, unable to release the nascent proteins.

or RF2 dissociation. Within this window, Api137 has to traverse the entire length of the exit tunnel to reach its binding site close to the PTC where it can establish interactions with the RF. Thus, Api137-dependent trapping of RF1 and RF2 is probably a fairly rare event in the context of the global cellular translation. However, the resulting complex is long lived (Fig. 2d), and the majority of RF1 and RF2 molecules will eventually be sequestered.

Recycling of RF1 and RF2 in the cell is facilitated by RF3, but RF3 does not prevent trapping of RF1 or RF2 by Api137 *in vitro* (Fig. 2f). Nevertheless, minimal inhibitory concentration (MIC) testing shows that cells lacking RF3 are eight times more sensitive to Api137 than those expressing RF3 (Supplementary Table 1). This suggests that RF3 can partly mitigate the Api137 effect, probably by speeding up RF1 or RF2 dissociation before Api137 binding or by stimulating the dissociation of the already trapped factors.

Because of its unique mechanism of action, Api137 and its analogs could serve as important tools for research and medicine. Api137 could have an application in synthetic biology in which interference with peptide release at engineered stop codons could stimulate the incorporation of noncanonical amino acids via stop codon suppression²⁹. The use of Api137 for medicine could go far beyond its known antibacterial action. Many human genetic disorders are caused by nonsense mutations. Although enabling premature stop codon readthrough by using translation-error-inducing compounds is one of the promising strategies, the decrease in translational accuracy makes such drugs highly toxic³⁰. The ability of Api137 to dramatically stimulate readthrough by interfering with the function of RFs provides new avenues for exploring this approach³¹, and our high-resolution structure of Api137 complexed with the bacterial ribosome can serve as a starting point for the rational design of specific inhibitors of eukaryotic translation termination.

METHODS

Methods, including statements of data availability and any associated accession codes and references, are available in the [online version of the paper](#).

Note: Any Supplementary Information and Source Data files are available in the online version of the paper.

ACKNOWLEDGMENTS

We thank I. Lomakin and M. Gagnon for helping us initiate this project. We also thank them and Y. Polikanov for critical discussions, T. Perez-Morales for experimental advice, A. Kefi for help with analysis of genome sequencing data, A. Bursy, O. Geintzler, S. Kappler, C. Kothe, T. Niese, S. Rieder, H. Sieber, T. Wiles, and M. Zimmermann for expert technical assistance. This work was supported by grant R01 GM 106386 from the US National Institutes of Health (to A.S.M. and N.V.-L.), iNEXT project 2259 (to D.N.W.), grants of the Forschergruppe FOR 1805 (to D.N.W., R.B. and M.V.R.) and a project grant in the framework of the Sonderforschungsbereich SFB860 (to M.V.R.) from the Deutsche Forschungsgemeinschaft (DFG).

AUTHOR CONTRIBUTIONS

Members of the A.S.M. and N.V.-L. labs (T.F., D.K., N.V.-L. and A.S.M.) carried out biochemical, microbiological and genetic experiments. Members of the M.V.R. lab (C.M., P.K. and M.V.R.) performed kinetic analysis, and members of the D.N.W. lab (M.G., O.B., R.B. and D.N.W.) carried out structural studies. N.V.-L., A.S.M., M.V.R. and D.N.W. designed the study and oversaw the experiments. T.F., C.M. and M.G. designed and performed the experiments and analyzed the data. P.K. and D.K. performed the experiments. N.V.-L., A.S.M., M.V.R., D.N.W., T.F., C.M. and M.G. wrote the paper.

COMPETING FINANCIAL INTERESTS

The authors declare no competing financial interests.

Reprints and permissions information is available online at <http://www.nature.com/reprints/index.html>. Publisher's note: Springer Nature remains neutral with regard to jurisdictional claims in published maps and institutional affiliations.

1. Korostelev, A.A. Structural aspects of translation termination on the ribosome. *RNA* **17**, 1409–1421 (2011).
2. Bremer, H. & Dennis, P. in *Escherichia coli and Salmonella: Cellular and Molecular Biology* Vol. 2 (eds. Neidhardt, F.C. et al.) Ch. 97 (ASM Press, 1996).
3. Schmidt, A. et al. The quantitative and condition-dependent *Escherichia coli* proteome. *Nat. Biotechnol.* **34**, 104–110 (2016).
4. Koutmou, K.S., McDonald, M.E., Brunelle, J.L. & Green, R. RF3:GTP promotes rapid dissociation of the class 1 termination factor. *RNA* **20**, 609–620 (2014).
5. Shi, X. & Joseph, S. Mechanism of translation termination: RF1 dissociation follows dissociation of RF3 from the ribosome. *Biochemistry* **55**, 6344–6354 (2016).
6. Kaji, A. et al. The fourth step of protein synthesis: disassembly of the posttermination complex is catalyzed by elongation factor G and ribosome recycling factor, a near-perfect mimic of tRNA. *Cold Spring Harb. Symp. Quant. Biol.* **66**, 515–530 (2001).
7. Zasloff, M. Antimicrobial peptides of multicellular organisms. *Nature* **415**, 389–395 (2002).
8. Scocchi, M., Mardirossian, M., Runti, G. & Benincasa, M. Non-membrane permeabilizing modes of action of antimicrobial peptides on bacteria. *Curr. Top. Med. Chem.* **16**, 76–88 (2016).
9. Li, W. et al. Proline-rich antimicrobial peptides: potential therapeutics against antibiotic-resistant bacteria. *Amino Acids* **46**, 2287–2294 (2014).
10. Seefeldt, A.C. et al. Structure of the mammalian antimicrobial peptide Bac7(1–16) bound within the exit tunnel of a bacterial ribosome. *Nucleic Acids Res.* **44**, 2429–2438 (2016).
11. Roy, R.N., Lomakin, I.B., Gagnon, M.G. & Steitz, T.A. The mechanism of inhibition of protein synthesis by the proline-rich peptide oncocin. *Nat. Struct. Mol. Biol.* **22**, 466–469 (2015).
12. Seefeldt, A.C. et al. The proline-rich antimicrobial peptide Onc112 inhibits translation by blocking and destabilizing the initiation complex. *Nat. Struct. Mol. Biol.* **22**, 470–475 (2015).
13. Gagnon, M.G. et al. Structures of proline-rich peptides bound to the ribosome reveal a common mechanism of protein synthesis inhibition. *Nucleic Acids Res.* **44**, 2439–2450 (2016).
14. Krizsan, A., Prah, C., Goldbach, T., Knappe, D. & Hoffmann, R. Short proline-rich antimicrobial peptides inhibit either the bacterial 70S ribosome or the assembly of its large 50S subunit. *ChemBioChem* **16**, 2304–2308 (2015).
15. Castle, M., Nazarian, A., Yi, S.S. & Tempst, P. Lethal effects of apidaecin on *Escherichia coli* involve sequential molecular interactions with diverse targets. *J. Biol. Chem.* **274**, 32555–32564 (1999).
16. Krizsan, A. et al. Insect-derived proline-rich antimicrobial peptides kill bacteria by inhibiting bacterial protein translation at the 70S ribosome. *Angew. Chem. Int. Edn Engl.* **53**, 12236–12239 (2014).
17. Berthold, N. et al. Novel apidaecin 1b analogs with superior serum stabilities for treatment of infections by gram-negative pathogens. *Antimicrob. Agents Chemother.* **57**, 402–409 (2013).
18. Hartz, D., McPhee, D.S., Traut, R. & Gold, L. Extension inhibition analysis of translation initiation complexes. *Methods Enzymol.* **164**, 419–425 (1988).
19. Mattiuzzo, M. et al. Role of the *Escherichia coli* SbmA in the antimicrobial activity of proline-rich peptides. *Mol. Microbiol.* **66**, 151–163 (2007).
20. Uno, M., Ito, K. & Nakamura, Y. Functional specificity of amino acid at position 246 in the tRNA mimicry domain of bacterial release factor 2. *Biochimie* **78**, 935–943 (1996).
21. Dreyfus, M. & Heurguér-Hamard, V. Termination troubles in *Escherichia coli* K12. *Mol. Microbiol.* **79**, 288–291 (2011).
22. Kuhlenkötter, S., Wintermeyer, W. & Rodnina, M.V. Different substrate-dependent transition states in the active site of the ribosome. *Nature* **476**, 351–354 (2011).
23. Korostelev, A., Zhu, J., Asahara, H. & Noller, H.F. Recognition of the amber UAG stop codon by release factor RF1. *EMBO J.* **29**, 2577–2585 (2010).
24. Pierson, W.E. et al. Uniformity of peptide release is maintained by methylation of release factors. *Cell Rep.* **17**, 11–18 (2016).
25. Gao, H. et al. RF3 induces ribosomal conformational changes responsible for dissociation of class I release factors. *Cell* **129**, 929–941 (2007).
26. Gong, F. & Yanofsky, C. Instruction of translating ribosome by nascent peptide. *Science* **297**, 1864–1867 (2002).
27. Uehara, Y., Hori, M. & Umezawa, H. Specific inhibition of the termination process of protein synthesis by negamycin. *Biochim. Biophys. Acta* **442**, 251–262 (1976).
28. Svidritskiy, E., Ling, C., Ermolenko, D.N. & Korostelev, A.A. Blasticidin S inhibits translation by trapping deformed tRNA on the ribosome. *Proc. Natl. Acad. Sci. USA* **110**, 12283–12288 (2013).
29. Des Soye, B.J., Patel, J.R., Isaacs, F.J. & Jewett, M.C. Repurposing the translation apparatus for synthetic biology. *Curr. Opin. Chem. Biol.* **28**, 83–90 (2015).
30. Keeling, K.M., Xue, X., Gunn, G. & Bedwell, D.M. Therapeutics based on stop codon readthrough. *Annu. Rev. Genomics Hum. Genet.* **15**, 371–394 (2014).
31. Roy, B. et al. Ataluren stimulates ribosomal selection of near-cognate tRNAs to promote nonsense suppression. *Proc. Natl. Acad. Sci. USA* **113**, 12508–12513 (2016).

ONLINE METHODS

Peptides and oligonucleotides. Api137 was synthesized by NovoPro Biosciences Inc. Onc112 was synthesized by GenScript. The 'start-stop' mRNA (**Supplementary Table 2**) was purchased from IBA GmbH. The 2XermCL_S10_UAG construct was synthesized by Eurofins. DNA oligonucleotides were synthesized by Integrated DNA Technologies.

Generation of templates for *in vitro* translation and toeprinting. The DNA templates for toeprinting (**Supplementary Table 2**) were generated by PCR using AccuPrime DNA Polymerase (Thermo Fisher Scientific) and primers listed in **Supplementary Table 3**. The synthetic template *yrbA-fs15* was prepared using three overlapping primers (T7-IR-AUG, IR-*yrbA-fs15*-RF1 and posT-NV1) in a single PCR reaction. The *ermCL* template was created by PCR amplification of the gene from the plasmid pERMCT7-M³² using primers T7 and *ermCL*-UAG. The complete sequences of the templates are shown in **Supplementary Table 2**.

Toeprinting reactions were carried out in 5 μ l of PURExpress transcription-translation system (New England Biolabs) as previously described^{32,33}. The reverse transcription on the *ermCL* template was carried out using the primer *ermCL*-TP-term. The final concentrations of Api137 and Onc112 in the reactions were 50 μ M; the PrAMPs were added as stock solutions in water.

Selection of Api137-resistant mutants. The first round of selection of Api137-resistant mutants was performed with the *E. coli* strain SQ110, derived from the K12 strain (**Supplementary Table 4**). An overnight culture grown in LB medium was diluted 100-fold into fresh medium containing a subinhibitory concentration of Api137 (10 μ M). After 24 h of growth at 37 °C, the culture was diluted 100-fold into 1 ml fresh LB medium containing 50 μ M Api137. The culture was passaged one more time at 100 μ M Api137 (eight-fold MIC). The dilutions of cell culture were plated on LB agar. After overnight incubation, the *sbmA* gene was PCR amplified from 20 individual colonies using primers *SbmA*-seq-fwd and *SbmA*-seq-rev and sequenced. All but one clone had mutations in the *sbmA* gene. The Api137-resistant clone with the WT *sbmA* sequence (clone SQ110 ApiR21 in **Supplementary Table 4**) was grown in liquid culture; genomic DNA was isolated and prepared for sequencing using a Nextera XT kit (Illumina). Sequencing was performed on an Illumina NextSeq500 instrument (paired-end, 2 \times 150 base reads) at the DNA Services facility at UIC. After mapping the reads to the genome of the strain SQ110 (ref. 34), the single mutation A722G in the *prfA* gene was identified. The presence of the mutation was verified by PCR amplification of the *prfA* gene using primers *PrfA*-seq-fwd and *PrfA*-seq-rev from the parent and mutant strains and sequencing.

E. coli strain BL21(DE3) (**Supplementary Table 4**) was used in the second selection experiment. In order to avoid selection of *sbmA* mutants, before selection cells were transformed with the multicopy plasmid pZ α -SbmA encoding the functional SbmA transporter. The pZ α -SbmA plasmid was prepared by amplifying the *E. coli* *sbmA* gene using primers *SbmA*-seq-fwd and *SbmA*-EcoRI-rev, cutting the PCR product with restriction enzymes NdeI and EcoRI and ligating the resulting DNA fragment into the pZ α plasmid³⁵ cut with the same enzymes. For selection of Api137-resistant mutants, the overnight culture of BL21(DE3)/pZ α -SbmA cells was diluted 1:100 in LB medium containing ampicillin (100 μ g/ml) and 0.1 μ M IPTG and grown at 37 °C until reaching A_{600} of 0.5. 2 ml (approximately 10⁹ cells) was plated on LB agar supplemented with 100 μ g/ml ampicillin, 0.1 μ M IPTG and 12 μ M (four-fold MIC) Api137. After overnight incubation at 37 °C, ten colonies appeared. The *prfA*, *prfB* and *prfC* genes were PCR amplified using primer pairs *PrfA*-seq-fwd with *PrfA*-seq-rev, *PrfB*-seq-fwd and *PrfB*-seq-rev, or *PrfC*-seq-fwd with *PrfC*-seq-rev, respectively, and sequenced. Five clones had mutations in the *prfB* gene: three had the C784T and two had the A839T mutation. The genome of one of the remaining five clones was sequenced and revealed the presence of the G241A mutation in the *rplP* gene encoding ribosomal protein uL16. The presence of this mutation in this and four remaining clones was verified by PCR amplification of the *rplP* gene using primers *RplP*-seq-fwd and *RplP*-seq-rev and sequencing.

The MICs of Api137 for the parental strains and selected resistant mutants were determined by microbroth dilution technique in 96-well plates. Specifically, exponentially growing cells were diluted to the final density $A_{600} = 0.002$, 100 μ l of the culture were placed in the wells, and after the addition of Api137, plates were incubated overnight at 37 °C. The minimal Api137 concentration preventing appearance of the visible cell density was recorded as the MIC.

Preparation of PreHC for fast kinetics experiments. All experiments were performed in buffer A (50 mM Tris-HCl, pH 7.5, 70 mM MgCl₂, 30 mM KCl, 7 mM MgCl₂) at 37 °C unless stated otherwise. Ribosomes from the *E. coli* strain MRE600, *E. coli* initiation factors IF1, IF2 and IF3, f[³H]Met-tRNA^{fMet} and its fluorescein-labeled version f[³H]Met-tRNA^{fMet}(Flu) were prepared as described^{36,37}. PreHC was assembled on the synthetic 'start-stop' mRNA (**Supplementary Table 2**) and purified through sucrose cushion as described³⁸. The extent of f[³H]Met-tRNA^{fMet} binding was better than 95% as determined by nitrocellulose-filter binding. The pellets of PreHC were resuspended in buffer A, flash frozen in liquid nitrogen, and stored at -80 °C.

Single-cysteine mutants RF1 S167C, RF1 S167C D241G and the K12-type RF2 A246T variant were generated by site-directed mutagenesis of the corresponding plasmids. C-terminally 6xHis-tagged RF1 and RF2 were purified and *in vitro* methylated by PrmC according to the published protocol²². RF3 was purified as described³⁸.

Peptide hydrolysis assay. f[³H]Met-tRNA^{fMet} hydrolysis was monitored under single-round conditions, by mixing [³H]PreHC (0.1 μ M), preincubated with 0–100 μ M Api137, with RF1 (1 μ M) in a quench-flow apparatus at 37 °C. Reactions were quenched with a 10% trichloroacetic acid (TCA) solution in 50% ethanol. The extent of hydrolysis was assessed by means of liquid scintillation counting of the supernatants after centrifugation for 30 min at 16,000 \times g at 4 °C. To measure peptide release under multturnover conditions, [³H]PreHC (0.1 μ M) was preincubated with RF3 (0.1 μ M), GTP (1 mM), pyruvate kinase (0.1 mg/ml), and phosphoenol pyruvate (3 mM) for 15 min at 37 °C. The concentration of Api137, when present, was 1 μ M. Time courses were started by addition of RF1 or RF2 (10 nM), and after quenching the reactions with a 10% TCA solution in 50% ethanol, the samples were processed as described above.

Preparation of quencher-labeled RF1_{Qsy}. Prior to labeling, RF1s containing a single cysteine was incubated for 30 min at room temperature with a ten-fold molar excess of Tris(2-carboxyethyl)phosphine (TCEP, Sigma). The quencher dye QSY9 (Thermo Fisher) was dissolved in DMSO and added to the RF1 solution at a ten-fold molar excess. The labeling reaction was incubated for 1 h at room temperature with vigorous shaking and stopped by the addition of 2 mM DTT. The excess dye was removed by gel filtration on a PD10 column (GE Healthcare), and protein purity was checked by means of SDS-PAGE. The extent of RF1 labeling (as analyzed by absorbance) was greater than 80%.

Measuring kinetics of RF1 binding and dissociation. Rapid kinetics measurements were performed on an SX-20MV stopped-flow apparatus (Applied Photophysics, Leatherhead, UK). Experiments were performed by rapidly mixing equal volumes (60 μ l) of f[³H]Met-tRNA^{fMet}(Flu)-carrying PreHC (0.05 μ M), preincubated with Api137, for 2 min at room temperature and RF1_{Qsy} (0.15 μ M) at 37 °C. Fluorescein was excited at 470 nm and fluorescence emission was monitored after passing a KV500 filter (Schott). Time courses were evaluated by fitting using exponential functions by GraphPad Prism software. Dissociation rates (k_{off}) were determined by chase experiments. PreHC_{flu} (0.05 μ M) was preincubated with 0.15 μ M RF1_{Qsy} to generate PostHC_{flu} in the absence or presence of 1 μ M Api137. PreHC was then rapidly mixed with a ten-fold excess of unlabeled RF1 and RF3-GTP (1 mM); pyruvate kinase (0.1 mg/ml) and phosphoenol pyruvate (3 mM) were present in both syringes. The increase of fluorescence upon dissociation of RF1_{Qsy} was monitored as described above.

Chemical probing of Api137 interaction with the ribosome. PostHC was prepared by incubating 70S ribosomes (9 μ M) with tRNA^{fMet} (18 μ M) and start-stop mRNA (18 μ M) at 37 °C for 30 min in buffer A containing 20 mM MgCl₂. PostHC (0.2 μ M) was incubated in 50 μ l of reaction buffer B (250 mM K-Borate, 50 mM MgCl₂, 500 mM NH₄Cl) with RF1 (1 μ M) and/or Api137 (50 μ M) at 37 °C for 10 min. Modification with dimethylsulfate (Sigma-Aldrich) and quenching were carried out at 37 °C for 10 min as described³⁹. rRNA was isolated using phenol extraction, and the distribution of modifications was analyzed by primer extension using primers L2667 and L2180.

Cell-free translation and analysis of peptidyl-tRNA accumulation. To prepare the templates for translation in the *E. coli* S30 Extract System for Linear Templates (Promega), the *tnaC* gene was first amplified by PCR from genomic DNA of *E. coli*

MG1655 using primer Ptrc-tnaC-2 in combination with either tnaC-UGA-rev or tnaC-UAG-rev. These PCR fragments were cloned into the SmaI site of pUC18, and the *tnaC* template was reamplified with primers Ptrc-eCLi and rev-44.

The transcription–translation reactions were carried out in a total volume of 5 μ L. The reactions contained 0.5 pmol of the *tnaC* DNA template, 2 μ Ci [35 S]L-methionine (specific activity 1,175 Ci/mmol, MP Biomedicals). When needed, the reactions were supplemented with 50 μ M of Ap137, 5 mM tryptophan or 3.7 μ M of purified RF1. The reactions were incubated at 37 °C for 30 min and then, when needed, split into two aliquots, one of which was treated for 5 min at 37 °C with 0.5 μ g RNase A (Sigma-Aldrich). The translation products were precipitated with four volumes of cold acetone and resolved in 16.5% Tris-Tricine gels that preserve the integrity of peptidyl-tRNA⁴⁰. Gels were dried, exposed to the phosphoimager screen and scanned on a Typhoon scanner (GE).

In vivo suppression of premature stop codon. The *E. coli* strain with a premature stop codon in the *lacZ* gene was generated by subjecting the SQ171- Δ tolC strain (**Supplementary Table 4**) to chemical mutagenesis and selecting *lacZ*-deficient mutants. For this procedure, an overnight culture of SQ171- Δ tolC was diluted 1:200 into fresh LB medium supplemented with kanamycin (30 μ g/ml), grown at 37 °C until reaching A_{600} of 0.1, then exposed to 0.1% of ethyl methanesulfonate for 1 h. Cells were washed twice with LB medium and plated at high density on LB agar supplemented with kanamycin (50 μ g/ml), X-gal (40 μ g/ml), and IPTG (0.3 mM). White colonies were selected and restreaked on fresh kanamycin (50 μ g/ml), X-gal (40 μ g/ml), and IPTG (0.3 mM) LB-agar plates. The presence of mutations was detected by PCR amplification of the *lacZ* gene and sequencing. The clone designated SQ171-tolC/W3 (**Supplementary Table 4**) contained the C2035T mutation, which changed Gln679 of the encoded β -galactosidase to a UAG stop codon.

To test the stop codon suppressing activity of Ap137, SQ171- Δ tolC/W3 cells were grown in LB medium supplemented with 50 μ g/ml of kanamycin. Upon reaching A_{600} of 1.0, 0.5 ml were mixed with 3.5 mL of LB agar (0.6%) kept at 50 °C and poured on an LB-agar plate containing kanamycin (50 μ g/ml), IPTG (0.2 mM) and X-gal (80 μ g/ml). After solidification of the soft agar, 1 μ l of a 50 mg/ml solution of streptomycin (100 μ g) or 1 μ l of a 2 mM solution of Ap137 (4.6 μ g) were spotted on top of the cell lawn. The plate was incubated overnight at 37 °C. Stop codon readthrough activity was revealed by a blue halo around the spotted antibiotic.

Purification of RF1 for cryo-electron microscopy. N-terminally 6 \times His-tagged *E. coli* RF1 was overexpressed in BL21 *E. coli* cells grown at 37 °C from overnight culture in LB medium and in the presence of 100 μ g/mL ampicillin. Protein expression was induced at A_{600} of 0.4 by adding IPTG to a final concentration of 1 mM. RF1 was expressed from pET28-plasmid kindly provided by R. Green (John Hopkins University). After 1 h of expression, cells were lysed using a microfluidizer. The cell lysate was cleared by centrifugation in a SS34 rotor (Sorval) at 4 °C and 44,100 $\times g$ for 30 min. Purification of His-tagged RF1 was done with Protino Ni-NTA agarose beads (Macherey-Nagel). The final eluate was applied onto a Superdex HiLoad S75 16/600 column (GE Healthcare) to yield the final concentrated protein in gel filtration buffer (50 mM HEPES pH 7.4, 50 mM KCl, 100 mM NaCl, 2% glycerol and 5 mM 2-mercaptoethanol).

Sample preparation for cryo-electron microscopy. ErmCL_S10_UAG-SRCs (stalled ribosome complexes) were generated following the same disome purification procedure as previously described^{41,42}. The 2XermCL_S10_UAG template was based on the 2XermCL_disome construct described previously⁴¹ except that the Ser10 codon was replaced by a UAG stop codon (**Supplementary Table 2**).

In vitro translation of the 2XermCL_S10_UAG template was performed using the Rapid Translation System RTS100 *E. coli* HY Kit (5PRIME) in the presence of 50 μ M Ap137. Disomes were isolated using sucrose density gradients (10–55% sucrose in buffer A, containing 50 mM HEPES-KOH, pH 7.4, 100 mM KOAc, 25 mM Mg(OAc)₂, 6 mM 2-mercaptoethanol, 20 μ M Ap137 and one Complete EDTA-free Protease Inhibitor cocktail (Roche)) as previously described^{41,42}. The final purified complex was reincubated with a 2.5-fold excess of RF1 and 50 μ M Ap137 for 15 min at 37 °C.

Cryo-electron microscopy and single-particle reconstruction. A total of 5 A_{260} /ml Ap137–RF1 complex was applied to 2 nm precoated Quantifoil R3/

holey carbon supported grids and vitrified using a Vitrobot Mark IV (FEI, Eindhoven). Data collection was performed using an FEI Titan Krios transmission electron microscope equipped with a Falcon II direct electron detector with a Falcon III chip (FEI, Eindhoven) at 300 kV using a pixel size of 1.084 Å and a defocus range of 0.7–2.5 μ m. The data collection yielded a total number of 5,132 micrographs. Each micrograph was recorded as a series of ten frames (2.5 e[−]/Å² dose per frame). All frames (accumulated dose of 28 e[−]/Å²) were aligned using the Motion correction software⁴³, and power spectra, defocus values, astigmatism and estimation of micrograph resolution were determined by CTFFIND4 (ref. 44). Micrographs showing Thon rings beyond 3.2-Å resolution were further manually inspected for good areas and power-spectra quality. Automatic particle picking was performed using SIGNATURE⁴⁵, and single particles were processed using the FREALIGN Software package⁴⁶. Initial alignment was performed with 116,212 particles using the *E. coli* 70S ribosome as a reference structure. Subsequently, particles were subjected to 3D classification resulting in six classes with a maximum resolution extending to <3.4 Å (0.143 FSC) for class 1 (**Supplementary Fig. 4a–c**). 3D classification and initial alignment was performed using 3-times-decimated data. The local resolution of the final maps was computed using ResMap⁴⁷ (**Supplementary Fig. 4e–g**). The final maps were sharpened by dividing the maps by the modulation transfer function of the detector and by applying an automatically determined negative *B* factor to the maps using RELION⁴⁸.

Molecular modeling and map-docking procedures. The molecular model of the 70S ribosome was based on *E. coli*-70S-EF-Tu structure⁴⁹. RF1 was modeled based on the previously reported RF1 structure (PDB 5J3C)²⁴. The Ile-tRNA model was generated based on the previously described P-site tRNA⁵⁰. The models were initially adjusted and refined using Coot⁵¹. Ap137 was modeled *de novo* into the map using Coot. The complete atomic model of the *E. coli* ribosome was refined using phenix.real_space_refine⁵² with secondary structure restraints calculated by PHENIX⁵². Cross-validation against overfitting (**Supplementary Fig. 4d**) was performed as described elsewhere⁵³. The statistics of the refined model were obtained using MolProbity⁵⁴ and are presented in **Table 1**.

Figure preparation. Figures showing electron densities and atomic models were generated using either UCSF Chimera⁵⁵ or PyMol Molecular Graphic Systems (version 1.8, Schrödinger).

A **Life Sciences Reporting Summary** for this article is available.

Data availability. The cryo-EM density map of the Ap137-RF1-ribosome complex has been deposited in the Electron Microscopy Data Bank under accession code EMD 3730. The corresponding molecular model has been deposited in the Protein Data Bank under accession code PDB 5O2R. Source data for **Figure 2b,c,e,f** and **Supplementary Figure 3** are available online. All other data are available from the corresponding author upon reasonable request.

32. Vazquez-Laslop, N., Thum, C. & Mankin, A.S. Molecular mechanism of drug-dependent ribosome stalling. *Mol. Cell* **30**, 190–202 (2008).
33. Orelle, C. *et al.* Identifying the targets of aminoacyl-tRNA synthetase inhibitors by primer extension inhibition. *Nucleic Acids Res.* **41**, e144 (2013).
34. Quan, S., Skovgaard, O., McLaughlin, R.E., Buirman, E.T. & Squires, C.L. Markerless *Escherichia coli* *rrn* deletion strains for genetic determination of ribosomal binding sites. *G3 (Bethesda)* **5**, 2555–2557 (2015).
35. Bailey, M., Chettiar, T. & Mankin, A.S. Induction of *erm(C)* expression by noninducing antibiotics. *Antimicrob. Agents Chemother.* **52**, 866–874 (2008).
36. Rodnina, M.V. & Wintermeyer, W. GTP consumption of elongation factor Tu during translation of heteropolymeric mRNAs. *Proc. Natl. Acad. Sci. USA* **92**, 1945–1949 (1995).
37. Milon, P. *et al.* Transient kinetics, fluorescence, and FRET in studies of initiation of translation in bacteria. *Methods Enzymol.* **430**, 1–30 (2007).
38. Peske, F., Kuhlenkötter, S., Rodnina, M.V. & Wintermeyer, W. Timing of GTP binding and hydrolysis by translation termination factor RF3. *Nucleic Acids Res.* **42**, 1812–1820 (2014).
39. Merryman, C. & Noller, H.F. in *RNA:Protein Interactions, A Practical Approach* (ed. Smith, C.W.J.) 237–253 (Oxford University Press, 1998).
40. Schägger, H. & von Jagow, G. Tricine-sodium dodecyl sulfate-polyacrylamide gel electrophoresis for the separation of proteins in the range from 1 to 100 kDa. *Anal. Biochem.* **166**, 368–379 (1987).
41. Arenz, S., Nguyen, F., Beckmann, R. & Wilson, D.N. Cryo-EM structure of the tetracycline resistance protein TetM in complex with a translating ribosome at 3.9-Å resolution. *Proc. Natl. Acad. Sci. USA* **112**, 5401–5406 (2015).

42. Arenz, S. *et al.* Molecular basis for erythromycin-dependent ribosome stalling during translation of the ErmBL leader peptide. *Nat. Commun.* **5**, 3501 (2014).
43. Li, X. *et al.* Electron counting and beam-induced motion correction enable near-atomic-resolution single-particle cryo-EM. *Nat. Methods* **10**, 584–590 (2013).
44. Rohou, A. & Grigorieff, N. CTFFIND4: fast and accurate defocus estimation from electron micrographs. *J. Struct. Biol.* **192**, 216–221 (2015).
45. Chen, J.Z. & Grigorieff, N. SIGNATURE: a single-particle selection system for molecular electron microscopy. *J. Struct. Biol.* **157**, 168–173 (2007).
46. Grigorieff, N. FREALIGN: high-resolution refinement of single particle structures. *J. Struct. Biol.* **157**, 117–125 (2007).
47. Kucukelbir, A., Sigworth, F.J. & Tagare, H.D. Quantifying the local resolution of cryo-EM density maps. *Nat. Methods* **11**, 63–65 (2014).
48. Scheres, S.H. RELION: implementation of a Bayesian approach to cryo-EM structure determination. *J. Struct. Biol.* **180**, 519–530 (2012).
49. Fischer, N. *et al.* Structure of the *E. coli* ribosome-EF-Tu complex at <3 Å resolution by Cs-corrected cryo-EM. *Nature* **520**, 567–570 (2015).
50. Huter, P. *et al.* Structural basis for ArfA-RF2-mediated translation termination on mRNAs lacking stop codons. *Nature* **541**, 546–549 (2017).
51. Emsley, P. & Cowtan, K. Coot: model-building tools for molecular graphics. *Acta Crystallogr. D Biol. Crystallogr.* **60**, 2126–2132 (2004).
52. Adams, P.D. *et al.* PHENIX: a comprehensive Python-based system for macromolecular structure solution. *Acta Crystallogr. D Biol. Crystallogr.* **66**, 213–221 (2010).
53. Brown, A. *et al.* Tools for macromolecular model building and refinement into electron cryo-microscopy reconstructions. *Acta Crystallogr. D Biol. Crystallogr.* **71**, 136–153 (2015).
54. Chen, V.B. *et al.* MolProbity: all-atom structure validation for macromolecular crystallography. *Acta Crystallogr. D Biol. Crystallogr.* **66**, 12–21 (2010).
55. Pettersen, E.F. *et al.* UCSF Chimera—a visualization system for exploratory research and analysis. *J. Comput. Chem.* **25**, 1605–1612 (2004).

Life Sciences Reporting Summary

Nature Research wishes to improve the reproducibility of the work that we publish. This form is intended for publication with all accepted life science papers and provides structure for consistency and transparency in reporting. Every life science submission will use this form; some list items might not apply to an individual manuscript, but all fields must be completed for clarity.

For further information on the points included in this form, see [Reporting Life Sciences Research](#). For further information on Nature Research policies, including our [data availability policy](#), see [Authors & Referees](#) and the [Editorial Policy Checklist](#).

► Experimental design

1. Sample size

Describe how sample size was determined.

n.a.

Data exclusions

Describe any data exclusions.

n.a.

Replication

Describe whether the experimental findings were reliably reproduced.

All attempts of replication were successful.

Randomization

Describe how samples/organisms/participants were allocated into experimental groups.

n.a.

Blinding

Describe whether the investigators were blinded to group allocation during data collection and/or analysis.

n.a.

Note: all studies involving animals and/or human research participants must disclose whether blinding and randomization were used.

Statistical parameters

For all figures and tables that use statistical methods, confirm that the following items are present in relevant figure legends (or in the Methods section if additional space is needed).

^a Confirmed

- The exact sample size (n) for each experimental group/condition, given as a discrete number and unit of measurement (animals, litters, cultures, etc.)
- A description of how samples were collected, noting whether measurements were taken from distinct samples or whether the same sample was measured repeatedly
- A statement indicating how many times each experiment was replicated
- The statistical test(s) used and whether they are one- or two-sided (note: only common tests should be described solely by name; more complex techniques should be described in the Methods section)
- A description of any assumptions or corrections, such as an adjustment for multiple comparisons
- The test results (e.g. *P* values) given as exact values whenever possible and with confidence intervals noted
- A clear description of statistics including central tendency (e.g. median, mean) and variation (e.g. standard deviation, interquartile range)
- Clearly defined error bars

See the web collection on [statistics for biologists](#) for further resources and guidance.

► Software

Policy information about [availability of computer code](#)

7. Software

Describe the software used to analyze the data in this

Phenix 1.11.1-2575 (phenix.real_space_refine) was used for model refinement and

study.

statistics read-out using "phenix.molprobity". In addition, molprobity statistics were generated using "http://molprobity.biochem.duke.edu/index.php". Further analysis of e.g. electrostatic interactions, as well as preparation of figures was done using Pymol 1.8.6.0.

For manuscripts utilizing custom algorithms or software that are central to the paper but not yet described in the published literature, software must be made available to editors and reviewers upon request. We strongly encourage code deposition in a community repository (e.g. GitHub). *Nature Methods* [guidance for providing algorithms and software for publication](#) provides further information on this topic.

► Materials and reagents

Policy information about [availability of materials](#)

8. Materials availability

Indicate whether there are restrictions on availability of unique materials or if these materials are only available for distribution by a for-profit company.

All unique materials are available from standard commercial sources, as stated in detail in the Methods section.

9. Antibodies

Describe the antibodies used and how they were validated for use in the system under study (i.e. assay and species).

No antibodies were used.

10. Eukaryotic cell lines

- State the source of each eukaryotic cell line used.
- Describe the method of cell line authentication used.
- Report whether the cell lines were tested for mycoplasma contamination.
- If any of the cell lines used are listed in the database of commonly misidentified cell lines maintained by [ICLAC](#), provide a scientific rationale for their use.

No eukaryotic cell lines were used.

No eukaryotic cell lines were used.

No eukaryotic cell lines were used.

n.a.

Animals and human research participants

Policy information about [studies involving animals](#); when reporting animal research, follow the [ARRIVE guidelines](#)

1. Description of research animals

Provide details on animals and/or animal-derived materials used in the study.

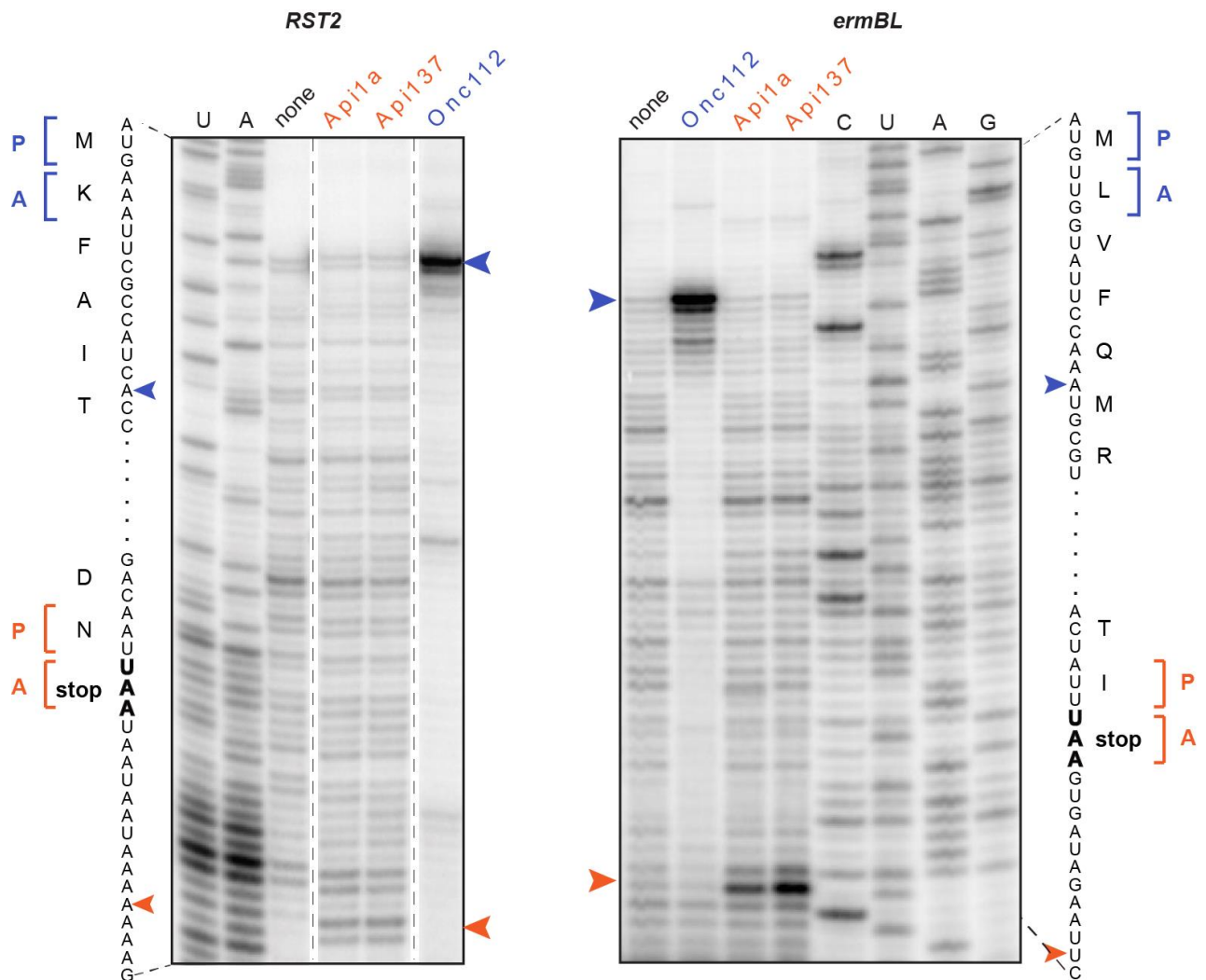
No animals were used.

Policy information about [studies involving human research participants](#)

2. Description of human research participants

Describe the covariate-relevant population characteristics of the human research participants.

The study did not involve human research participants.

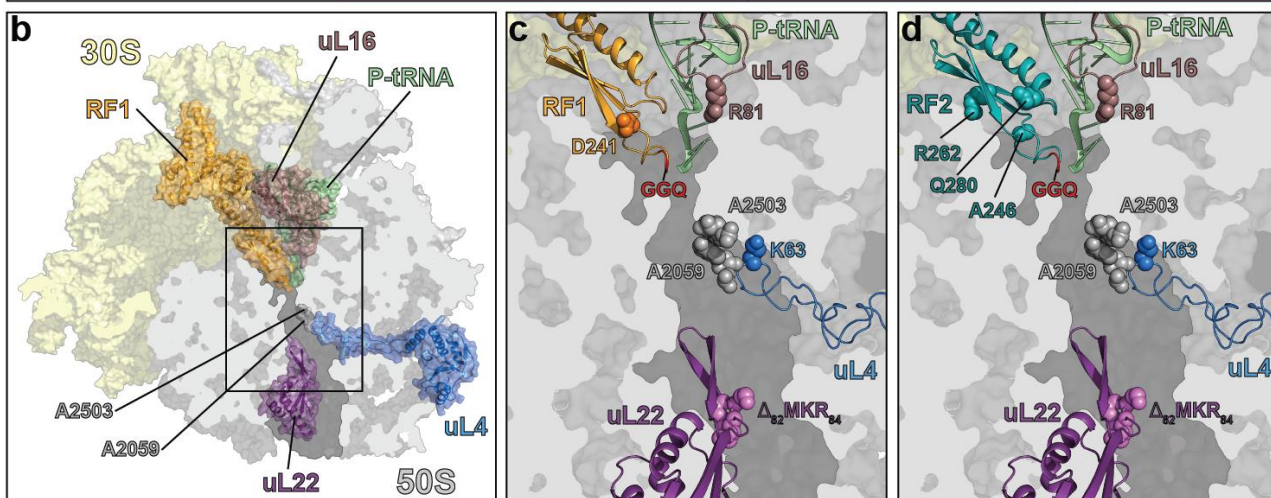


Supplementary Figure 1

Api137-induced ribosome stalling at the end of the ORFs

Toeprinting analysis of translation arrest in the synthetic ORF *RST2* (left) and the natural ORF *ermBL* (right) mediated by PrAMPs. The toeprint bands corresponding to the ribosomes arrested by Api137 or the natural apidaecin 1a (Api1a) at the stop codon of the ORF are indicated with orange arrowheads; the bands representing the ribosome arrested by Onc112 at the start codon are marked with blue arrowheads. Sequencing lanes are shown. The nucleotides corresponding to the toeprint bands are indicated in the gene sequence on the side of the gels; orange brackets indicate codons positioned in the P- and A- sites of the Api-stalled ribosome; blue brackets indicate codons in the P- and A- sites of the Onc112-stalled ribosome. The gels are representatives of two independent experiments.

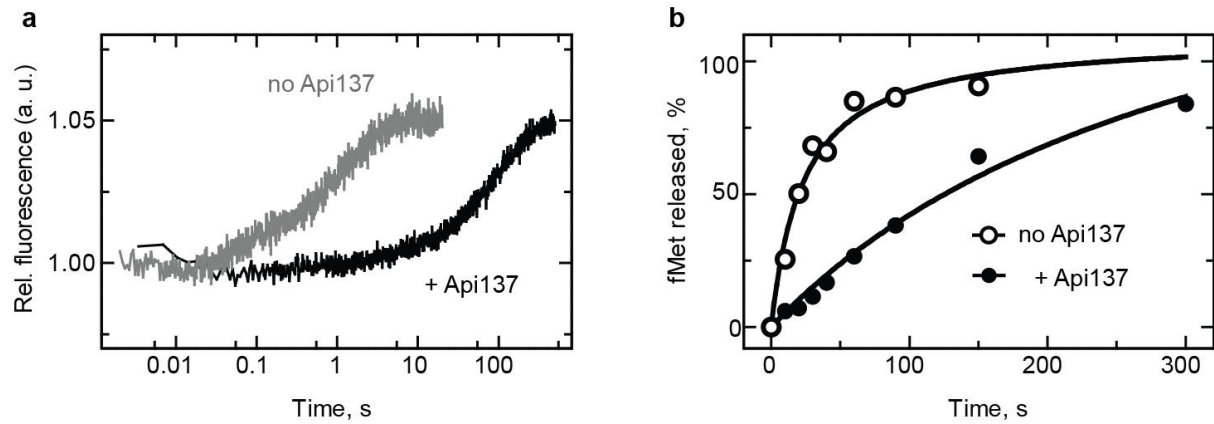
a <i>E. coli</i> strain		Minimal inhibitory concentration [μ M]	Fold change
SQ171	wild type	12.5	
	23S rRNA: A2059C	100	8
	23S rRNA: A2503G	> 100	> 8
SQ110	wild type	12.5	
	SbmA: Ser251TAG (*)	> 100	> 8
	RF1: Asp241Gly (*)	> 100	> 8
BL21 (pZa-SbmA)	wild type	0.75	
	RF2: Arg262Cys (*)	> 100	> 128
	RF2: Gln280Leu (*)	50	64
AB301	wild type	12.5	
	uL4: Lys63Glu	> 100	> 8
	uL22: Δ_{82} MKR ₈₄	> 100	> 8



Supplementary Figure 2

Api137-resistance mutations.

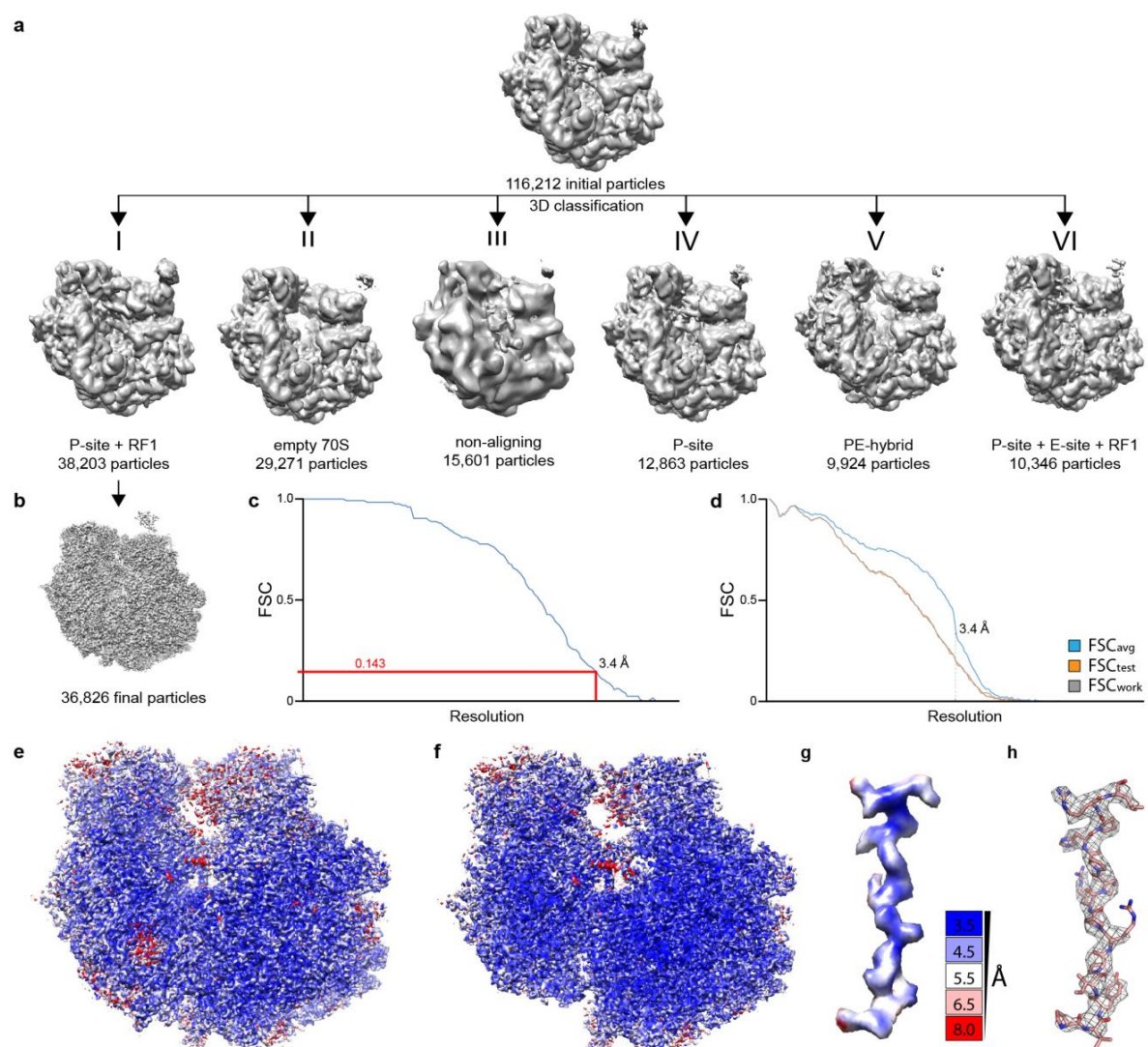
a, Effect of the newly-isolated (marked by asterisks) or tested mutations on sensitivity of *E. coli* cells to Api137. The RF1 mutation is highlighted in orange; RF2 mutations, teal; rRNA mutations, grey; uL16, brown; uL4, blue; uL22, purple. Each MIC was determined in at least two independent experiments. **b-d**, Location of resistance mutations within the context of the terminating ribosome. **b**, Transverse section of the 50S ribosomal subunit (grey) of the 70S ribosome (30S subunit, yellow) showing the location of ribosomal proteins uL4, uL16, uL22 or 23S rRNA nucleotides (grey) whose mutations confer resistance to Api137. The region enlarged in **(c)** is boxed. **c-d**, Location of Api137 resistance mutations (spheres) in 23S rRNA (grey), ribosomal proteins uL4 (blue), uL16 (brown) and uL22 (purple), as well as **(c)** RF1 (orange) or **(d)** RF2 (teal). The GGQ motif of RF1 and RF2 is colored red in **(c)** and **(d)**.



Supplementary Figure 3

Mutations allow faster dissociation of RF1 and RF2 from the PostHC.

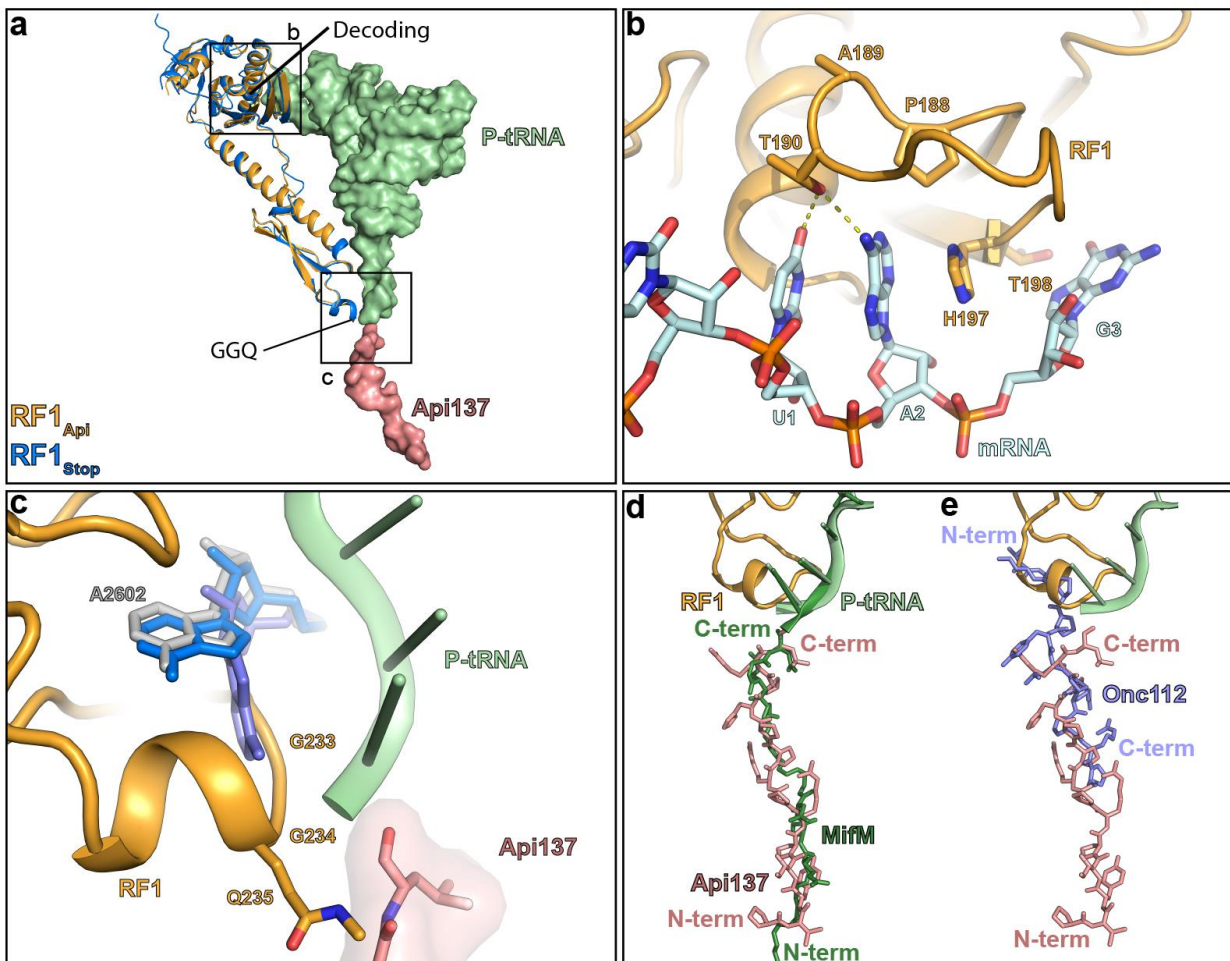
a, Dissociation of RF1(D241G) from the PostHC in the presence of Api137. RF1(D241G)_{Q_{SY}} was incubated with PreHC_{Flu} (0.05 μ M) to generate PostHC_{Flu} and then mixed with a 10-fold excess of unlabeled RF1 and RF3·GTP in the absence (grey) or in the presence (black) of Api137 (1 μ M). The traces represent the average of up to eight technical replicates. No dissociation of wt RF1 in the presence of Api137 was observed under the same experimental conditions (Fig. 2f). **b**, Peptide hydrolysis by K12 strain-specific RF2(Ala246Thr) at turnover conditions in the absence (open circles) or in the presence (closed circles) of Api137 (1 μ M). In the presence of Api137, the peptide hydrolysis reaction proceeds faster when it is catalyzed by the K12 strain RF2, compared to the B strain RF2 (Fig. 2c).



Supplementary Figure 4

In silico sorting and resolution of the Api-RF1-70S complex.

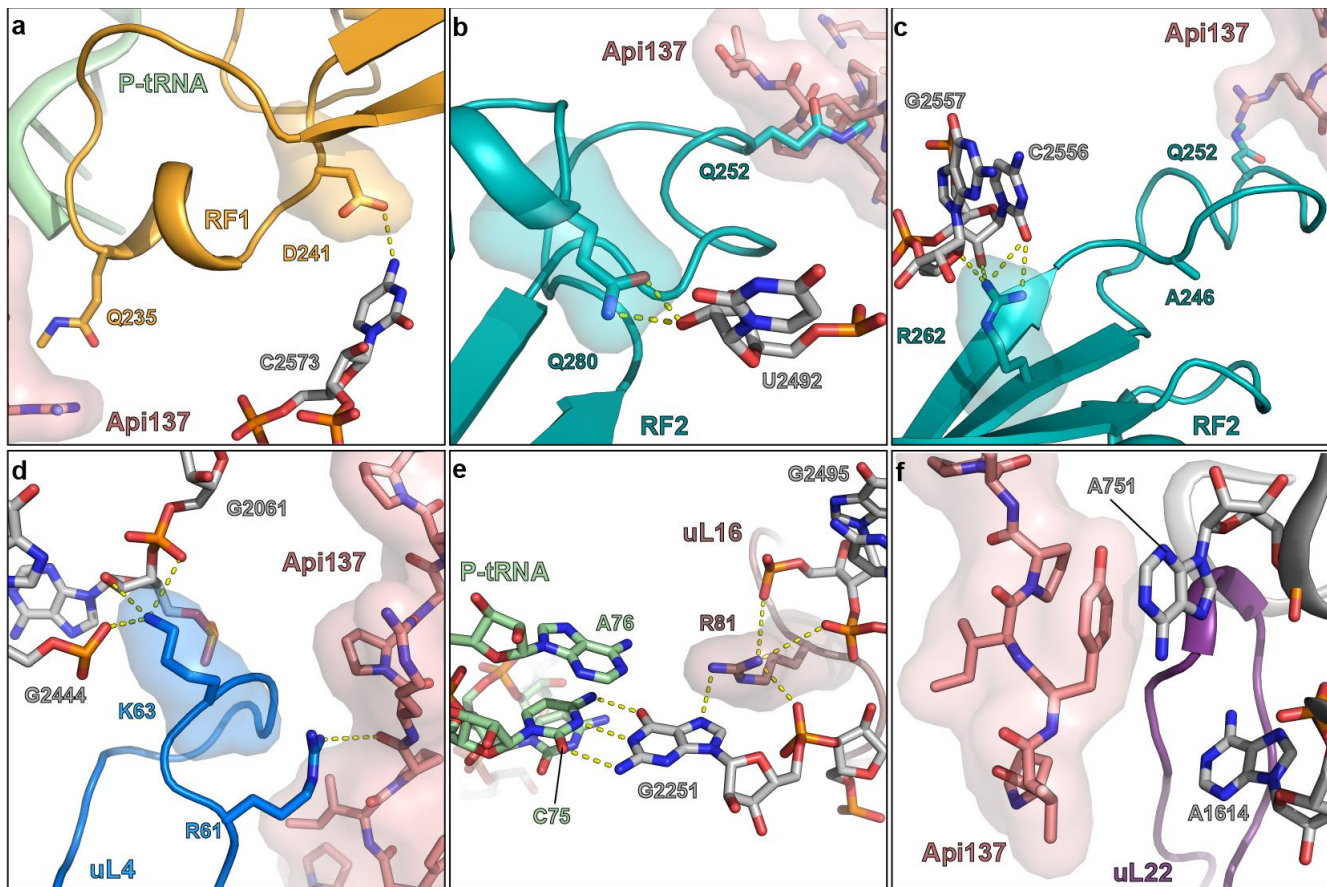
a, *In silico* sorting was performed with the FreAlign 9.11 software package (as described in Grigorieff, N., *J. Struct. Biol.* **157**, 117-125 (2007)). Initial alignment of 116,212 particles was followed by 3D classification, resulting in six different classes. Class 1 (38,203 particles) was further refined, yielding a (b) final reconstruction consisting of 36,826 particles, with (c) an average resolution of 3.4 Å (based on the Fourier shell correlation (FSC) curve at FSC 0.143). **d**, Validation of the fit of molecular models to cryo-EM map for the Api137-RF1-70S complex. FSC curves calculated between the refined model and the final map (blue), with the self- and cross-validated correlations in orange and black, respectively. Information beyond 3.4 Å was not used during refinement and preserved for validation. (e) Side view and (f) transverse section of the cryo-EM map of Api137-RF1-70S complex colored according to local resolution as shown previously (Kucukelbir, A., Sigworth, F. J. & Tagare, H. D., *Nat. Methods* **11**, 63-65 (2014)). **g-h**, Cryo-EM density for Api137 (g) colored according to local resolution and (h) shown as grey mesh with molecular model for residues 5-18.



Supplementary Figure 5

Features of the Api137-RF1-70S complex.

a, RF1 (orange), deacylated P-site tRNA (green) and Api137 (salmon) in the Api137-RF1-70S complex. The position of RF1 during canonical termination is shown in blue (PDBID 5J30; Pierson, W. E. *et al.*, *Cell Rep.* **17**, 11-18 (2016)). Boxed regions are zoomed in the panels (b) and (c). **b**, Interaction of the PAT motif of RF1 (orange) with the UAG stop codon of the mRNA (cyan) in the Api137-RF1-70S complex. **c**, A2602 of the 23S rRNA is in the rotated conformation as observed in previous RF1-70S structures (Korostelev, A. *et al.*, *EMBO J.* **29**, 2577-2585 (2010); Pierson, W. E. *et al.*, *Cell Rep.* **17**, 11-18 (2016); Laurberg, M. *et al.*, *Nature* **454**, 852-857 (2008); Svidritskiy, E. & Korostelev, A. A., *Structure* **23**, 2155-2161 (2015)). Conformation of A2602 (grey) in Api137-RF1-70S complex compared to A2602 (blue) during canonical termination (PDBID 5J30; Pierson, W. E. *et al.*, *Cell Rep.* **17**, 11-18 (2016)) and A2602 (slate) from the pre-attack state (PDBID 1VY4; Polikanov, Y. S., Steitz, T. A. & Innis, C. A., *Nat. Struct. Mol. Biol.* **21**, 787-793 (2014)). Api137 (salmon) and P-site tRNA (green) are shown for reference. **d**, **e**, The binding position of Api137 (salmon) relative to the (d) MifM nascent chain (dark green; Sohmen, D. *et al.*, *Nat. Commun.* **6**, 6941 (2015)) or (e) antimicrobial peptide Onc112 (slate; Seefeldt, A. C. *et al.*, *Nat. Struct. Mol. Biol.* **22**, 470-475 (2015)). In (d) and (e) the orientations of the peptides are indicated.



Supplementary Figure 6

Mutations that increase resistance to Api137

(a-c) Location of residues in (a) RF1 (orange) and (b, c) RF2 (teal) that increase resistance to Api137 when mutated. Site of mutations are shown in stick and surface representation and glutamines of the GGQ motif (Gln235 in RF1 and Gln252 in RF2) are shown as sticks for reference. (d-f) Location of Api137 resistance mutations in ribosomal proteins. (d) Lys63 in uL4 (blue) interacts with 23S rRNA residues G2061 and G2444. (e) Deletion of $_{82}\text{MKR}_{84}$ (outside of the figure boundaries) in uL22 (purple) confers resistance to Api137 presumably by changing the geometry of the uL22 exit tunnel loop and disrupting Api137 interaction with neighboring 23S rRNA nucleotides (grey), such as A751. (f) The mutation of Arg81 in uL16 (brown) may relieve Api137-mediated RF1 and RF2 trapping by indirectly destabilizing interactions of deacylated tRNA with the P-site mediated by G2251 of the 23S rRNA.

Supplementary Table 1. Deletion of the RF3-encoding *prfC* gene affects minimal inhibitory concentration (MIC) of Api137

<i>E. coli</i> strain	MIC [μM]
wild type (BW25113) ^{a)}	6.25
Δ xylA ^{b)}	6.25
Δ prfC ^{c)}	0.75

^{a)} Parental *E. coli* K-type strain

^{b)} The *xylA::kan* strain, where an unrelated gene was inactivated, was used as an additional negative control

^{c)} The *prfC::kan* strain

Supplementary Table 2: DNA & RNA templates

Promoter – blue, ORF – red, annealing site for toeprinting primer – purple, annealing site for oligonucleotide for RNase H treatment of disomes – green. Start codons of the ORFs are shown in bold, stop codons are underlined.

Name	DNA Sequence (5' – 3')
yrbA-fs	TAATACGACTCACTATAGGGCTTAAGTATAAGGAGGAAAACAT ATGAT ATACCCCTGCGGAGTGGCGCGATCGCAA ACTGAACGGCTT <u>AG</u> GCCGACCTCGACAGTTGGATTACGTGCTGAATCCTGATGCGATGTC GAG <u>TTAATAAGCAAAATT</u> CATTATAACC
ermCL-UAG	TTAACGACTCACTATAGGGATTGTGAGCGGATAACAATTGCTAGT CTTAAGTTTATAAGGAGGAAAAAA <u>ATGGCATT</u> TTAGTATTTGT AATCAGCACAGTCATTATCAACCAAACAAAAA <u>TAG</u> GTGGTTATAATG AATCGTTAATAAGCAAAATTCAATT <u>AACCAA</u> TTAAAGAGGGTTATAA
RST2	TAATACGACTCACTATAGGGCTTAAGTATAAGGAGGAAAACAT ATGTA TTGGGTAACCTCACGTCA <u>GGCAAT</u> TGCTGAAAATCCATGGCTTCGA AGACTGCGC <u>TA</u> TAATAATAAAAAAGTGA <u>TAGAATT</u> CTATCGTTAAT AAGCAAAATTCAATTATAACC
ermBL	TAATACGACTCACTATAGGGCTTAAGTATAAGGAGGAAAAAA <u>ATGTT</u> GGTATT <u>CCAAT</u> CGTAATGTAGATAAAACAT <u>CTACTATT</u> <u>AA</u> GTGATA GAATTCTATC <u>GTTAATAAGCAAAATT</u> CAATTATAACC
Start-Stop	GGCAAGGAGGUAAA <u>AUGUAA</u> ACGAUU
tnaC-UAG	ACATGGATTCT <u>TGACAATT</u> ATCAT <u>CGGCTCGTATA</u> ATGTGTGG <u>AGTT</u> TTATAAGGAGGAAAACAT ATGAAT ATCTTACATATATGTGTGACCTCAA AATGGTCAATATT GACAACAAAATT <u>GTG</u> CAT <u>ACCGCC</u> <u>TTAG</u>
tnaC-UGA	ACATGGATTCT <u>TGACAATT</u> ATCAT <u>CGGCTCGTATA</u> ATGTGTGG <u>AGTT</u> TTATAAGGAGGAAAACAT ATGAAT ATCTTACATATATGTGTGACCTCAA AATGGTCAATATT GACAACAAAATT <u>GTG</u> CAT <u>ACCGCC</u> <u>TTGA</u>
2XermCL_S10_UAG	<u>UAAAACGACUCACUUAUAGGG</u> AGUUUUUAUAGGAGGAAAAAA <u>AUGG</u> <u>GCAUUUUUAGUAUUUUUUGUAUC</u> <u>UAG</u> ACAGUUCAUUAUCAACCAAA CAAAAAAA <u>AGUUUUUAUAGGAGGAA</u> AAAAAU <u>AUGGGCAUUUUUAGU</u> <u>AUUUUUUGUAUC</u> <u>UAG</u> ACAGUUCAUUAUCAACCAAAACAAAAAAUAA

Supplementary Table 3: DNA primers used in this study

Name	Sequence
T7-IR-AUG	TAATACGACTCACTATAGGGCTTAAGTATAAGGAGGAAAACATATG
IR-yrbA-fs15- RF1	GTATAAGGAGGAAAACATATGATATACCCCTGCGGAGTGGCGCGATCGCAAACTGAACGGCTTAGGCCGACCTCGACAGTTGGAT
posT-NV1	GGTTATAATGAATTTGCTTATTAACTCGACATCGCATCAGGATTGAC
	GTGAATCCAACCTGTCGAGGTGCG
T7	TAATACGACTCACTATAGGG
ermCL-UAG	TTATAACCCTTTAATTGGTTATAATGAATTTGCTTATTAACGATTCA
	TATAACCACCTATT
ermCL-TP-term	TTATAACCCTTTAATTGGTT
SbmA-seq-fwd	CATTGGCTGACGCTTGTA
SbmA-seq-rev	TACTACACCCCGCTAAAACC
SbmA-EcoRI- rev	TGACGGCGGAAATTCTTCT
PrfA-seq-fwd	CTGAATATTCTGCGCGACAG
PrfA-seq-rev	CAGGATTTCAGCATCACGC
PrfB-seq-fwd	GCTCTTATCACCACGCTTTG
PrfB-seq-rev	GTTCATTGTTAAGATCGACTACC
PrfC-seq-fwd	GAAGGTAAGCTGGATATGCTG
PrfC-seq-rev	GCTTCTGATAACGTAGCCAG
rplP-seq-fwd	CGTTAAAGTGTGGATCTCAAAGG
rplP-seq-rev	CACTTGCTTCAACAGGTGAG
L2667	GGTCCTCTCGTACTAGGAGCAG
L2180	GGGTGGTATTCAAGGTCGG
Ptrc-tnaC	ACATGGATTCTGACAATTAAATCATCGGCTCGTATAATGTGTGGA
	AGTTTATAAGGAGGAAAACATATG
tnaC-UAG-rev	GCAAACTAAGGGCGGTGATCGAC
tnaC-UGA-rev	GCAAATCAAGGGCGGTGATCGAC

Supplementary Table 4: Bacterial strains used in this study

<i>E. coli</i> strain	Type	Source
SQ171	K-strain; F-, $\Delta(rrsH\text{-}aspU)794(\text{:FRT})$, λ^- , $\Delta(rrfG\text{-}rrsG)791(\text{:FRT})$, $\Delta(rrf\text{-}rrsD)793(\text{:FRT})$, <i>rph-1</i> , $\Delta(rrsC\text{-}trpT)795(\text{:FRT})$, $\Delta(rrsA\text{-}rrfA)792(\text{:FRT})$, $\Delta(rrsB\text{-}rrfB)790(\text{:FRT})$, $\Delta(rrsE\text{-}rrfE)789(\text{:FRT})$, ptRNA67, pKK3535	Quan, S. et al., <i>G3</i> 5 , 2555-2557 (2015)
SQ110	K-strain, F-, $\Delta(rrsH\text{-}aspU)794(\text{:FRT})$, λ^- , $\Delta(rrfG\text{-}rrsG)791(\text{:FRT})$, $\Delta(rrf\text{-}rrsD)793(\text{:FRT})$, <i>rph-1</i> , $\Delta(rrsC\text{-}trpT)795(\text{:FRT})$, $\Delta(rrsA\text{-}rrfA)792(\text{:FRT})$, $\Delta(rrsB\text{-}rrfB)790(\text{:FRT})$, ptRNA67	Quan, S. et al., <i>G3</i> 5 , 2555-2557 (2015)
SQ110 ApiR2	derived from SQ110, <i>sbmA</i> (C752A)	<i>this study</i>
SQ110 ApiR21	derived from SQ110, <i>prfA</i> (A722G)	<i>this study</i>
BL21 (DE3)	B-strain; F-, <i>lon-11</i> , $\Delta(ompT\text{-}nfrA)885$, $\Delta(galM\text{-}ybhJ)884$, $\lambda DE3$ [<i>lacI</i> , <i>lacUV5</i> - <i>T7 gene 1</i> , <i>ind1</i> , <i>sam7</i> , <i>nin5J</i>], $\Delta 46$, [<i>mal</i> '] _{K-12} (λ^S), <i>hsdS10</i>	Wood, W.B., <i>J Mol Biol</i> 16 , 118-133 (1966); Studier, F.W. & Moffatt, B.A., <i>J Mol Biol</i> 189 , 113-30 (1986)
BL21 ApiR10	derived from BL21 (DE3), <i>rplP</i> (G241A), pZ α -SbmA	<i>this study</i>
BL21 ApiR11	derived from BL21 (DE3), <i>prfB</i> (C784T), pZ α -SbmA	<i>this study</i>
BL21 ApiR12	derived from BL21 (DE3), <i>prfB</i> (A839T), pZ α -SbmA	<i>this study</i>
AB301	K-strain; Hfr(PO21), <i>relA1</i> , <i>spoT1</i> , <i>metB1</i>	Bouck, N. & Adelberg, E.A., <i>J Bacteriol</i> 102 , 688-701 (1970)
N281	K-strain; Hfr(PO21), <i>relA1</i> , <i>rplV281</i> , <i>spoT1</i> , <i>metB1</i>	Wittmann, H.G. et al., <i>Mol Gen Genet</i> 127 , 175-89. (1973); Chittum, H.S. & Champney, W.S., <i>J Bacteriol</i> 176 , 6192-8 (1994).
N282	K-strain; Hfr(PO21), <i>relA1</i> , <i>rplD282</i> , <i>spoT1</i> , <i>metB1</i>	Wittmann, H.G. et al., <i>Mol Gen Genet</i> 127 , 175-89. (1973); Chittum, H.S. & Champney, W.S., <i>J Bacteriol</i> 176 , 6192-8 (1994).
SQ171- $\Delta toIC$	derived from SQ171; $\Delta toIC$, pCSacB	Kannan, K., Vázquez-Laslop, N. & Mankin, A.S., <i>Cell</i> 151 , 508-520 (2012)
SQ171- $\Delta toIC$ /W3	derived from SQ171- $\Delta toIC$, <i>lacZ</i> (C2035T) pCSacB	<i>this study</i>
BW25113	F-, $\Delta(araD\text{-}araB)567$, $\Delta lacZ4787(\text{:rrnB-3})$, λ^- , <i>rph-1</i> , $\Delta(rhaD\text{-}rhaB)568$, <i>hsdR514</i>	Baba, T. et al., <i>Mol Syst Biol</i> 2 , 2006 0008 (2006)
BW25113 $\Delta xylA$ (JW3537)	F-, $\Delta(araD\text{-}araB)567$, $\Delta lacZ4787(\text{:rrnB-3})$, λ^- , $\Delta xylA748\text{:kan}$, <i>rph-1</i> , $\Delta(rhaD\text{-}rhaB)568$, <i>hsdR514</i>	Baba, T. et al., <i>Mol Syst Biol</i> 2 , 2006 0008 (2006)
BW25113 $\Delta prfC$ (JW5873)	F-, $\Delta(araD\text{-}araB)567$, $\Delta lacZ4787(\text{:rrnB-3})$, λ^- , <i>rph-1</i> , $\Delta(rhaD\text{-}rhaB)568$, <i>hsdR514</i> , $\Delta prfC770\text{:kan}$	Baba, T. et al., <i>Mol Syst Biol</i> 2 , 2006 0008 (2006)